Tarduno, J.A., Duncan, R.A., Scholl, D.W., et al., 2002
Proceedings of the Ocean Drilling Program, Initial Reports Volume 197

4. SITE 1204[1]

Shipboard Scientific Party[2]

BACKGROUND AND SCIENTIFIC OBJECTIVES

Site 1204 was the second Leg 197 site aimed at determining whether the Emperor Seamounts formed above a fixed or moving hotspot source that is presently located beneath Hawaii at ~19°N. (For more background on the hotspot hypothesis and the paleomagnetic test that is the primary objective of Leg 197, readers are directed to the **"Leg 197 Summary"** chapter and **"Background and Scientific Objectives,"** p. 1, in the "Site 1203" chapter). Site 1204 was targeted to be close to Site 883, drilled during Leg 145 in the summit region of Detroit Seamount (Rea, Basov, Janecek, Palmer-Julson, et al., 1993). The recovered section from two holes drilled at Site 883 guided our site selection. Specifically, biostratigraphic analyses of claystone recovered above basement in Hole 883E constrain the basement to be in the same Late Cretaceous stage (i.e., Campanian) as that cored at Detroit Seamount Sites 884 and 1203 (Fig. **F1**). Therefore, several aspects of the hotspot test could be addressed by the recovery of a deeper basement section near Site 883.

F1. Site 1204 location map, p. 37.

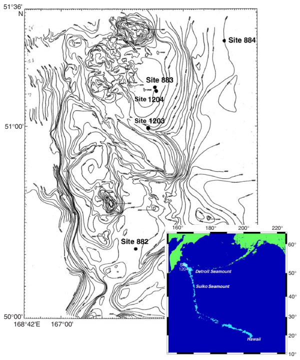

Specifically, we sought to confirm and further refine paleomagnetic constraints available from Site 884, on the eastern flank of Detroit Seamount, by obtaining paleomagnetic data from a nearby summit site (Fig. **F1**). Prior paleomagnetic analyses of 81-Ma basalt (Keller et al., 1995) recovered at Site 884 indicate a paleolatitude of 36.2° +6.9°/–7.2° (95% confidence interval), suggesting considerable southward motion of the Hawaiian hotspot source since the Late Cretaceous (Tarduno and Cottrell, 1997; Cottrell and Tarduno, in press).

Drilling of two basement holes at Site 883 resulted in 37.8 and 26.7 m of penetration (in Holes 883E and 883F, respectively). Analyses of basalt samples from these holes indicate paleomagnetic inclination values compatible with those recorded at Site 884 (Cottrell and Tarduno, 2001). But the characteristic remanence directions from the lava flows

---

[1] **Examples of how to reference the whole or part of this volume.**
[2] **Shipboard Scientific Party addresses.**

Ms 197IR-104

recovered at Site 883 do not appear to sample the full range of expected secular variation of the geomagnetic field. Accordingly, we planned to acquire additional lava flows erupted over a time longer than those recovered in Holes 883E and 883F. The available biostratigraphic ages suggest that it may be possible to combine paleomagnetic data from several of the basement sites on Detroit Seamount to derive the high-resolution, time-averaged determination of paleolatitude needed for the hotspot test.

Drilling at Site 1204 was also intended to provide additional data for evaluating the geochemical evolution of the Hawaiian plume. Prior analyses of basalt samples from Site 883 have indicated a transitional tholeiitic to alkalic composition (Keller et al., 1995), but alteration in the rocks recovered limits their use for radiometric and some geochemical studies. A deeper sampling of less altered rocks could provide material useful for further insight into the possibility that the plume source changed composition with time (M. Regelous et al., unpubl. data) and whether mantle upwelling beneath a spreading ridge interacted with the hotspot source (Keller et al., 2000) during the Campanian.

Site 1204 was chosen along a preexisting analog seismic reflection line (Lonsdale et al., 1993) and two digital seismic reflection profiles collected by the *JOIDES Resolution* en route to the site (see **"Operations,"** p. 2, and **"Underway Geophysics,"** p. 33). These surveys revealed a flat, cleanly imaged basement surface at Site 883 beneath ~850 m of sedimentary beds that are mainly composed of the Oligocene and younger Meiji drift deposits (Rea et al., 1995). Site 1204 was positioned ~0.5 km from Site 883 to avoid drilling pipe left at Site 883 during Leg 145 (Rea, Basov, Janecek, Palmer-Julson, et al., 1993). Coring at Site 1204 was planned to begin in the lower sedimentary section to both characterize the depositional environment of the basement–sediment transition and to determine the age of the transition using micropaleontological data.

OPERATIONS

Transit to Site 1204 and Underway Survey

The provisional location of Site 1204 was at or close to Site 883, where ~38 m of basalt had been penetrated and partly cored during Leg 145. The site survey was under way 1 hr after departing Site 1203.

After the vessel slowed to 6 kt, seismic equipment and the magnetometer were deployed and the survey was started using one 80-in^3 water gun and a single-channel Teledyne hydrophone streamer. Reflection profiles of good quality were displayed on two software-controlled EPC recorders operating at different scanning speeds. The position selected was ~0.5 km from the six holes cored and drilled during Leg 145 at Site 883. At 1500 hr on 25 July 2001, the seismic equipment was retrieved as the vessel came about to return to Site 1204. Thrusters were lowered, and the vessel was maneuvered to the Global Positioning System (GPS) coordinates of the new location by 1534 hr. The hydrophones were then lowered, concurrent with the making up of a new bottom-hole assembly (BHA). A beacon was deployed at 1614 hr. The 37-nmi survey was accomplished in 6.2 hr at an average speed of 6.0 kt.

Hole 1204A

After the vessel settled on location, the corrected precision depth recorder (PDR) depth referenced to the dual elevator stool (DES) was obtained and indicated 2604.4 m. The BHA was made up of a 9.875-in rotary core barrel (RCB), a medium-hard formation C-4 bit, a mechanical bit release, a modified head sub, an outer core barrel, a modified top sub, a modified head sub, seven 8.25-in drill collars, a tapered drill collar, six 5.25-in drill pipe segments, and one crossover sub.

Hole 1204A was spudded with the RCB at 2015 hr on 25 July. The drill string was drilled ahead with a center bit in place to a depth of 761.9 meters below seafloor (mbsf), where coring was initiated in nannofossil ooze and chalk. Coring advanced through 57.6 m of sediment at an average rate of penetration (ROP) of 28.8 m/hr (recovery = 66.3%). Basement coring began with Core 197-1204A-7R (819.5–829.0 mbsf). As coring progressed, a low-pressure system developed and the weather deteriorated. By the early morning hours of 28 July, vessel heave was occasionally measured at 16 ft. Winds were 25–30 kt from the northwest, and seas were estimated between 10 and 12 ft from the northwest. The main swell emanated from the north-northeast. The barometer was steady at 1000 mbar.

After Core 197-1204A-10R (843.3–857.9 mbsf; ROP = 2.0 m/hr) was recovered (recovery = 79%) (basalt), seawater was observed flowing back at the rig floor connection, indicating that the float valve was jammed open (probably with basalt fragments). Three runs were made with the deplugger before the flow was stopped. Coring resumed with Core 197-1204A-11R (857.9–862.7 mbsf), representing a 4.8-m advance. No recovery was achieved, but because the core catcher had one finger missing, the core might have slipped out during recovery of the core barrel. A fresh core barrel was dropped, and Core 197-1204A-12R (862.7–867.5 mbsf; ROP = 3.8 m/hr) was cored an additional 4.8 m. The core barrel was recovered empty. A deplugger was deployed with paint on the latch dogs to verify the engagement of the core barrel in the BHA. The deplugger was recovered and appeared to have engaged in the latch sleeve. It was surmised that a formation change signaled by the increased ROP could have involved the coring of volcaniclastic sediment, and because of the large heave the sediment was not recovered. A fresh core barrel was dropped, and Core 197-1204A-13R (867.5–877.1 mbsf; ROP = 2.6 m/hr) advanced 9.6 m. The core barrel was recovered empty.

In a last attempt to save the hole, a fifth deplugger run was made and engagement with the latch sleeve was suggested by the abrasion on the latch dogs of the rotary assembly. This time, Core 197-1204A-14R (877.1–880.3 mbsf; ROP = 5.5 m/hr) was intentionally advanced only 3.2 m. Because no recovery was achieved, the drill string was tripped to the surface to determine the mechanical reason for the failure to recover core. Because of rough sea conditions, the deployment of a free-fall funnel was not attempted. Total core recovered from Hole 1204A was 55.86 m (recovery = 47.2%) (Table T1).

T1. Coring summary, Site 1204, p. 105.

When the BHA was recovered, the bit was removed and the throat of the bit was found to be full of basaltic debris, some of which was current-rounded pebbles. The bottom of the mechanical bit release below the float valve was also jammed with basalt. The total amount of recovered basalt filled one 1.5-m section. The bit was in very good condition (1, 1, NO, E, 1/16, HP, RR) after accumulating 30.3 total rotating hours. Of the total rotating hours, 10 hr was required to drill 762 m of sediment and an additional 2 hr was needed to core the basal ~58 m of sediment. The remaining 18.3 hr was expended penetrating 60 m into basement.

The latch sleeve was inspected and was found to be in gage with no apparent wear. A new C-4 bit was affixed to a fresh mechanical bit release, and the drill string was deployed to spud Hole 1204B. This incident was classified as weather induced. The active heave compensator was in operation during this incident.

Hole 1204B

The vessel was offset 100 m southeast of Hole 1204A, and Hole 1204B was spudded at 2015 hr on 28 July. The seafloor was tagged at 2381.0 m relative to the DES on the rig floor.

The RCB system was drilled ahead with an average ROP of 73.7 m/hr to a depth of 810.7 mbsf. This depth was estimated to be within 5–10 m of basement. The first core (197-1204B-1R [810.7–820.3 mbsf]) (Table T1) contacted basement at a depth of 816.0 mbsf. Coring then advanced without incident to a depth of 906.3 mbsf. After recovering Core 197-1204B-11R, seawater was flowing back at the rig floor level from the open end of the drill string, indicating that basalt had jammed in the float valve. This was the same phenomenon that forced an early cancellation of Hole 1204A. It required six deployments of the deplugger and one core barrel round trip to clear the obstruction from the float valve. The time expended in this process was 8.8 hr.

Coring resumed, and Hole 1204B had been deepened to 954.5 mbsf when time expired on site. A total of 138.5 m of basaltic basement was cored (average recovery = 38.0%). The cored sedimentary section was 5.3 m (recovery = 62.5%). The average ROP in basement was 3.6 m/hr. The basement ROP ranged from 0.9 m/hr (Core 197-1204B-9R [887.1–888.8 mbsf]) to 5.5 m/hr in the bottom 19.3 m of the hole. An operation problem required using the aft coring line to retrieve Core 197-1204B-17R. Total core recovered from Hole 1204B was 55.93 m (recovery = 38.9%) (Table T1).

The drilling equipment was secured in preparation for the 2-day transit to Site 1205 at Nintoku Seamount. This included the complete disassembly of the BHA. Although the bit had acquired 50.4 hr of use, it appeared to be in excellent shape with only two plugged nozzles to show that it had been in service. The bit was slightly under gage with all the inserts in the cones and no chipped teeth. The beacon was successfully recovered. The vessel began the transit to the next site at 2100 hr on 1 August.

LITHOSTRATIGRAPHY

Coring at Site 1204 began beneath the Meiji drift sequence (Rea, Basov, Scholl, and Allan, 1995) at a depth of ~762 mbsf, recovering a relatively condensed sequence of nannofossil chalk with volcanic ash layers of middle Eocene to late Paleocene age. Two holes, 1204A and 1204B, were drilled at the site, located ~500 m southeast of Site 883 (Leg 145) (Rea, Basov, Janecek, Palmer-Julson, et al., 1993). Time constraints limited the coring of sediment to the last 54.5 m (Hole 1204A) and 3.3 m (Hole 1204B) above basement encountered at ~817 and ~810 mbsf, respectively. RCB recovery of the sedimentary sequence was 90.7% (Core 197-1204A-1R) to 48.1% (Core 197-1204A-2R) in Hole 1204A and 48.4% in Hole 1204B (Core 197-1204B-1R).

Core descriptions in Hole 1204A are based on visual core observations, analysis of smear slides, inspection of magnetic susceptibility data, and chemical analyses of carbonate content, which together provided information for constraining the unit boundaries. Additional observations have been made on selected cores (e.g., Cores 197-1204A-3R, 5R, and 6R) for better understanding of instrumental (magnetic susceptibility) and lithostratigraphic (i.e., color, texture, and composition) correlations. Magnetic susceptibility was measured at 5-cm resolution (see **"Physical Properties,"** p. 30).

In general, bedding in the sediment is not disturbed by the drilling. Moderate bioturbation, horizontal to subhorizontal *Zoophycos* trace fossils, and vertical burrows are sparse throughout. Thin laminations and discordant and undulating bedding planes are common and indicate deposition by bottom currents.

In Hole 1204A, four lithostratigraphic units (Units I, II, III, and IV) of Late Cretaceous (Campanian) to middle Eocene age as constrained by nannofossil analyses (see **"Biostratigraphy,"** p. 10) are present. The units are characterized by finely laminated chalk alternating with clayey nannofossil chalk and clay, which are interbedded with massive to laminated and strongly altered to unaltered volcaniclastic material. The lowermost unit has been divided into two subunits, IVA and IVB, on the basis of compositional (Table T2) and lithologic variability (Figs. **F2, F3, F4**). The two subunits are recognized in both Holes 1204A and 1204B but differ in thickness between sites. In Hole 1204B, Unit IV was recovered in the single core (197-1204B-1R) (Fig. F3).

The upper part of Hole 1204A (Unit I) consists almost exclusively of calcareous pelagic chalk with a high nannofossil content ($CaCO_3$ = 50.6–92.0 wt%; average = 77.4 wt%; N = 6). In Unit II, nannofossil content drops to 3%–30%, although the measured carbonate content varies widely (0.77–88.75 wt%; average = 46.1 wt%; N = 18). The Unit I/II boundary is also associated with an abrupt upward decrease in volcanic components (i.e., opaque minerals, Fe oxides, ash particles, and related alteration products such as palagonite and clay).

In Unit II, clay-sized carbonate particles (transparent to translucent calcareous clay) dilute the nannofossil content and represent the main source of carbonate in the sediment. This sequence contains a zone of sedimentary slumping (Fig. **F4A**), also preserved at Site 883 and at Site 884 (at the base of the eastern flank of Detroit Seamount) in the form of blocks of well-bedded ash layers (Fig. **F4A**). These ash layers also produce elevated peaks in magnetic susceptibility (Fig. F2).

In Unit III, consisting of chalk of early Eocene age (see **"Biostratigraphy,"** p. 10), carbonate accumulation and preservation reach optimum values and $CaCO_3$ never drops below 82 wt% (Fig. F2A; Table T2). Unbroken and fragmented foraminifers reach maximum abundance in interval 197-1204A-5R-2, 85–112 cm (802.6–802.9 mbsf). Also, calcite and dolomite peaks are in phase with altered feldspars. Volcanic ash and palagonite fragments are virtually absent in this unit but increase in abundance (to maximum values) in Unit III and Subunit IVA, which are Late Cretaceous to late Paleocene in age. At the Subunit IVA/IVB boundary, altered volcaniclastic clay and silt give way to a redeposited low-carbonate diamictite (Fig. F3) that was more completely recovered in Hole 1204B.

T2. Carbonate abundance data, p. 107.

F2. Hole 1204A components vs. magnetic susceptibility, p. 38.

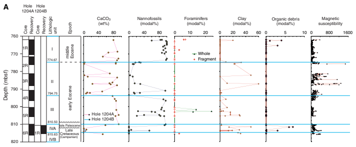

F3. Hole 1204B components vs. magnetic susceptibility, p. 40.

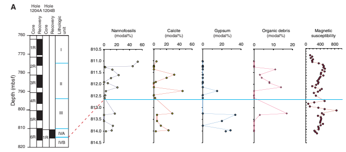

F4. Lithologies observed at Site 1204, p. 42.

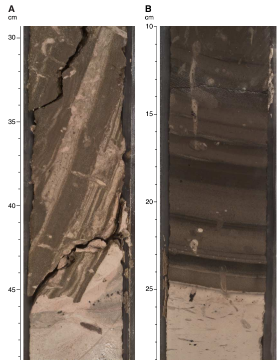

Description of Lithologic Units

Unit I

Interval: 197-1204A-1R-1, 0 cm, to 2R-3, 17 cm
Depth: 761.9–774.7 mbsf
Age: middle Eocene

Unit I (761.9–774.7 mbsf) is characterized by light colors and consistently high carbonate values (51–92 wt%) (Table T2) that are directly related to the high content of nannofossils (80%–100%) and foraminifer fragments (up to 6%). Contacts are mainly sharp and often penetrated by horizontal and vertical burrows.

The unit is also characterized by low magnetic susceptibility values (20×10^{-6} to 100×10^{-6} SI) (Fig. F2). Differences in color in calcareous and nannofossil chalk (i.e., pinkish white and light gray and light brownish gray) are due to varying amounts of clay, Fe oxide, carbonate, and organic debris. In this unit the magnetic susceptibility values ($\geq 120 \times 10^{-6}$ SI) appear to be correlated with several factors, including slight changes in grain size (i.e., clay to silt) and composition (e.g., Fe oxide and carbonate). Specifically, magnetic susceptibility seems to be sensitive to the presence of low but variable abundances of Fe oxide in the sediment (see **"Site 1204 Smear Slides,"** p. 80).

The Unit I/II boundary at Section 197-1204A-2R-3, 17 cm (774.7 mbsf), is at the upward termination of the cyclic deposition of ash-rich yellowish brown silt and nannofossil beds. This boundary is a sharp contact between very pale brown (10YR 8/3) chalk and the underlying brown beds. At the same depth nannofossil content decreases abruptly downward, from ~98% to 27%, along with the carbonate content (Fig. F2A; Table T2). Magnetic susceptibility peaks seem to correlate with composition, thickness, intensity, and structure of each single brown bed. For example, in Section 197-1204A-3R-1, the presence of 5- to 7-cm-thick beds is correlated with magnetic susceptibility values of 500×10^{-6} and 720×10^{-6} SI, whereas values of 450×10^{-6} to 500×10^{-6} SI are present in intervals containing thinner brown laminae (<1 cm) of silt-sized volcanic material.

Unit II

Interval: 197-1204A-2R-3, 17 cm, to 4R-3, 105 cm
Depth: 774.7–794.8 mbsf
Age: early to middle Eocene

Unit II contains nannofossil chalk and calcareous to clayey nannofossil chalk that exhibit pervasive submillimeter lenticular and undulating laminations. They are interbedded with brown to very dark gray beds of unaltered vitric ash with coccoliths as a secondary component. Centimeter- to decimeter-thick beds of dark yellowish brown (10YR 4/4) and black (5YR 2.5/1) volcaniclastic sandy silt contain unaltered and altered (palagonite) glass fragments. Sometimes, the brown beds are distinctly laminated, whereas on other occasions they are structureless with vertical burrows at the top. The brown beds generally contain more altered glass (palagonite) than the black beds.

The thickest bed is 57 cm and is sharply laminated with unaltered glass fragments at the bottom (intervals 197-1204A-3R-4, 120–125 cm, and 3R-5, 15–27 cm) and glass fragments altered to palagonite at the top (intervals 197-1204A-3R-4, 130–135 cm, and 3R-5, 5–13 cm) (e.g., Fig. **F4B**). The occurrence of such a thick volcanic interval explains the highest magnetic susceptibility values (1100×10^{-6} to 1300×10^{-6} SI) obtained for sediment in this hole.

A highly tilted "rotated block" of laminated volcaniclastic sediment (brown Fe oxide and palagonite-rich silt to silty clay), which is scoured and burrowed at its top, is present in interval 197-1204A-3R-2, 17–45 cm. This block is associated with high magnetic susceptibility values (up to 700×10^{-6} SI) and lies on folded and laminated calcareous chalk (see Fig. **F4A**). This suggests tectonically induced postdepositional slumping or sliding, although this interpretation should be taken with caution because it is based only on a preliminary examination of this core section.

The Unit II/III boundary is at Section 197-1204A-4R-3, 105 cm (794.8 mbsf). At this level nannofossil and carbonate abundance shows an abrupt downward increase (Fig. **F2A**). This boundary is associated with a downcore decrease in the magnetic susceptibility amplitude from maxima of 370×10^{-6} to 180×10^{-6} SI rather than with an abrupt shift in the absolute values at the lithologic boundary.

Unit III

Interval: 197-1204A-4R-3, 105 cm, to 6R-1, 60 cm
Depth: 794.8–810.5 mbsf
Age: late Paleocene to early Eocene

Unit III is white nannofossil chalk interbedded with clayey nannofossil chalk and nannofossil-foraminifer chalk. Magnetic susceptibility values rarely exceed 300×10^{-6} SI. These dominant lithofacies and the highest carbonate measurements (82.3–92.7 wt%; average = 87.4%; $N = 6$) indicate stable conditions for the deposition and/or preservation of biogenic carbonate.

The Unit III/IV boundary at Section 197-1204A-6R-1, ~60 cm (810.5 mbsf), is characterized by a sharp and bioturbated contact between light reddish brown (5YR 6/4) nannofossil chalk and pale red (10YR 6/3) clay-rich calcareous chalk (Fig. **F4C**).

Unit IV

Interval: 197-1204A-6R-1, 60 cm, to 6R-5, 32 cm, and 197-1204B-1R-1, 0 cm, to 1R-3, 31 cm
Depth: 810.5–815.8 and 810.7–814.0 mbsf
Age: Late Cretaceous (Campanian) to late Paleocene.

This unit has been divided into two subunits, IVA and IVB.

Subunit IVA

Interval: 197-1204A-6R-1, 60 cm, to 6R-5, 13 cm, and 197-1204B-1R-1, 0 cm, to 1R-2, 47 cm
Depth: 810.5–815.6 and 810.7–812.7 mbsf
Age: Late Cretaceous (Campanian) to late Paleocene.

In Hole 1204A, Subunit IVA is thicker (i.e., 511 cm thick) than in Hole 1204B (i.e., 197 cm thick) (Fig. **F3**).

A sharp drop occurs in nannofossil and carbonate content in Subunit IVA (late Paleocene to Late Cretaceous). Nannofossil chalks ($CaCO_3$ = 57.5 wt%; *N* = 1) are frequently interbedded with Fe oxides and palagonite-rich clay ($CaCO_3$ = 0.11–0.23 wt%; *N* = 2) and/or nannofossil clay that is more depleted in nannofossil and carbonates ($CaCO_3$ = 7.2 wt%; *N* = 1).

In Subunit IVA bioturbated yellow and brown beds of silty clay and olive clay are interbedded with coarse- to fine-grained sediment containing volcanic ash. Yellow-olive-brown to olive clay includes fine black specks of Fe/Mn oxides (confirmed by inductively coupled plasma–atomic emission spectroscopy [ICP-AES] analysis) exhibiting spotty to laminated or vertical dendritic patterns produced by diagenetic growth. Similar centimeter-thick beds of this material alternate with more bioturbated ones, which are brown to yellow layered clay (after volcanic ash?) and finely laminated clayey Fe oxide–rich nannofossil chalk (interval 197-1204A-6R-3, 78–105 cm).

The basal section of Subunit IVA (i.e., interval 197-1204A-6R-3, 105 cm, to 6R-5, 12 cm) contains a thick (1.64 m) olive palagonite clay interval that exhibits consistently low magnetic susceptibility values (i.e., 50×10^{-6} to 100×10^{-6} SI). This is a typical signature for this lithology and is the same for thinner centimeter- to decimeter-thick beds. These are present throughout the Fe oxide–bearing chalky beds showing higher values (i.e., 150×10^{-6} to 450×10^{-6} SI) for the subunit.

Subunit IVA brackets the Cretaceous/Tertiary (K/T) boundary (upper Paleocene to upper Campanian), but its location and recovery remains uncertain (see **"Biostratigraphy,"** p. 10).

The Subunit IVA/IVB boundary (Fig. **F3**) corresponds to a sharp contrast between olive palagonite clay (Subunit IVA) and diamictite (Subunit IVB). The sharp change in the magnetic susceptibility corresponds to the marked compositional contrast across the contact between the firm olive clay and mud conglomerates (diamictite). This boundary is characterized by the same magnetic susceptibility signature in the two holes. Specifically, magnetic susceptibility values are 70×10^{-6} to 350×10^{-6} SI in Hole 1204A and 150×10^{-6} to 450×10^{-6} SI in Hole 1204B for Subunits IVA and IVB, respectively.

Subunit IVB

Interval: 197-1204A-6R-5, 13 cm, to 6R-5, 32 cm, and 197-1204B-1R-2, 47 cm, to 1R-3, 31 cm
Depth: 815.6–815.8 and 812.7–814.0 mbsf
Age: Late Cretaceous (Campanian) to late Paleocene.

In Hole 1204A Subunit IVB is condensed (19 cm thick), whereas in Hole 1204B Subunit IVB is ~144 cm thick (Fig. **F3**). In Hole 1204B, Subunit IVB consists of poorly lithified and generally unsorted conglomerate (diamictite). Pebble-sized clasts are densely packed in a carbonate-poor silt-clay matrix ($CaCO_3$ = 1.2–4.6 wt%; *N* = 2). The clasts consist of (1) silty clay and clay grains (mud grains) and (2) rounded to subangular pebbles of basalt and red silty sandstone. Sand to gravel-sized grains have a range of colors, reflecting differences in their make up, such as Fe oxide, palagonite, and gypsum-rich clay (see **"Site 1204 Smear Slides,"** p. 80; Fig. **F3A**). Sand-sized crystals of tabular gypsum were observed (≥63–2000 µm) in sieved samples in intervals 197-1204B-1R-2, 30–31 cm, and 1R-2, 111–112 cm. Because of their mixed Maastrichtian to Campanian age (see **"Biostratigraphy,"** p. 10) and reworked materials, Subunit IVB can be defined as a resedimented diamictite, and the lithologic logs in Figure F3B reflect this variation in the bulk compositions of matrix and clasts.

Discussion

Integration of the work done by the sedimentology and physical properties groups provided better synopsis and constraints on the origin of the volcaniclastic and biogenic sediment recovered at Site 1204. Magnetic susceptibility data commonly correlate with lithology in Holes 1204A and 1204B and aided interhole correlation. Because of low drilling disturbance in Holes 1204A and 1204B, magnetic susceptibility data were more useful in detecting lithologic boundaries and compositional/textural changes than in Hole 1203A.

High-resolution shipboard observations have raised questions related to the Upper Cretaceous/Tertiary sedimentation before deposition of the Meiji drift sequence. First, the Hole 1204B lowermost Subunit IVA has a different thickness than Subunit IVA in Hole 1204A (spaced at ~100 m). This observation and the evidence of heterogeneous, unsorted detrital material (i.e., nannofossil chalk, palagonite clay, gypsiferous clay, red sandstone, and basalt pebbles) and reworked debris suggest erosion from various source areas (e.g., shallow-water marine sediment, subaerial and submarine lava flows, and subaerial sedimentary sequences). Second, the exact position of the K/T boundary in Subunit IVA remains uncertain.

In the upper units of Hole 1204A, two periods of persistent calcareous sedimentation (Units I and III) are associated with current-related structures (e.g., undulating microlaminations) and intense bioturbation. This indicates good ventilation at the ocean floor and stable conditions for biogenic calcareous deposition and carbonate preservation during early to middle Eocene time.

However, more intense volcanic activity and occasional periods of regional tectonic instability occurred during the deposition of Unit II (early to middle Eocene time) on the slopes of Detroit Seamount. This is suggested by intraformational sediment folding and slumped blocks, also preserved at Sites 883 and 884 (Rea, Basov, Janecek, Palmer-Julson, et al., 1993) that might be responsible for regional downslope sediment redistribution (Schlanger and Premoli-Silva, 1981; Rea and Thiede, 1981). The strong reduction in preservation or deposition of carbonate observed for the lower Eocene pelagic sediment seems to be associated with frequent episodes of nearby volcanic (subaerial) activity, as recognized both at scattered locations in the central North Pacific Ocean (Vallier et al., 1983) and during Leg 145.

At Site 883 the carbonate content was suggested to be entirely regulated by the sedimentation of calcareous nannofossils rather than other detrital calcareous components (Rea, Basov, Janecek, Palmer-Julson, et al., 1993). However, at the top of the lower Eocene sequence (Unit II) the total carbonate ($CaCO_3$) does not appear to be correlated with the relative abundance of calcareous nannofossils. Further work is needed to confirm this observation and examine its potential implication.

BIOSTRATIGRAPHY

Calcareous Nannofossils

We made biostratigraphic assignments to core catcher and other selected samples using calcareous nannofossils. Figure **F5** presents summaries of biozonal assignments. Abundance and distribution of nannofossils in each sample studied were recorded in the paleontology (PAL) database and are shown in Tables **T3** and **T4.**

F5. Calcareous nannofossil zones, p. 44.

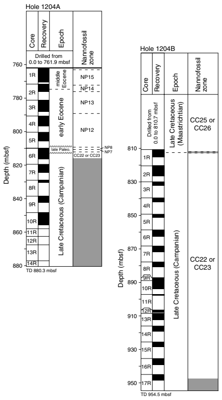

T3. Distribution, abundance, and biozones of nannofossils, p. 108.

T4. Distribution, abundance, and biozones of nannofossils, p. 110.

Hole 1204A

Hole 1204A was drilled in a water depth of 2371 m. The hole was drilled ahead to 761.9 mbsf with the rotary core bit, where coring commenced. Basalt was reached at Section 197-1204A-6R-5, 10 cm. Samples from Cores 197-1204A-1R to 6R contain nannofossils ranging from few to common in abundance. Preservation ranges from poor to moderate.

Zonation

We assign Samples 197-1204A-1R-1, 50–51 cm, to 1R-CC, to Zone NP15 (middle Eocene), based on the presence of *Nannotetrina fulgens* and the absence of *Discoaster lodoensis* and *Reticulofenestra umbilicus*. Samples 197-1204A-2R-1, 50–51 cm, to 2R-3, 50–51 cm, are in Zone NP14 (which spans the early Eocene/middle Eocene boundary), as indicated by the presence of *D. lodoensis* and *Discoaster sublodoensis*. Samples 197-1204A-2R-CC to 3R-CC lack *D. sublodoensis*. A few specimens of overgrown *Tribrachiatus orthostylus* are present in these samples, but we believe these specimens to be reworked from Zone NP12 below, where *T. orthostylus* is a common component of the assemblage. We therefore discount the few specimens of *T. orthostylus* in these cores and assign Samples 197-1204A-2R-CC to 3R-CC to Zone NP13 (early Eocene). Samples 197-1204A-4R-1, 50–51 cm, to 5R-CC, contain *D. lodoensis* and *T. orthostylus,* indicating Zone NP12 (early Eocene).

Sample 197-1204A-6R-1, 25–26 cm, contains *Heliolithus riedelii, Heliolithus kleinpellii,* and *Fasciculithus tympaniformis* but lacks *Discoaster multiradiatus,* indicating Zone NP8 (late Paleocene). Therefore, a hiatus exists between Samples 197-1204A-5R-CC and 6R-1, 25–26 cm, representing at least 3.4 m.y. (duration of the NP9–NP11 zonal interval). Zone NP8 continues downward to Sample 197-1204A-6R-1, 58–59 cm. Samples 197-1204A-6R-1, 79–80 cm, to 6R-1, 107–108 cm, are in Zone NP7, based on the presence of *Discoaster mohleri* and the absence of *H. riedelii*.

The next nannofossil-bearing sample is 197-1204A-6R-2, 86–87 cm, which contains *Quadrum trifidum,* indicating a Campanian age (Zone CC22 or CC23). Although the CC22/CC23 zonal boundary marker (*Eiffellithus eximius*) is not present, *Aspidolithus parcus* is present in the sample. The extinction of *A. parcus* is most often given in the literature as occurring low in Zone CC23 at 74.5 Ma (e.g., Erba et al., 1995) (see also Table **T3**). However, a recent compilation of Late Cretaceous zonations and datums by Burnett (1998) places the extinction of *A. parcus* higher in Zone CC23, at a level just below the Campanian/Maastrichtian boundary, which is dated at 71.3 Ma. *Q. trifidum* is also present in Sample 197-1204A-6R-3, 80–81 cm, again indicating Zone CC22 or CC23.

Closely spaced "toothpick" samples taken from the 128 cm of altered volcanic ash layers separating the lowermost Paleocene sample (197-1204A-6R-1, 107–108 cm) and the uppermost Campanian sample (197-1204A-6R-2, 86–87 cm) contain no nannofossils.

Hole 1204B

Hole 1204B was drilled in a water depth of 2370 m. The hole was drilled ahead to 810.7 mbsf with the rotary core bit. The first core taken contains the sediment/basalt contact in Section 197-1204B-1R-3, 33 cm. Samples 197-1204B-1R-1, 5–6 cm, to 1R-1, 31–32 cm, contain common to abundant, mostly poorly preserved nannofossils. The samples are dominated by species of *Micula,* including *M. decussata, M. swastica, M. concava,* and *M. murus.* The presence of *M. murus* indicates these samples are in upper Zone CC25 or CC26 (Maastrichtian). Samples between 197-1204B-1R-1, 125–126 cm, and 1R-2, 35–36 cm, are barren. Samples 197-1204B-1R-2, 89–90 cm, to 1R-3, 19–20 cm, contain few moderately preserved nannofossils, including *Q. trifidum* and *A. parcus.* These species indicate Zone CC22 or CC23 (Campanian), the same zonal assignment made in Hole 1204A (Fig. F5). A sample in the last core taken, Sample 197-1204B-17R-3, 80–81 cm, also contains *Q. trifidum,* indicating the same zonal interval is present to the bottom of the hole.

PHYSICAL VOLCANOLOGY AND IGNEOUS PETROLOGY

Site 1204 is ~57.3 km (31 nmi) north of Site 1203 (see **"Background and Scientific Objectives,"** p. 1) and within ~0.5 km of Site 883, where basement rocks were recovered from Detroit Seamount during Ocean Drilling Program (ODP) Leg 145 (Rea, Basov, Janecek, Palmer-Julson, et al., 1993). At Site 883, basalt was recovered from Holes 883E (penetration = 37.8 m; recovery = 63%) and 883F (penetration = 26.7 m; recovery = 41%), which was comprised of fractured and altered plagioclase-phyric pillow basalt and massive basalt lava flows.

Two holes (1204A and 1204B), ~100 m apart, were drilled at this site. The minimum age of basement in both holes is constrained to Late Cretaceous (Campanian; 71–76 Ma) by nannofossils in the immediately overlying sediment (see **"Biostratigraphy,"** p. 10). In Hole 1204A, basement was encountered at 819.5 mbsf (drilling depth [815.6 mbsf curated depth]) and drilled to 880.3 mbsf. Approximately 22.1 m of basement was recovered from Sections 197-1204A-6R-5 to 10R-6 (recovery = 52%). An additional 22.4 m of basement core was penetrated (Cores 197-1204A-11R to 14R), but there was no recovery because of a clogged bit. We divided the basement rocks into two units: clastic sediment (Unit 1) and basaltic lava flows (Unit 2). Subunit 1a is a diamictite, whereas Subunit 1b is a basalt lithic breccia. Unit 2 is composed of an aphyric to moderately olivine-plagioclase-phyric basalt consisting of multiple lobes (Table T5; Fig. F6).

T5. Division, naming, and recovery of basement units, p. 111.

F6. Recovery, age, and lithology of basement, p. 45.

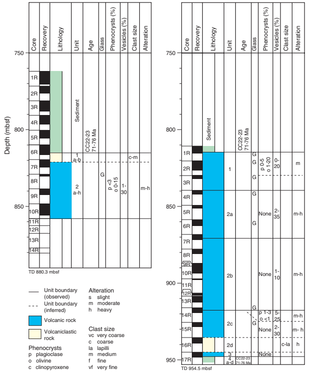

In Hole 1204B, basement was encountered at 816 mbsf (drilling depth [814.0 mbsf curated depth]) and drilled to 954.4 mbsf. Approximately 53.2 m of basement core was recovered from a penetration of 140.5 m (recovery = 37.9%). We divided the basement into four units: Unit 1 is an aphyric basalt, Units 2a–2d consist of the sequence aphyric basalt-diabase-aphyric basalt-hyaloclastite lapilli breccia, Unit 3 is an aphyric basalt, and Unit 4 is dominantly composed of calcareous sandstone and mudstone subdivided into Subunits 4a–4d (Table T5; Fig. F6). Nannofossils in Subunit 4b show the same age range (71–76 Ma) as the oldest nannofossils in the overlying sediment (Fig. F6; see also **"Biostratigraphy,"** p. 10).

Macroscopic Description

The major lithologic characteristics of Site 1204 rocks are summarized in Figure F6.

Hole 1204A

A subplanar, apparently conformable contact between Unit 1 and the overlying fine-grained, deepwater Campanian (71–76 Ma) sediment is seen in Section 197-1204A-6R-5 at 815.60 mbsf. Subunit 1a consists of a diamictite containing highly altered, aphyric vesicular basalt clasts up to 1 cm in diameter in a calcareous matrix. The upper part of Subunit 1b is composed of calcareous volcaniclastic sandstone and grades downward to breccia containing fragments of highly altered vesicular basalt and completely devitrified glass in a calcareous sandstone matrix (Fig. F7). Toward the bottom of Unit 1, the degree of abrasion and sorting decreases and the size and angularity of the clasts increase. Basalt clasts are similar in lithology to the underlying lava of Unit 2.

F7. Altered glass and vesicular basalt in carbonate cement, p. 46.

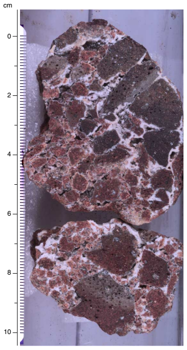

The contact between Subunit 1b and the underlying basalt of Unit 2 was not observed. It is inferred to lie at the bottom of Section 197-1204A-7R-1 (820.95 mbsf). Unit 2 is composed of aphyric to olivine-plagioclase-phyric basalt. The unit was divided into lobes, and the criteria for determining these subunit boundaries included changes in the phenocryst and vesicle content and the presence of glassy or aphanitic quenched lobe margins. We identified eight pahoehoe lobes (Subunits 2a–2h) that range in thickness from a few decimeters to several meters. These lobes probably represent a single lava flow. The thickest lobe (Subunit 2h) at the base of the Hole 1204A core was not fully recovered but it is >8 m thick. It has a smooth pahoehoe lobe surface, a vesicular upper crust (Sections 197-1204A-9R-4 to 10R-2), and a massive, nonvesicular lobe interior (Sections 197-1204A-10R-3 to 10R-6).

Unit 2 consists of aphyric basalt with variable amounts (0–10 modal%) of olivine microphenocrysts. Plagioclase phenocrysts are scarce but make up to 3 modal% of the rock in Section 197-1204A-9R-2. Phenocrysts are set in a fine-grained to aphanitic groundmass consisting of plagioclase, clinopyroxene, opaque oxides, and glass. Olivine microphenocrysts have been completely replaced, and their presence was inferred from pseudomorphs of carbonate and Fe oxyhydroxide. Plagioclase is typically clouded with sericite, and glass is partly to completely altered. A sharp alteration front is present in Core 197-1204A-10R, where the rock color changes from yellowish brown to green gray (see **"Alteration and Weathering,"** p. 20).

Many of the lavas are highly vesicular (up to 35 modal%) (1- to 4-mm-diameter vesicles), especially close to lobe margins. Pipe vesicles are common near lobe bases, and small vesicle cylinders (2–5 mm wide) are frequently found in the massive lobe interiors. Vesicles are variably filled with secondary minerals; calcite is the most common. Unfilled vesicles generally have an inner coating of clay minerals and Fe oxyhydroxide.

Hole 1204B

The lithologic components of the Hole 1204B rocks are listed by section in Table T6 and are summarized in Figure F6 and Table T5. The Hole 1204B lava units generally consist of multiple flow lobes that were identified using the criteria of variable vesicularity, presence of glassy (pahoehoe) lobe margins, and/or change in groundmass crystallinity and granularity (Table T6). Because of the <50% recovery (Fig. F6), we did not divide the basalt into subunits based on lobes.

T6. Lithologic components of basement units, Hole 1204B, p. 112.

Unit 1 consists of at least nine pahoehoe lobes, ~0.3 to 5.0 m thick, with variable vesicularity. They are composed of aphyric basalt with minor olivine (3%–8%) and scarce plagioclase (1%–5%) microphenocrysts (Table T6). When olivine is present, it is as either a microphenocryst or a groundmass phase. In the upper part of Unit 1 (Sections 197-1204B-1R-3 to 2R-2), the cooling cracks of the lava are filled with fine- to coarse-grained carbonate sandstone, which in places shows well-developed planar laminated bedding (Fig. F8). The lower part of Subunit 2a (i.e., Sections 197-1204B-3R-1 to 4R-1) consists of <1-m-thick lobes intercalated with decimeter-thick intervals of lapilli breccia consisting of 2- to 30-mm angular fragments of vesicular basalt glass and lava lithics embedded in fine- to medium-grained carbonate sand. The basalt lapilli breccia fragments are of the same lithology as the associated lobes. This lithofacies association shows that the lava flow interacted with a preexisting carbonate sand layer, forming the brecciated intervals in the process, most likely by quenched fragmentation. Furthermore, this occurrence suggests a significant time gap in the lava accumulation, and it is the basis of our division between Units 1 and 2.

F8. Laminated carbonate sand filling joints in basalt lobes, p. 47.

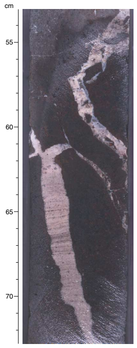

The basalt is moderately to highly altered with olivine completely replaced by carbonate or Fe oxyhydroxide, but plagioclase and pyroxene in the groundmass are only slightly to moderately altered (see **"Alteration and Weathering,"** p. 20). Glassy lobe margins are mostly altered to dark brown palagonite and clay, but some unaltered "islands" remain (e.g., interval 197-1204B-3R-2, 97–100 cm).

Subunit 2a consists of at least 30 variably vesicular, decimeter- to meter-thick lava flow lobes that are composed of aphyric basalt (Table T6). These lobes are moderately to highly altered basalt with petrographic characteristics that are indistinguishable from the basalt of Unit 1. A distinct lobe boundary is present at Section 197-1204B-7R-3, 30 cm. Farther downsection (at 125 cm) a sharp transition is present, although without clear indication of a lobe boundary, from highly vesicular aphanitic to fine-grained basalt to sparsely vesicular, medium-grained basalt with distinctive ophitic to subophitic (diabasic) texture. This transition marks our division between Subunits 2a and 2b (Table T5). Because this diabase appears to be a coarser-grained version of Subunit 2a, it is designated Subunit 2b rather than a new unit. At a depth of ~94 m into the basement, the grain size of the diabase begins to decrease and grades back into aphyric basalt that is virtually indistinguishable from that in Subunit 2a. A smooth-surfaced glassy (pahoehoe) lobe margin at ~918 mbsf (~104 m into basement) marks the base of Subunit 2b (Table T5).

The diabase is characterized by fine- to medium-grained plagioclase laths enclosed in large (≤6 mm) clinopyroxenes. As in the lava flows above, olivine microphenocrysts are completely replaced by Fe oxyhydroxide in oxidized regions and bluish-greenish gray clay in reduced regions (see **"Alteration and Weathering,"** p. 20). Vesicles in the reduced regions are filled with the same blue-gray clay that replaces the olivine and some of the groundmass, making the original proportions of these constituents difficult to estimate.

From 918 to 935 mbsf a series of vesicular pahoehoe lobes are present that we designate as Subunit 2c (Tables T5, T6). In terms of lithology, this unit is indistinguishable from the overlying lava flows; it contains sparse plagioclase and olivine (completely replaced by Fe oxyhydroxides) microphenocrysts. Underlying Subunit 2c is ~9.7 m of matrix-supported hyaloclastite lapilli breccia, Subunit 2d, consisting of angular basalt lapilli to breccia fragments in a matrix of fine lapilli (Table T5). Large basalt clasts are also present, and some are difficult to distinguish from discrete flows within the breccia sequence. Below the hyaloclastite breccia, a >2.3-m-thick aphyric basalt unit is present; it consists of at least five pahoehoe lobes (Table T6). In terms of its volcanic architecture and petrographic characteristics, this basalt is identical to the overlying flows in Unit 2, but it has a more evolved composition (see **"Geochemistry,"** p. 17). Therefore, this sequence of aphyric lobes is designated as Unit 3. The basal contact of Unit 3 is sharp and dips at 40° with glassy lobe margins resting directly on Subunit 4a.

Subunit 4a is a calcareous sandstone that exhibits disturbed bedding with steeply dipping (50°–60°) coarse sand and fine gravel layers that have convoluted and irregular bedding planes. The bedding in the sandstone is concordant with and roughly parallel to the basal contact of Unit 3, indicating that the disturbance is related to the emplacement of the lava flow onto unconsolidated sand. This disturbance is not found in the calcareous mudstone that makes up Subunit 4b, which may indicate that only part of Subunit 4a was recovered (Table T6). Subunit 4c is a clast-supported vitric-lithic lapilli breccia that is exceptionally matrix poor and exhibits inverse size grading. The lower contact with the underlying sandstone (Subunit 4d) is characterized by load casts indicating rapid deposition for the lapilli breccia, which may have been emplaced as a grain flow. Subunit 4d is a cross-stratified calcareous sand containing dispersed 2- to 10-mm lava lithic fragments (see **"Site 1204 Core Descriptions,"** p. 1).

Volcanology

We interpret the basalt units in Holes 1204A and 1204B to be pahoehoe lava flows because they consist of multiple lobes confined by smooth glassy lobe margins that are highly vesicular (Table T6). Several lobes show the threefold division into vesicular upper crust, massive lobe interior, and vesicular lower crust that is characteristic of pahoehoe lavas formed by an endogenous mode of emplacement (i.e., transport under insulating crust and growth by lava inflation) (Hon et al., 1994; Self et al., 1998). The internal architecture of the >8-m-thick pahoehoe lobe at the base of Hole 1204A and Subunit 2b in Hole 1204B is similar to that of large inflated pahoehoe sheet lobes (Thordarson and Self, 1998). Their presence within a package of smaller pahoehoe lobes is consistent with this interpretation.

We have identified the following lithofacies associations in the Hole 1204B succession: pahoehoe lava (Unit 3) resting on calcareous sediment (Unit 4), thick pahoehoe lava (Subunits 2a–2c) capping a hyaloclastite lapilli breccia, and a relatively thin pahoehoe flow containing intervals of lapilli breccia mixed with carbonate sand toward its base. These facies associations along with the pahoehoe nature of the lavas suggest that these flows originated from subaerial vents and were emplaced in a nearshore environment (see also Fig. F56, p. 83, in the "Leg

197 Summary" chapter). Finally, the presence of lapilli breccia mixed with carbonate sand on the top of the pahoehoe lava flow in Hole 1204A and the striking resemblance of Hole 1204A lavas to Subunit 2b–2c lavas in Hole 1204B in terms of their morphology, petrography, and chemical composition strongly suggest that these packages may be correlated. If this interpretation is correct, then the thick pahoehoe sheet lobe at the base of Hole 1204A most likely corresponds to the sheet lobe represented by Subunit 2b in Hole 1204B.

Nearby Holes 883E and 883F (Fig. F1) also recovered lava flows with multiple lobes that we infer are analogous to the pahoehoe lava flows in Holes 1204A and 1204B. Specifically, 27 basement units were identified in Hole 883E and 16 in Hole 883F; these units were defined on the basis of glassy margins and carbonate sediment filling voids between adjacent lobe bases of glassy margins and carbonate (Rea, Basov, Janecek, Palmer-Julson, et al., 1993). The basement units defined by Rea, Basov, Janecek, Palmer-Julson, et al. (1993) range in thickness from 0.2 to 2.7 m, and these units are equivalent to our definition of lobes. In their overall architecture and lobe structure the lava flows from Holes 883E and 883F and Holes 1204A and 1204B are identical. Therefore, we conclude that at Sites 883 and 1204, the basement consists of compound pahoehoe lavas erupted in a similar environment.

Petrography

Silicate Mineralogy

Lavas from Holes 1204A and 1204B are typically aphyric and range in grain size from basalt to diabase; diabase is present only in Hole 1204B. Plagioclase phenocrysts (0%–2%) can be distinguished by their more equant form, compared to those in the groundmass, and the presence of well-defined oscillatory zoning and fracturing (Fig. F9). Olivine, now pseudomorphed by Fe oxyhydroxide, iddingsite, and calcite (Fig. F10), is euhedral and typically of a similar size to the groundmass (≤0.8 mm), although its morphology may imply it is a microphenocrystic phase. Unaltered olivine is present in one section (interval 197-1204B-3R-2, 97–100 cm) in a glassy lobe margin (Figs. F11, F12). These olivines also contain melt inclusions (Fig. F13).

The groundmass of the basalt and diabase typically consists of skeletal or elongate plagioclase surrounded by clinopyroxene oikocrysts in a subophitic texture (Fig. F14). Clinopyroxenes range up to 5 mm in size and typically display a dusty pink color and weak pleochroism (Fig. F15), indicative of elevated Ti contents and suggesting an alkaline affinity for the lavas.

Glass and titanomagnetite are also present in the groundmass. Glass forms up to 30% and titanomagnetite up to 8% of the groundmass in lobe interiors. Glass is completely altered to green and brown clay and Fe oxyhydroxide, whereas the titanomagnetite shows partial to complete alteration to maghemite. In segregated areas adjacent to vesicles, clinopyroxene and titanomagnetite are concentrated, each displaying an acicular form (dendritic for titanomagnetite) indicative of a quench texture (Fig. F16). Clinopyroxene in segregated material found in vesicle cylinders (e.g., Sample 197-1204B-15R-1, 15–18 cm) (Fig. F17) and lining vesicles exhibits more pronounced pleochroism than it does in the groundmass.

Vesicles are present (0%–15%) and are round to irregular in form, are <1.5 mm in size, and are typically lined with green clay and filled with

F9. Optical zonation in a plagioclase phenocryst, p. 48.

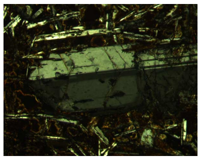

F10. Olivine pseudomorphed by Fe oxyhydroxide and goethite, p. 49.

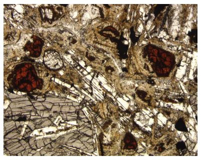

F11. Unaltered olivine and plagioclase in glassy lobe margin, p. 50.

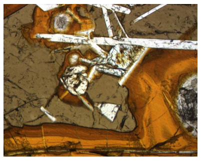

F12. Another view of unaltered olivine and plagioclase in glassy lobe margin, p. 51.

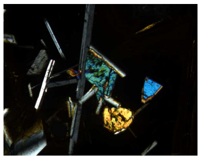

F13. Unaltered olivine with melt inclusions and plagioclase in glassy lobe margin, p. 52.

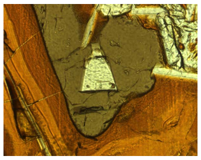

F14. Clinopyroxene partially enclosing plagioclase, p. 53.

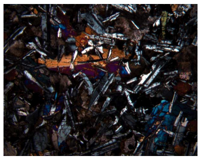

calcite, although some remain unfilled. The abundance of calcite is apparent in the chemical analyses. For example, Sample 197-1204A-7R-3, 36–37 cm, has the highest loss on ignition (LOI) (9.5 wt%) and the highest CaO contents (19.4 wt%) of the Site 1204 samples analyzed (Table T7).

No petrographic differences exist between the lavas of Holes 1204A and 1204B, apart from a coarsening in grain size in the Subunit 2b diabase in Hole 1204B. In contrast, most of the lavas at Site 1203 contain more plagioclase and olivine phenocrysts, both present as glomerocrysts.

Opaque Mineralogy

We note that the opaque mineralogy of the basalt and diabase units from Holes 1204A and 1204B is dominated by oxide and oxyhydroxide minerals (Table T8). The change in color from yellowish orange brown to greenish blue gray noted in Cores 197-1204A-10R and 197-1204B-9R and 13R conform with a change in alteration conditions from oxidizing to reducing (see **"Alteration and Weathering,"** p. 20). Sulfide, dominantly secondary pyrite, is present only in these greenish blue-gray, reduced regions (e.g., Fig. F18). Primary sulfide is extremely rare and is present only as blebs of micrometer-sized unidentifiable sulfide included in the primary silicate and oxide minerals.

The opaque mineralogy in the majority of the lavas consists of primary titanomagnetite with secondary maghemite, goethite, and Fe oxyhydroxide. Note that here, as in other Leg 197 site reports, we do not distinguish between maghemite and titanomaghemite (or Ti-bearing maghemite), as they are indistinguishable using reflected-light microscopy. Fe oxyhydroxide is a term used for a group of Fe-rich secondary minerals that have poor crystal form and include goethite when it is amorphous (α-FeOOH), akaganeite (ß-FeOOH), lepidocrocite (γ-FeOOH), feroxyhyte (δ-FeOOH), and ferrihydrite ($5Fe_2O_3{\cdot}9H_2O$) (see Waychunas, 1991). As is evident from Table T8, goethite in the igneous basement rocks from Site 1204 is generally well developed; where it exhibits a crystalline form and can be polished (e.g., Fig. F19), it is noted as a separate, identifiable mineral from Fe oxyhydroxide.

Titanomagnetite ($Fe^{2+}_{1+x}Fe^{3+}_{2-2x}Ti^{4+}_{x}O_4$) is present throughout the igneous basement at Site 1204. It is converted to cation-deficient titanomagnetite and eventually to maghemite (or titanomaghemite: $[(Fe^{3+}_{0.96}[\ ]_{0.04})(Fe^{2+}_{0.23}Fe^{3+}_{0.99}Ti^{4+}_{0.42}[\ ]_{0.37}O_4)]$ after Collyer et al., 1988, where [ ] represents cation vacancies) by oxidation at temperatures below ~250°C (Collyer et al., 1988; Goss, 1988; Banerjee, 1991). The oxidation process requires the addition of oxygen to the crystal boundary, as cations are not being removed; only their valence state is raised (Lindsley, 1976; Waychunas, 1991). Maghemite is metastable with respect to hematite, and the structure may require bonded water or H^+ ions for stabilization (Waychunas, 1991). Structurally, maghemite is a defect spinel with incomplete cation site occupancy.

In the basement sequence from both holes at Site 1204, where the alteration environment has been reducing (i.e., in the greenish blue-gray regions of the cores), titanomagnetite has not been visually altered (Fig. F18). However, where alteration has been oxidizing, titanomagnetite shows slight (Fig. F20A, F20B, F20C, F20D, F20E, F20F) to complete (Fig. F21A, F21B) alteration to maghemite (see also Table T7). Generally, maghemite engulfs titanomagnetite from the rim to the center of the crystal (e.g., Fig. F22A, F22B), but in some cases, maghemite growth

F15. Pink clinopyroxene partially enclosing plagioclase, p. 54.

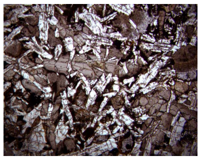

F16. Clinopyroxene and titanomagnetite on margin vesicle, p. 55.

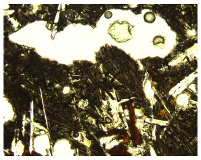

F17. Vesicle cylinder with clinopyroxene and titanomagnetite, p. 56.

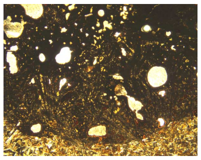

T7. ICP-AES whole-rock analysis for basalt, p. 114.

T8. Petrographic summary of opaque minerals in basalt, p. 116.

F18. Unaltered titanomagnetite and pyrite in reducing alteration zone, p. 57.

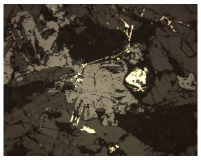

F19. Titanomagnetite with coronas of maghemite, p. 58.

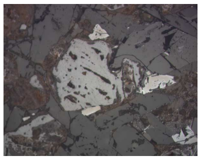

has exploited cleavage planes, leaving only relict strips of the titanomagnetite (Fig. F23A, F23B). Maghemite exhibits exsolution and breakdown in the more highly oxidized samples. For example, in Sample 197-1204B-10R-3, 25–27 cm, it has exsolved a darker gray-brown phase along cleavage planes (e.g., Fig. F24A, F24B). We tentatively suggest that this texture is caused by the Ti content of the maghemite reaching a concentration where it can not longer be accommodated, and it combines with the remaining Fe^{2+} to form ulvöspinel or ilmenite. Evidence that maghemite has become unstable is seen in Figure F25, where the rim of maghemite is degraded before complete replacement of the titanomagnetite has been achieved. We interpret this to indicate the continued presence of circulating water under low temperatures (≤150°C?) altering the maghemite to Fe oxyhydroxide rather than completing the transition to hematite.

Geochemistry

Major and trace element abundances were determined by ICP-AES (see **"Igneous Petrology,"** p. 16, in "Physical Volcanology and Igneous Petrology" in the "Explanatory Notes" chapter) for five samples from Hole 1204A and sixteen samples from Hole 1204B (Table T7). All samples from Site 1204 are alkalic basalt. The composition of lava flows from Hole 1204A and Subunits 2a and 2b in Hole 1204B overlap those from Site 883 (Fig. F26). Samples from Units 1, 2a, 2c, and 3 in Hole 1204B have the highest total alkali contents. Samples from Subunit 2a in Hole 1204B have relatively low SiO_2 contents (Fig. F26). Samples of Unit 1 and Subunit 2a lava from Hole 1204B and three samples from Site 883 have the lowest MgO contents of lavas recovered from Detroit Seamount (Table T7; Fig. F27). The Subunit 2a sample with the highest MgO content (Sample 197-1204B-7R-3, 42–44 cm) (Table T7) is the lowermost Subunit 2a sample analyzed. It is similar in composition to Subunit 2b samples (e.g., Fig. F27). It is possible that this sample is from the vesicular flow top of Subunit 2b (Table T6).

The samples are all altered, and LOI ranges from 1.93 to 9.48 wt% (Table T7; see also **"Alteration and Weathering,"** p. 20). The three Site 1204 samples (197-1204A-7R-3, 36–37 cm; 197-1204B-6R-4, 21–24 cm; and 197-1204B-7R-3, 140–142 cm) with the highest LOI have anomalously high CaO contents (15.4–19.4 wt%) (Table T7; Fig. F28). The sample with the highest LOI (Sample 197-1204A-7R-3, 36–37 cm) also has a low SiO_2 abundance (Table T7; Fig. F26). After normalization to a volatile-free basis, the other major and trace element abundances, including total alkali content, in this sample are comparable with those in the other four samples analyzed from Hole 1204A (Figs. F26, F27, F29). Apparently, this sample contains ~20 modal% carbonate, probably a result of abundant carbonate-filled vesicles. We infer that all samples with >15 wt% CaO (Table T7; Fig. F28) contain a secondary carbonate component, commonly introduced as vesicle fillings.

At a given MgO content, the Site 1204 basalt has TiO_2 contents intermediate between basalt from Site 884 and the alkalic lavas from Site 1203 (Fig. F27). In this TiO_2 vs. MgO plot, basalt compositions from Sites 883 and 1204 overlap and generally have slightly higher TiO_2 at a given MgO than the Site 1203 transitional to tholeiitic basalt.

Because Ti and Zr are incompatible and relatively immobile during alteration, we use a Ti vs. Zr plot to further investigate the petrogenesis of lavas forming Detroit Seamount (Fig. F29). Except for lavas from

F20. Titanomagnetite replacement by maghemite, p. 59.

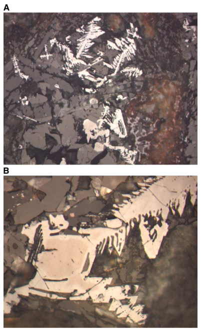

F21. Titanomagnetite replaced by maghemite, p. 62.

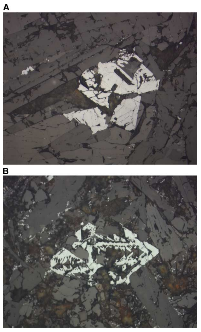

F22. Relict titanomagnetite with maghemite coronas, p. 63.

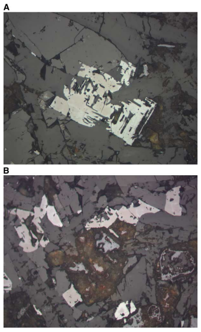

F23. Maghemite replacement of titanomagnetite, p. 64.

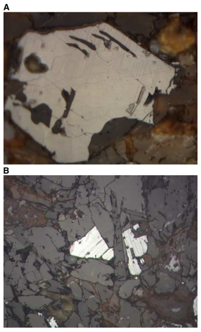

Units 23 and 26 at Site 1203, all of the Detroit Seamount lavas define a near-linear trend with Ti/Zr = 92 ± 7, very close to the primitive mantle estimate of 116 (Sun and McDonough, 1989). Basalt from Site 884 and the olivine-rich basalt (picrites) from Site 1203 have the lowest Ti and Zr abundances. For Site 884 basalt, a depleted source has been inferred (Keller et al., 1995, 2000; M. Regelous et al., unpubl. data), and for the Site 1203 picrites, the low abundances are the result of olivine accumulation. The highest Ti and Zr abundances are in the alkalic lavas from Site 1203. Since these have relatively high MgO contents (Table **T7**), their high Ti and Zr abundances are unlikely to be a result of extensive crystal fractionation.

Basalt from Site 883, Hole 1204A, and Subunits 2b and 2c from Hole 1204B have similar Ti contents, but these Site 1204 samples have slightly higher Zr contents than Site 883 lavas (Fig. **F29**). Since different analytical techniques were used for analyzing Site 883 lavas (X-ray fluorescence and inductively coupled plasma–mass spectroscopy]) (Keller et al., 1995; M. Regelous et al., unpubl. data) and Site 1204 lavas (ICP-AES) (see **"Igneous Petrology,"** p. 16, in "Physical Volcanology and Igneous Petrology" in the "Explanatory Notes" chapter), this difference in Zr content must be evaluated with shore-based analyses. We note, however, that most of the Site 1204 basalt ranges to higher Y contents than Site 883 basalt (Fig. **F30**), so it is possible that there are small but significant geochemical differences between lava flows from Sites 883 and 1204.

The low MgO lavas from Unit 1 and Subunit 2a in Hole 1204B have higher Ti and Zr abundances than other Site 1204 lavas, and this result is likely to be a result of extensive crystal fractionation. Some caution is required in interpreting the petrogenesis of Unit 1 and Subunit 2a basalt because two of the four samples from these units are anomalously enriched in P and Ba (Table **T7;** Fig. **F30**). These anomalies are likely to be the result of secondary apatite (see **"Alteration and Weathering,"** p. 20). Apatite in these samples is not obvious in thin section, but it may occur in the groundmass and as vesicle linings. The sample with the highest P content (Sample 197-1204B-4R-3, 29–31 cm) is also elevated in Y (Fig. **F30**), an element enriched in apatite, but these samples do not have anomalous Ti and Zr contents (Table **T7;** Fig. **F29**).

Detroit Seamount: Important Characteristics of the Igneous Basement at Four Drill Sites

Detroit Seamount has been sampled by six drill holes (Holes 883E, 883F, 884E, 1203A, 1204A, and 1204B, with basement penetrations of 37.8, 26.7, 87.0, 452.6, 47.3, and 140.5 m, respectively). Site 884 was in relatively deep water (3824 m) on the eastern flank of the seamount, whereas Sites 883, 1203, and 1204 were drilled in shallower water (2370–2593 m) on the plateau of the seamount (Fig. **F1**). Important results include the following:

1. Only tholeiitic basalt is present at Site 884, whereas tholeiitic and alkalic basalt are present at Site 1203 and transitional to alkalic basalt is present at Sites 883 and 1204. At Site 1203, the upper part of the ~453-m basement penetration includes nonvesicular pillow lavas, thick vesicular simple pahoehoe lavas (i.e., single-sheet lobes), and volcaniclastic sequences that indicate emplacement at shallow-water depths in a distal environment, relative to source vents. In the lower part of the sequence drilled

F24. Maghemite exsolving ulvöspinel or ilmenite, p. 65.

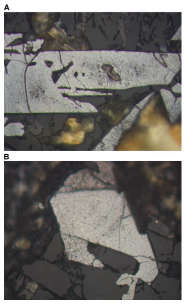

F25. Maghemite before replacement of titanomagnetite, p. 66.

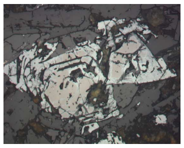

F26. Alkali vs. SiO_2 plot, p. 67.

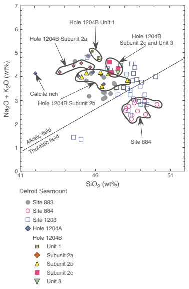

F27. TiO_2 vs. MgO, p. 68.

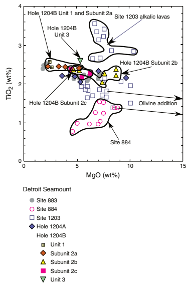

F28. CaO vs. loss on ignition, p. 69.

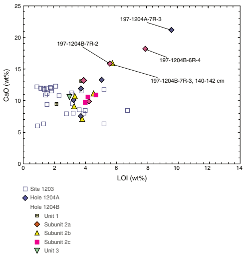

at Site 1203, thick (up to 65 m) vesicular compound pahoehoe lava flows suggest eruption in a subaerial environment with subsequent flow into shallow water. The presence of thick (up to 14 m) scoria fall deposits indicates close proximity to source vents. Much like the lower parts of the Site 1203 core, the pahoehoe lava flows at Site 1204 and the associated carbonate sand and hyaloclastite suggest that this part of the volcanic sequence originated from subaerial vents and was emplaced in a nearshore environment (see also Fig. **F56,** p. 83, in the "Leg 197 Summary" chapter).

2. Radiometric ages are available only for Site 884 basalt (81 Ma) (Keller et al., 1995). However, age constraints from nannofossils in the immediately overlying sediment and in sediment intercalated with the basalt (e.g., at the bottom of Hole 1204B and in Hole 1203A) show that recovered basalt from Sites 1203 and 1204 erupted at a younger age, in the interval 71–76 Ma.
3. The tholeiitic basalt at Site 884 is distinctive in its older age and geochemical characteristics. Relative to other lavas from Detroit Seamount, it is more depleted in abundances of incompatible elements and was derived from a parental magma that was unlike the parental magma composition for basalt from Sites 883, 1203, and 1204. The parental magma for Site 884 basalt had incompatible element abundances similar to that of mid-ocean-ridge basalt (MORB) parental magmas.
4. Four holes (883E, 883F, 1204A, and 1204B) are located within 500 m of each other (Fig. **F1**). In detail, the lava flows from these holes vary in composition. Nevertheless, after accounting for the effects of postmagmatic alteration, all lavas from these holes are transitional to alkalic basalt derived from parental magmas that had similar geochemical characteristics.
5. Most of the basalt at Site 1203 is intermediate in composition between basalt erupted at Sites 883 and 884. In the lower part of the Site 1203 core, however, there is alkalic basalt with relatively high MgO contents (6.3–9.9 wt%) coupled with high TiO_2 (2.6–3.4 wt%) and Zr (200–330 ppm) abundances. A subgroup of these alkalic lavas has an unusually low Ti/Zr ratio (~62). These alkalic lavas were derived from a parental magma that was geochemically distinct from the parental magma inferred for other alkalic basalt from Site 1203 as well as that from Site 1204.
6. Compared to the shield-stage tholeiitic basalt erupted at Hawaiian volcanoes, such as Mauna Kea Volcano, the tholeiitic to transitional basalt from Detroit Seamount has lower abundances of incompatible elements at a given MgO content. The alkalic basalt in the lower part of Hole 1203A is similar in composition to postshield and late-shield alkalic lavas erupted at Mauna Kea Volcano, but the lower Sr and Ba content of the Site 1203 samples is an important difference (see Fig. **F46,** p. 97, in the "Site 1203" chapter). Most importantly, the presence of this Site 1203 alkalic basalt beneath tholeiitic basalt contrasts with the shield (tholeiitic basalt) to postshield (alkalic basalt) transition that is characteristic of Hawaiian volcanoes and some Emperor Seamounts, such as Suiko and Ojin Seamounts.

F29. Ti vs. Zr, p. 70.

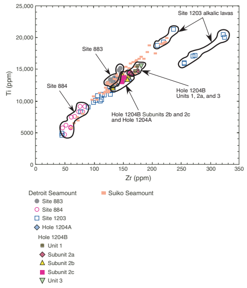

F30. Y, P, Sr, and Ba vs. Zr, p. 71.

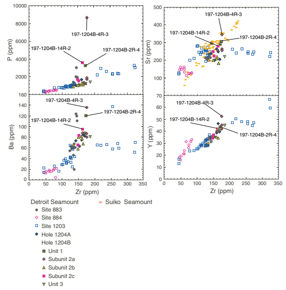

ALTERATION AND WEATHERING

Six basement units have been identified at Site 1204: two were defined in Hole 1204A and four were defined in Hole 1204B. In Hole 1204A, the sequence includes one basaltic unit and one unit composed of volcaniclastic breccia (see **"Physical Volcanology and Igneous Petrology,"** p. 11). In Hole 1204B, three lava flow units were identified, Unit 2 being subdivided into four subunits (2a, 2b, 2c, and 2d) (see **"Physical Volcanology and Igneous Petrology,"** p. 11). The lava flow subunits overlie a fourth subunit of volcaniclastic breccia. Unit 4 is a calcareous vitric-lithic sandstone.

All lava flows and volcaniclastic sediments have undergone secondary alteration. Alteration mineralogy as well as vesicle and vein fillings were defined in rocks from Site 1204 by color, habit, and hardness in hand specimen, by optical properties in thin section, and by analogy with well-studied minerals identified during previous legs.

The effects of alteration in rocks from Site 1204 are defined in the basaltic units in terms of (1) alteration assemblages and vein and vesicle filling and (2) alteration chemistry.

Alteration Assemblages and Vein and Vesicle Fillings

In this section, we describe the alteration color, mineral assemblages, and vein and vesicle fillings of basaltic lava flows recovered at Site 1204 (Holes 1204A and 1204B). All basalt pieces recovered are slightly to highly altered (Figs. **F31, F32**). Alteration degree is higher overall in lobed units (Hole 1204A, Unit 2; Hole 1204B, Units 1, 2a, 2c, and 3) than in the massive Hole 1204B Subunit 2b diabase (see **"Physical Volcanology and Igneous Petrology,"** p. 11). The degree of alteration also increases toward veins and glassy lobe margins, where it is high. Within the massive Hole 1204B Subunit 2b and massive interiors of lobes, alteration is slight to moderate.

Sample color is the first indication of alteration conditions. Two main alternating colors, with very sharp contacts, were observed in the sequences of Holes 1204A and 1204B (Figs. **F33, F34**). In the first color type, colors range from grayish brown (10YR 5/2) to light brownish gray (10YR 6/2), brownish yellow (10YR 6/8), or yellowish brown (2.5YR 5/4). In the second color type, basalt is characterized by a gray-green (5BG 4/1) color. These colors can be directly related to the oxidation state of the alteration process: oxidizing conditions in the brownish zones and reducing conditions in the greenish zones.

In the following sections, the alteration assemblages along with vesicle and vein fillings are described for each color type. Downhole alteration assemblages and vesicle and vein fillings are summarized in Figures **F31** (Hole 1206A) and **F32** (Hole 1204B). All information was also recorded in the alteration and vein logs (see **"Site 1204 Alteration Logs,"** p. 114, and **"Site 1204 Vein Logs,"** p. 116).

Overall, the alteration assemblages are dominated by carbonate (calcite) precipitation and clay. The latter are mainly brown to green smectite (saponite and/or nontronite). In both Holes 1204A and 1204B, zeolite minerals were also identified. These are fibrous zeolite with a small amount of analcite (see **"Site 1204 Thin Sections,"** p. 83).

F31. Alteration minerals and vein and vesicle fillings, Hole 1204A, p. 72.

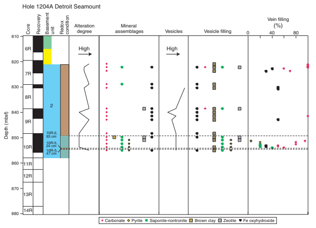

F32. Alteration minerals and vein and vesicle fillings, Hole 1204B, p. 73.

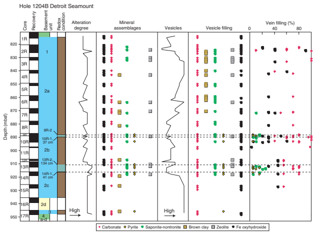

F33. Contact between oxidizing and reducing zones, p. 74.

F34. Another oxidizing/reducing zone contact, p. 75.

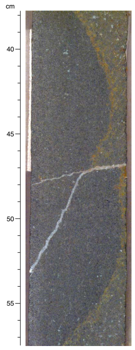

Oxidizing Zone

Zones of oxidizing alteration were observed in Hole 1204A, Unit 2, from the top of Section 197-1204A-7R-2 (820.95 mbsf) through Section 10R-2, 93 cm (850.7 mbsf). Another smaller interval is recorded between Sections 197-1204A-10R-5, 24 cm (854.06 mbsf), and 10R-5, 47 cm (854.29 mbsf) (Fig. F31). In Hole 1204B, oxidizing zones are observed from the top of Section 197-1204B-1R-3 (814.03 mbsf) through the bottom of Section 9R-1 (887.29 mbsf). The second oxidizing zone is between Sections 197-1204B-10R-1, 37 cm (889.17 mbsf), and 13R-2, 134 cm (911.11 mbsf). Two additional oxidizing zones are recorded between Section 197-1204B-14R-1, 41 cm (916.31 mbsf), and the bottom of Subunit 2c (935.20 mbsf) and in Unit 3 from 944.90 to 947.26 mbsf (Fig. F32).

The alteration assemblage in these zones is dominated by Fe oxyhydroxide, which is sometimes well crystallized as goethite associated with carbonate (calcite), brown clay, and zeolite. The alteration assemblage is also composed of minor amounts of green clay (saponite and/or nontronite) (Hole 1204B, Subunit 2a) (Fig. F32).

Vesicles are mostly filled with carbonate (calcite). However, some display mixed fillings of carbonate (calcite), brown clay, minor amounts of green clay (saponite and/or nontronite), and zeolite (phillipsite?). When unfilled, vesicles are lined with either Fe oxyhydroxide (sometime crystallized as goethite) or zeolite (phillipsite?) (Figs. F31, F32).

Veins do not exhibit a preferred orientation in either hole. Veins are 1–30 mm wide and are filled with assemblages of carbonate (calcite) and Fe oxyhydroxide (sometimes as goethite) in various proportions (Figs. F31, F32). Minor amounts of green clay (saponite and/or nontronite) were recognized in veins from Hole 1204B (Fig. F32).

Reducing Zones

Zones of reducing conditions were identified in both Site 1204 holes (1204A and 1204B). Two reducing zones were identified next to the bottom of Hole 1204A, between Sections 197-1204A-10R-2, 93 cm (850.7 mbsf), and 10R-5, 24 cm (854.06 mbsf), and between Section 10R-5, 47 cm (854.29 mbsf), and the bottom of the recovered section of Hole 1204A (856.56 mbsf). Two other reducing zones were identified in Hole 1204B, between the top of Sections 197-1204B-9R-2 (88.29 mbsf) and 10R-1, 37 cm (889.17 mbsf), and between Sections 13R-2, 134 cm (911.11 mbsf), and 14R-1, 41 cm (916.31 mbsf).

The characteristic alteration assemblage in these zones consists of green clay (saponite and/or nontronite) and secondary sulfide (pyrite and rare chalcopyrite). This assemblage also contains carbonate (calcite) and zeolite. Minor amounts of Fe oxyhydroxide are sometimes present in these zones, which could represent the last stages of seafloor weathering.

In Hole 1204A, vesicles are filled mostly with green clay (saponite) and secondary pyrite (Fig. F35). When unfilled, vesicles are lined with brown clay and/or zeolite. In the Hole 1204B sequence, vesicles are filled mainly with an assemblage of carbonate (calcite), green clay (saponite), and secondary pyrite. When unfilled, vesicles are lined with zeolite.

Veins are 0.1–5 mm wide, thinner than in the oxidizing zones. They are filled with carbonate (calcite), green clay (saponite), and pyrite in

F35. Megavesicle filled with saponite and pyrite, p. 76.

various proportions. Minor amounts of Fe oxyhydroxide are sometimes present and could represent later stages of seafloor weathering.

Alteration Chemistry

As noted for Hole 1203A (see **"Alteration and Weathering,"** p. 24, in the "Site 1203" chapter), only the freshest samples were analyzed for major and trace element contents. Therefore, the chemical variations reported here might not be representative of the overall alteration-related chemical effects downhole. Variations in the abundances and ratios of some chemical elements (K_2O, Cu/Zr, Co/Zr, and Zn/Zr) and LOI vs. depth are reported in Figures **F36** (Hole 1204A) and **F37** (Hole 1204B).

F36. LOI, K_2O, Cu/Zr, Co/Zr, and Zn/Zr, Hole 1204A, p. 77.

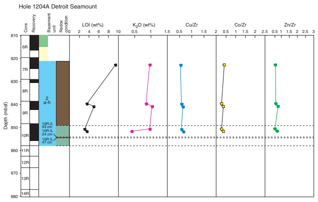

In Hole 1204A, LOI decreases downhole from ~10 wt% in the upper part of the oxidizing zone to ~4 wt% at the bottom of the first oxidizing zone and 3 wt% in the first reducing zone. This trend confirms macroscopic and petrographic observation of the samples. K_2O displays a similar pattern, in that abundances are high in oxidizing zones (~1 wt%) and lower in the reducing zone (lowered to 0.5 wt%). In contrast to Site 1203 (see **"Alteration and Weathering,"** p. 24, in the "Site 1203" chapter), Cu/Zr, Co/Zr, and Zn/Zr ratios are constant downhole (Fig. **F36**). The incompatible element Zr is used as a normalization element to diminish the effect of crystal fractionation and to highlight any variations that might be ascribed to alteration processes.

F37. LOI, K_2O, Cu/Zr, Co/Zr, and Zn/Zr, Hole 1204B, p. 78.

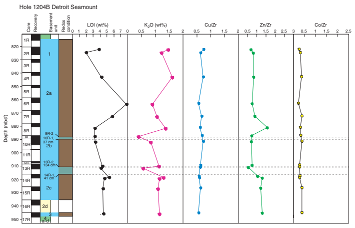

LOI varies downhole in the Hole 1204B sequence. This trend confirms macroscopic and petrographic observation of the samples. LOI values are ~3–4 wt% in Unit 1 and the top part of Subunit 2a, reaching a maximum at the bottom of Subunit 2a (e.g., 7.81 wt% [Sample 197-1204B-6R-4, 21–24 cm]) and decreasing to 3–4 wt% in Subunits 2b, 2c, and Unit 3. Overall, LOI values are slightly lower (~3 wt%) in the massive Subunit 2b (diabase). As previously noted in Hole 1204A, K_2O abundances are different between oxidizing and reducing zones. In oxidizing zones, K_2O values are high (1–1.5 wt%). On the contrary, K_2O is low in reducing zones (≤0.5 wt%). As in Hole 1204A, Cu/Zr and Co/Zr ratios are constant with depth in Hole 1204B. However, some variations were noted in the Zn/Zr ratios. Zn/Zr ratios are high for Sample 197-1204B-8R-3, 53–55 cm, and for the four samples from Subunit 2c and Unit 3 (Fig. **F37**).

In both Hole 1204A and 1204B sequences, the constant Cu/Zr, Co/Zr, and Zn/Zr ratios indicate that these trace metals were not mobilized during alteration processes, with the exception of the previously noted variations of Zn/Zr ratios. No secondary phases containing Zn (such as sphalerite, [Zn, Fe]S) were identified during thin section examination, and further shore-based studies are needed to investigate this feature. Variations of K_2O abundances downhole indicate a different mobilization of alkalis between oxidizing and reducing zones. By comparison with unaltered rocks from Hawaiian volcanoes (Fig. **F38**), K_2O abundances are likely at or slightly lower than the original unaltered rock in reducing zones and are much higher in oxidizing zones. This is a common feature seen on Figure **F38,** where K_2O against Zr abundances are reported for Site 1204 (Holes 1204A and 1204B) together with data from Site 1203, ODP Leg 145 Sites 883 and 884 (Rea, Basov, Janecek, Palmer-Julson, et al., 1993; Keller et al., 1995), and unaltered Hawaiian lavas from Mauna Kea Volcano and Loihi Seamount (Frey et al., 1990, 1991; Rhodes, 1996). Two groups are identified—one with low K_2O val-

F38. Zr vs. K_2O for Site 1204, Site 1203, Hawaiian lavas, and Sites 883 and 884, p. 79.

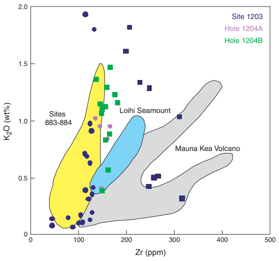

ues and another with high values. Samples from the first group were taken from reducing zones, and samples from the second group were taken from oxidizing zones. K_2O was therefore likely taken up by oxidized rocks and released in reduced zones.

Volcaniclastic Units

Subunit 1a in Hole 1204A consists of a medium-grained volcaniclastic breccia, containing highly altered, aphyric vesicular basalt clasts in a calcareous matrix. This passes downward into the upper part of Subunit 1b, which is composed of volcaniclastic sandstone and breccia containing fragments of highly altered vesicular basalt and completely devitrified brown glass in a calcareous matrix. Subunit 2d in Hole 1204B consists of angular basalt lapilli to breccia fragments in a matrix of fine lapilli. Some alteration features associated with these deposits are described in **“Physical Volcanology and Igneous Petrology,”** p. 11.

Summary

All igneous rocks recovered at Site 1204 (Holes 1204A and 1204B) have undergone low-temperature alteration. Alteration features are defined in the basaltic units in terms of secondary mineral paragenesis, apparent as vesicle filling, vein filling, and replacement of groundmass and primary minerals. Overall, the basalt flows are slightly altered in the massive units (Hole 1204B, Subunit 2b) and in interiors of lobes (Holes 1204A, Unit 2, and Hole 1204B, Units 1, 2a, 2c, and 3) (see also **“Physical Volcanology and Igneous Petrology,”** p. 11). Toward the margins of lobes, the degree of alteration is high. The alteration sequence is dominated by carbonate (calcite) formation, brown and green clay (saponite and/or nontronite), and zeolite minerals. Alteration conditions change in both sequences (Holes 1204A and 1204B) from oxidizing to reducing conditions, as highlighted by the change in color from brown to gray green. Oxidizing zones are characterized by Fe oxyhydroxide and goethite formation, and reducing zones are characterized by green clay (saponite) and secondary pyrite precipitation. Vesicle and vein fillings present the same features. Contacts between the different zones are very sharp and indicate an abrupt change in the oxidation state of circulating fluids. Reducing zones are mainly recorded in the more massive units, where fluid circulation is more restricted and water/rock ratios are likely to be lower because of lower permeability of the rock. This suggests that oxidizing and reducing alteration regimes were coeval, although Fe oxyhydroxide is sometimes superposed in reducing zones. These could correspond to later episodes of seafloor weathering at low temperature and with high water/rock ratios. The occurrence of saponite and zeolite in both regimes indicates that the temperature remained similar for both types of alteration, which is a further argument for coeval oxidizing and reducing alteration episodes. Temperatures estimated for saponite formation are in the range of 15°–170°C (Alt, 1995).

K_2O was mobilized during alteration event(s) in a different manner depending on the alteration type. K_2O is high in oxidizing zones and low in reducing zones. Other trace elements and trace metals apparently have not been mobilized, as expected for low-temperature alteration events. Seawater-derived fluids probably reacted at low temperature with the upper lava sequences, leading to Fe oxyhydroxide formation, and became more reduced farther down in the sequence (alkali and oxygen depleted), leading to sulfide precipitation and alkali leaching. All sequences from Site 1204 were likely altered in the so-called "seafloor weathering and alkali fixation" zone of Alt (1995).

PALEOMAGNETISM AND ROCK MAGNETISM

Paleomagnetic and rock magnetic measurements at Site 1204, on the summit region of Detroit Seamount, were aimed at assessing the natural remanent magnetization (NRM) of the basement rocks recovered. Data from the site were sought for comparison with results from Site 884 (Tarduno and Cottrell, 1997), located to the northeast on the eastern flank of the seamount. Basalt and sediment discrete samples (minicores) were used for measurements. In addition, the magnetization of sediment recovered above basement in Hole 1204A was measured to define geomagnetic polarity. For magnetostratigraphic analysis, half-round core sections were analyzed.

Paleomagnetism of Sedimentary Rocks Recovered above Basement

The sedimentary rocks recovered from Hole 1204A are mostly chalk and altered volcanic ash (see **"Lithostratigraphy,"** p. 4). A zone of resedimented chalk is present in Core 197-1204A-3R. NRMs from archive half-round core sections (Cores 197-1204A-1R to 6R) were measured using the shipboard 2-G Enterprises superconducting quantum interference device (SQUID) magnetometer. The measurement interval was 5 cm. Progressive alternating-field (AF) demagnetizations were applied to peak fields of up to 40 mT.

For many intervals this demagnetization treatment was successful in removing secondary magnetizations and in defining a characteristic remanent magnetization (ChRM) of normal and reversed polarity (Fig. F39). From some intervals, the NRM was found to be composed of an apparent present-day (Barton et al., 1995) or Brunhes-age component overprinting a clearly defined reversed polarity ChRM (Fig. F39B). However, for other intervals the direction defined during progressive AF demagnetization deviated significantly from the origin of orthogonal vector plots (Fig. F40). This departure from ideal behavior signifies the presence of a high-coercivity magnetic component. For such intervals, the AF treatment was ineffective in isolating the ChRM and the data cannot be used to assign geomagnetic polarity.

We base the preliminary geomagnetic polarity column on demagnetization data showing a linear decay to the origin of orthogonal vector plots. Specifically, inclination values derived from vector end points after AF demagnetization were used to assign polarity (Fig. F41).

Although rotary drilling can sometimes result in severe disruption of sedimentary rocks, the cores recovered from Hole 1204A generally consist of long consolidated sections with only minor disturbance. Artifacts caused by edge effects of adjacent core pieces, however, are to be expected in the raw data. Our polarity analysis follows the conventions applied in our investigation of sediment cores recovered at Site 1203. A polarity was assigned only if several consecutive measurement intervals demonstrated a consistent polarity; single-point estimates suggesting a polarity opposite to that of adjacent intervals were ignored in this preliminary analysis.

F39. Vector plots: sediment above basement, Hole 1204A, p. 80.

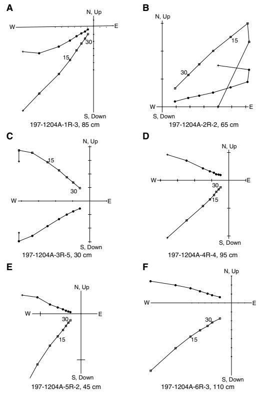

F40. Vector plots showing departures from ideal behavior, p. 81.

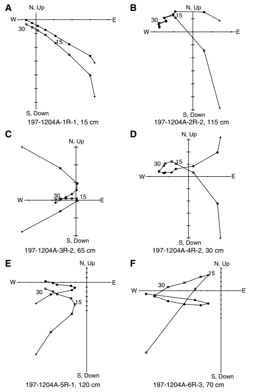

F41. Paleomagnetic inclinations vs. depth, p. 82.

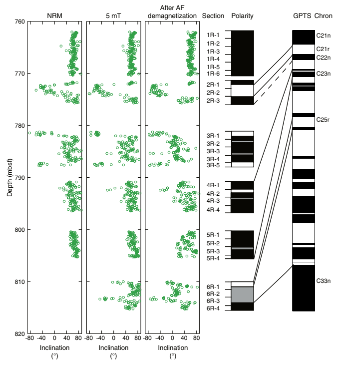

Correlations with the Geomagnetic Polarity Timescale

Using the available nannofossil data (see **“Biostratigraphy,”** p. 10), we have drawn preliminary correlations of the polarity intervals identified to the geomagnetic polarity timescale. Core 197-1204A-1R has been assigned to the middle Eocene NP15 nannofossil zone. This assignment suggests that the normal polarity interval identified in the core probably corresponds to polarity Chron C21n, which is assigned an age of 47 Ma (Cande and Kent, 1995; Berggren et al., 1995). The majority of Core 197-1204A-2R has been assigned to the NP14 nannofossil zone; the base of the recovered interval is assigned to Zone NP13. These assignments suggest that the normal–reversed–normal polarity succession observed in Core 197-1204A-2R (Fig. **F41**) corresponds to the C22n–C21r–C21n polarity chron sequence, which has an age between 49 and 47 Ma (Cande and Kent, 1995; Berggren et al., 1995). Sediment recovered from Core 197-1204A-3R represents a slide or slump; because of the likelihood of magnetic resetting resulting from sedimentary processes, we have not considered correlations of the observed magnetic record with the geomagnetic polarity timescale.

Cores 197-1204A-4R and 5R, assigned to nannofossil Zone NP12, correlate well with normal polarity Chron C23, (~51 Ma) (Cande and Kent, 1995). Nannofossil analyses indicate that Core 197-1204A-6R represents a condensed section spanning the late Paleocene to Late Cretaceous. Nannofossil Zones NP8 and NP7 are assigned to the top of the core. A significant hiatus is present at the base of Section 197-1204A-6R-1; sediment lower in the core is assigned to the late Campanian CC22–CC23 nannofossil zone. This assignment suggests that the normal polarity interval identified at the base of Core 197-1204A-6R corresponds to Chron C33n.

Rock Magnetism of Basalt and Sediment Comprising Basement

The basement section at Site 1204 is dominated by basaltic lava flows (see **“Physical Volcanology and Igneous Petrology,”** p. 11, and **“Discussion,”** p. 29). The lowermost core recovered consisted of volcaniclastic and calcareous marine sediment. All samples for paleomagnetic and rock magnetic analyses were collected as drilled minicores.

F42. Poorly defined magnetic components, Hole 1204A basalt, p. 83.

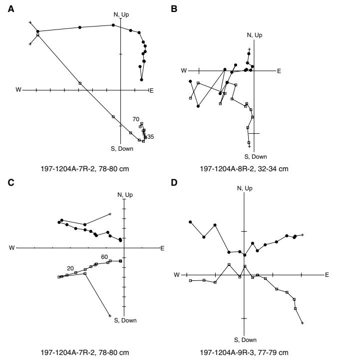

F43. Poorly defined magnetic components, Hole 1204B basalt, p. 84.

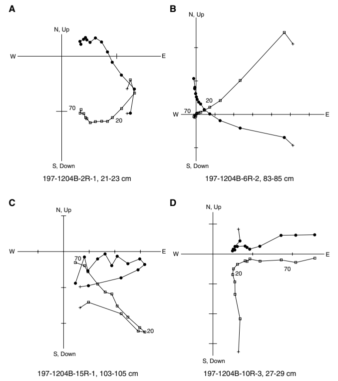

Magnetic Susceptibility, Koenigsberger Ratio, and Median Destructive Field

Low-field volume-specific magnetic susceptibility (*K*) was measured with a Kappabridge KLY-2 magnetic susceptibility meter. Magnetic susceptibility values in Hole 1204A range from 0.2×10^{-3} to 26×10^{-3} SI, with an arithmetic mean value of 6.9×10^{-3} SI. For Hole 1204B, magnetic susceptibility values range from 0.06×10^{-3} to 14×10^{-3} SI, with an arithmetic mean value of 3.9×10^{-3} SI. The Koenigsberger ratio (*Q*) ranges from 5.6 to 45.0 in Hole 1204A (mean = 20.6). In Hole 1204B, *Q* values range from 0.4 to 31.0 (mean = 7.4). Median destructive fields (MDFs) of NRM were calculated based on stepwise AF demagnetization curves. However, data from some samples did not show a monotonic decrease in intensity, suggesting the presence of multiple NRM components (see Fig. **F42; “Discussion,”** p. 29). In particular, the demagnetization data from some samples appear to show a low-coercivity component of magnetization oriented roughly antiparallel to that carried at higher coercivities (see Fig. **F43**). Because of this complex directional structure, we chose not to calculate MDFs for such samples. The MDF values that could be calculated range from 7.1 to 33.9 mT (mean = 16.4 mT) for Hole 1204A and 7.0 to 47.5 mT (mean = 22.9 mT) for Hole 1204B. Downcore changes in these rock magnetic parameters are shown in Figures **F44** and **F45.** In general, susceptibility and *Q*-ratio values are lower than those derived from Site 1203 basalt samples.

Lowrie-Fuller Tests

The Lowrie-Fuller test (Lowrie and Fuller, 1971) was performed on five basalt samples from Hole 1204A and nine basalt and diabase samples from Hole 1204B. In interpreting these data in terms of magnetic domain state, we rely on the relative shapes of the anhysteretic remanent magnetization (ARM) and saturation isothermal remanent magnetization (SIRM) demagnetization curves. For a few samples (e.g., Sample 197-1204A-8R-2, 132–134 cm) (Fig. **F46**), the two demagnetization curves are similar and clear constraints on magnetic domain state are not possible. In other samples, the decay of ARM relative to SIRM allowed an interpretation, but it should be emphasized that this interpretation also relies on the assumption that the samples contain a simple magnetite or titanomagnetite mineralogy (see **"Discussion,"** p. 29). Given this assumption, the rapid decay of ARM relative to SIRM for some samples suggests the presence of multidomain grains (e.g., Samples 197-1204A-107R-1, 125–127 cm, and 197-1204B-4R-2, 63–65 cm) (Fig. **F46**). In other samples, the resistance of ARM to demagnetization relative to SIRM suggests the presence of single-domain to pseudo-single-domain grains (e.g., Samples 197-1204A-10R-4, 138–140 cm; 197-1204B-9R-2, 8–10 cm; and 13R-3, 33–35 cm) (Fig. **F46**).

Isothermal Remanent Magnetization Acquisition and Coercivity of Remanence Measurements

Isothermal remanent magnetization (IRM) acquisition and backfield IRM acquisition were measured on the same samples used for the Lowrie-Fuller tests. These data were used to derive values of coercivity of remanence, which is an estimate of magnetic hardness (or the resistance and, hence, stability of the remanent magnetization to change by external stimuli).

Stepwise IRMs were imparted in the +x-direction (sample coordinates) using an IM-10 impulse magnetizer until the saturation remanence (M_{rs}) was reached. Then the samples were direct-current demagnetized by giving them a stepwise IRM in the –x-direction. The remanence decreases to zero at the coercivity of remanence (H_{cr}) and culminates in $-M_{rs}$, the negative saturation remanence (Fig. **F47**). Results of these measurements are summarized in Table **T9.** M_{rs} values range from 118 to 365 A/m (mean = 260 A/m) for Hole 1204A and from 115 to 311 A/m (mean = 179 A/m) for Hole 1204B. H_{cr} values range from 6.0 to 31.5 mT (mean = 20.5 mT) for Hole 1204A and from 4.6 to 34.5 mT (mean = 19.2 mT) for Hole 1204B.

Interestingly, samples that have single domain–like behavior according to the Lowrie-Fuller test have a low coercivity of remanence (e.g., Samples 197-1204A-10R-4, 138–140 cm; 197-1204B-9R-2, 8–10 cm; and 197-1204B-13R-3, 33–35 cm) (Fig. **F47**). Samples having a multidomain-like behavior according to the Lowrie-Fuller test have higher coercivity of remanence values (e.g., Samples 197-1204A-107R-1, 125–127 cm,

F44. Magnetic susceptibility, Koenigsberger ratio, and MDF, Hole 1204A, p. 85.

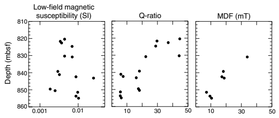

F45. Magnetic susceptibility, Koenigsberger ratio, and MDF, Hole 1204B, p. 86.

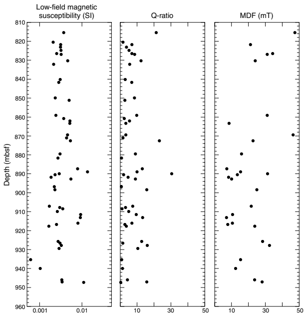

F46. Examples of Lowrie-Fuller tests, p. 87.

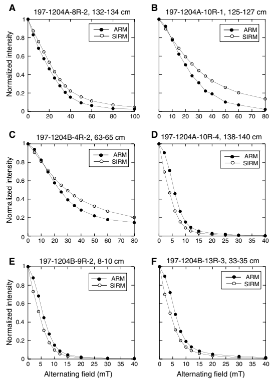

F47. IRM and backfield IRM, p. 88.

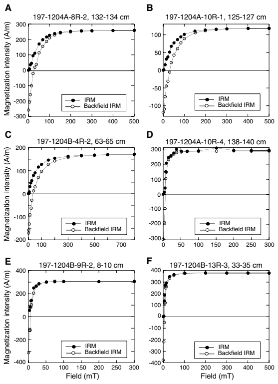

T9. Rock magnetic parameters for basalt samples, p. 117.

and 197-1204B-4R-2, 63–65 cm) (Fig. **F47**). This pattern is opposite from that expected for a simple magnetite or titanomagnetite remanence carrier.

Contrasting Magnetic Properties between Brown and Green-Gray Basalt Samples

Basaltic rocks from Holes 1204A and 1204B can be categorized into two types based on visual core descriptions, the rock magnetic properties described above, and observations from reflected-light microscopy (see **"Physical Volcanology and Igneous Petrology,"** p. 11). Most samples are light brown and have natural remanent magnetizations that are occasionally resistant to the highest alternating field applied (80 mT) (see Figs. **F42, F48, F49**). Sometimes brown samples show irregular directional changes during AF demagnetization. Microscopic observation under reflected light reveals that the primary titanomagnetite grains in this type of sample have been partially to completely altered to titanomaghemite. Exsolution lamella of ilmenite were observed only occasionally (see Table **T7**). Groundmass and vesicles are generally filled with iron oxyhydroxides, including goethite. These lines of evidence suggest that the brown basalt samples were subjected to relatively extensive low-temperature oxidation (see **"Alteration and Weathering,"** p. 20). Diffusion of ferric ions from the primary titanomagnetite during low-temperature oxidation (Furuta, 1993) might have contributed to the formation of goethite and amorphous iron oxyhydroxides.

In general, goethite is highly resistant to AF magnetization. Titanomaghemite has a resistance to AF demagnetization that is higher than that of unoxidized titanomagnetite. But a considerable overlap in coercivity between titanomagnetite and titanomaghemite is expected in a natural sample because the coercivities of each mineral phase also depend on grain size. The presence of goethite and titanomaghemite, together with the possibility that the former mineral can carry a magnetization component different from the characteristic remanent magnetization (see **"Characteristic Remanent Magnetization Directions and Inferred Paleolatitudes,"** p. 29), explains the inadequacy of AF demagnetization in producing a smooth decrease in NRM for some samples. It also explains the somewhat contradictory results of the Lowrie-Fuller test and the coercivity of remanence data, as the former relies on a simple, one-component magnetite (or titanomagnetite) composition for meaningful assignment of magnetic domain state. Similarly, coercivity of remanence data are difficult to interpret uniquely when multiple rock magnetic components are present.

The second type of basalt sample identified is green gray. These samples show a rapid and smooth demagnetization behavior with the application of progressively higher peak alternating fields (see Figs. **F50D, F51B, F51C, F52B, F52D, F52F**). The MDFs of the NRM and the coercivity of remanence are relatively low. In Figure **F53,** a clear contrast of rock magnetic properties between brown and green-gray samples is shown. The green-gray basalt samples are also altered (see **"Physical Volcanology and Igneous Petrology,"** p. 11, and **"Alteration and Weathering,"** p. 20) but apparently under reducing conditions. Groundmass and vesicles are filled with blue-green clay minerals, and secondary pyrite is common. Importantly, iron oxyhydroxide is absent.

Reflected-light microscopy (see **"Physical Volcanology and Igneous Petrology,"** p. 11) suggests that the green-gray samples contain, on average, unaltered titanomagnetite that is larger in grain size than that

F48. Incompletely demagnetized basalt, Hole 1204A, p. 89.

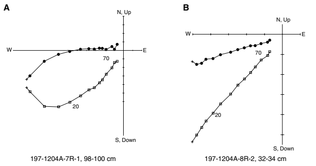

F49. Incompletely demagnetized basalt, Hole 1204B, p. 90.

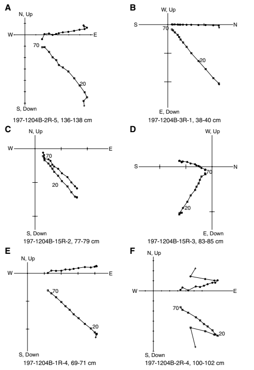

F50. Orthogonal vector plots for Hole 1204A basalt, p. 91.

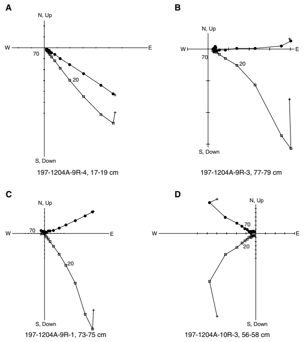

F51. Orthogonal vector plots for Hole 1204B basalt, p. 92.

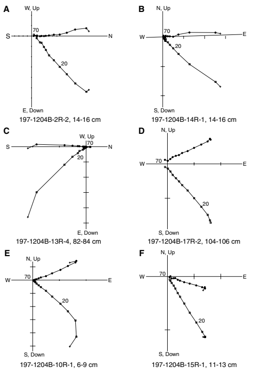

observed in brown samples. To explain the relatively low MDF and H_{cr} values from such samples, we speculate that some of the primary fine-grained titanomagnetite (of single-domain size) might have been dissolved under the reducing conditions signified by the presence of secondary pyrite. Accordingly, the magnetic properties of this type of basalt sample might be dominated by the larger multidomain titanomagnetite that survived reductive alteration.

In general, the multiple magnetic minerals present in the basalt samples from Holes 1204A and 1204B highlight the need for detailed thermal demagnetization studies to separate overprints and characteristic remanent magnetizations. Nevertheless, AF demagnetization data from select samples (especially less oxidized samples) provide a first-order means of estimating the potential time sequence recorded by the basalt sections in Holes 1204A and 1204B.

Paleomagnetism of Basalt and Sediment Comprising Basement

Minicore samples of basalt from Holes 1204A and 1204B were measured using the 2-G Enterprises SQUID magnetometer. A few volcaniclastic samples from Hole 1204B were also studied. After the measurement of the untreated NRM, samples were progressively demagnetized by AF demagnetization. A 5-mT field increment was used between 5 and 50 mT, and a 10-mT step was used after 50 mT to a peak applied field of 80 mT. The demagnetization data from the samples were plotted on orthogonal vector plots to examine the stability and component structure of the NRM.

Demagnetization Behavior

Approximately 70% of the minicore samples from Holes 1204A and 1204B showed simple demagnetization patterns, with linear vector decay to the origin of orthogonal vector plots after the removal of a viscous overprint (which was generally removed after demagnetization to 5–10 mT) (see Figs. F50, F53). Samples with such stable behavior included the diabase recovered from Hole 1204B (Fig. F51). In ~30% of the samples measured, however, a high-coercivity component was not completely demagnetized by the highest peak AF demagnetization applied. For some of these samples, the demagnetization data defined a linear component (see Figs. F48, F52), which could be fit with principal component analysis (Kirschvink, 1980). Approximately one-half of the samples that showed a high-coercivity component also showed a more complex overall directional pattern during demagnetization. These patterns included the definition of an overprint of apparent opposite polarity to the (generally poorly defined) ChRM and unstable directional behavior during the demagnetization (Figs. F42, F49).

We observed a general correspondence between the directional behavior described above and the rock magnetic sample types discussed above. In general, samples showing a more complex magnetic behavior were more oxidized. The NRM of reduced green-gray samples had a simpler apparent magnetic component structure.

Somewhat surprisingly, we note that two hyaloclastite lapilli breccia samples from Hole 1204B basement Subunit 2d (see **"Physical Volcanology and Igneous Petrology,"** p. 11) carry a stable remanent magnetization. This magnetization must postdate emplacement of the breccia (Graham, 1949) if temperatures were below the Curie temperatures of

F52. Orthogonal vector plots for Hole 1204B diabase, p. 93.

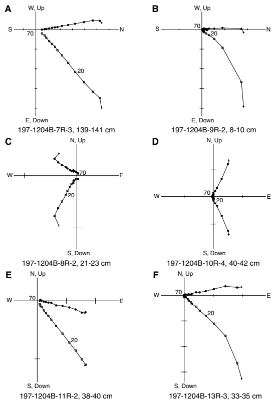

F53. MDF for brown and green-gray basalt, p. 94.

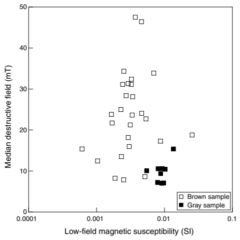

potential primary magnetic carriers, as seems to be the case from the overall alteration state of the adjacent units (see **"Alteration and Weathering,"** p. 20). Whereas the coercivity range and demagnetization range of basalt samples from Holes 1204A and 1204B are consistent with a thermoremanent origin of the ChRM, we relate the directions isolated from the breccia to a chemical remanent magnetization process. Goethite may be an important remanence carrier in the breccia. We further note that the chemical event responsible for the magnetization of this breccia may also be responsible for the complex magnetic behavior of some basalt samples from both Holes 1204A and 1204B.

Characteristic Remanent Magnetization Directions and Inferred Paleolatitudes

All samples analyzed were of normal polarity; a few apparent reversed polarity samples were attributed to accidental inversions of core pieces during sample handling after recovery. ChRM directions for basalt and sediment were fit using principal component analysis (Kirschvink, 1980). In general, the characteristic remanent directions were defined between 20 and 70 mT for basalt samples. Maximum angular deviations of line fits to the demagnetization data were generally <5°–10°. ChRM inclinations from each basement unit and subunit were averaged using the method of McFadden and Reid (1982) to obtain inclination averages.

Nine samples from Hole 1204A yielded an inclination unit average of 55.5° (95% confidence interval = 7.5°) (Table **T10**). This value yields a nominal paleolatitude of 36.0°N. The paleolatitude is a nominal value because secular variation of the geomagnetic field will not be averaged by a single lava flow unit if cooling is rapid and the magnetization is imparted by a thermoremanent magnetization process.

T10. ChRM inclinations and summary statistics, p. 118.

Three relatively thick lava flow units were described from the Hole 1204B core recovered. Basement Unit 2, however, was further divided into four subunits (see **"Physical Volcanology and Igneous Petrology,"** p. 11). Here, we treat each of the subunits as an independent time unit. The exceptionally large vertical extent of Unit 2 (and the associated duration of cooling) (Jaeger, 1964) suggests that the magnetization acquired by the subunits may be separated on a timescale of decades to a few hundred years. Using six independent paleomagnetic units for Hole 1204B, we derive a mean inclination of 58.9° (95% confidence interval = 6.1°) (Table **T10**). This inclination suggests a paleolatitude of 39.7°N (95% confidence interval = +7.4°/–6.3°).

Discussion

The overall estimated dispersion of the paleomagnetic data ($S = 8.4$) from Hole 1204B indicates that some time has been averaged. However, the value is less than that predicted from global lava flow data spanning the 45- to 80-Ma interval (McFadden et al., 1991). This suggests that the sequence has not sampled the full range of geomagnetic secular variation at the site. This conclusion and the estimated paleolatitude rely on the accuracy of the AF demagnetizations applied. Because of the alteration of the basalt section (and especially the potential presence of goethite) in Holes 1204A and 1204B, however, thermal demagnetization studies will be required to confirm the ChRM directions, paleolatitude, and angular dispersion reported here.

The presence of ferromagnetic alteration minerals, however, may offer another opportunity to address the paleolatitude of Detroit Seamount. If overprints can be isolated from data generated by detailed stepwise thermal demagnetizations and if this alteration occurred soon after emplacement of the basalt (as suggested by our preliminary measurements), it might be possible to derive a paleolatitude estimate from the overprint directions. Such overprints often span enough time to average secular variation (e.g., Van der Voo et al., 1978).

Although the data from Holes 1204A and 1204B must be confirmed by shore-based analyses, they yield paleolatitude estimates (36.0° and 39.7°N, respectively) that are compatible with the preliminary data from Site 1203 and the paleolatitude estimate (36°; 95% confidence interval = ±7°N) obtained from analyses of older basalt (81 Ma) recovered at Site 884 (Tarduno and Cottrell, 1997) that average secular variation. The difference between the Site 884 data and the latitude of Hawaii stimulated the paleomagnetic investigation of the fixed hotspot hypothesis during Leg 197.

PHYSICAL PROPERTIES

All cores from Holes 1204A and 1204B were run through the multisensor track (MST). For Core 197-1204A-1R through Section 6R-4 and Sections 197-1204B-1R-1 and 1R-2, measurements were made of magnetic susceptibility, gamma ray attenuation (GRA) bulk density, and natural gamma radiation (NGR) on unsplit core sections. For the remaining cores, all of which contained basement material, only NGR measurements were made on the MST. Compressional wave velocities were measured on split cores in the transverse x-direction for sediment cores (Cores 197-1204A-1R through 6R, and Sections 197-1204B-1R-1 and 1R-2) and in the x- and z-directions for discrete basement samples. Index properties, including bulk density, water content, porosity, and grain density, were determined on discrete samples at a frequency of at least one per core. Thermal conductivity was determined for basement samples also at a frequency of at least one per core.

MST Measurements

Magnetic Susceptibility

Volume-normalized magnetic susceptibility was determined on Cores 197-1204A-1R through 6R and Sections 197-1204B-1R-1 and 1R-2 at 5-cm intervals (Table T11; Figs. F54B, F55B). In the upper part of Hole 1204A, values generally range between ~10 × 10^{-6} and 150 × 10^{-6} SI. However, a slight increase in susceptibility can be seen at ~776 mbsf, close to the boundary between sedimentary Units I and II. Magnetic susceptibilities are somewhat elevated in the upper parts of Unit II relative to the other sedimentary units, ranging up to 1500 × 10^{-6} SI; this may be due to increased amounts of volcanic and Fe-rich material (see **"Lithostratigraphy,"** p. 4). Values decrease below ~790 mbsf and then remain relatively constant to the base of Unit II and throughout Unit III. Magnetic susceptibility values in Subunit IVA appear to increase slightly with depth. The boundary between Subunits IVA and IVB is marked by a decrease in magnetic susceptibility.

For Hole 1204B, magnetic susceptibility ranges from ~68 × 10^{-6} to 850 × 10^{-6} SI (mean = 357 × 10^{-6} SI). In the upper 0.5 m of the core, val-

T11. MST magnetic susceptibility, p. 119.

F54. GRA density, magnetic susceptibility, and NGR, Hole 1204A, p. 95.

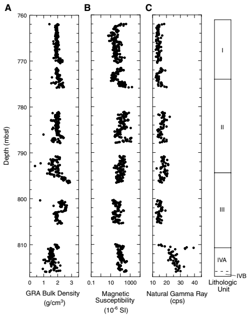

F55. GRA density, magnetic susceptibility, and NGR, Hole 1204B, p. 96.

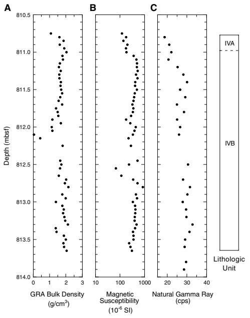

ues are <200 × 10^{-6} SI. An increase occurs at 811.0 mbsf, corresponding to the boundary between sedimentary Subunits IVA and IVB (Fig. **F55B**); this appears to be the reverse of the trend seen in the Hole 1204A data. From 811.0 to 811.9 mbsf, values remain relatively constant at ~420 × 10^{-6} SI. The interval from 811.9 to ~813.0 mbsf is marked by widely varying magnetic susceptibilities, ranging between 68 × 10^{-6} and 850 × 10^{-6} SI; this corresponds to a large variation in lithology at this depth. Below 813.0 mbsf, magnetic susceptibility again remains relatively constant to the base of the sediments.

GRA Density

Bulk density was measured by the GRA densitometer every 5 cm on whole sections of Cores 197-1204A-1R through 6R and Sections 197-1204B-1R-1 and 1R-2 (Table **T12**). Downhole in Hole 1204A, GRA bulk densities remain approximately constant at ~2 g/cm³ until ~795 mbsf, where a rather abrupt density increase to ~2.5 g/cm³ was measured (Fig. **F54A**). This is close to the boundary between sedimentary Units II and III. Density then remains high in Unit III until ~803 mbsf, where a sharp decrease in bulk density to ~2 g/cm³ was noted. The boundary between sedimentary Units III and IV, at ~811 mbsf, is marked by a further small decrease in bulk density. Bulk densities in Unit IV have a mean value of ~1.65 g/cm³ and appear to increase slightly with increasing depth.

T12. GRA bulk density, p. 120.

Only two full sediment core sections were recovered from Hole 1204B; in these sections GRA bulk density generally ranges from 1.08 to 2.15 g/cm³ (mean = 1.70 g/cm³) (Fig. **F55A**). In sedimentary Subunit IVA, density shows an overall increase with depth. In Subunit IVB, density varies little with depth until ~812 mbsf. Below this depth a wider variation in GRA bulk densities can be seen.

A number of sample points from Holes 1204A and 1204B show very low GRA bulk density values (<<1 g/cm³). These density values are probably artifacts produced by drilling disturbance.

Natural Gamma Radiation

NGR was measured every 10 cm on both unsplit sediment and basalt cores from Holes 1204A and 1204B (Table **T13**). Total counts are reported here because the corrected counts (which are less by ~16 counts per second [cps]) include negative values, which are physically unreasonable. In the sediment section of Hole 1204A, gamma ray values are fairly constant between 760 and 810 mbsf (Figs. **F54C, F56A**), with most values between ~12 and 22 cps. However, higher counts were measured below 810 mbsf, in the lowest few meters of sediment above the basement. In Unit IV, NGR measurements mostly range between 20 and 30 cps and show an overall increase with depth. A particularly large peak of ~40 cps is present at the boundary between sedimentary Units III and IV at 810.7 mbsf.

T13. Natural gamma ray measurements, p. 121.

F56. NGR measurements, p. 97.

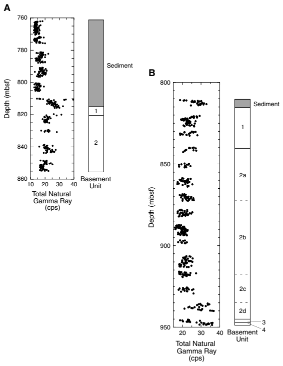

In the sedimentary section of Hole 1204B (Figs. **F55C, F56B**), which consists of Unit IV only, total NGR values mostly range between 20 and 32 cps (mean = 27 cps). Subunit IVA is characterized by a total NGR value of ~20 cps; the boundary between this unit and Subunit IVB is marked by an increase in NGR.

For basement rocks, NGR values show an overall decrease with depth to the base of the hole in Hole 1204A (Fig. **F56A**) and to ~900 mbsf in Hole 1204B (Fig. **F56B**). This may correspond to an increasing degree of reduction downhole in this zone (see **"Alteration and Weathering,"** p. 20). The lowest NGR measurements in the basement of Hole 1204B are observed at the center of Subunit 2b (872–918 mbsf), an aphyric diabase (see **"Physical Volcanology and Igneous Petrology,"** p. 11). From 900 to ~930 mbsf in Hole 1204B, the mean NGR value is somewhat higher, at ~22 cps. At depths >930 mbsf, increased natural gamma ray counts are observed in Subunit 2d, a hyaloclastite lapilli breccia, and the sediments of Unit 4, with values ranging up to 37 cps.

Core Imaging

Whole-round core images were taken of cylindrical pieces from both the Hole 1204A and 1204B cores, representing 25% and 70% of the recovered material, respectively. Because of time restrictions at Site 1204, downhole logging measurements were not made; hence, correlation of core image and logging data is not possible at this site. However, core images were still acquired to provide a visual record of the recovered material.

Thermal Conductivity

Thermal conductivity was measured at a frequency of one to two measurements per core for basement sections from Holes 1204A and 1204B (Table **T14**). Only four measurements were made in Hole 1204A, due to the small amount of basement material recovered. Thermal conductivity values for these samples range from 1.61 to 1.91 W/(m·K), and values appear to decrease slightly with increasing depth.

In the volcanic basement of Hole 1204B, thermal conductivity generally ranges between 1.41 and 1.78 W/(m·K) (mean = ~1.60 W/[m·K]). There appears to be no systematic variation with depth (Fig. **F57**). Two samples have lower thermal conductivity values, 0.83 and 1.29 W/(m·K); these represent a hyaloclastite breccia and calcareous vitric sandstone, respectively.

Index Properties

Index properties were determined at a frequency of one sample per core for discrete samples from Holes 1204A and 1204B. Values of wet mass, dry mass, and dry volume of discrete samples were measured and used to calculate moisture content, bulk density, grain density, and porosity (Table **T15;** Figs. **F58, F59**).

In the sedimentary units from Hole 1204A (Cores 197-1204A-1R through 6R), bulk density remains approximately constant at 1.9 g/cm³ between 762 and 811 mbsf. Trends in this upper section of Hole 1204A show some limited correlation with the GRA density measured on the MST (Fig. **F58A, F58B**). However, the section from 795 to 811 mbsf with higher GRA densities is not observed in the index properties data; this may be simply the result of the lower sampling frequency represented by the discrete samples. Below 811 mbsf in Unit IV, bulk densities from Holes 1204A and 1204B range between 1.55 and 1.94 g/cm³ (apart from one outlier), corresponding to lower GRA densities in the same depth interval.

Grain density in sediment from Holes 1204A and 1204B varies very little downhole, with values of ~2.7–2.8 g/cm³. An exception is seen in Section 197-1204A-6R-4 at a depth of ~815 mbsf, for which both bulk and grain density <1 g/cm³ was determined. Porosity is also constant at

T14. Thermal conductivity, p. 122.

F57. Thermal conductivity, p. 98.

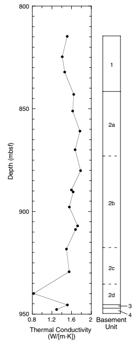

T15. Index properties, p. 123.

F58. Sedimentary unit index properties, p. 99.

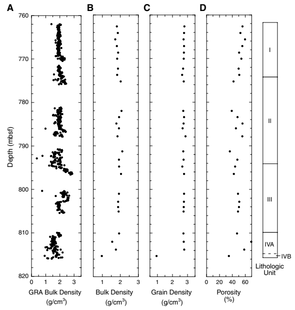

F59. Basement unit index properties, p. 100.

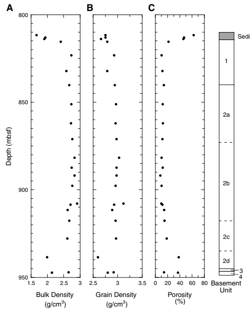

~50% between 762 and 811 mbsf. Below 811 mbsf in Unit IV, porosity ranges up to ~70%, with higher porosities corresponding to the lower bulk densities.

In the basement units of Holes 1204A and 1204B, the basaltic units have a bulk density between 2.41 and 2.91 g/cm^3; the average for all basalt is 2.71 g/cm^3. The grain density of basalt varies between 2.79 and 3.12 g/cm^3 (average = 2.95 g/cm^3), and porosity varies between 8.1% and 21.5% (average = 12.5%). No systematic downhole variation of density or porosity is apparent for the basaltic basement. Lower bulk densities of 1.99 and 2.14 g/cm^3 and correspondingly higher porosities of 38.4% and 37% were found for a hyaloclastite breccia and a sandstone in the basement, respectively. For the breccia, a lower grain density of 2.6 g/cm^3 was also determined.

Compressional Wave Velocity

Compressional wave velocity was determined from both split-core sections (Cores 197-1204A-1R through 6R and Sections 197-1204B-1R-1 through 1R-3) and discrete sample measurements (Table **T16;** Fig. **F60**). *P*-wave velocity was measured in only the x-direction for split sediment cores and ranges from ~1600 to ~2400 m/s. However, only 12 out of 32 samples has a *P*-wave velocity >1800 m/s; the average of all samples is 1860 m/s.

T16. Compressional wave velocity, p. 124.

F60. Compressional wave velocity, p. 101.

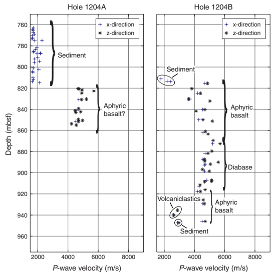

For discrete samples of basement material from Holes 1204A and 1204B, *P*-wave velocity was measured in x- and z-directions. For the basalt, the *P*-wave velocity ranges from 3600 to 5700 m/s, with velocities determined in x-direction generally lower than those determined in the z-direction. However, this is probably only an apparent anisotropy because to obtain a good signal on the unevenly cut minicores in the x-direction (along the axis of the minicores) larger amounts of water were needed to couple the PWS3 transducers than in the z-direction, where the surface is curved. In Hole 1204A, a smooth line through the data points suggests a decrease in *P*-wave velocity from the top of the basement section to the bottom of the hole in Subunit 2a (from ~5000 to 4500 m/s). However, this trend is uncertain because of the large spread of data points and the small basement penetration. In contrast, the data from Hole 1204B suggest an increase in *P*-wave velocity from the top of the basement section to a depth of ~872 mbsf, throughout the basalt in basement Unit 1 and Subunit 2a, from ~4500 to >5000 m/s. Throughout basement Subunit 2b (a diabase) (see **"Physical Volcanology and Igneous Petrology,"** p. 11), *P*-wave velocities decrease again with depth to ~4500 m/s then remain approximately constant at 4600 m/s in basement Subunit 2c and Unit 3. In basement Subunit 2d and basement Unit 4, a hyaloclastite and a sediment, respectively, *P*-wave velocities of 2600–2900 and ~2900 m/s were recorded.

UNDERWAY GEOPHYSICS

Seismic Reflection Profiling

Initial selection of proposed Site HE-3, which became Site 1204, was based on data gathered at ODP Site 883, where basement was reached at ~820 mbsf (Rea, Basov, Janecek, Palmer-Julson, et al., 1993). A single-channel seismic survey, 3.5-kHz PDR, and magnetometer survey were conducted in the vicinity of Site 883 to ensure proper hole location and suitability for basement drilling. A digital seismic line acquired by the *Faranella* in the vicinity of Site 883/1204 supplemented data acquired during our survey. Figure **F61** shows the track line of the Leg 197 survey superimposed on ETOPO5 seafloor bathymetry with a contour interval of 100 m. Tick marks along our survey lines mark half-hour intervals. The *Faranella* seismic line is labeled F2-87-AA (*Faranella*) and is annotated with its corresponding Julian day and Universal Time Coordinated (UTC) time markers.

Survey Lines 1 and 3 pass directly over Site 883. Approximately 4-km-long sections from Lines 1 and 3 are shown in Figures **F62** and **F63,** respectively. The midpoint of the active part of the streamer was ~218 m astern of the water gun source, which was ~4.5–6 m deep. The midpoint between the active section of the streamer and the water gun source was ~191 m astern of the ship's recorded GPS position. The water gun was fired every 6 s. Each shot record is 5 s in length, beginning 100 ms before the water gun was triggered. This 100-ms delay, created by the trigger control panel, was removed in SIOSEIS record processing. Ship speed averaged 5.91 kt (3.04 m/s) during Line 1 and 5.35 kt (2.75 m/s) during Line 3. All three lines were processed with SIOSEIS seismic processing software (version 2001.3) (**http://sioseis.ucsd.edu**), using predictive deconvolution, bandpass filtering from 40 to 100 Hz, and finite-difference migration applying a simple velocity model. Table **T17** shows the SIOSEIS script processing parameters for each line. Holes 1204A and 1204B are ~575 m along Line 3 southeast of Hole 883F.

Sites 883 and 1204 are located in the middle of a broad depression in the basement. This swale is ~1–2 km across and slightly >0.1 s two-way traveltime (TWT) deep. The ~1 s TWT to the basement at both sites corresponds to a sediment cover ~820 m thick, thus, to an average velocity of ~1640 m/s. A strong, nonreverberant, and low-frequency reflection, which is flat where Holes 1204A and 1204B are situated, marks the volcanic basement contact at ~4.2 s TWT in the deepest part of the basin. The basement contact can be identified elsewhere on the sections by an abrupt decrease in reflection coherency. The lack of laterally coherent internal reflectivity in the basement is consistent with the massive nature of the basalt cores recovered from Site 1204. This contrasts with Site 1203, where the presence of volcaniclastic sediment interbedded with massive lava flows caused reverberations that lasted >0.2 s TWT (see **"Underway Geophysics,"** p. 46, in the "Site 1203" chapter).

The sediment cap also exhibits some notable structure. The far left side of Figure **F63** between 3.8 and 3.9 s TWT shows successive southeast-dipping reflectors propagating to the right and downlapping to the southeast. Another large clinoform was imaged just above the basement on the far left of Figure **F63** at ~4.1 s TWT. The southeast-downlapping, sigmoidal nature of the clinoforms indicates a low-energy depositional environment with a sediment source somewhere to the northwest. Unlike Site 1203, the upper part of the sediment cover at Site 1204 lacks a low angular unconformity that would indicate a shifting pattern of erosion and deposition by the bottom current that shaped the formation of the Meiji sediment drift.

F61. Site 1204 seismic reflection survey, p. 102.

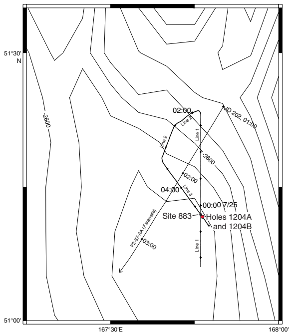

F62. Migrated time section of survey Line 1, p. 103.

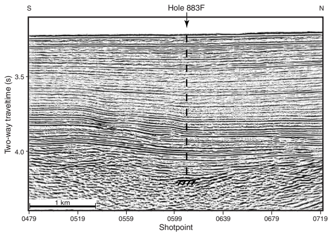

F63. Migrated time section of survey Line 3, p. 104.

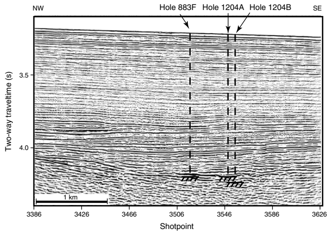

T17. SIOSEIS process parameters, p. 125.

REFERENCES

Alt, J.C., 1995. Subseafloor processes in mid-ocean ridge hydrothermal systems. *In* Humphris, S.E., Zierenberg, R., Mullineaux, L., and Thomson, R. (Eds.), *Seafloor Hydrothermal Systems: Physical, Chemical, Biological and Geological Interactions within Hydrothermal Systems.* Geophys. Monogr., Am. Geophys. Union, 91:85–114.

Banerjee, S.K., 1991. Magnetic properties of Fe-Ti oxides. *In* Lindsley, D.H. (Ed.), *Oxide Minerals: Petrologic and Magnetic Significance:* Rev. Mineral., 25:107–128.

Barton, C.E., Baldwin, R.T., Barraclough, D.R., et al., 1995. International Geomagnetic Reference Field, 1995 revision presented by IAGA Division V, Working Group 8. *Phys. Earth Planet. Int.,* 97:23–26.

Berggren, W.A., Kent, D.V., Swisher, C.C., III, and Aubry, M.-P., 1995. A revised Cenozoic geochronology and chronostratigraphy. *In* Berggren, W.A., Kent, D.V., Aubry, M.-P., and Hardenbol, J. (Eds.), *Geochronology, Time Scales and Global Stratigraphic Correlation.* Spec. Publ.—Soc. Econ. Paleontol. Mineral., 54:129–212.

Burnett, J.A., 1998. Upper Cretaceous. *In* Bown, P.R. (Ed.), *Calcareous Nannofossil Biostratigraphy:* London (Kluwer Academic Publishers), 132–199.

Cande, S.C., and Kent, D.V., 1995. Revised calibration of the geomagnetic polarity timescale for the Late Cretaceous and Cenozoic. *J. Geophys. Res.,* 100:6093–6095.

Collyer, S., Grimes, N.W., Vaughn, D.J., and Longworth, G., 1988. Studies of the crystal structure and crystal chemistry of titanomagnetite. *Am. Mineral.,* 73:153–160.

Cottrell, R.D., and Tarduno, J.A., in press. A Late Cretaceous pole for the Pacific plate: implications for apparent and true polar wander and the drift of hotspots. *Tectonophysics.*

Cottrell, R.D., and Tarduno, J.A., 2001. A Late Cretaceous paleomagnetic pole from Detroit Seamount: evidence for fast plate velocities rather than true polar wander. *Eos, Trans., Am. Geophys. Union,* 80:S418.

Cox, A.V., 1970. Latitude dependence of the angular dispersion of the geomagnetic field. *Geophys. J. R. Astron. Soc.,* 20:253–269.

Erba, E., Premoli Silva, I., and Watkins, D.K., 1995. Cretaceous calcareous plankton biostratigraphy of Sites 872 through 879. *In* Haggerty, J.A., Premoli Silva, I., Rack, F., and McNutt, M.K. (Eds.), *Proc. ODP, Sci. Results,* 144: College Station, TX (Ocean Drilling Program), 157–169.

Frey, F.A., Garcia, M.O., Wise, W.S., Kennedy, A., Gurriet, P., and Albarede, F., 1991. The evolution of Mauna Kea Volcano, Hawaii: petrogenesis of tholeiitic and alkalic basalts. *J. Geophys. Res.,* 96:14347–14375.

Frey, F.A., Wise, W.S., Garcia, M.O., West, H., Kwon, S.-T., and Kennedy, A., 1990. Evolution of Mauna Kea Volcano, Hawaii: petrologic and geochemical constraints on postshield volcanism. *J. Geophys. Res.,* 95:1271–1300.

Furuta, T., 1993. Magnetic properties and ferromagnetic mineralogy of oceanic basalts. *Geophys. J. Int.,* 113:95–114.

Goss, C.J., 1988. Saturation magnetization, coercivity and lattice parameter changes in the system Fe_3O_4–g-Fe_2O_3, and their relationship to structure. *Phys. Chem. Minerals,* 16:164–171.

Graham, J.W., 1949. The stability and significance of magnetism in sedimentary rock. *J. Geophys. Res.,* 54:131–167.

Hon, K., Kauahikaua, J.P., Denlinger, R., and Mackay, K., 1994. Emplacement and inflation of pahoehoe sheet flows: observations and measurements of active lava flows on Kilauea, Hawaii. *Geol. Soc. Am. Bull.,* 106:351–370.

Jaeger, J.C., 1964. Thermal effects of intrusions. *Rev. Geophys.,* 2:443–446.

Keller, R.A., Duncan, R.A., and Fisk, M.R., 1995. Geochemistry and $^{40}Ar/^{39}Ar$ geochronology of basalts from ODP Leg 145 (North Pacific Transect). *In* Rea, D.K., Basov, I.A., Scholl, D.W., and Allan, J.F. (Eds.), *Proc. ODP, Sci. Results,* 145: College Station, TX (Ocean Drilling Program), 333–344.

Keller, R.A., Fisk, M.R., and White, W.M., 2000. Isotopic evidence for Late Cretaceous plume-ridge interaction at the Hawaiian hotspot. *Nature,* 405:673–676.

Kirschvink, J.L., 1980. The least-squares line and plane and the analysis of palaeomagnetic data. *Geophys. J. R. Astron. Soc.,* 62:699–718.

Lindsley, D.H., 1976. The crystal chemistry and structure of oxide minerals as exemplified by the Fe-Ti oxides. *Rev. Mineral.* 3:L1–l60.

Lonsdale, P., Dieu, J., and Natland, J., 1993. Posterosional volcanism in the Cretaceous part of the Hawaiian hotspot trail. *J. Geophys. Res.,* 98:4081–4098.

Lowrie, W., and Fuller, M., 1971. On the alternating field demagnetization characteristics of multidomain thermoremanent magnetization in magnetite. *J. Geophys. Res.,* 76:6339–6349.

Macdonald, G.A., and Katsura, T., 1964. Chemical composition of Hawaiian lavas. *J. Petrol.,* 5:82–133.

McFadden, P.L., Merrill, R.T., McElhinny, M.W., and Lee, S., 1991. Reversals of the Earth's magnetic field and temporal variations of the dynamo families. *J. Geophys. Res.,* 96:3923–3933.

McFadden, P.L., and Reid, A.B., 1982. Analysis of paleomagnetic inclination data. *Geophys. J. R. Astron. Soc.,* 69:307–319.

Rea, D.K., Basov, I.A., Janecek, T.R., Palmer-Julson, A., et al., 1993. *Proc. ODP, Init. Repts.,* 145: College Station, TX (Ocean Drilling Program).

Rea, D.K., Basov, I.A., Krissek, L.A., and the Leg 145 Scientific Party, 1995. Scientific results of drilling the North Pacific Transect. *In* Rea, D.K., Basov, I.A., Scholl, D.W., and Allan, J.F. (Eds.), *Proc. ODP, Sci. Results,* 145: College Station, TX (Ocean Drilling Program), 577–596.

Rea, D.K., Basov, I.A., Scholl, D.W., and Allan, J.F. (Eds.), 1995. *Proc. ODP, Sci. Results,* 145: College Station, TX (Ocean Drilling Program).

Rea, D.K., and Thiede, J., 1981. Mesozoic and Cenozoic mass accumulation rates of the major sediment components in the Nauru Basin, Western Equatorial Pacific. *In* Larson, R.L., Schlanger, S.O., et al., *Init. Repts. DSDP,* 61: Washington (U.S. Govt. Printing Office), 549–555.

Rhodes, J.M., 1996. Geochemical stratigraphy of lava flows sampled by the Hawaii Scientific Drilling Project. *J. Geophys. Res.,* 101:11769–11780.

Schlanger, S.O., and Premoli-Silva, I., 1981. Tectonic, volcanic, and paleogeographic implications of redeposited reef faunas of Late Cretaceous and Tertiary age from the Nauru Basin and the Line Islands. *In* Larson, R.L., Schlanger, S.O., et al., *Init. Repts. DSDP,* 61: Washington (U.S. Govt. Printing Office), 817–827.

Self, S., Keszthelyi, L., and Thordarson, T., 1998. The importance of pahoehoe. *Annu. Rev. Earth Planet. Sci,* 26:81–110.

Sun, S.-S., and McDonough, W.F., 1989. Chemical and isotopic systematics of oceanic basalts: implications for mantle composition and processes. *In* Saunders, A.D., and Norry, M.J. (Eds.), *Magmatism in the Ocean Basins.* Spec. Publ.—Geol. Soc. London, 42:313–345.

Tarduno, J.A., and Cottrell, R.D., 1997. Paleomagnetic evidence for motion of the Hawaiian hotspot during formation of the Emperor Seamounts. *Earth Planet. Sci. Lett.,* 153:171–180.

Thordarson, T., and Self, S., 1998. The Roza Member, Columbia River Basalt Group—a gigantic pahoehoe lava flow field formed by endogenous processes. *J. Geophys. Res.,* 103:27411–27445.

Vallier, T.L., Dean, W.E., Rea, D.K., and Thiede, J., 1983. Geologic evolution of Hess Rise, central North Pacific Ocean. *Geol. Soc. Am. Bull.,* 94:1289–1307.

Van der Voo, R., Henry, S.G., and Pollack, H.N., 1978. On the significance and utilization of secondary magnetizations in red beds. *Phys. Earth Planet. Inter.,* 16:12–19.

Waychunas, G.A., 1991. Crystal chemistry of oxides and oxyhydroxides. *In* Lindsley, D.H. (Ed.), *Oxide Minerals: Petrologic and Magnetic Significance.* Rev. Mineral., 25:11–68.

Figure F1. Map showing location of Site 1204.

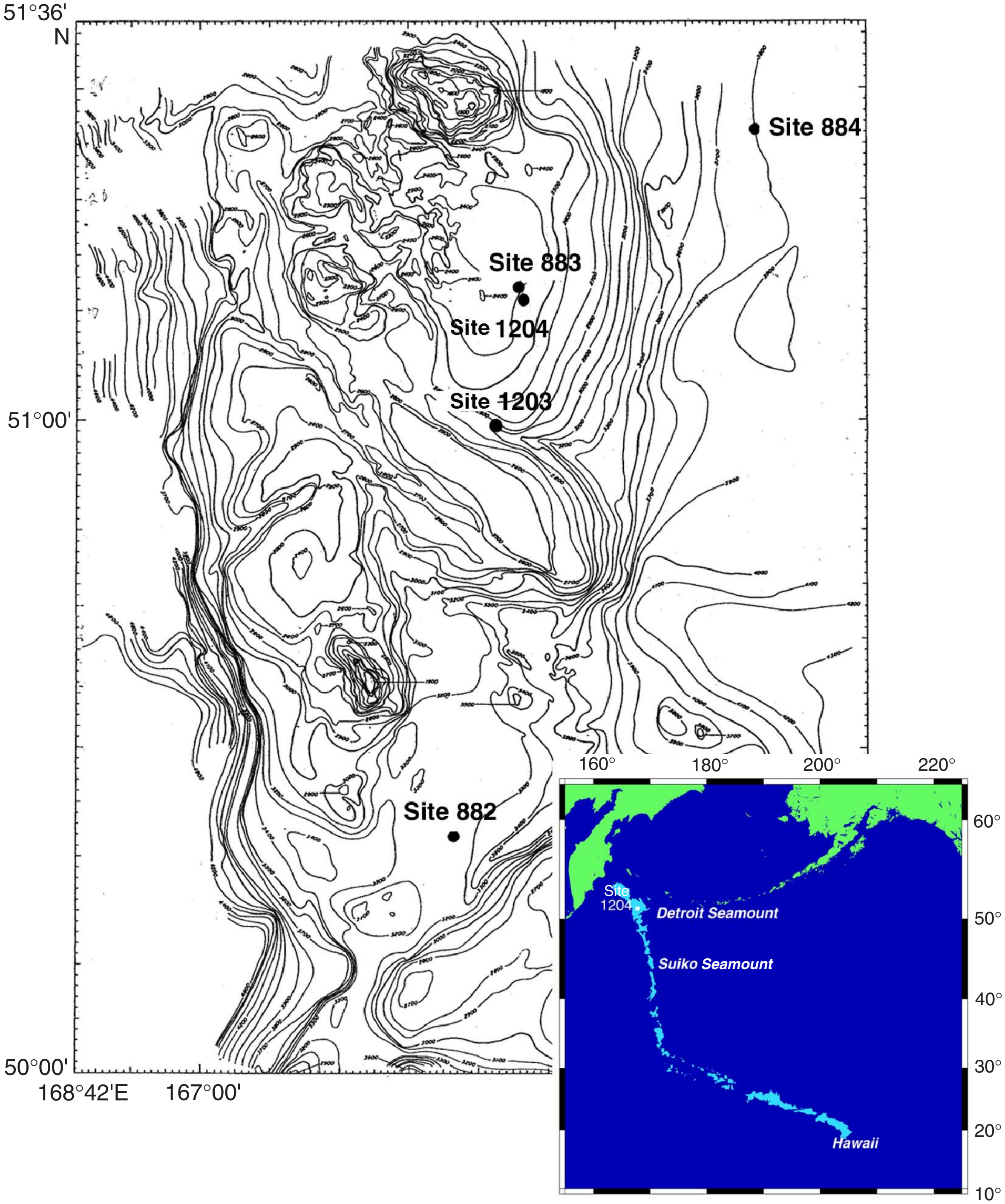

Figure F2. Hole 1204A lithology, units, time framework, and downhole variability of (**A**) carbonate, nannofossils, foraminifers, clay, and organic debris compared with measured magnetic susceptibility. (Continued on next page.)

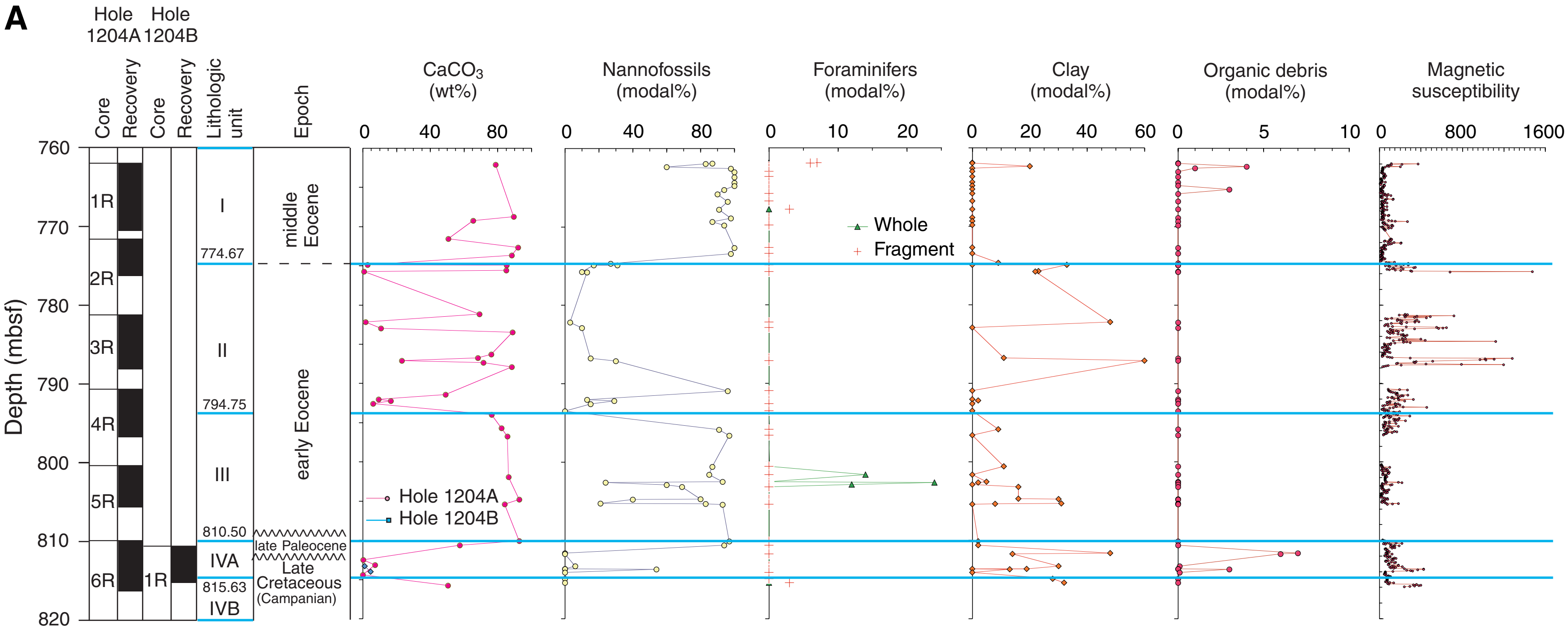

Figure F2 (continued). Hole 1204A lithology, units, time framework, and downhole variability of (**B**) others (defined in "Site 1204 Smear Slides," p. 80), palagonite/volcanic ash, opaque minerals/Fe oxides, detrital calcite + dolomite, and feldspar compared with magnetic susceptibility.

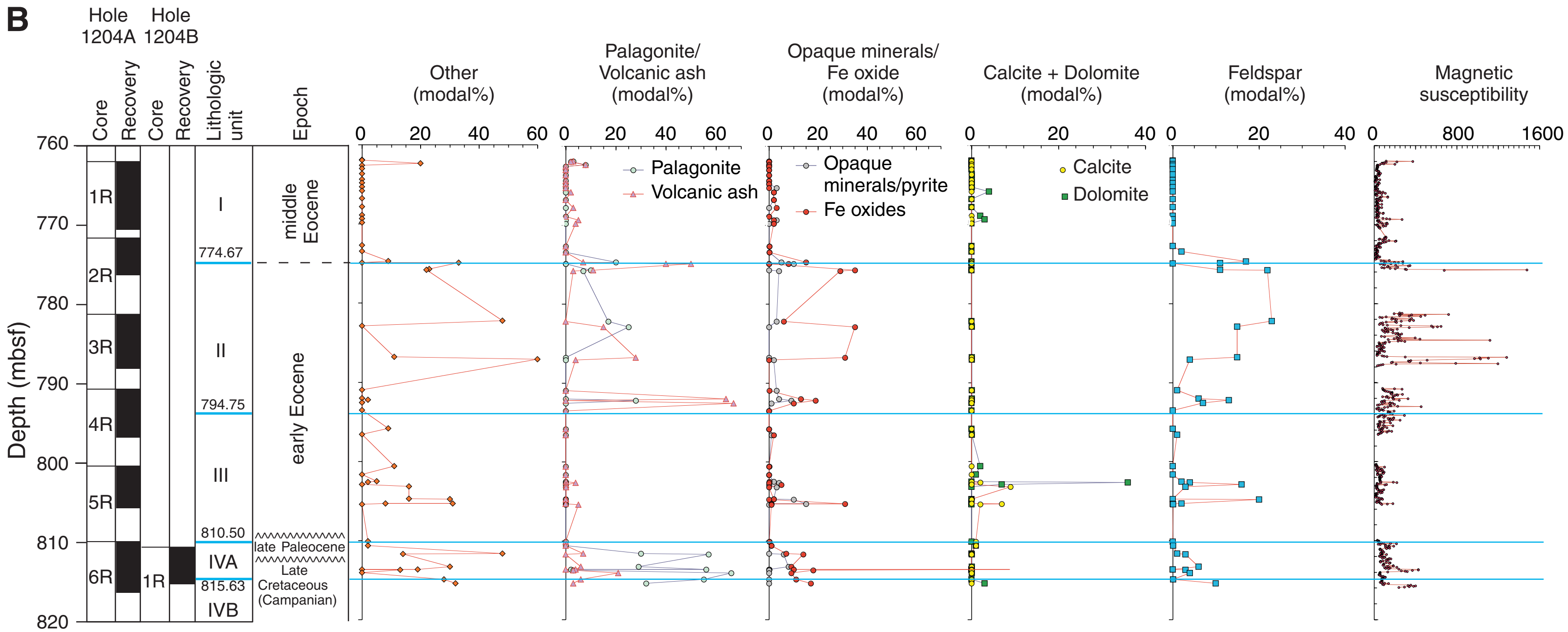

Figure F3. Detailed analysis of Hole 1204B. Variations in (**A**) nannofossils, calcite, gypsum, and organic debris compared with measured magnetic susceptibility. (Continued on next page).

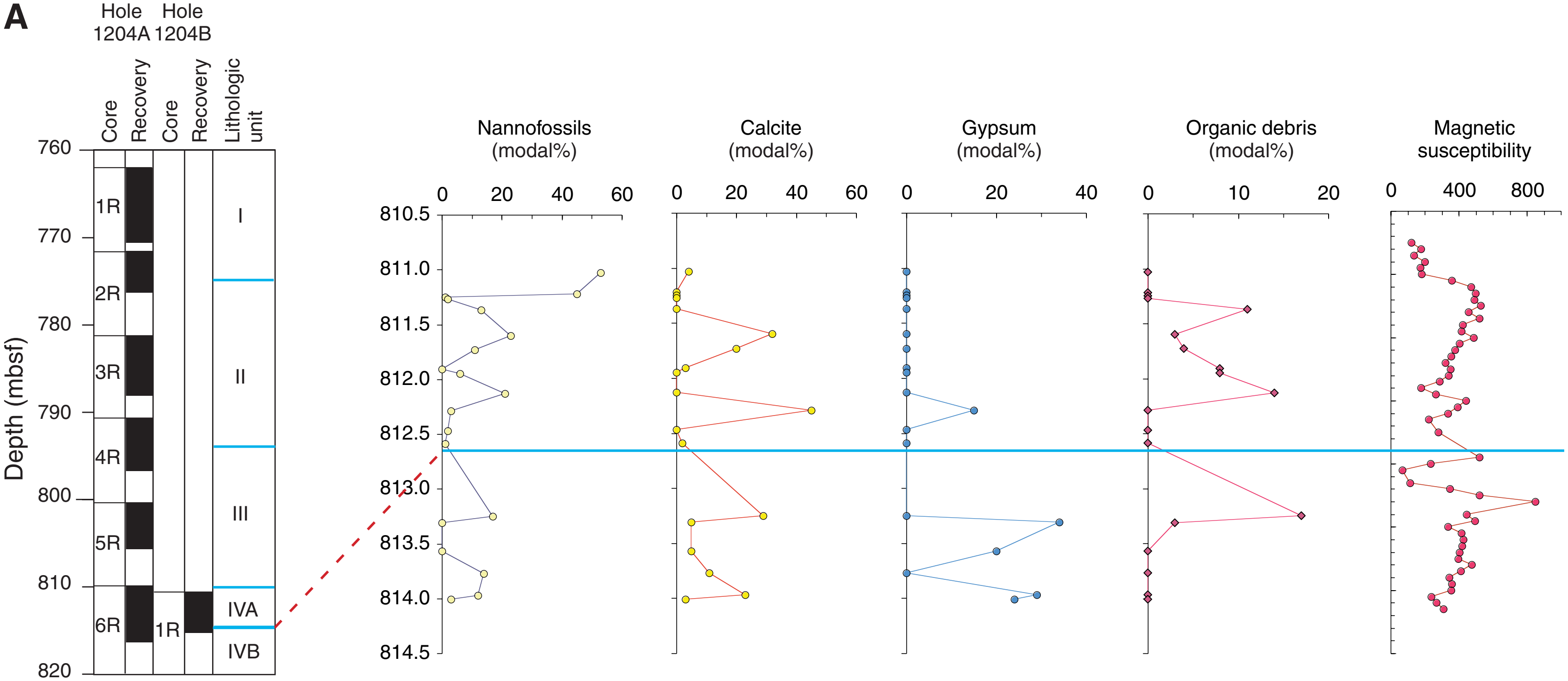

Figure F3 (continued). Variations in (**B**) others (defined in **"Site 1204 Smear Slides,"** p. 80), opaque minerals/Fe oxides, palagonite/volcanic ash, and clay compared with magnetic susceptibility.

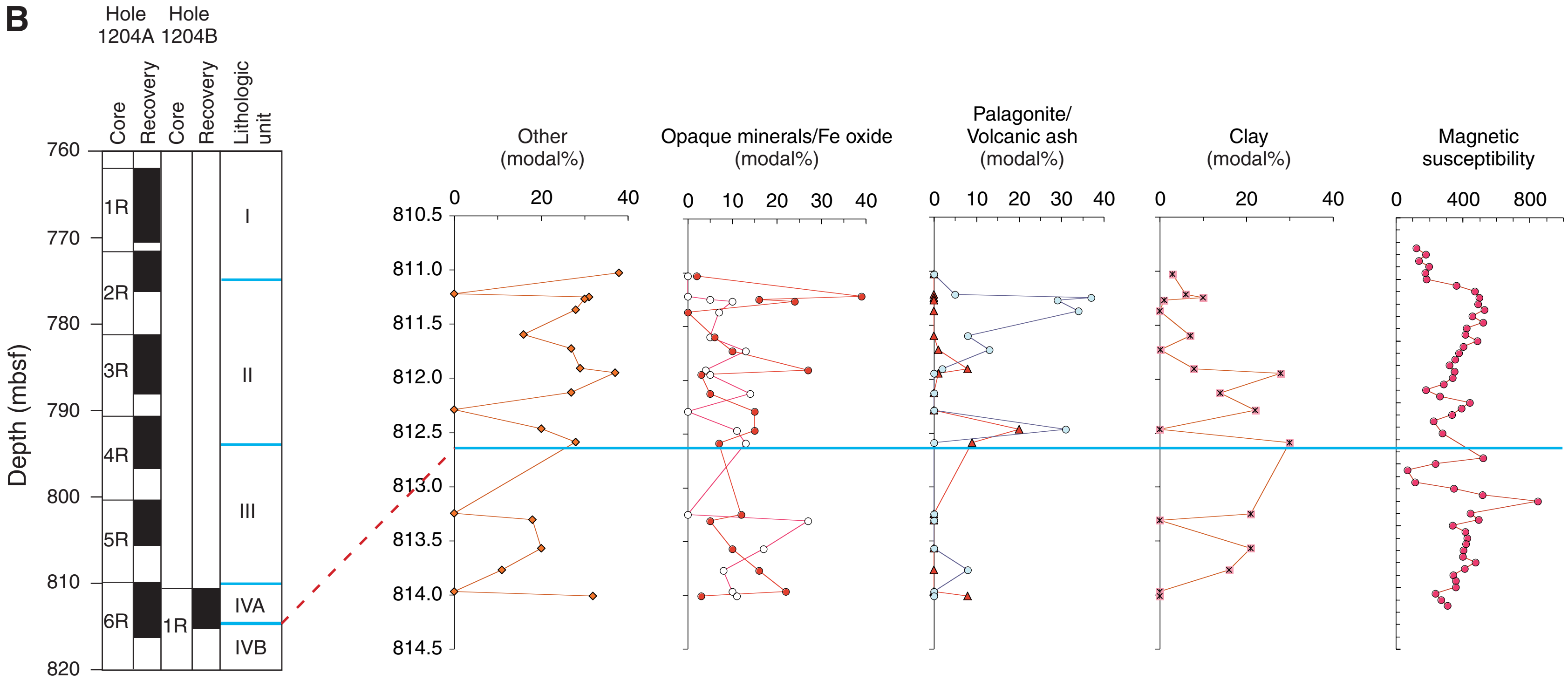

Figure F4. Close-up photographs of different lithologies observed at Site 1204. **A.** Rotated, broken body overlying a thick interval consisting of a thin-faulted very finely laminated bed (at 30–45 cm) and convoluted laminations (below 45 cm), likely indicating slumping. Note the 2-cm brown beds of silt volcanic material alternating with finely laminated, bioturbated (e.g., at 35–40 and 45–48 cm) and burrowed (i.e., at 37 and 42 cm) nannofossil chalk (interval 197-1204A-3R-2, 29–49 cm). **B.** Sharply laminated bed of fresh basaltic vitric ash with sharpness decreasing upward and vertically bioturbated at top (interval 197-1204A-3R-5, 10–29 cm). (Continued on next page.)

Figure F4 (continued). C. The boundary between Unit III and Subunit IVA (Section 197-1204A-6R-1, 45–64 cm). **D.** Dendritic Mn/Fe concretions in olive palagonite clay (interval 197-1204A-6R-1, 79–98 cm).

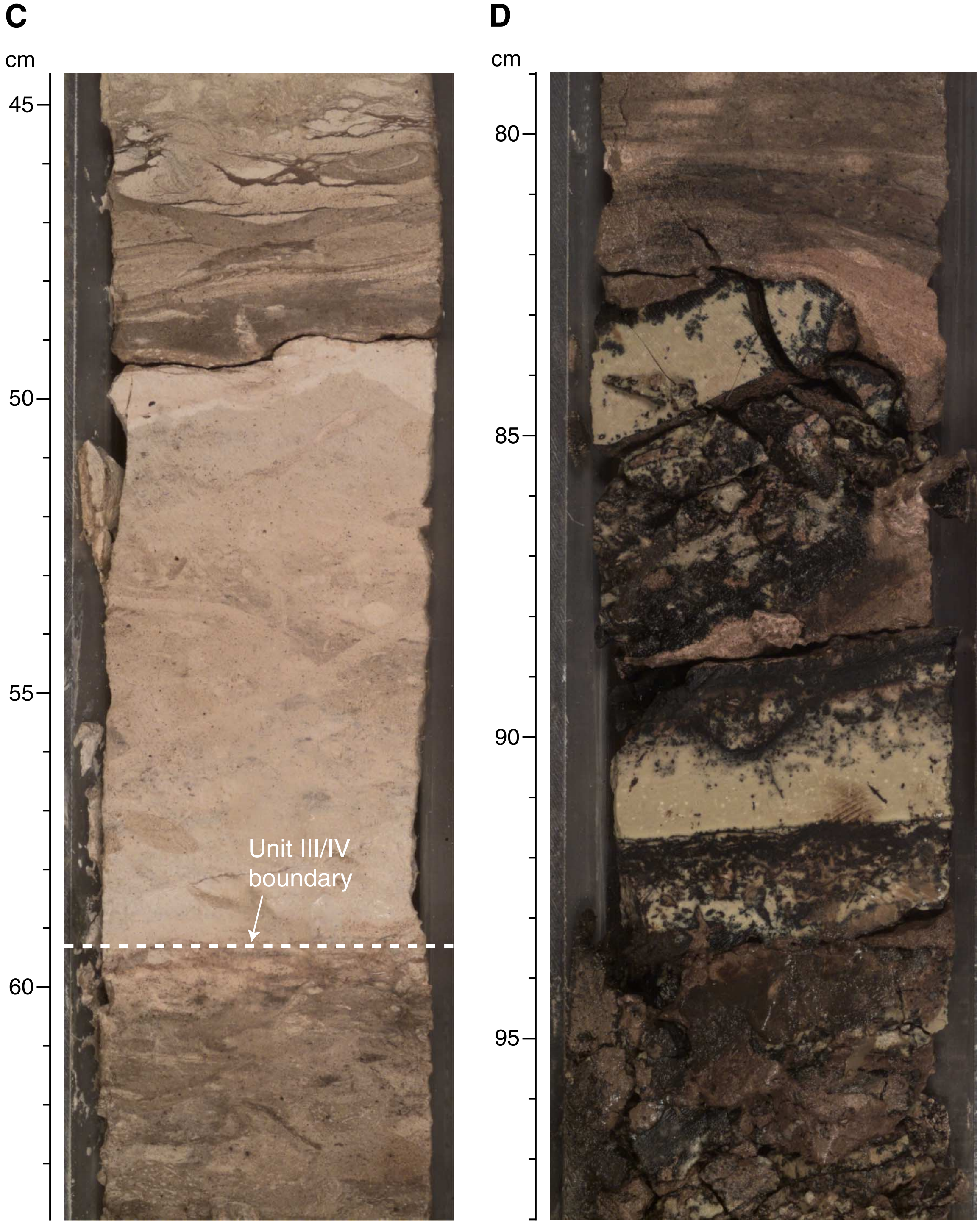

Figure F5. Calcareous nannofossil zones in Holes 1204A and 1204B plotted against core recovery and epochs. Positions of zonal boundaries are only approximate, owing to the scale of the diagram (see "Zonation," p. 10, in "Hole 1204A" in "Biostratigraphy" for accurate positions of boundaries).

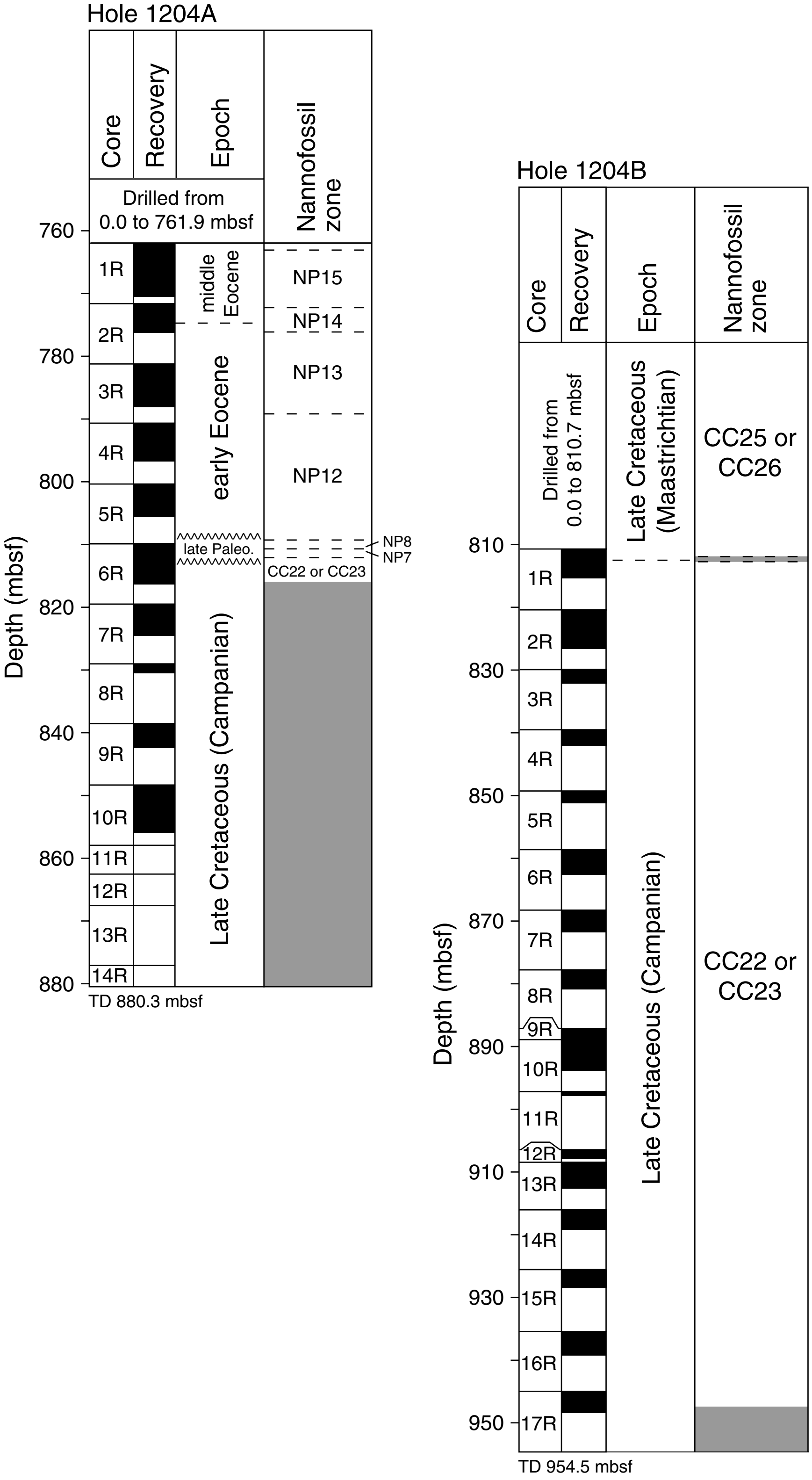

Figure F6. Diagram summarizing the recovery, age, and major lithologic features of the basement units from Holes 1204A and 1204B. TD = total depth.

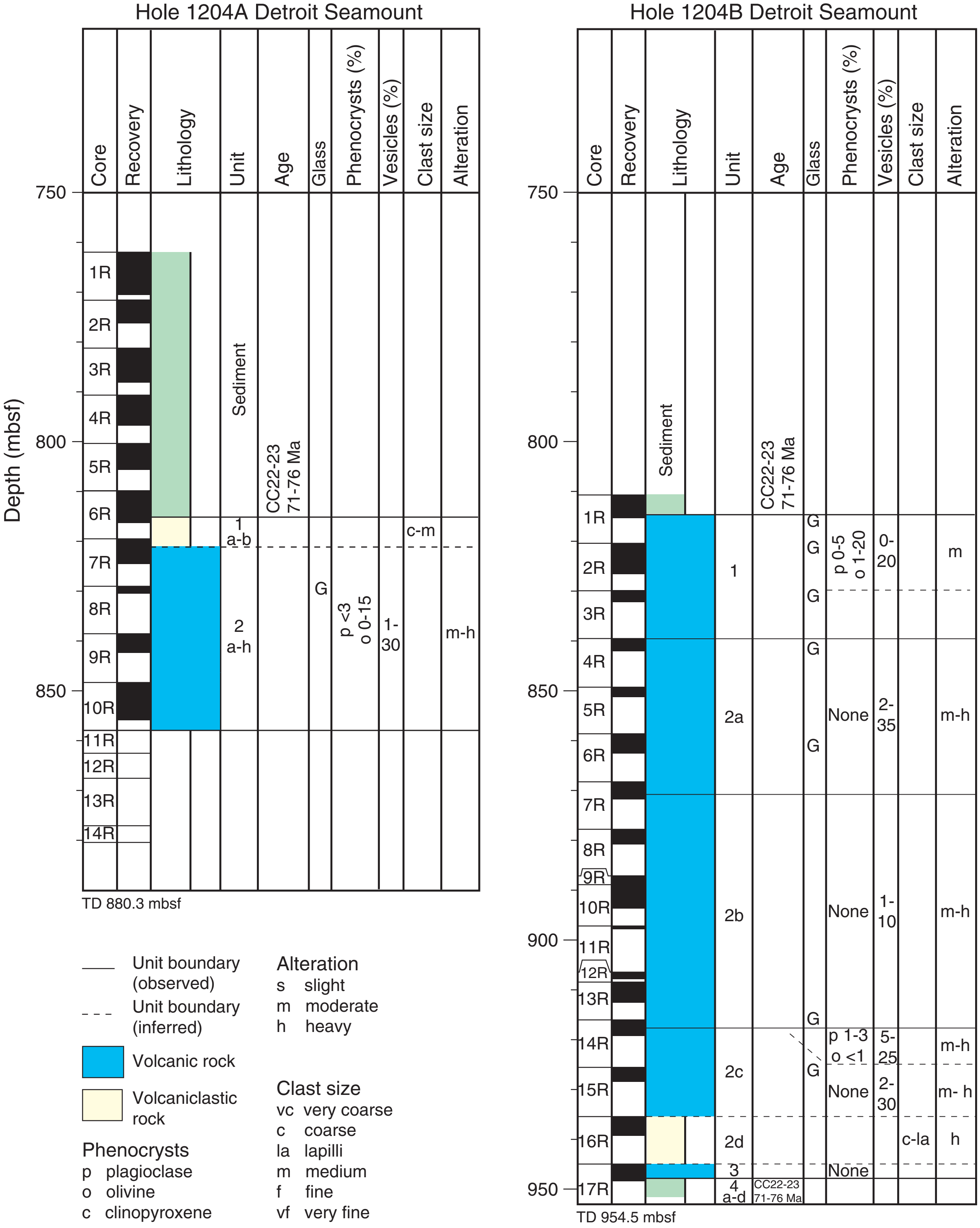

Figure F7. Photograph of Unit 1b breccia that contains angular fragments of altered glass and vesicular basalt in a carbonate cement (Section 197-1204A-7R-1 [Pieces 5 and 8]).

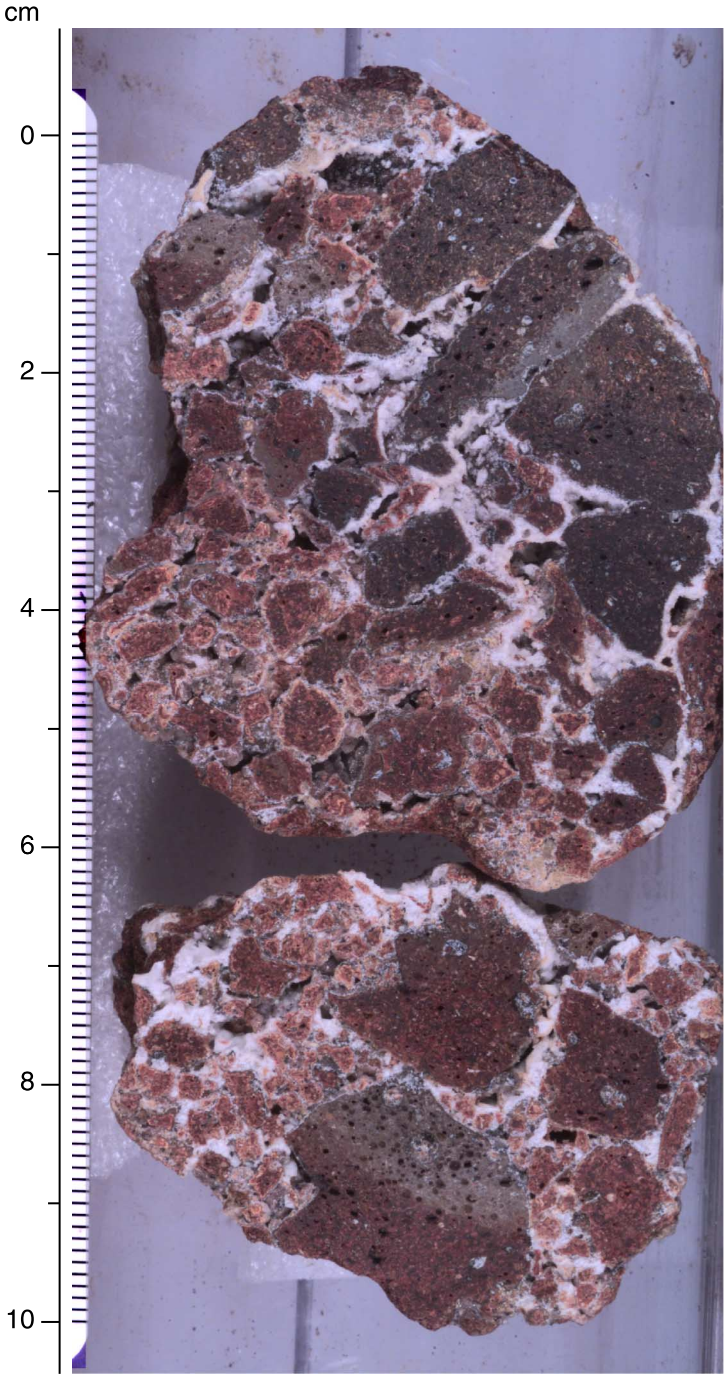

Figure F8. Photograph showing laminated carbonate sand filling joints in basalt lobes of Unit 1 (interval 197-1204B-2R-1, 53–73 cm).

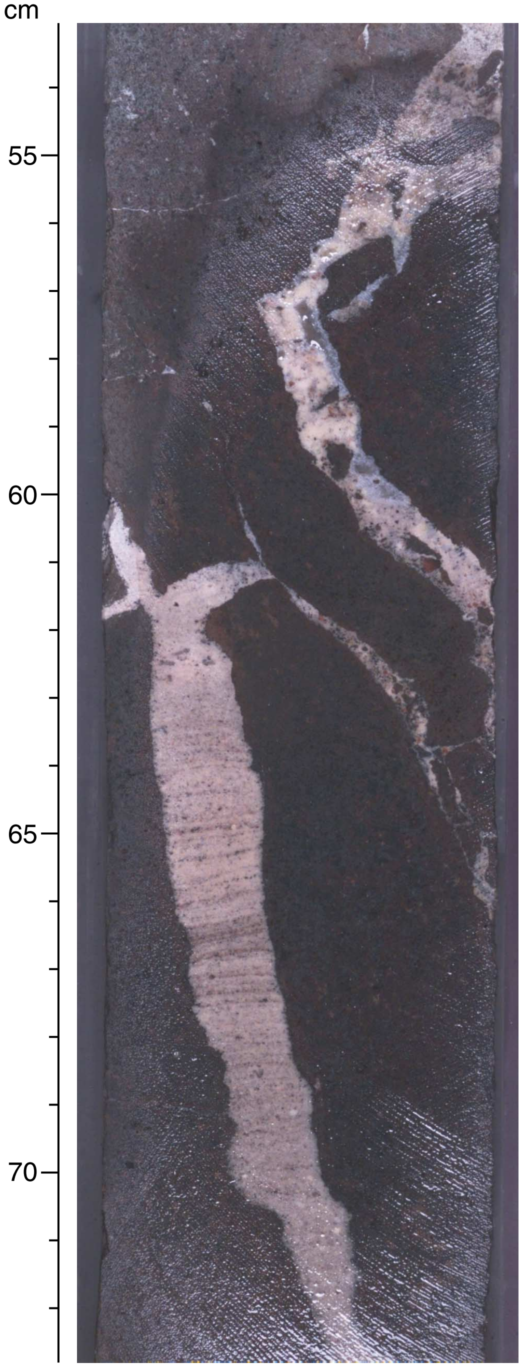

Figure F9. Photomicrograph showing optical zonation in a plagioclase phenocryst (Sample 197-1204B-14R-2, 115–117 cm) (cross-polarized light; field of view = 1.25 mm; photomicrograph 1204B-161).

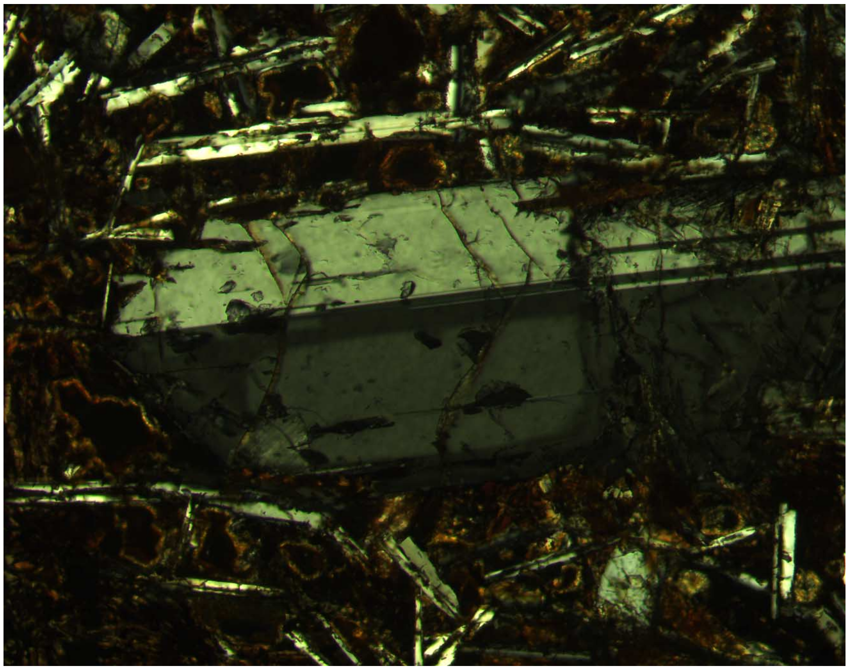

Figure F10. Photomicrograph of olivine entirely pseudomorphed by Fe oxyhydroxide and goethite and displaying euhedral shape and characteristic fracture associated with olivine (Sample 197-1204A-10R-2, 77–79 cm) (plane-polarized light; field of view = 2.5 mm; photomicrograph 1204A-126).

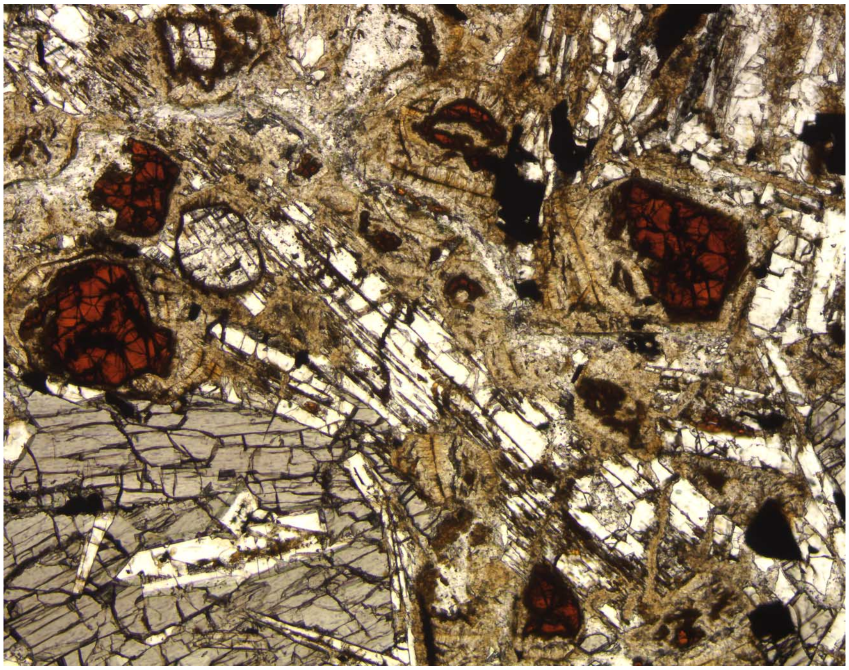

Figure F11. Photomicrograph showing unaltered olivine and plagioclase laths in a glassy lobe margin (Sample 197-1204B-3R-2, 97–100 cm) (plane-polarized light; field of view = 2.5 mm; photomicrograph 1204B-138).

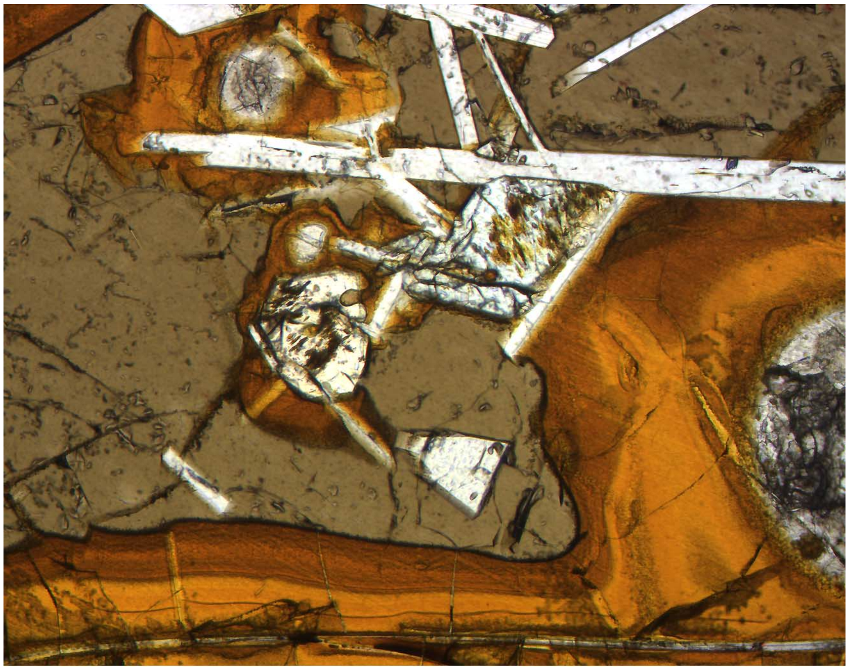

Figure F12. Photomicrograph showing unaltered olivine and plagioclase laths in glassy lobe margin (same view as Fig. F11, p. 50) (Sample 197-1204B-3R-2, 97–100 cm) (cross-polarized light; field of view = 2.5 mm; photomicrograph 1204B-156).

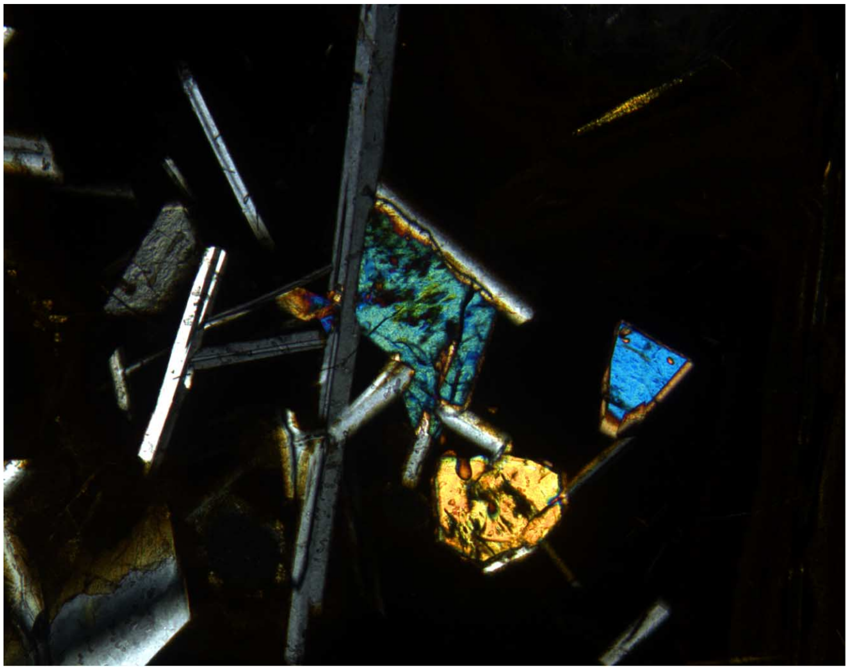

Figure F13. Photomicrograph showing unaltered olivine containing melt inclusions and plagioclase laths in glassy lobe margin (close-up view of Fig. F11, p. 50) (Sample 197-1204B-3R-2, 97–100 cm) (plane-polarized light; field of view = 1.25 mm; photomicrograph 1204B-140).

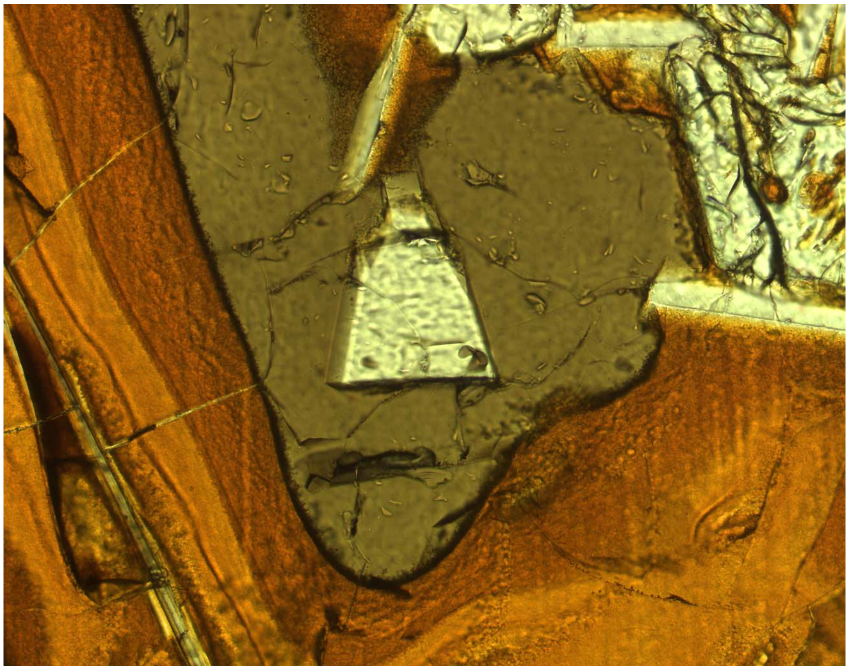

Figure F14. Photomicrograph of subophitic texture showing clinopyroxene partially enclosing plagioclase laths (Sample 197-1204B-7R-3, 140–142 cm) (cross-polarized light; field of view = 5 mm; photomicrograph 1204B-130).

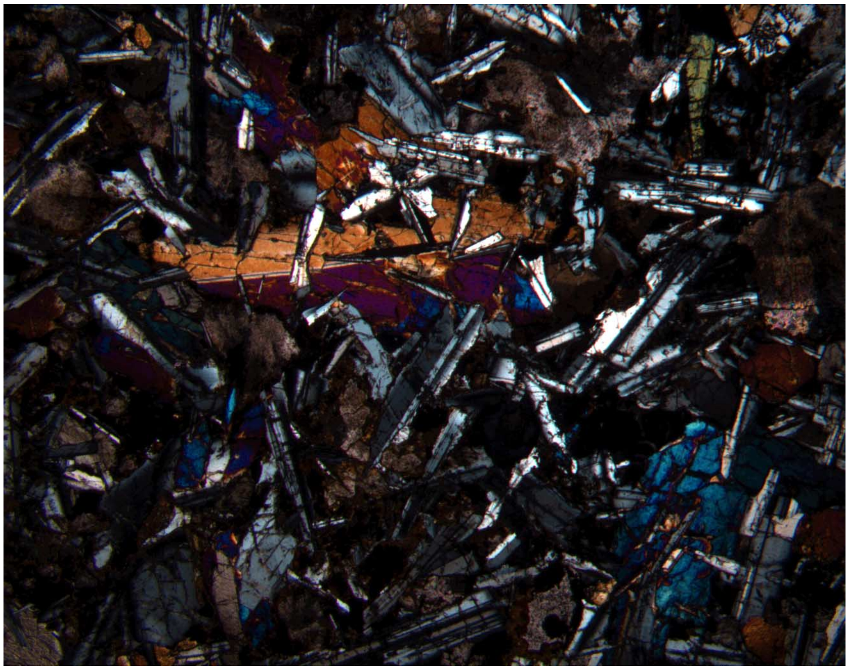

Figure F15. Photomicrograph of subophitic texture showing clinopyroxene with a pink hue partially enclosing plagioclase laths (Sample 197-1204B-7R-3, 140–142 cm) (plane-polarized light; field of view = 5 mm; photomicrograph 1204B-131).

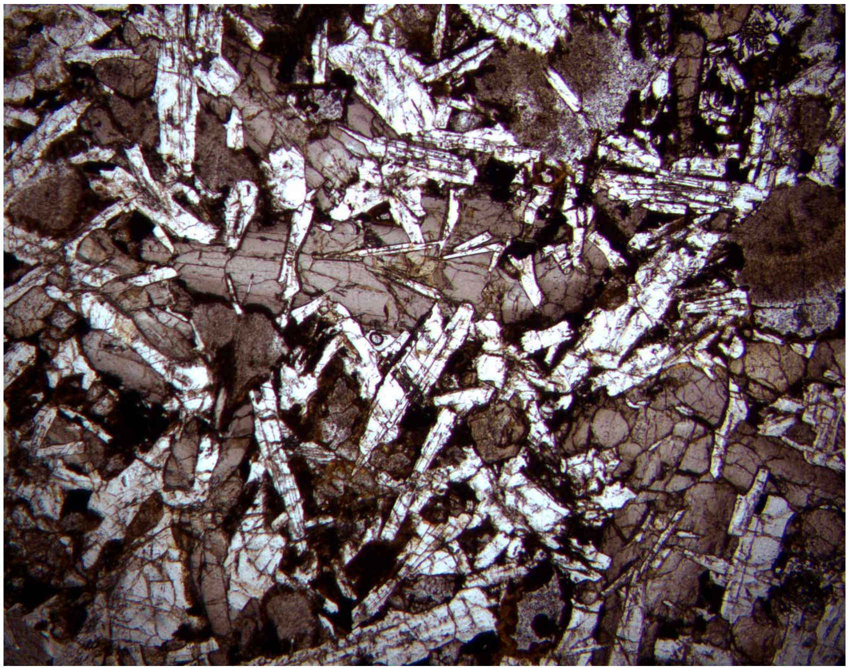

Figure F16. Photomicrograph of segregated material on margin of vesicle, with both clinopyroxene and titanomagnetite exhibiting acicular morphologies indicative of quenching (Sample 197-1204B-2R-2, 48–50 cm) (plane-polarized light; field of view = 1.25 mm; photomicrograph 1204B-157).

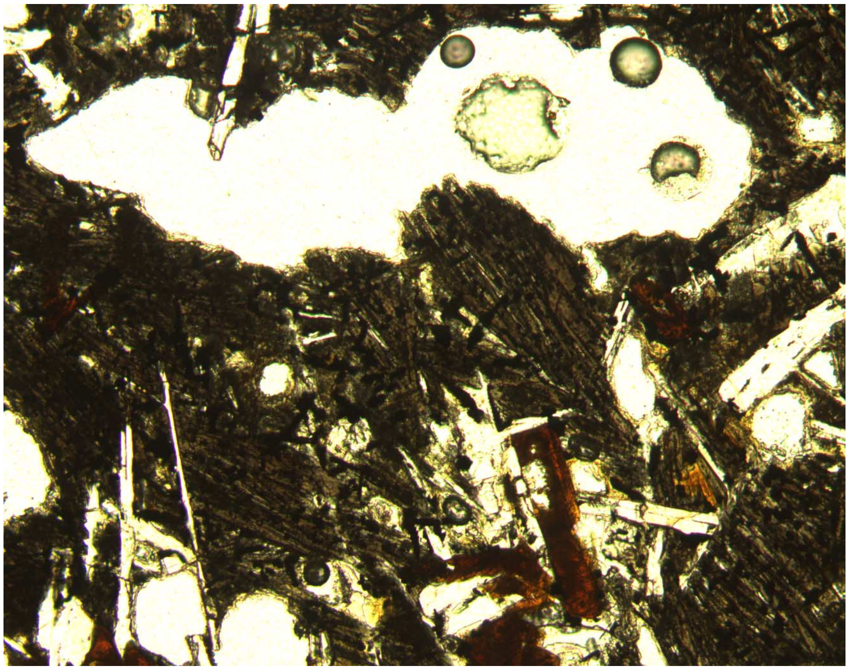

Figure F17. Photomicrograph of a vesicle cylinder containing segregated material consisting of clinopyroxene and titanomagnetite (Sample 197-1204B-15R-1, 15–18 cm) (plane-polarized light; field of view = 5 mm; photomicrograph 1204B-166).

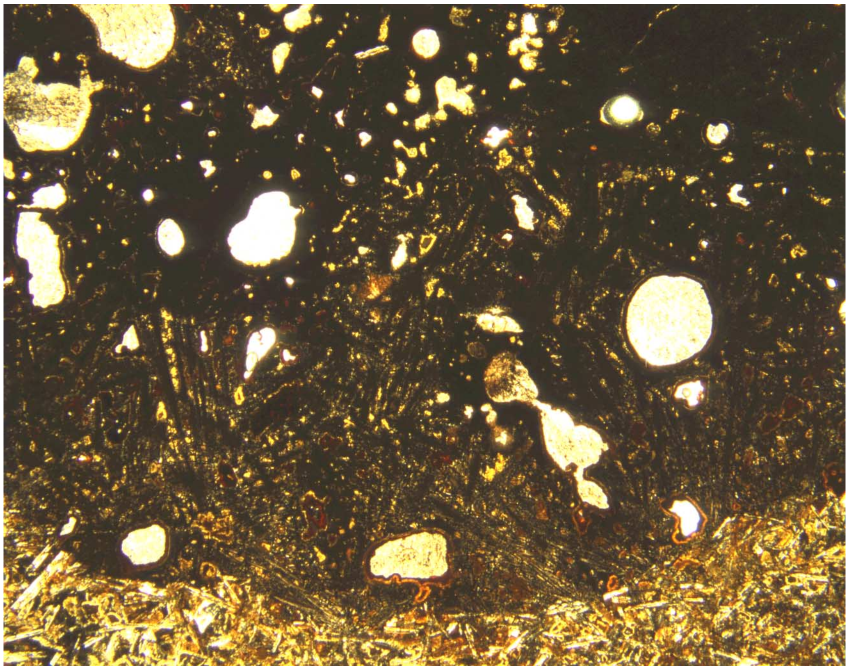

Figure F18. Photomicrograph of an unaltered titanomagnetite (gray-brown) and secondary pyrite (bright yellow) in a reducing alteration zone (Sample 197-1204B-9R-2, 22–24 cm) (reflected light; field of view = 1.25 mm; photomicrograph 1204B-153).

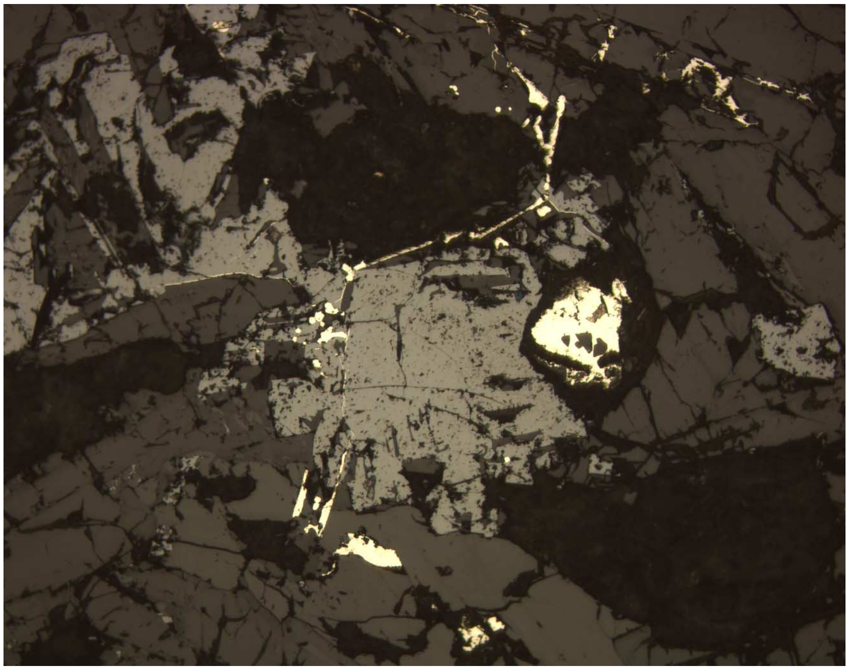

Figure F19. Photomicrographs of titanomagnetite (gray-brown) with coronas of maghemite (light gray-blue) (Sample 197-1204A-9R-1, 96–97 cm) (reflected light; field of view = 1.25 mm; photomicrograph 1204A-147).

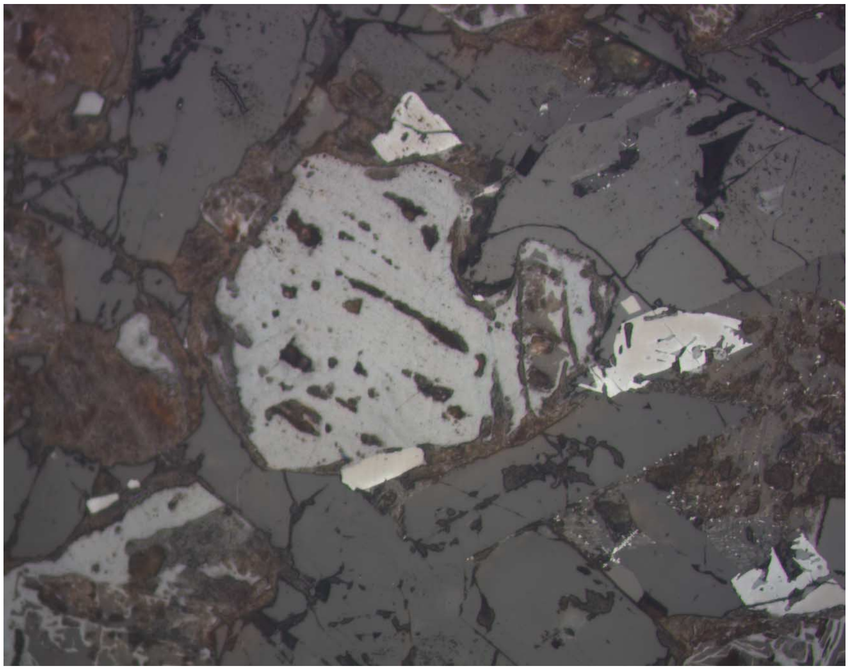

Figure F20. Reflected-light photomicrographs of titanomagnetite (gray-brown) showing variable degrees of replacement by maghemite (light gray-blue) throughout the basement sequence at Site 1204. **A.** Sample 197-1204A-9R-2, 50–51 cm (field of view = 0.625 mm; photomicrograph 1204A-114). **B.** Sample 197-1204A-9R-2, 50–51 cm (field of view = 0.625 mm; photomicrograph 1204A-115). (Continued on next two pages.)

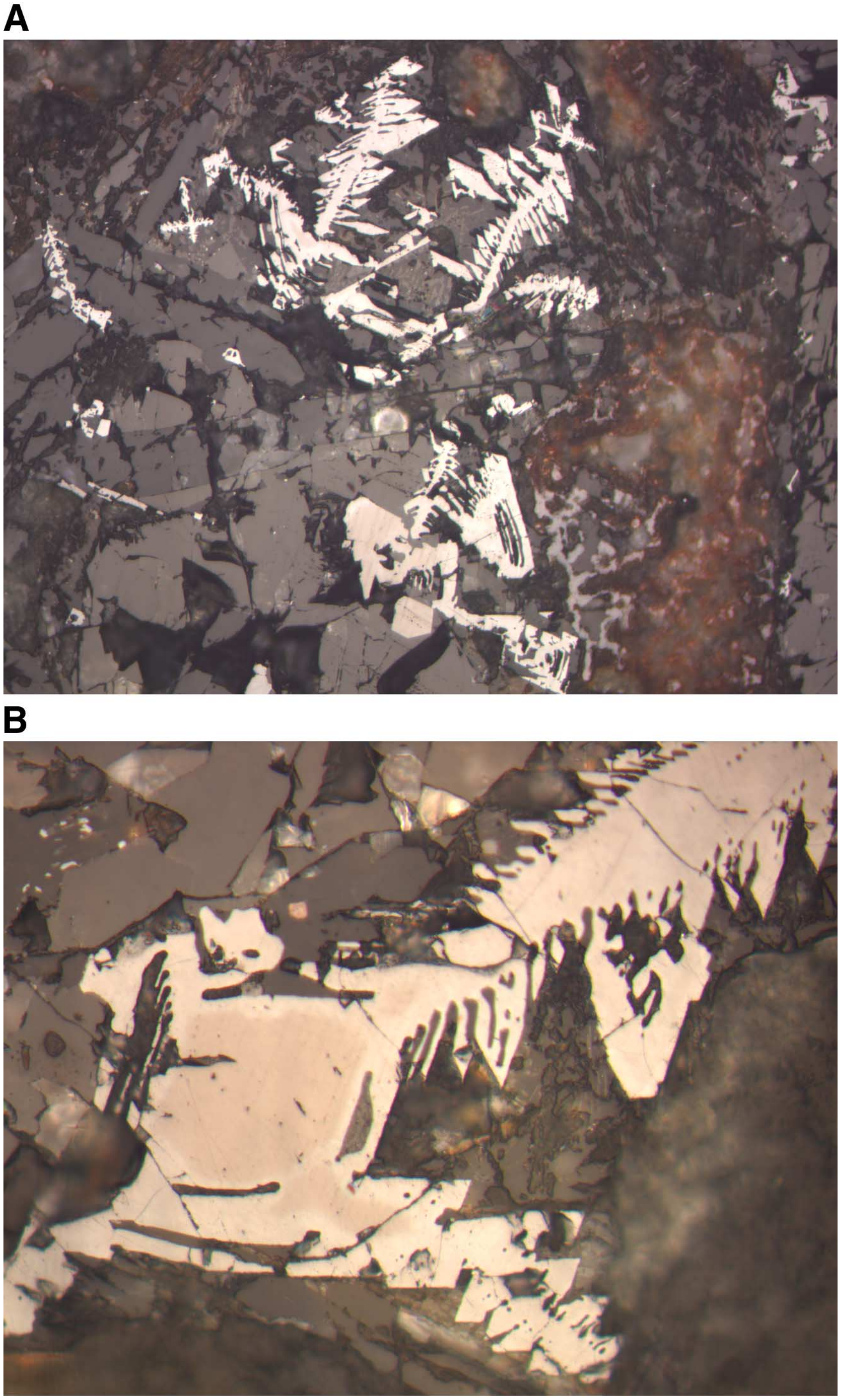

Figure F20 (continued). **C.** Sample 197-1204A-9R-2, 50–51 cm (field of view = 0.25 mm; photomicrograph 1204A-125). **D.** Sample 197-1204B-8R-3, 53–55 cm (field of view = 1.25 mm; photomicrograph 1204B-137). (Continued on next page.)

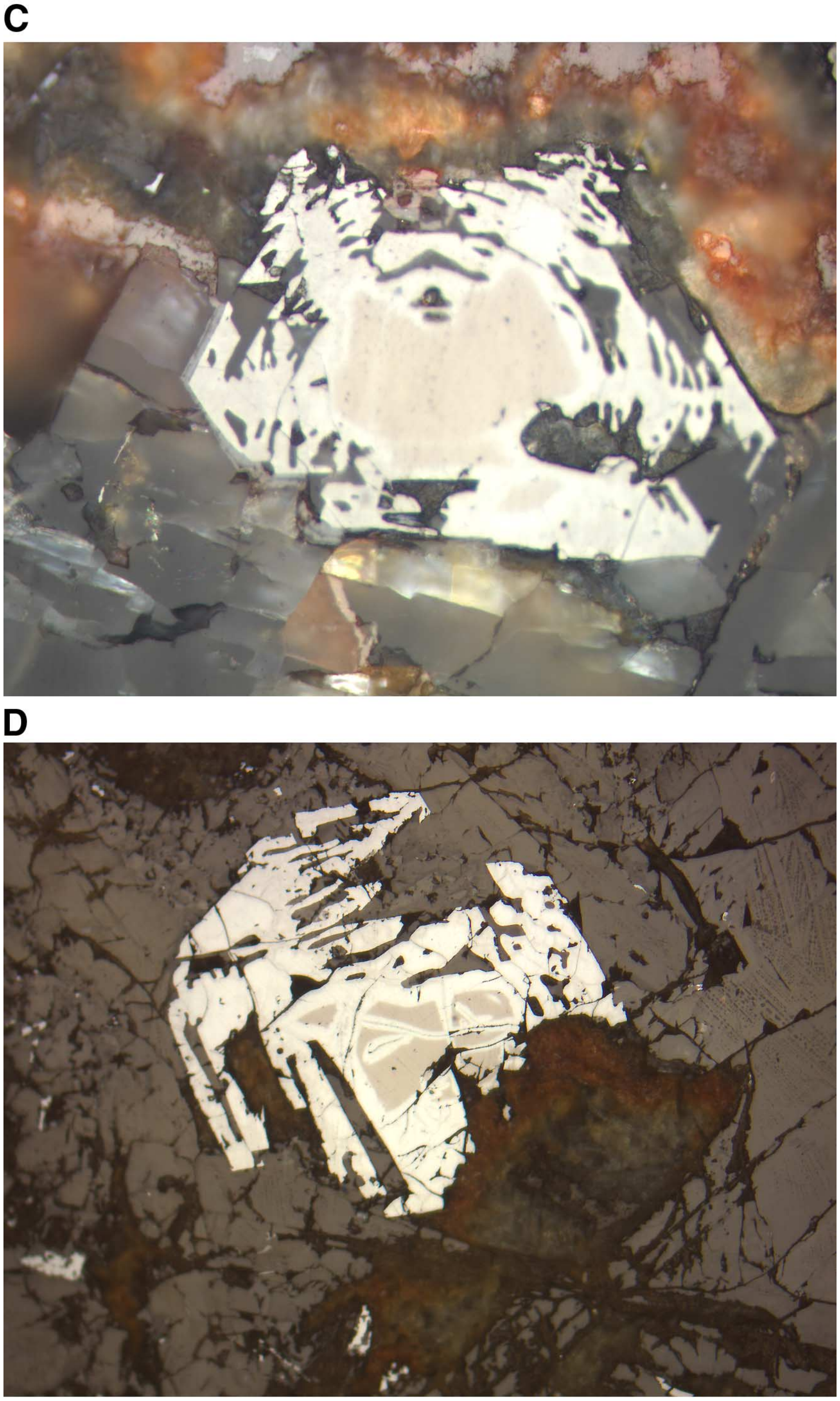

Figure F20 (continued.) E. Sample 197-1204B-8R-3, 53–55 cm (field of view = 0.625 mm; photomicrograph 1204B-141). **F.** Sample 197-1204B-2R-4, 87–89 cm (field of view = 0.625 mm; photomicrograph 1204B-148).

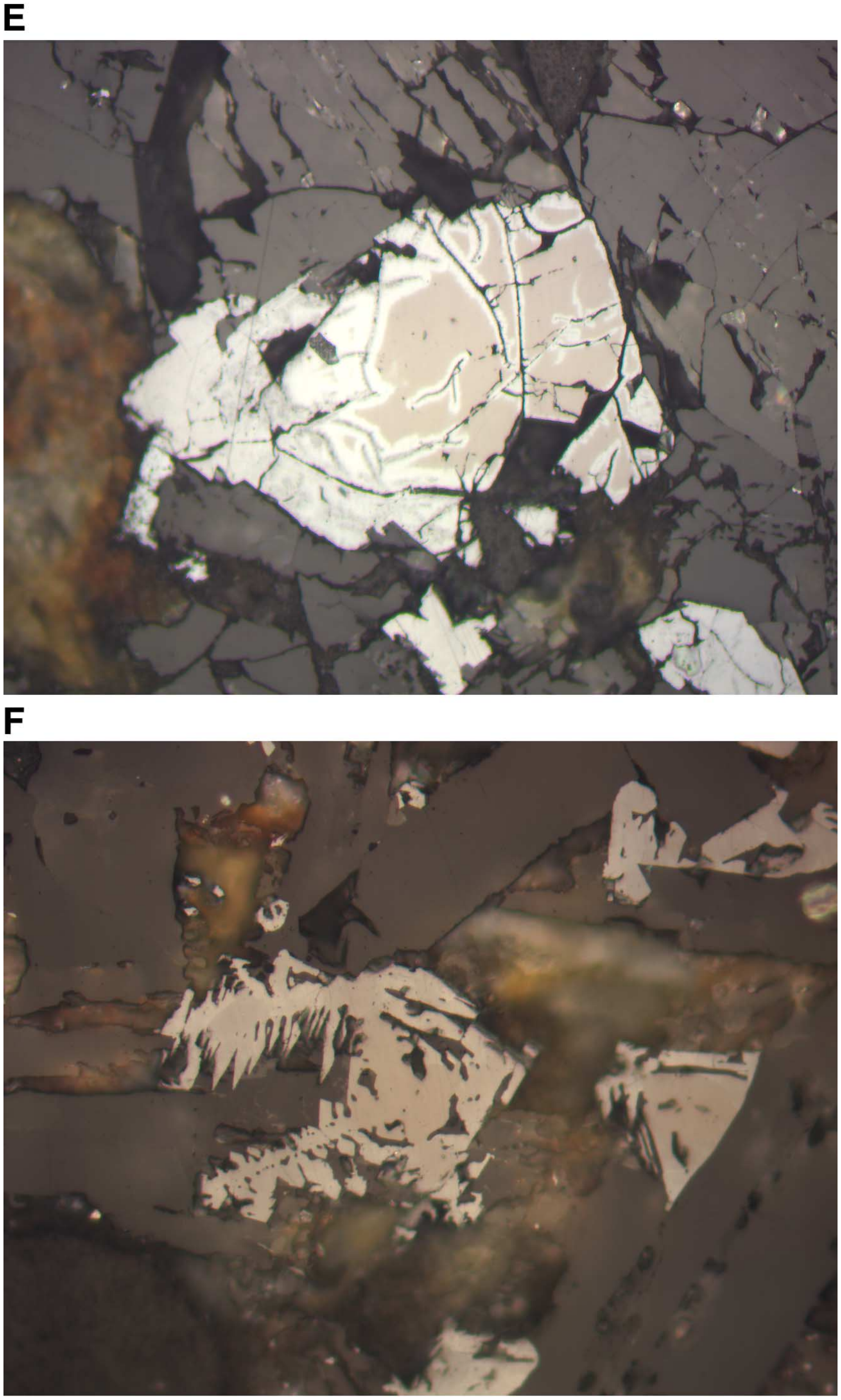

Figure F21. Reflected-light photomicrographs showing that titanomagnetite has been completely replaced by maghemite. **A.** Sample 197-1204B-10R-2, 77–79 cm (field of view = 0.625 mm; photomicrograph 1204A-155). **B.** Sample 197-1204B-7R-2, 129–131 cm (field of view = 0.625 mm; photomicrograph 1204B-151).

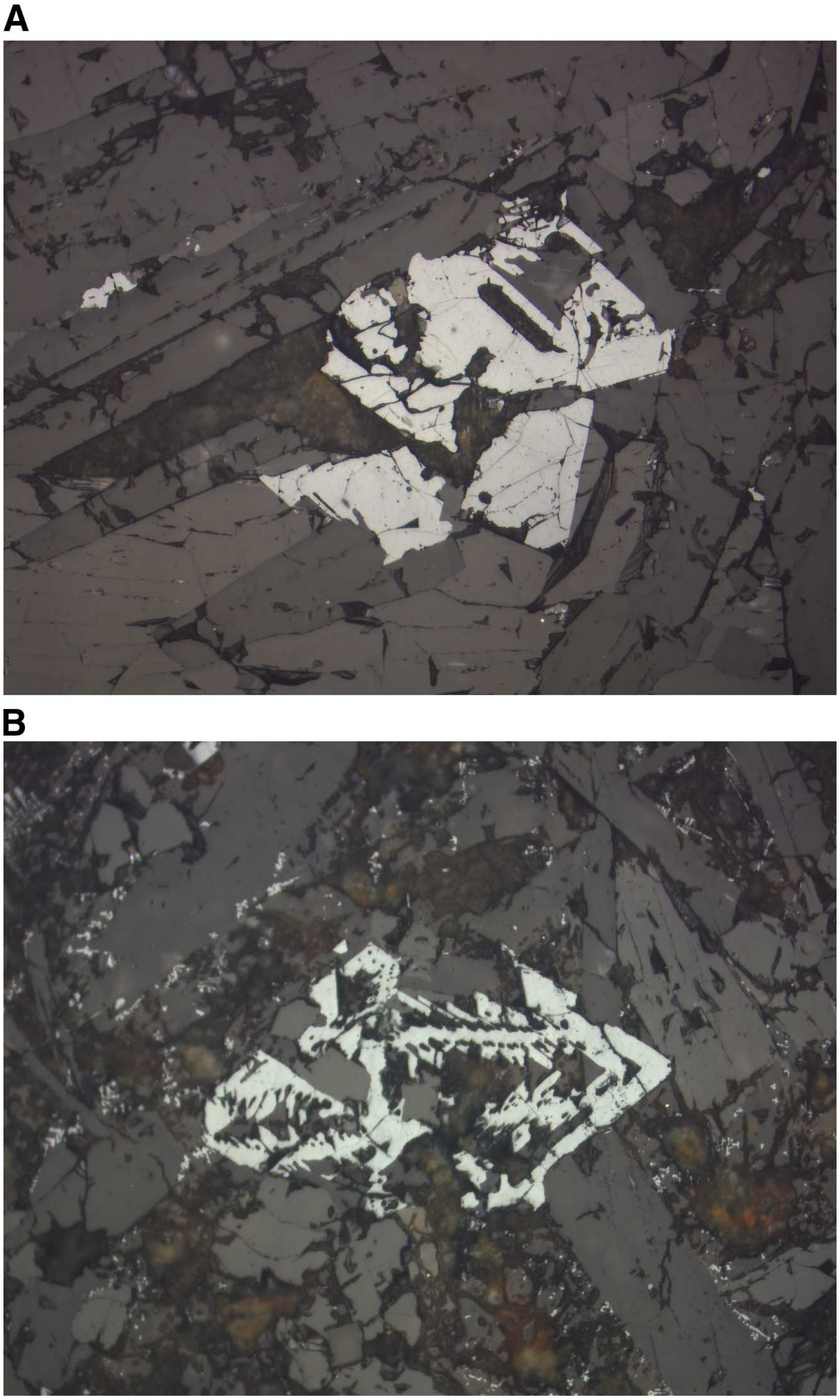

Figure F22. Reflected-light photomicrographs showing relict centers of titanomagnetite crystals with well-developed coronas of maghemite. **A.** Sample 197-1204B-7R-3, 140–142 cm (field of view = 0.625 mm; photomicrograph 1204B-150). **B.** A goethite mass is present in the center (dark gray-blue) (Sample 197-1204B-13R-2, 10–12 cm) (field of view = 0.625 mm; photomicrograph 1204B-154).

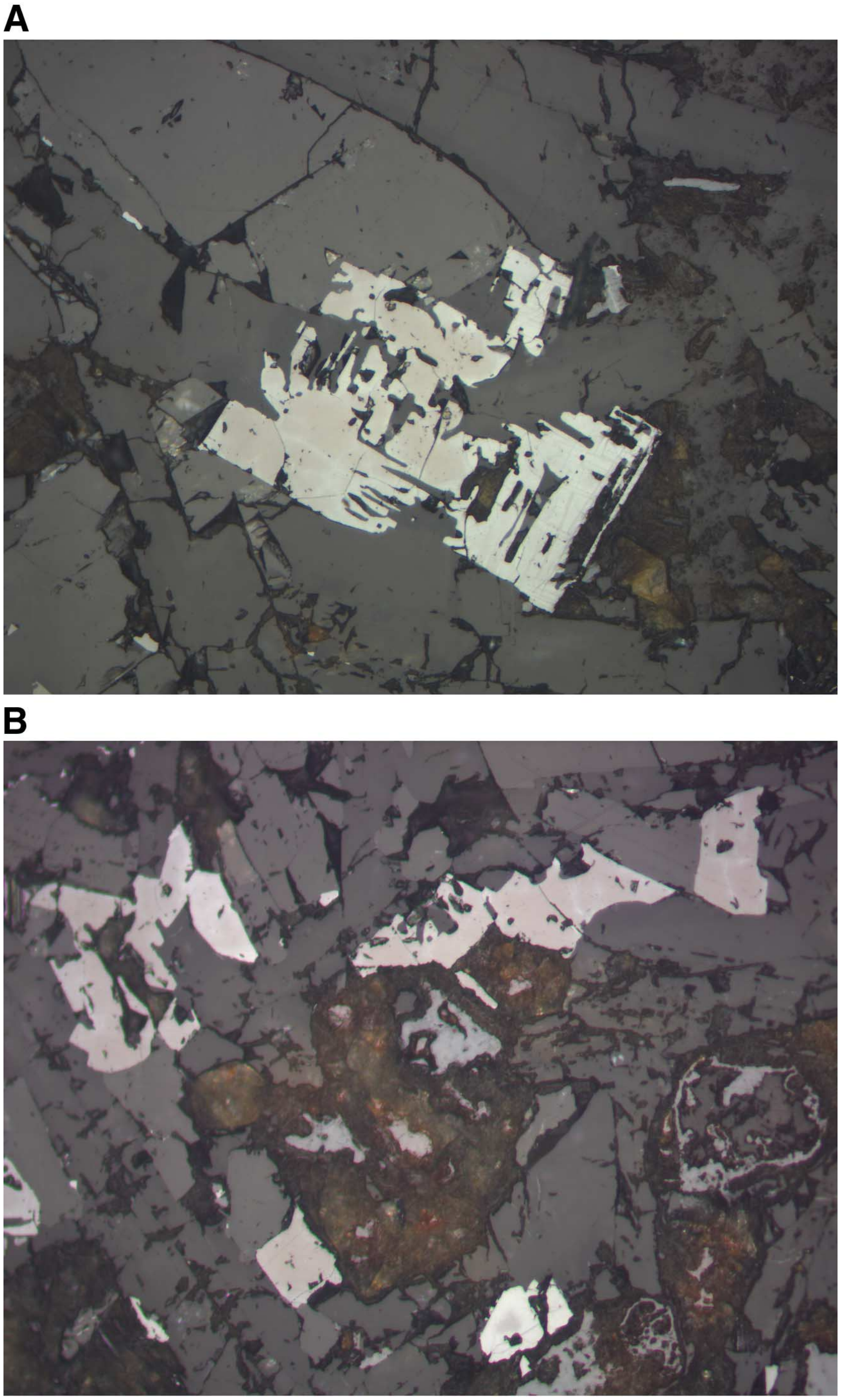

Figure F23. Reflected-light photomicrographs showing maghemite replacement of titanomagnetite along cleavage planes. Replacement is almost complete and only narrow relict bands remain, giving the maghemite the appearance of exsolving titanomagnetite. **A.** Sample 197-1204B-12R-1, 28–30 cm (field of view = 0.25 mm; photomicrograph 1204B-145). **B.** Sample 197-1204B-12R-1, 28–30 cm (field of view = 0.625 mm; photomicrograph 1204B-146).

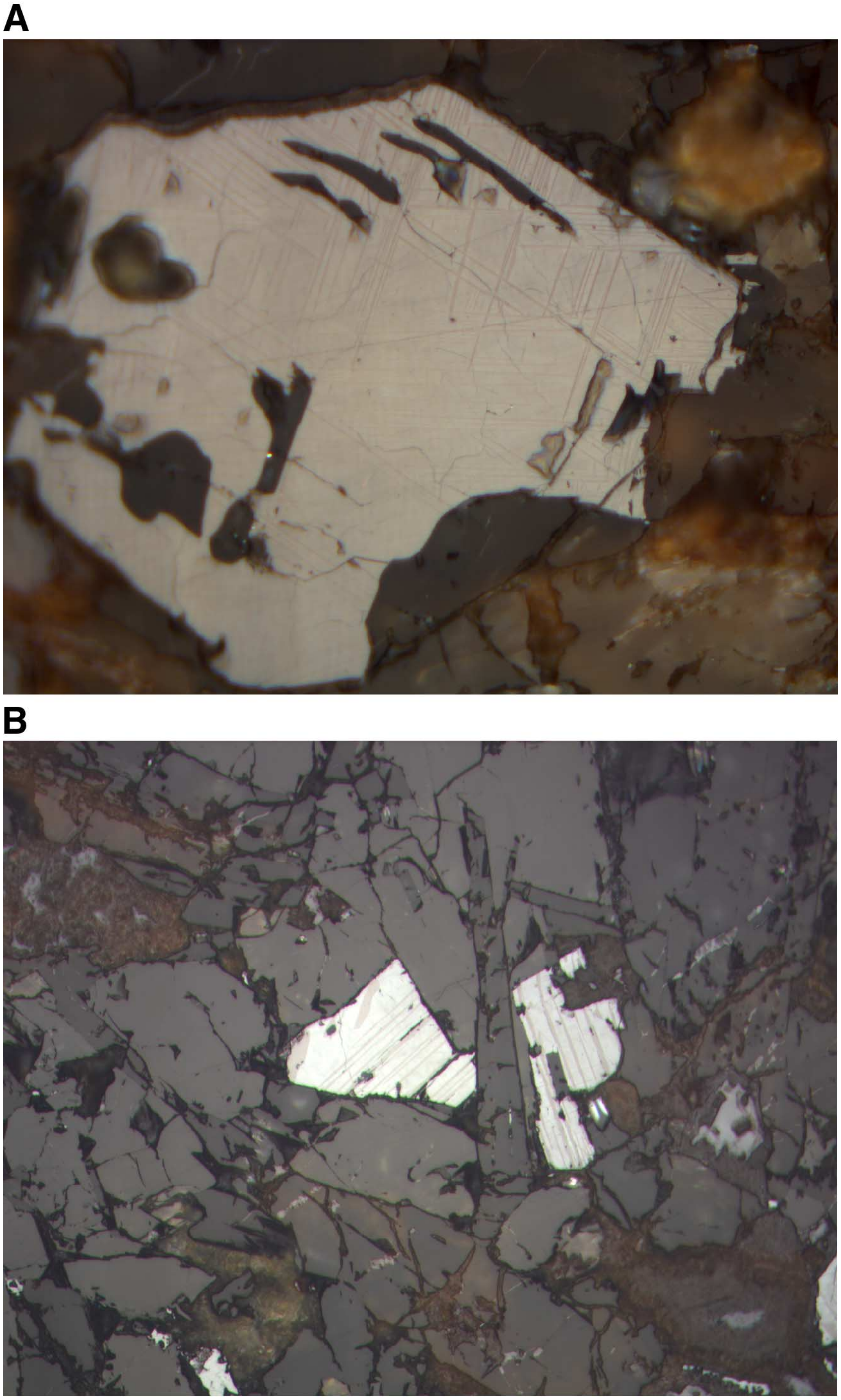

Figure F24. Reflected-light photomicrographs showing the instability of maghemite as it exsolves possibly ulvöspinel or ilmenite parallel to cleavage planes. **A.** Sample 197-1204B-10R-3, 25–27 cm (field of view = 0.25 mm; photomicrograph 1204B-142). **B.** Sample 197-1204B-10R-3, 25–27 cm (field of view = 0.625 mm; photomicrograph 1204B-144).

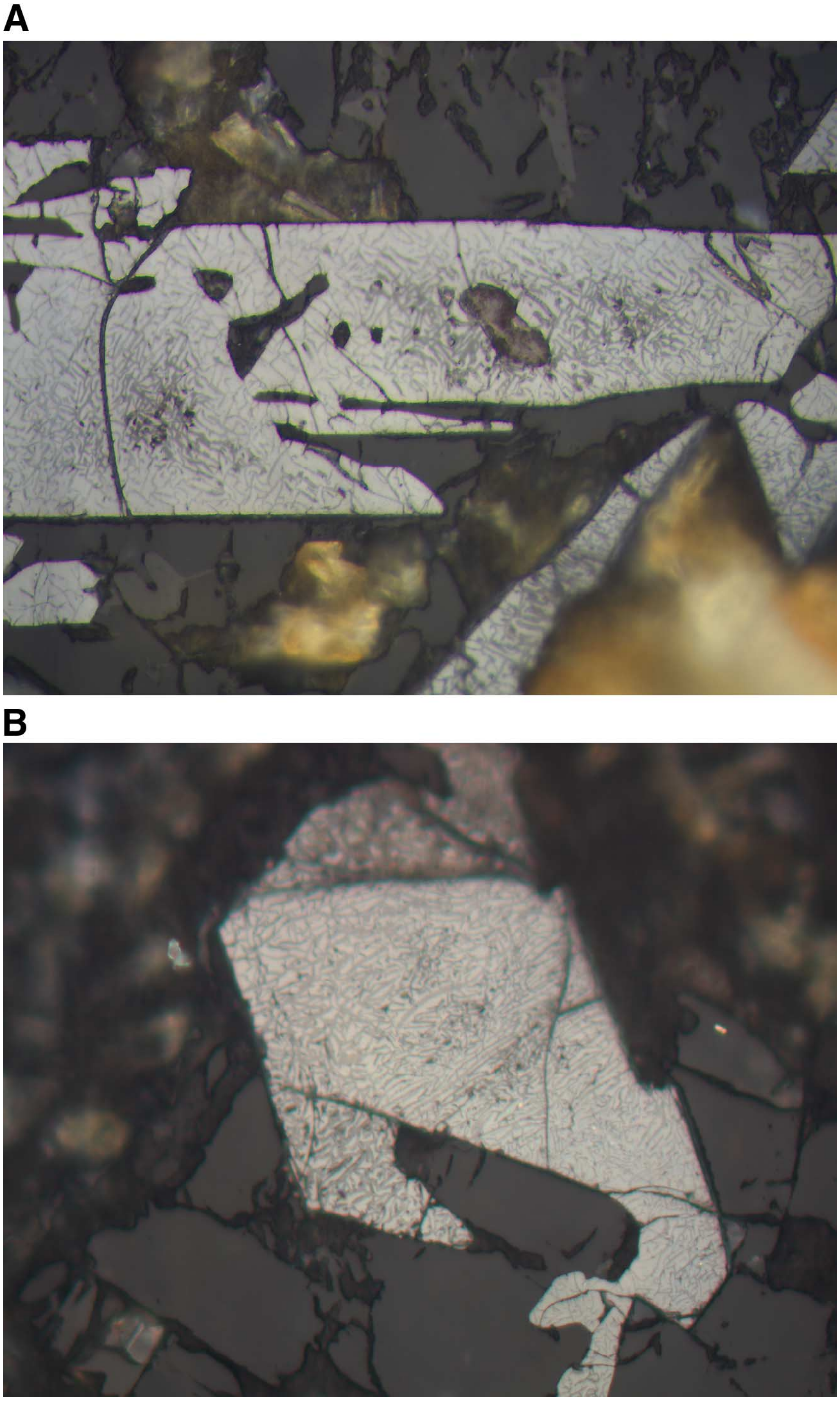

Figure F25. Photomicrograph showing the instability of maghemite (dusty light gray-blue) as it breaks down to Fe oxyhydroxide after replacement of titanomagnetite (gray-brown) (Sample 197-1204B-10R-3, 25–27 cm) (reflected light; field of view = 0.625 mm; photomicrograph 1204B-152).

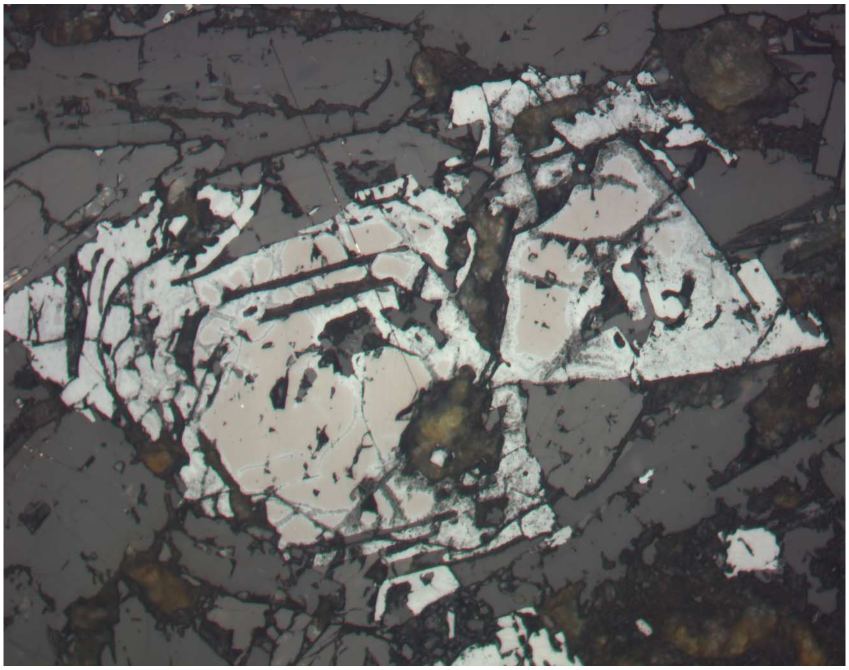

Figure F26. Total alkali content ($Na_2O + K_2O$) vs. SiO_2 classification plot for basaltic lava flows from Detroit Seamount. The solid diagonal line is the alkalic-tholeiitic dividing line for Hawaiian basalt (Macdonald and Katsura, 1964). Lavas from Site 884 are tholeiitic basalt, whereas lavas from Site 883 are alkalic basalt, although Keller et al. (1995) inferred that prior to alteration, these lavas were transitional between alkalic and tholeiitic basalt. Data for these two Leg 145 Sites in this and all subsequent figures are from Keller et al. (2000) and M. Regelous et al. (unpubl. data). Lavas from Site 1203 range from tholeiitic, overlapping with Site 884 lavas, to alkalic, overlapping with Site 883 lavas. The two Site 1203 basalts in the tholeiitic field at <45% SiO_2 are picritic as a result of olivine accumulation. All Site 1204 lavas plot in the alkalic field. Lavas from Hole 1204A and Subunit 2b in Hole 1204B overlap with lavas from Site 883. Lavas from Subunit 2a in Hole 1204B have high $Na_2O + K_2O$ and relatively low SiO_2, whereas Unit 1 lavas in Hole 1204B have the highest $Na_2O + K_2O$. The Hole 1204A sample labeled "Calcite rich" (Sample 197-1204A-7R-3, 36–37 cm, in Table T7, p. 114) shows the effect of secondary calcite present as vesicle filling.

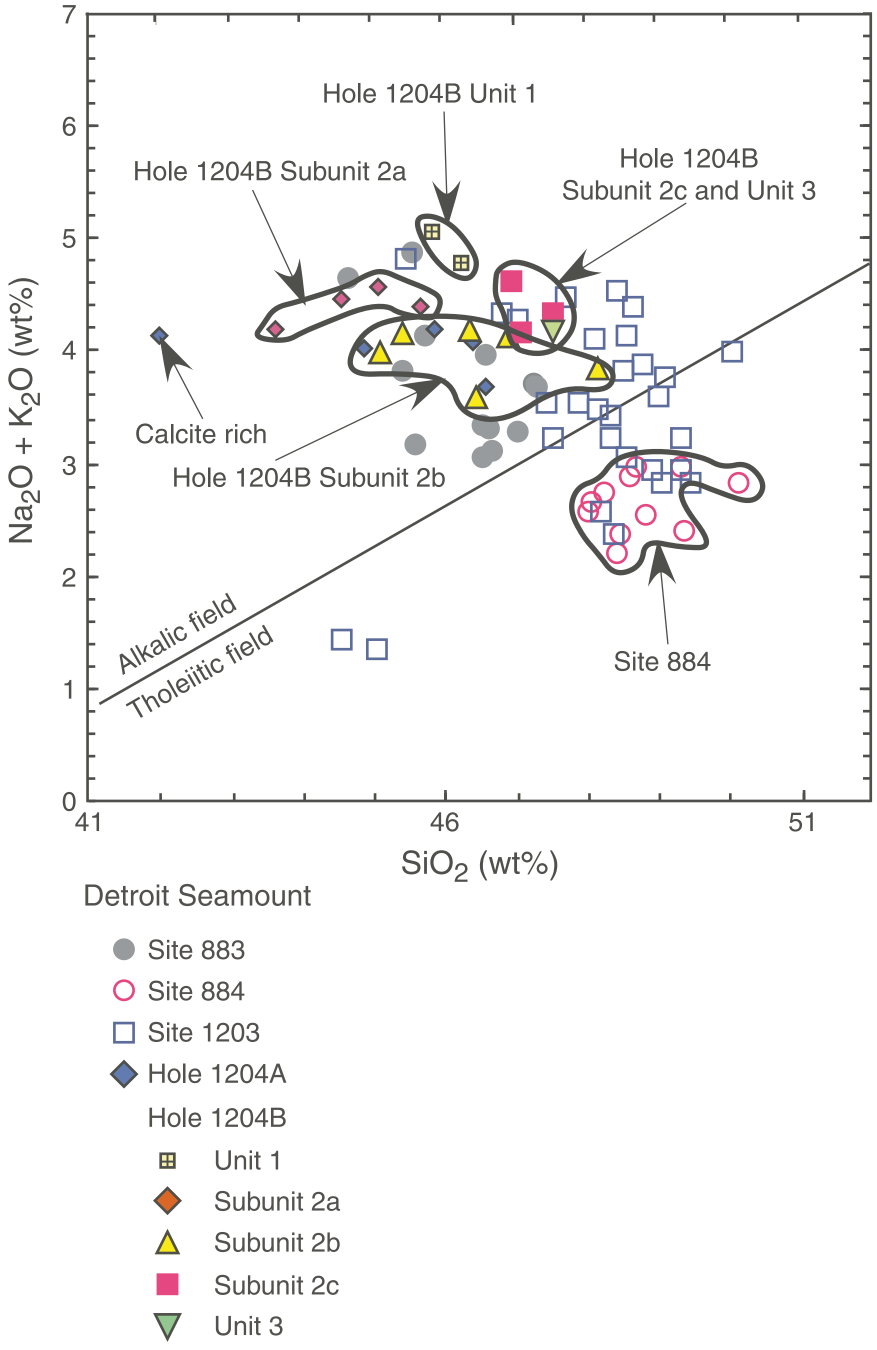

Figure F27. Abundance of TiO_2 vs. MgO showing that lavas from Detroit Seamount exhibit a wide range in TiO_2 at a given MgO content. TiO_2 abundance increases in the following order: Site 884 basalt < transitional and tholeiitic basalt from Site 1203 < Site 1204 basalt < alkalic basalt Units 23, 26, 29, and 30 from Site 1203. Note that three Site 883 lavas and the lavas from Unit 1 and Subunit 2a (except for the lowermost Subunit 2a sample) (Table T7, p. 114) in Hole 1204B have <4 wt% MgO.

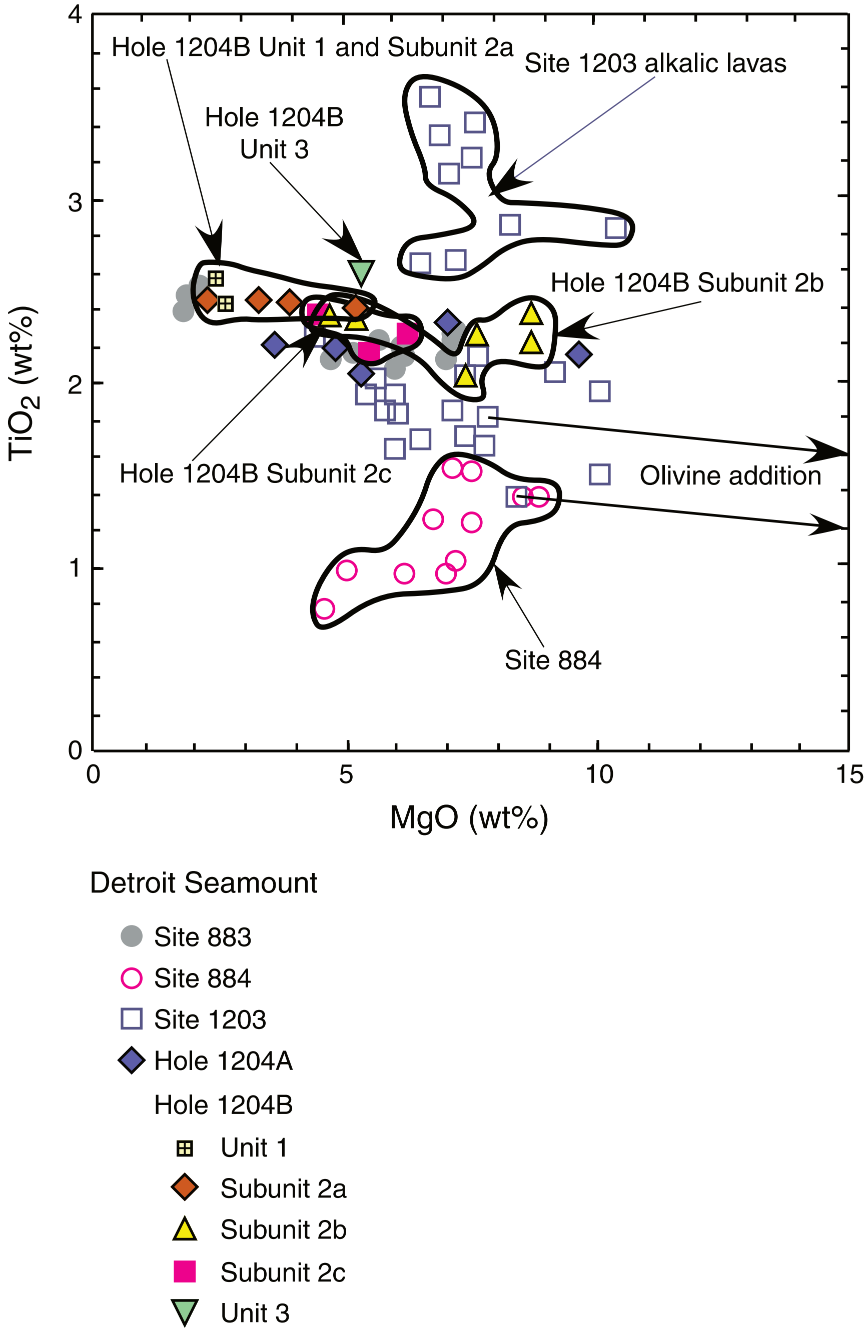

Figure F28. Abundance of CaO vs. loss on ignition (LOI). The three Site 1204 samples with atypically high CaO (>15 wt%) have relatively high LOI, reflecting CaO addition as secondary calcite.

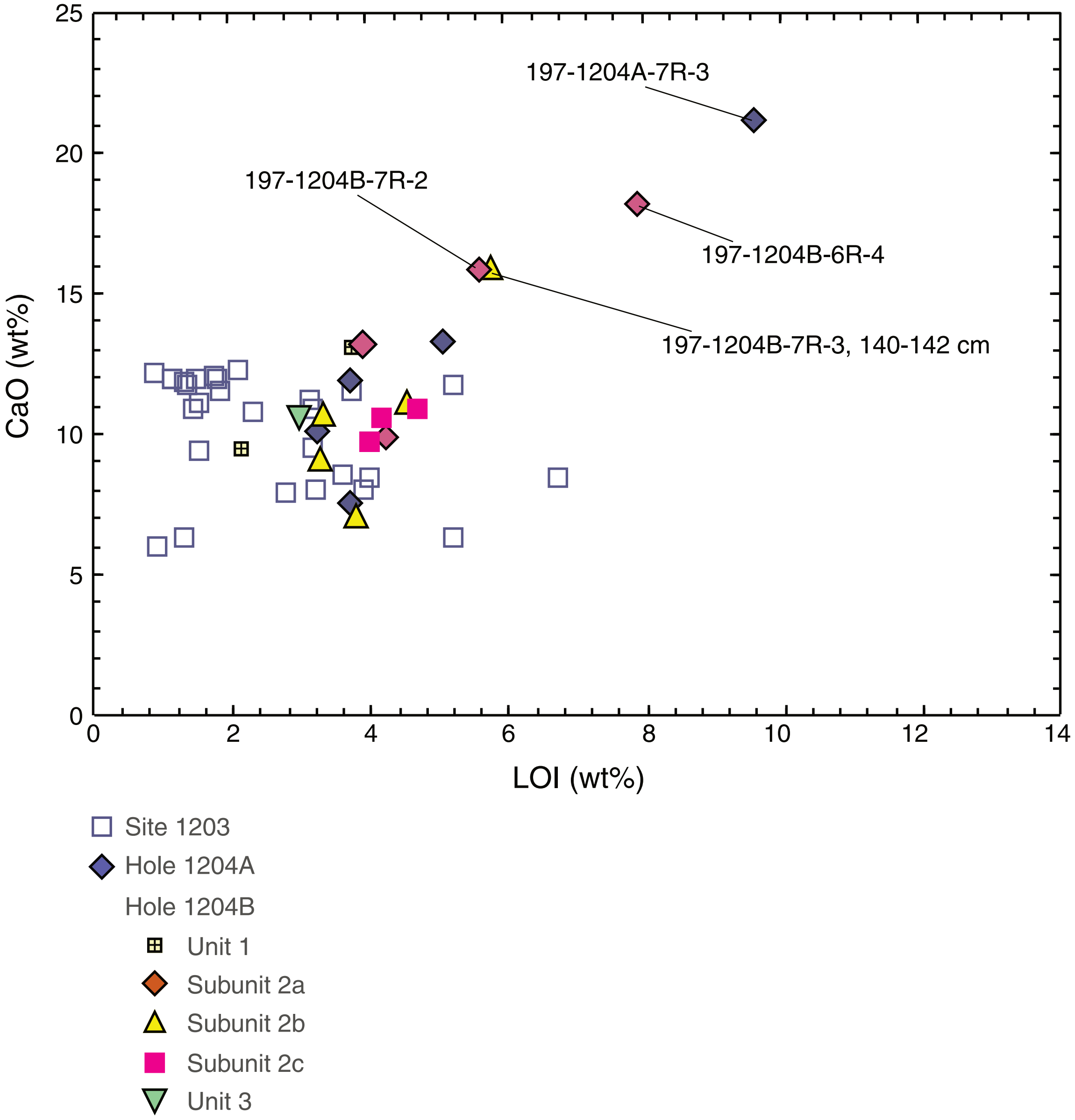

Figure F29. Abundance of Ti vs. Zr showing a near-linear trend for most of the lavas from Detroit Seamount. The slope of this trend defines a Ti/Z ratio of 92 ± 7, close to the primitive mantle estimate of 116 (Sun and McDonough, 1989). Basalt from Suiko Seamount defines a similar trend (data from M. Regelous et al., unpubl. data). Site 884 lavas and the two picrites from Site 1203 have the lowest abundances, and the alkalic basalt from Site 1203 has the highest abundances of Ti and Zr. Basalt from Hole 1204A and Subunits 2b and 2c of Hole 1204B are close to the field for Site 883 lavas, but Site 883 lavas have slightly lower Zr contents. Relative to Site 883 lavas, basalt from Units 1, 2a, and 3 of Hole 1204B has slightly higher Ti and Zr.

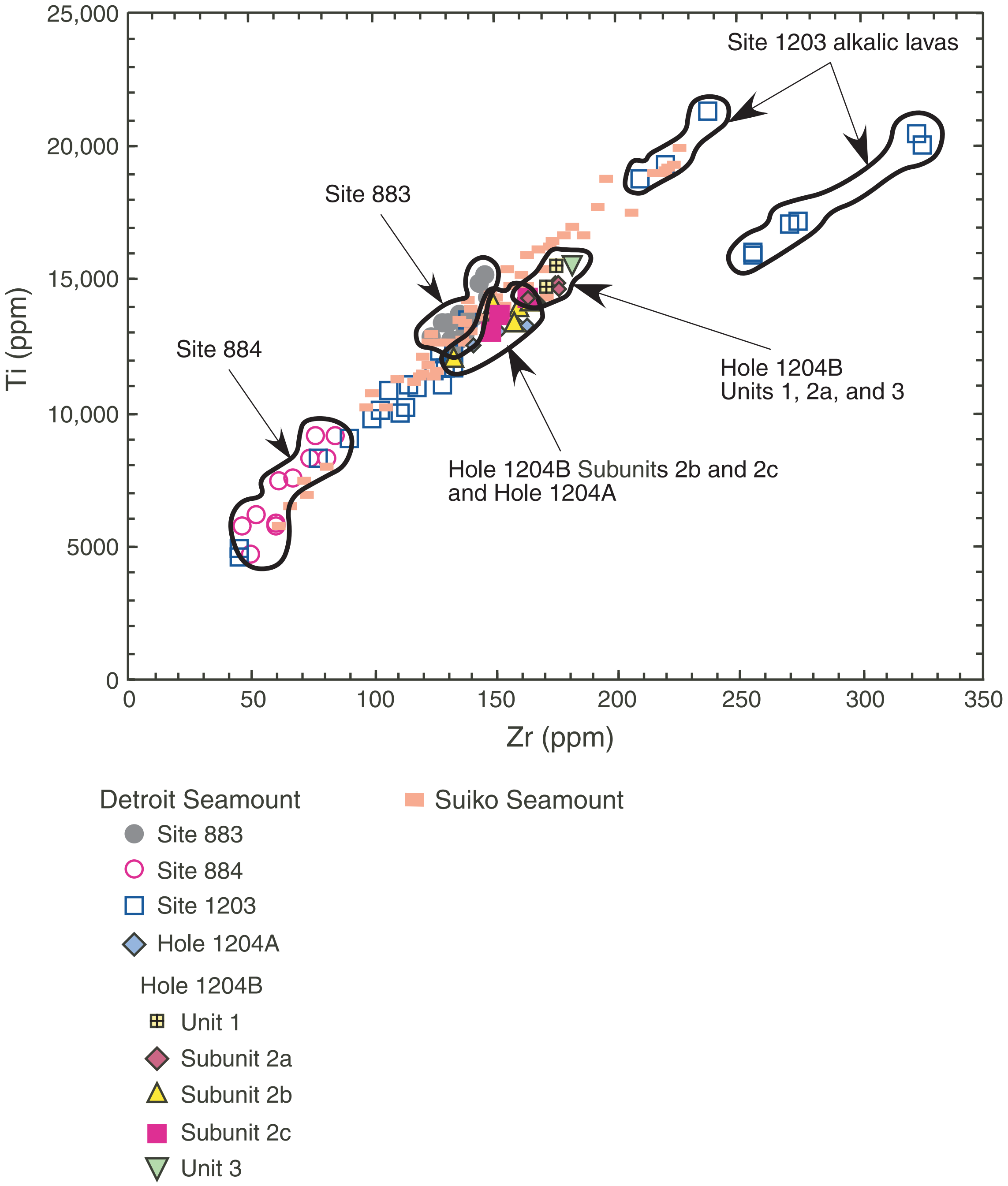

Figure F30. Abundances of the incompatible elements Y, P, Sr, and Ba vs. Zr, a relatively immobile incompatible element. In each panel there is a general positive trend that mimics the trend defined by basalt from Suiko Seamount (M. Regelous et al., unpubl. data). There are, however, some important exceptions. In the P and Ba panels, some Site 883 lavas and the three labeled Hole 1204B samples deviate from positive trend to high P and Ba contents. Also, in the Y, Sr, and Ba panels the alkalic lavas from Site 1203 define nearly horizontal slopes, indicating that abundances of these elements are decoupled from Zr abundances.

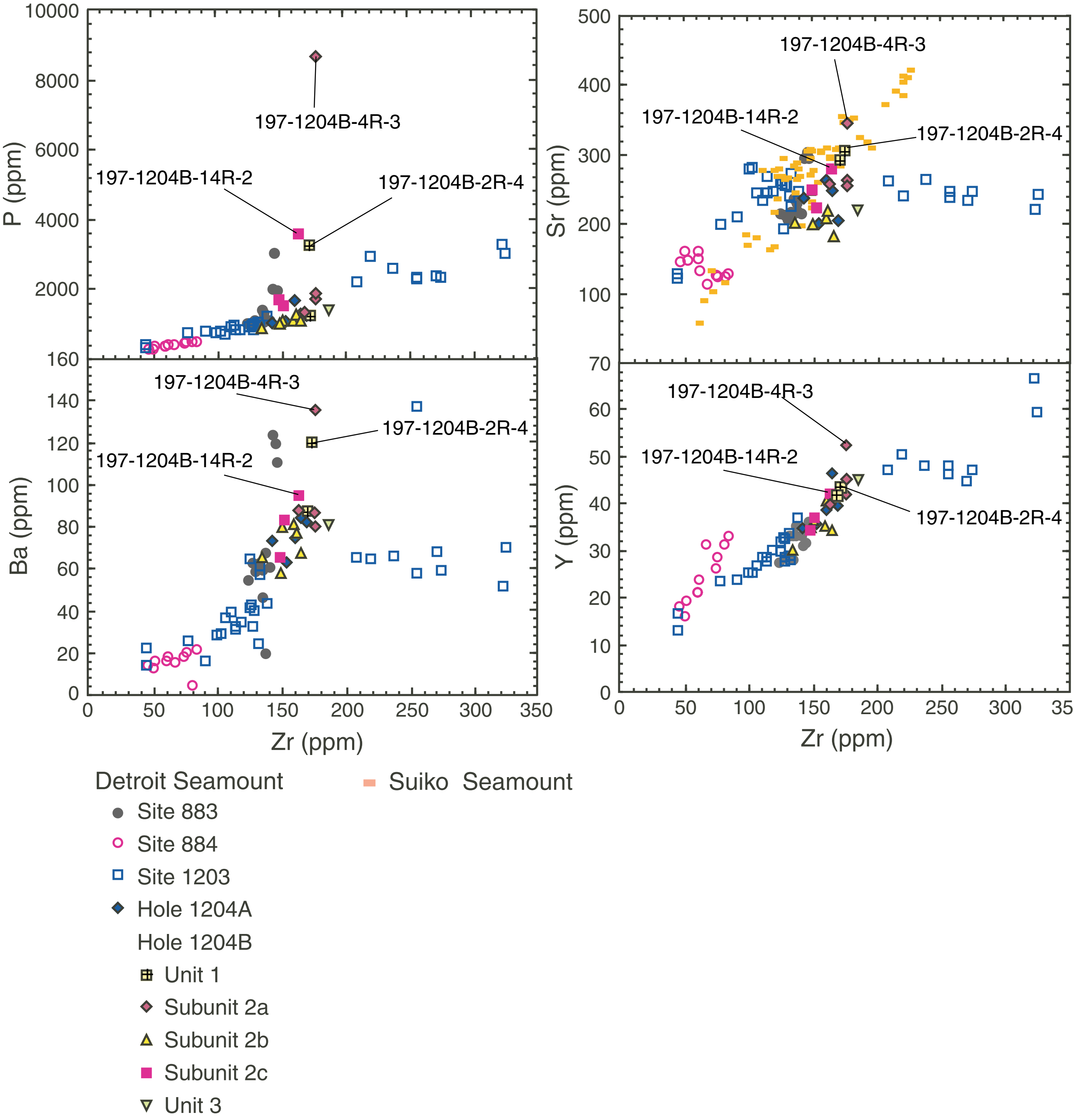

Figure F31. Composite figure showing the alteration degree, mineral assemblages, vesicle occurrence, and vesicle and vein fillings for Hole 1204A. Also shown is the core recovery downhole. Green = sedimentary units, yellow = volcaniclastic units, blue = lava flow units, brown = oxidizing alteration zones, gray green = reducing alteration zones.

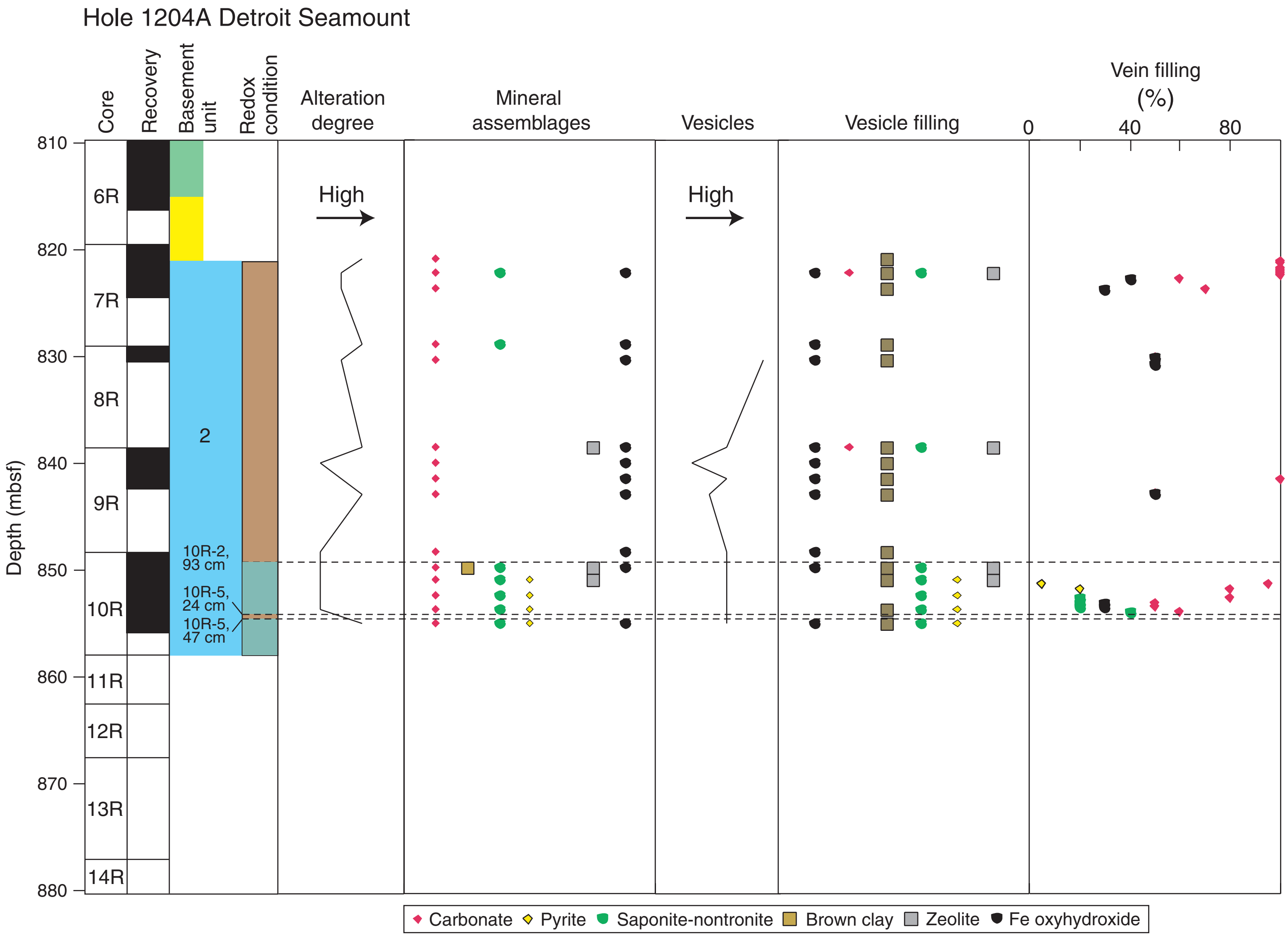

Figure F32. Composite figure showing the alteration degree, mineral assemblages, vesicle occurrence, and vesicle and vein fillings for Hole 1204B. Also shown is the core recovery downhole. Green = sedimentary units, yellow = volcaniclastic units, blue = lava flow units, brown = oxidizing alteration zones, gray green = reducing alteration zones.

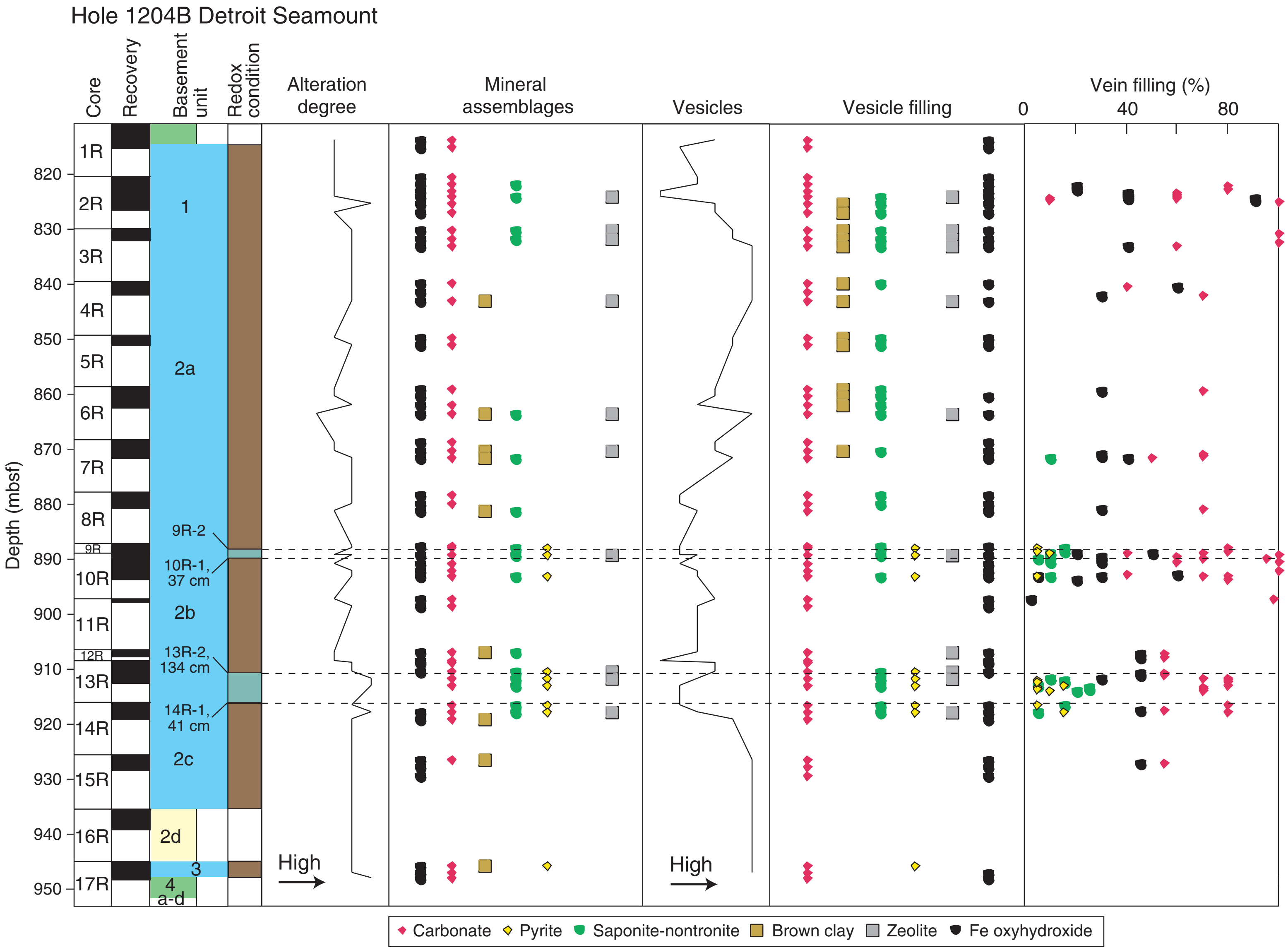

Figure F33. Photograph of the contact between an oxidizing and a reducing zone (interval 197-1204A-10R-5, 15–33 cm).

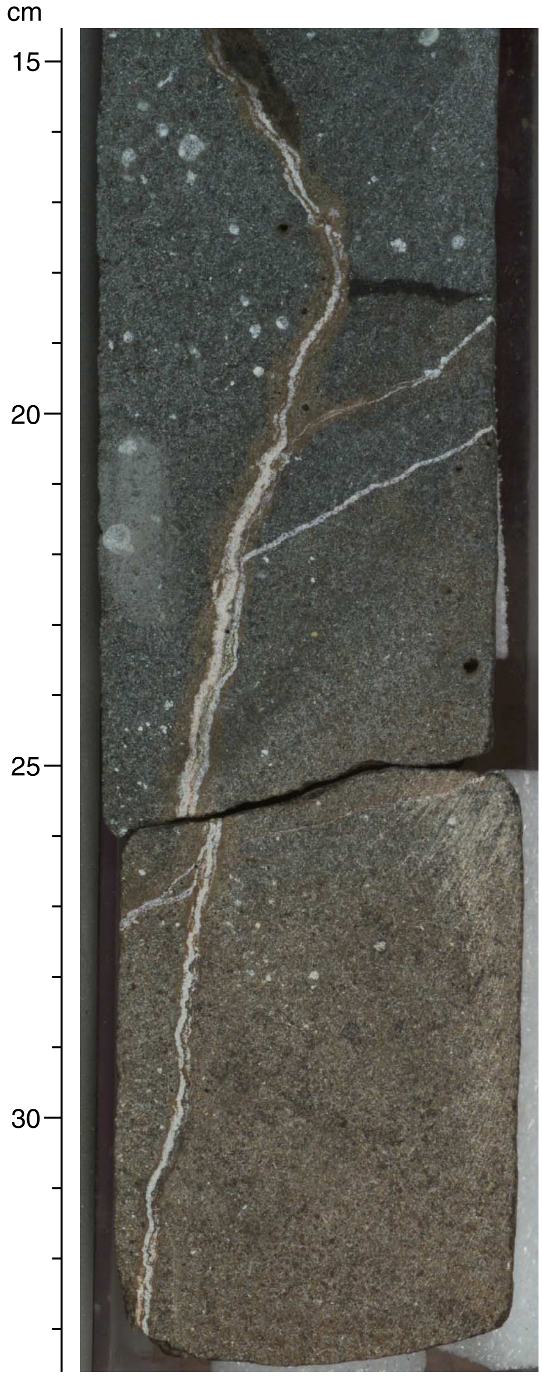

Figure F34. Photograph of the contact between an oxidizing and a reducing zone (interval 197-1204B-9R-3, 38–57 cm).

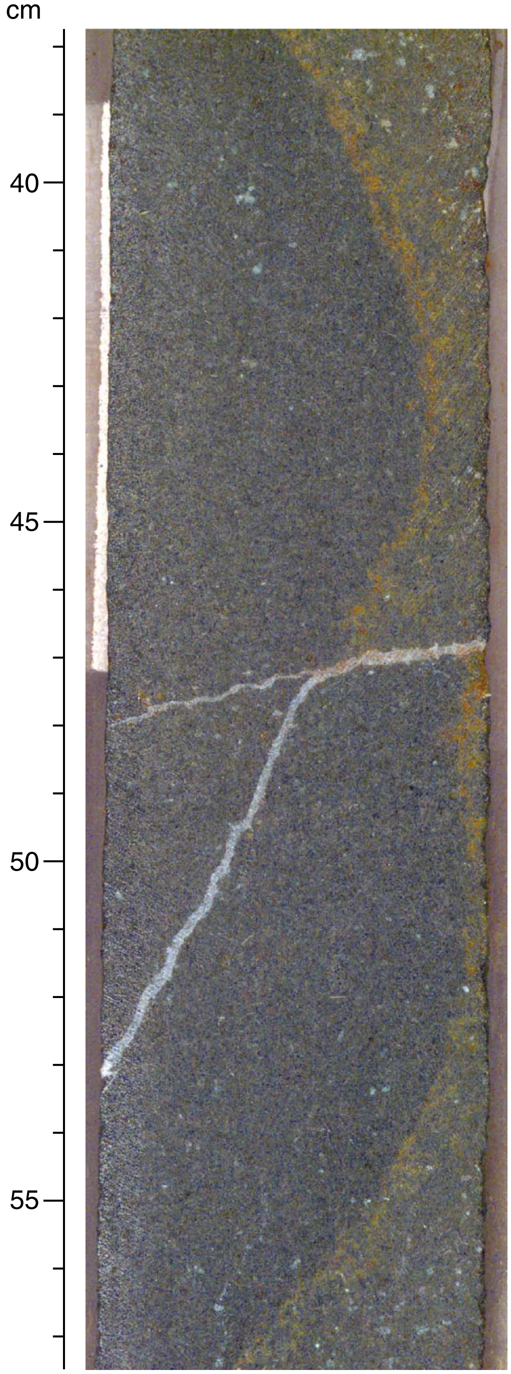

Figure F35. Close-up photograph of a megavesicle filled with saponite and pyrite (interval 197-1204A-10R-3, 98–100 cm). Note: the photograph was taken on the working half of the core.

Figure F36. Variations of LOI (loss on ignition) and K_2O abundances and Cu/Zr, Co/Zr, and Zn/Zr ratios with depth in the Hole 1204A sequence. Also shown is the core recovery downhole. Green = sedimentary units, yellow = volcaniclastic units, blue = lava flow units, brown = oxidizing alteration zones, gray green = reducing alteration zones.

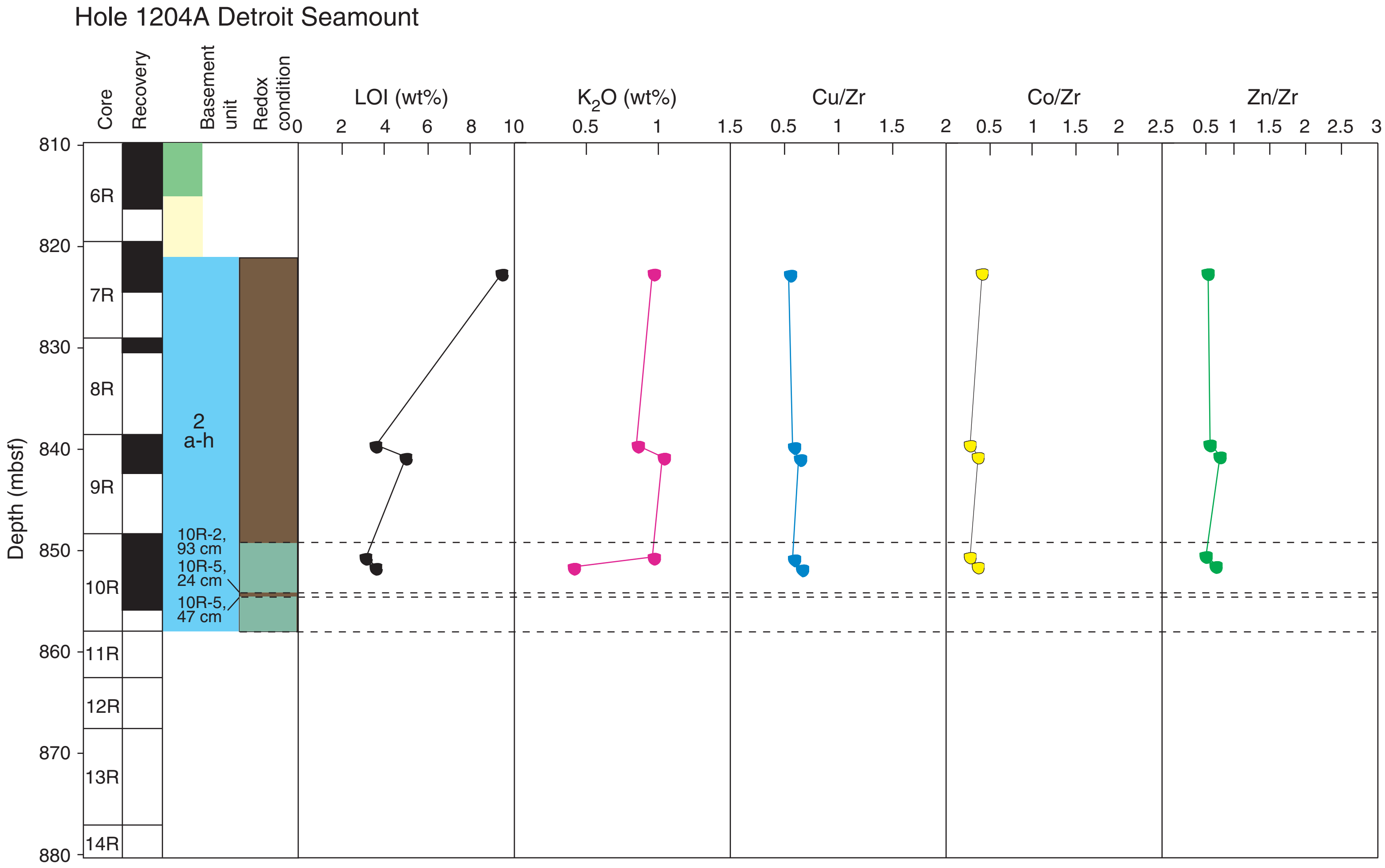

Figure F37. Variations of LOI (loss on ignition) and K_2O abundances and Cu/Zr, Co/Zr and Zn/Zr ratios with depth in Hole 1204B. Also shown is the core recovery downhole. Green = sedimentary units, yellow = volcaniclastic units, blue = lava flow units, brown = oxidizing alteration zones, gray green = reducing alteration zones.

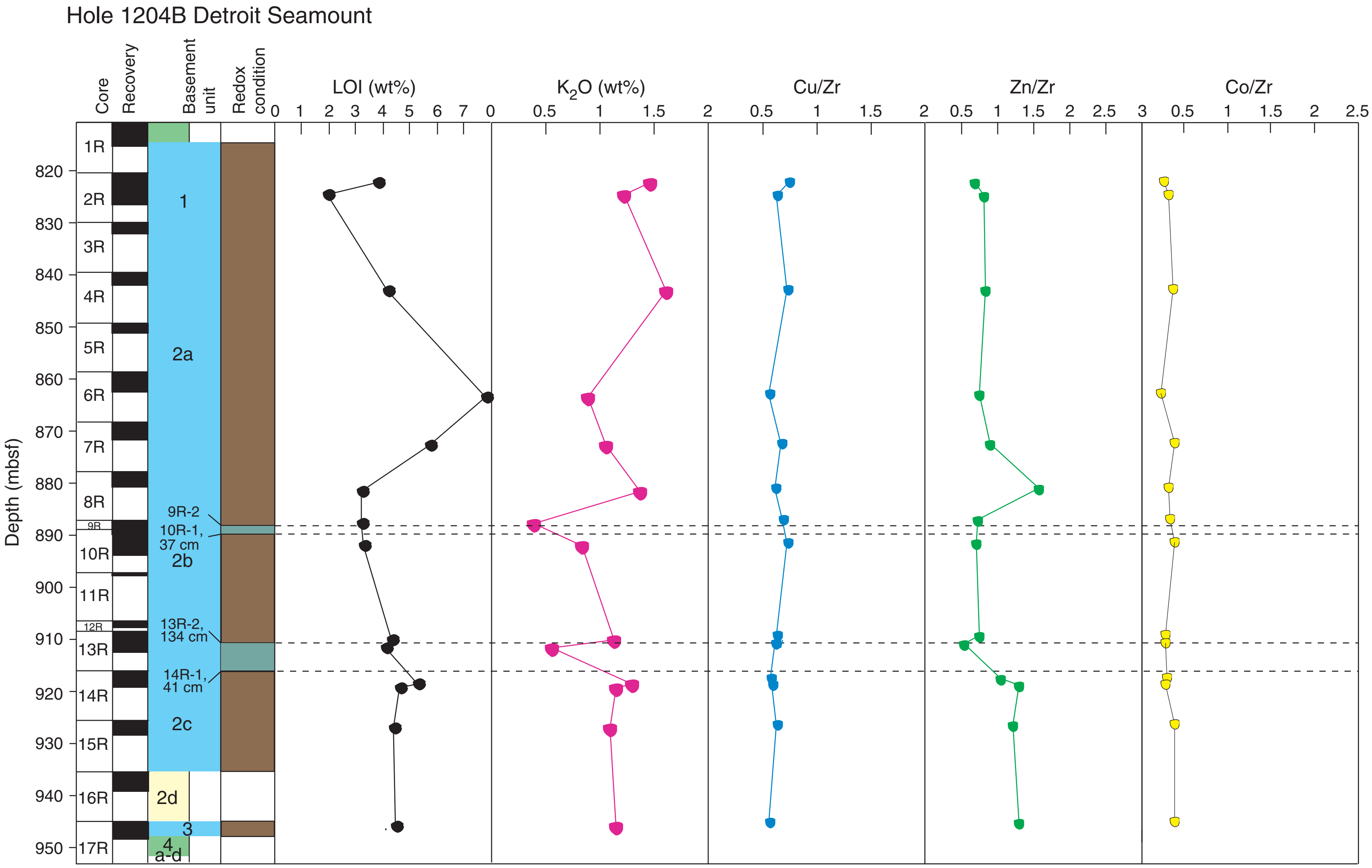

Figure F38. Zr vs. K_2O for Site 1204 (Holes 1204A and 1204B) samples, Site 1203, Hawaiian lavas (Mauna Kea Volcano and Loihi Seamount), and ODP Sites 883 and 884. Sources of data: Mauna Kea and Loihi: Frey et al. (1990, 1991), Macdonald and Katsura (1964), and Rhodes (1996). ODP Sites 883 and 884: Rea, Basov, Janecek, Palmer-Julson, et al. (1993) and Keller et al. (1995). For Site 1203 samples, circles = tholeiitic basalt, squares = alkali basalt (see also **"Alteration and Weathering,"** p. 24, in the "Site 1203" chapter).

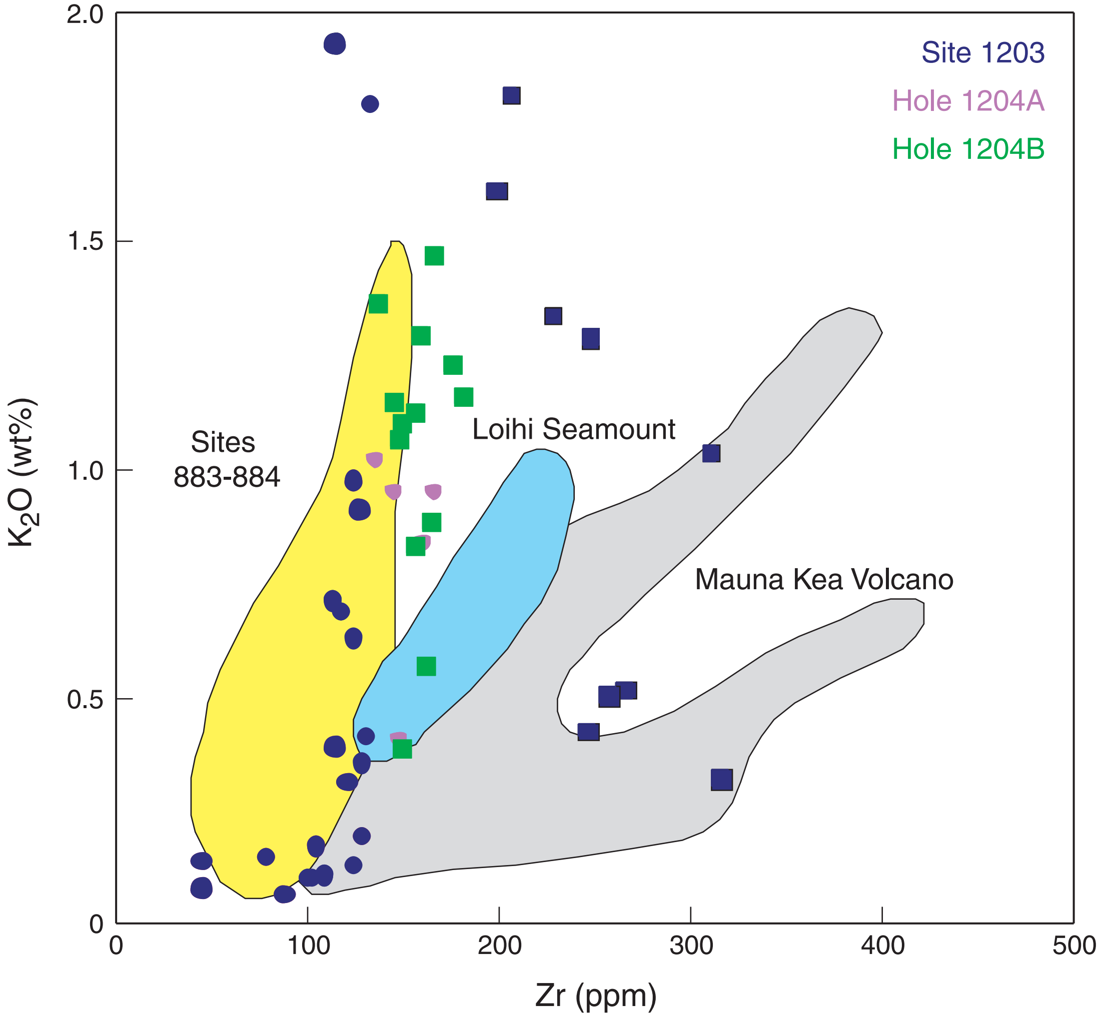

Figure F39. Example orthogonal vector plots for select levels of archive half-round sections of sediment recovered above basement in Hole 1204A: Samples (**A**) 197-1204A-1R-3, 85 cm, (**B**) 2R-2, 65 cm, (**C**) 3R-5, 30 cm, (**D**) 4R-4, 95 cm, (**E**) 5R-2, 45 cm, and (**F**) 6R-3, 110 cm. Numbers adjacent to the symbols signify alternating-field demagnetization level. Open squares = vertical projection of magnetization, solid circles = horizontal projection of magnetization.

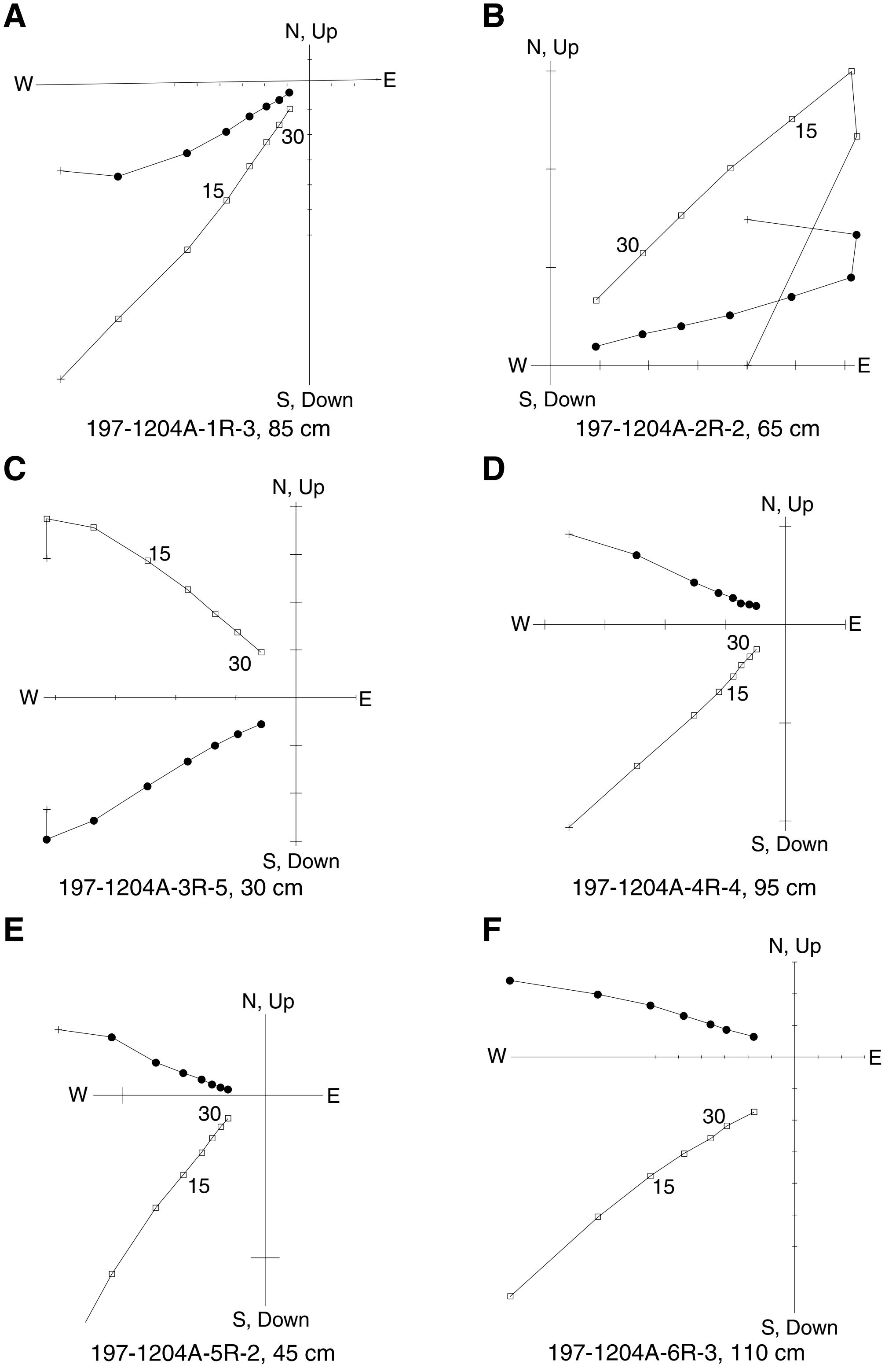

197-1204A-1R-3, 85 cm

197-1204A-2R-2, 65 cm

197-1204A-3R-5, 30 cm

197-1204A-4R-4, 95 cm

197-1204A-5R-2, 45 cm

197-1204A-6R-3, 110 cm

Figure F40. Example orthogonal vector plots for select levels of archive half-round sections of sediment recovered above basement in Hole 1204A showing departures of the magnetization from ideal behavior with alternating field demagnetization: Samples (**A**) 197-1204A-1R-1, 15 cm, (**B**) 2R-2, 115 cm, (**C**) 3R-2, 65 cm, (**D**) 4R-2, 30 cm, (**E**) 5R-1, 120 cm, and (**F**) 6R-3 70 cm. Numbers adjacent to symbols signify alternating-field demagnetization level. Open squares = vertical projection of magnetization, solid circles = horizontal projection of magnetization.

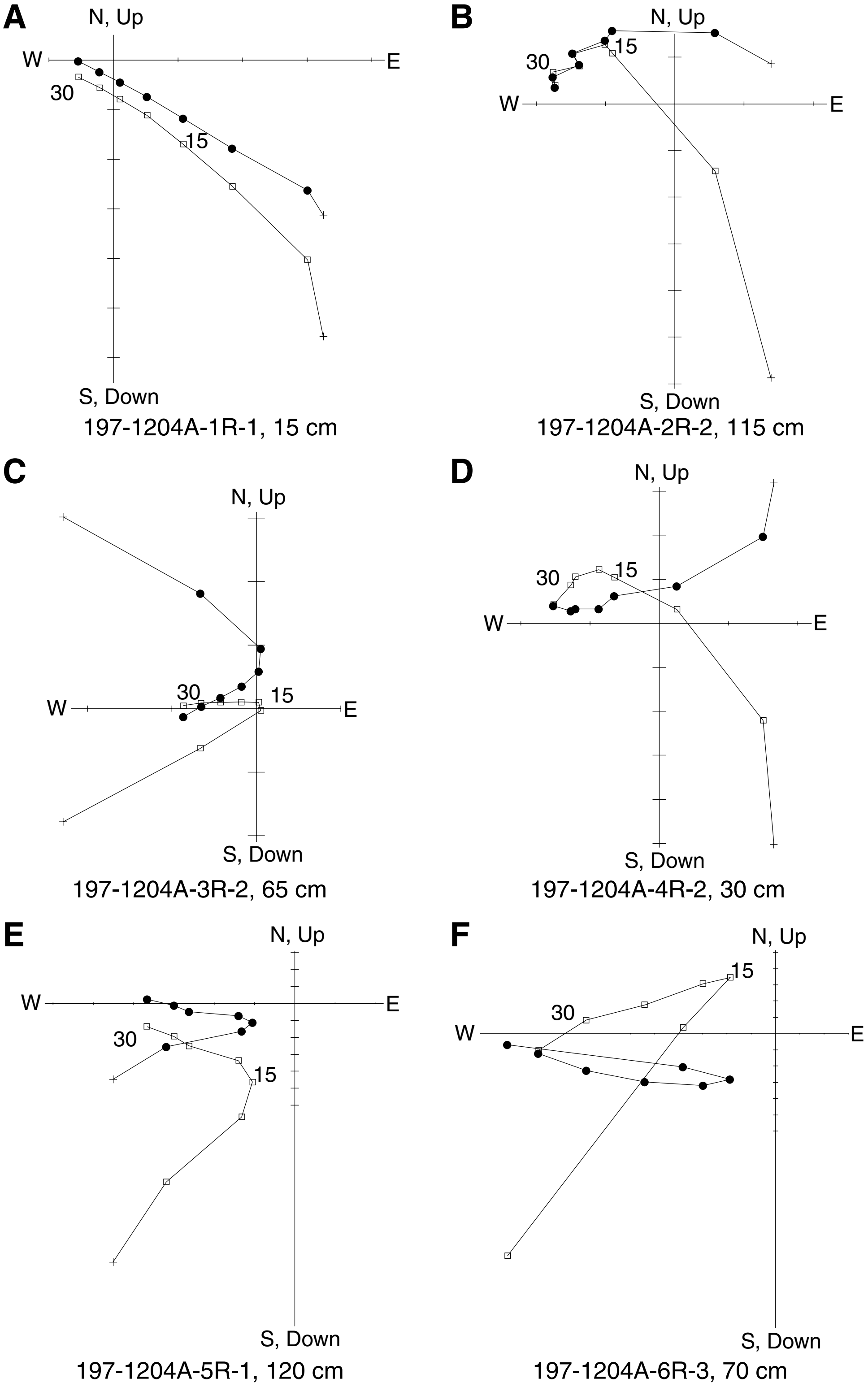

Figure F41. Summary polarity column of paleomagnetic inclinations vs. depth. Also shown are tie points linked to geomagnetic polarity for sediment recovered above basement in Hole 1204A. Geomagnetic polarity timescale is after Cande and Kent (1995). NRM = natural remanent magnetization, AF = alternating field.

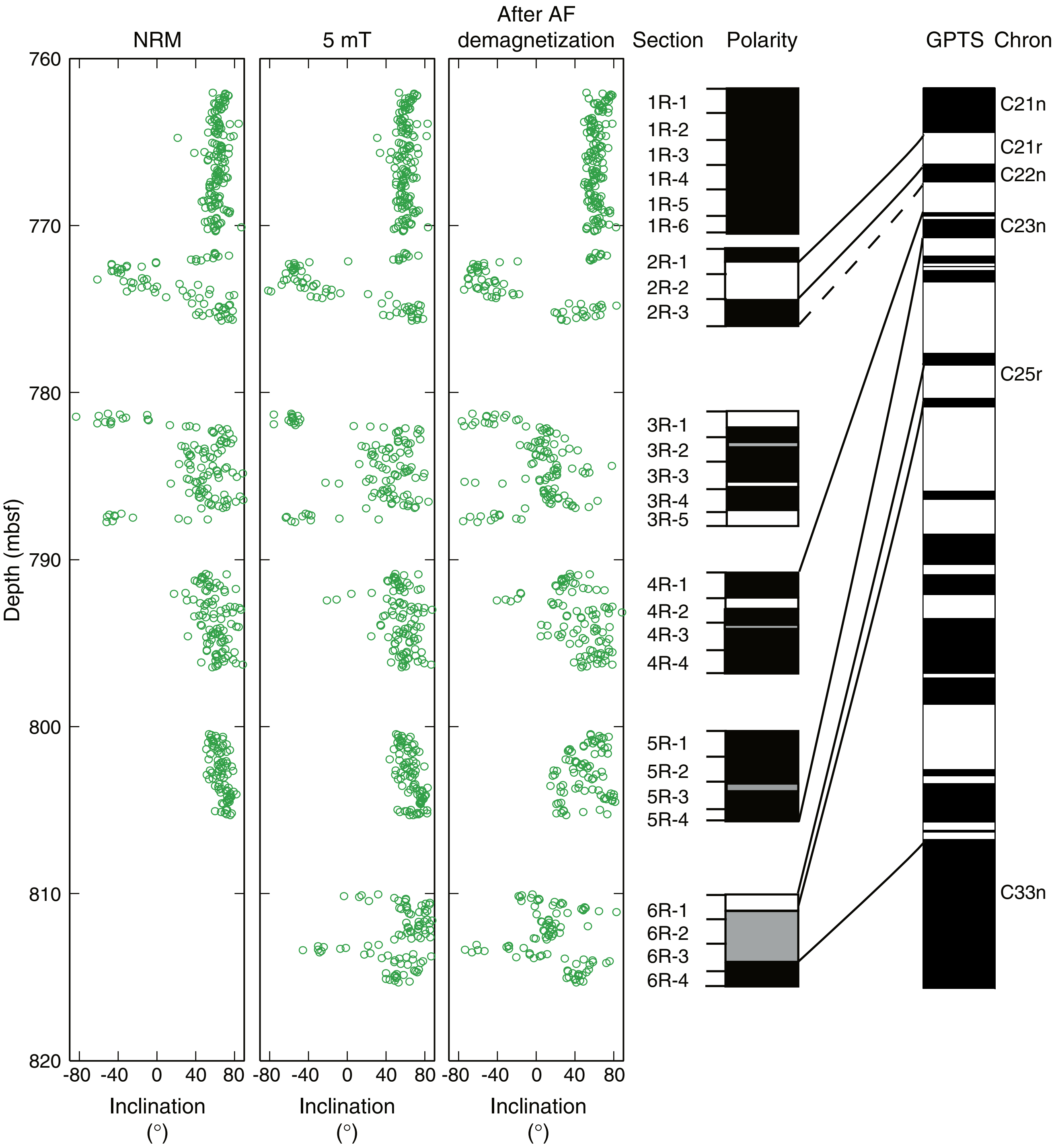

Figure F42. Example orthogonal vector plots showing poorly defined magnetic components recorded by Hole 1204A basalt: Samples (**A**) 197-1204A-7R-2, 78–80 cm, (**B**) 8R-2, 32–34 cm, (**C**) 7R-2, 78–80 cm, and (**D**) 9R-3, 77–79 cm. Open squares = vertical projection of magnetization, solid circles = horizontal projection of magnetization.

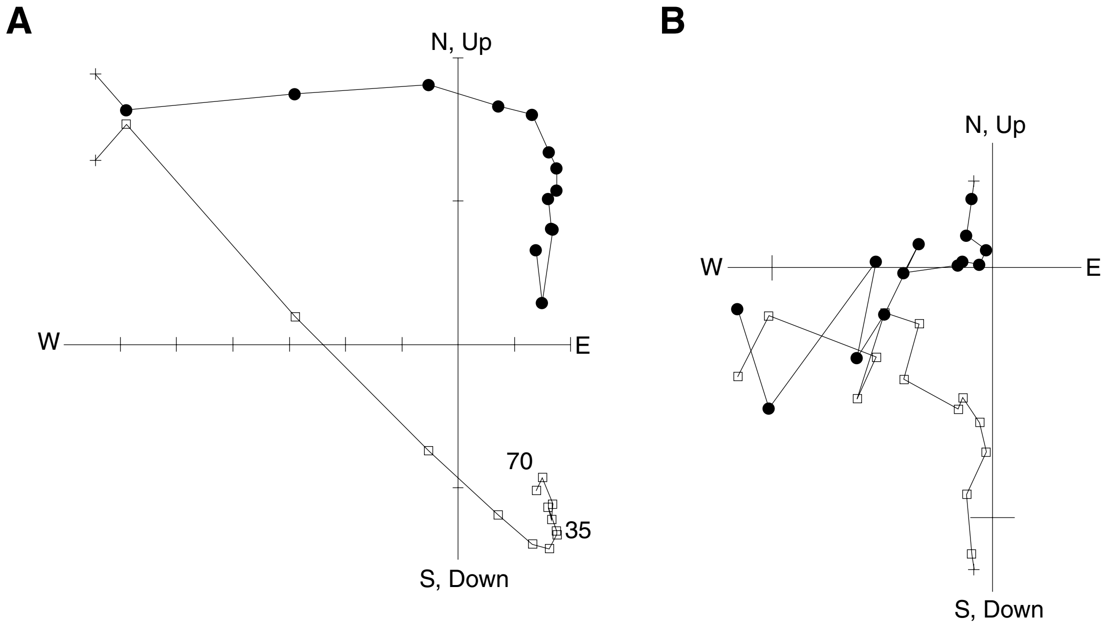

197-1204A-7R-2, 78-80 cm

197-1204A-8R-2, 32-34 cm

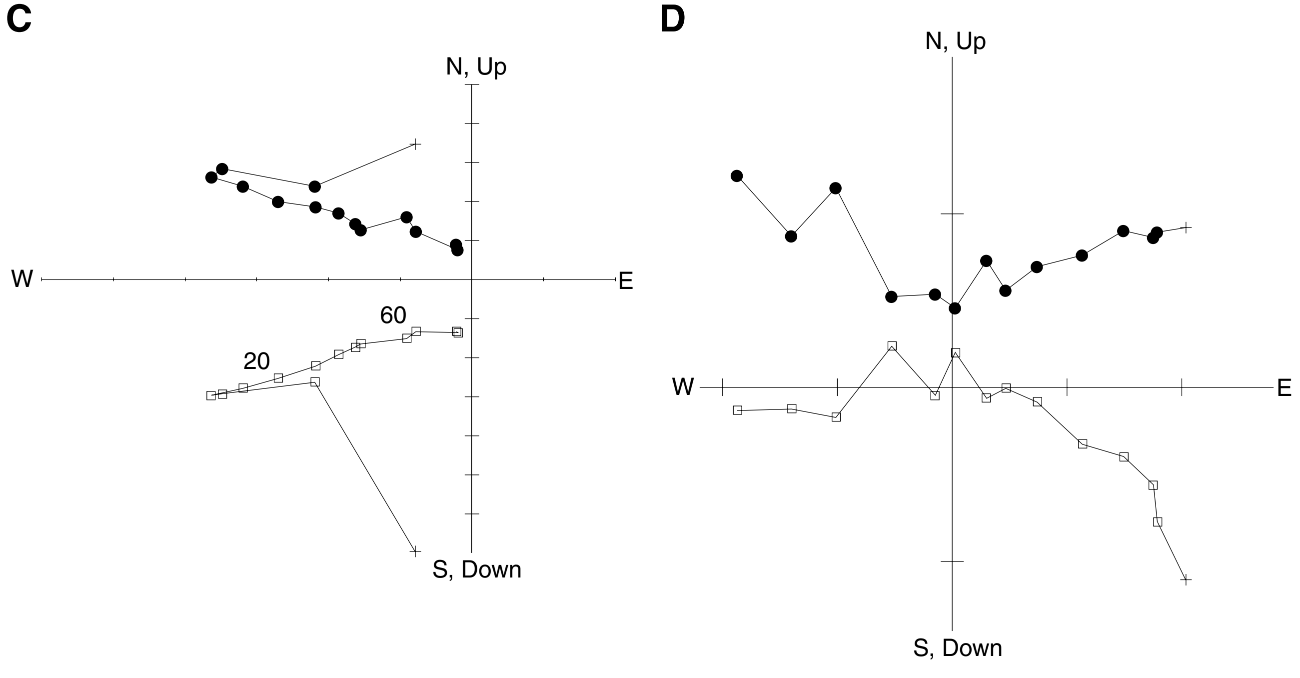

197-1204A-7R-2, 78-80 cm

197-1204A-9R-3, 77-79 cm

Figure F43. Example orthogonal vector plots showing poorly defined magnetic components recorded by Hole 1204B basalt: Samples (**A**) 197-1204A-2R-1, 21–23 cm, (**B**) 6R-2, 83–85 cm, (**C**) 15R-1, 103–105 cm, and (**D**) 10R-3, 27–29 cm. Open squares = vertical projection of magnetization, solid circles = horizontal projection of magnetization.

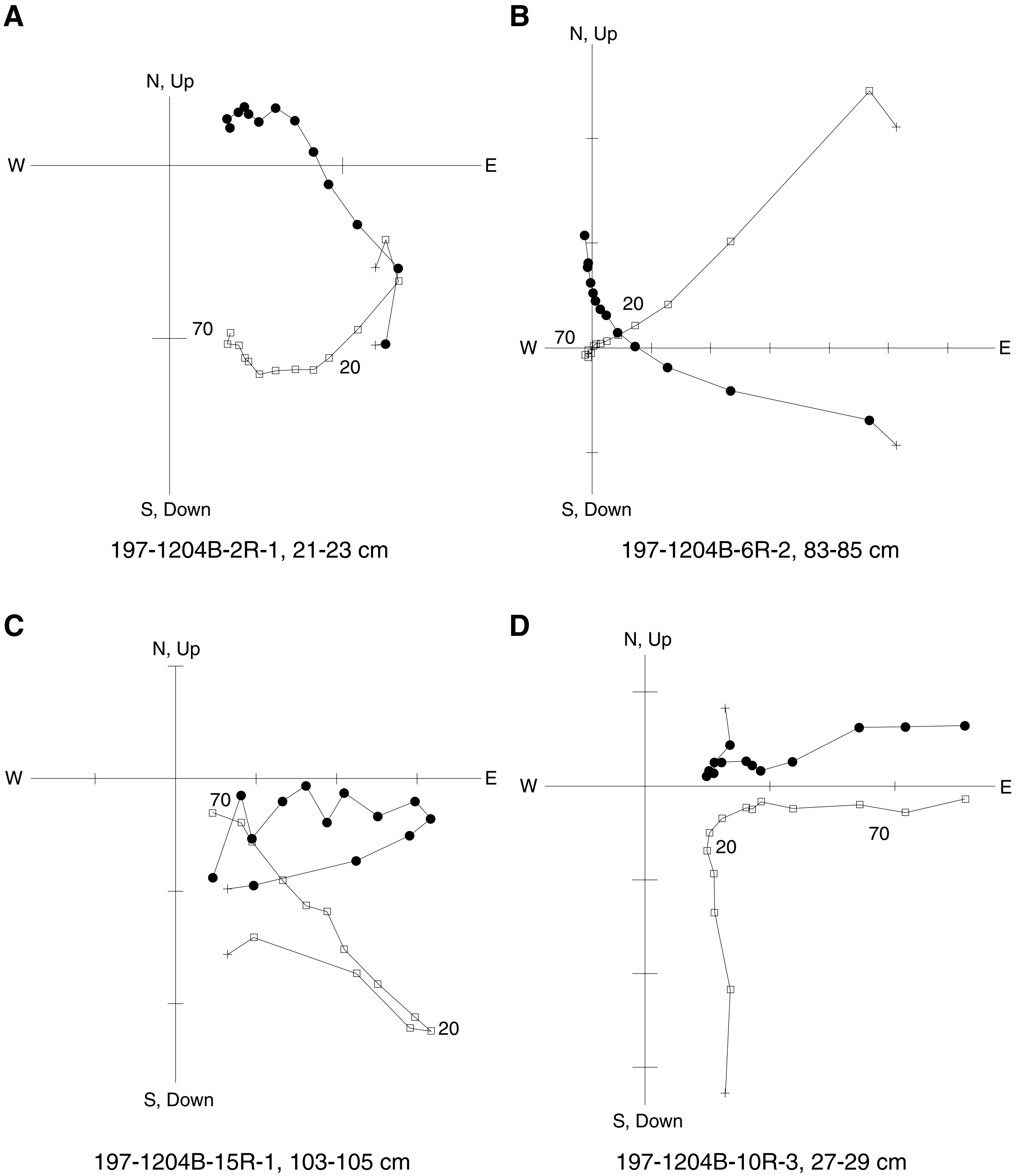

197-1204B-2R-1, 21-23 cm

197-1204B-6R-2, 83-85 cm

197-1204B-15R-1, 103-105 cm

197-1204B-10R-3, 27-29 cm

Figure F44. Low-field volume-normalized (bulk) magnetic susceptibility, Koenigsberger ratio, and median destructive field (MDF) vs. depth for Hole 1204A basalt samples.

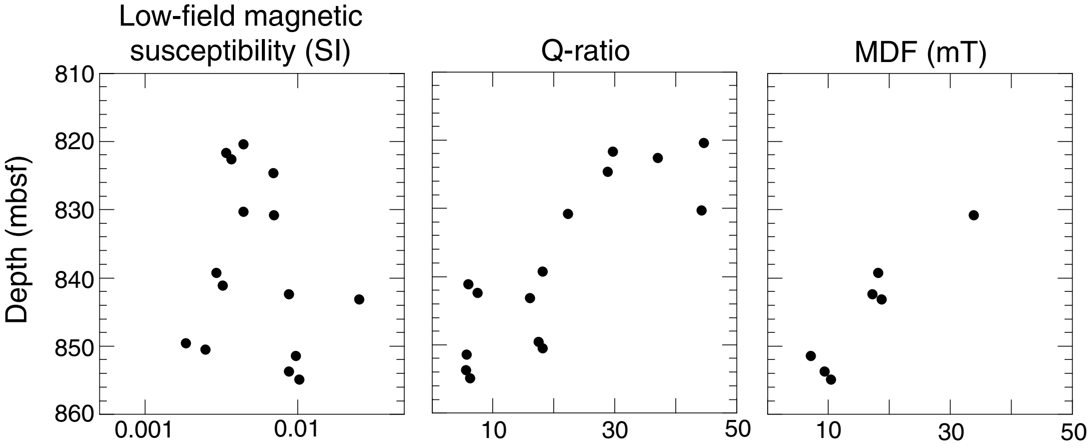

Figure F45. Low-field volume-normalized (bulk) magnetic susceptibility, Koenigsberger ratio, and median destructive field (MDF) vs. depth for Hole 1204B basalt samples.

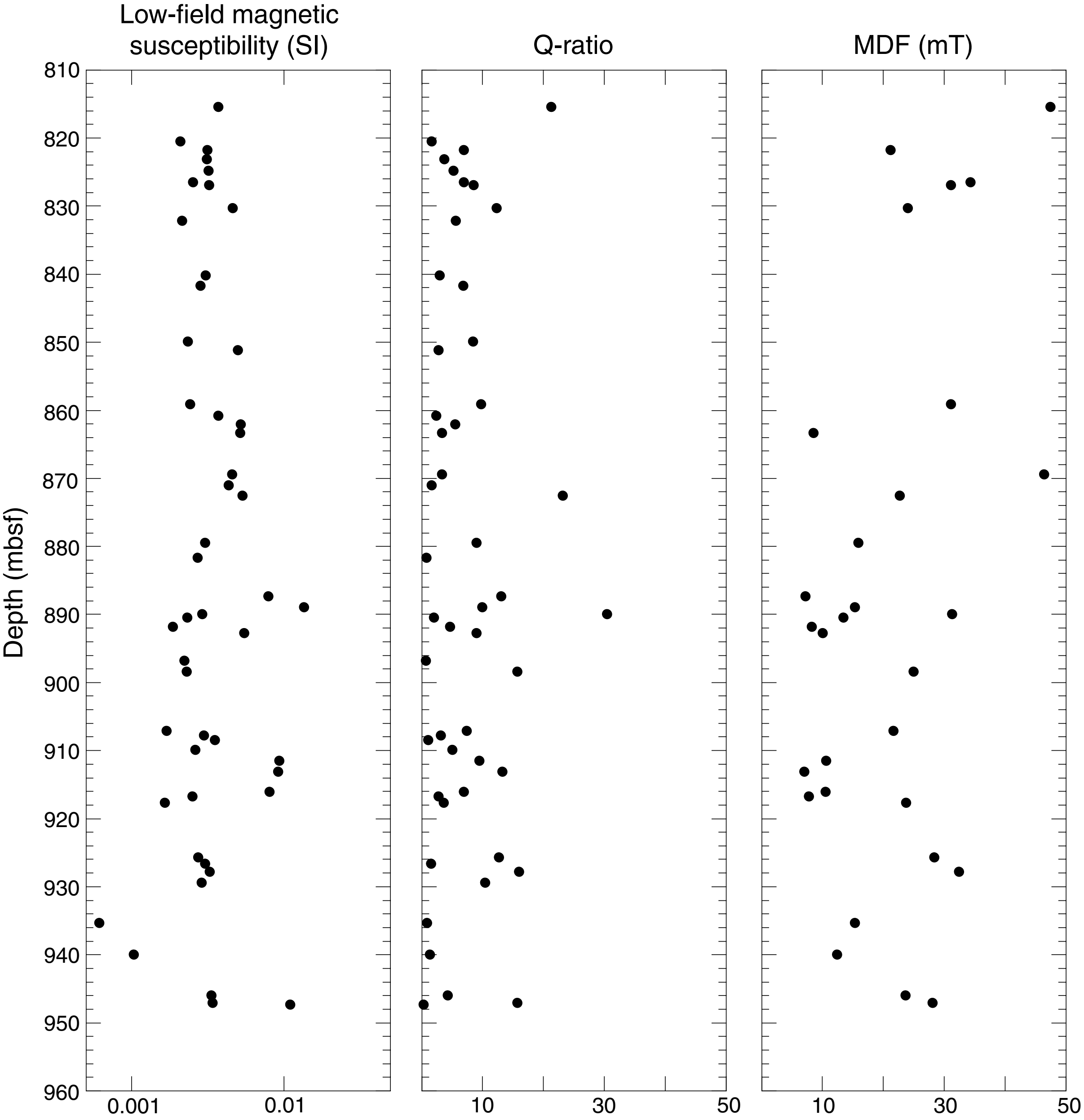

Figure F46. Examples of Lowrie-Fuller (Lowrie and Fuller, 1971) tests conducted on basalt samples: Samples (**A**) 197-1204A-8R-2, 132–134 cm, (**B**) 197-1204A-10R-1, 125–127 cm, (**C**) 197-1204B-4R-2, 63–65 cm, (**D**) 197-1204A-10R-4, 138–140 cm, (**E**) 197-1204B-9R-2, 8–10 cm, and (**F**) 197-1204R-13R-3, 33–35 cm. ARM = anhysteretic remanent magnetization, SIRM = saturation isothermal remanent magnetization.

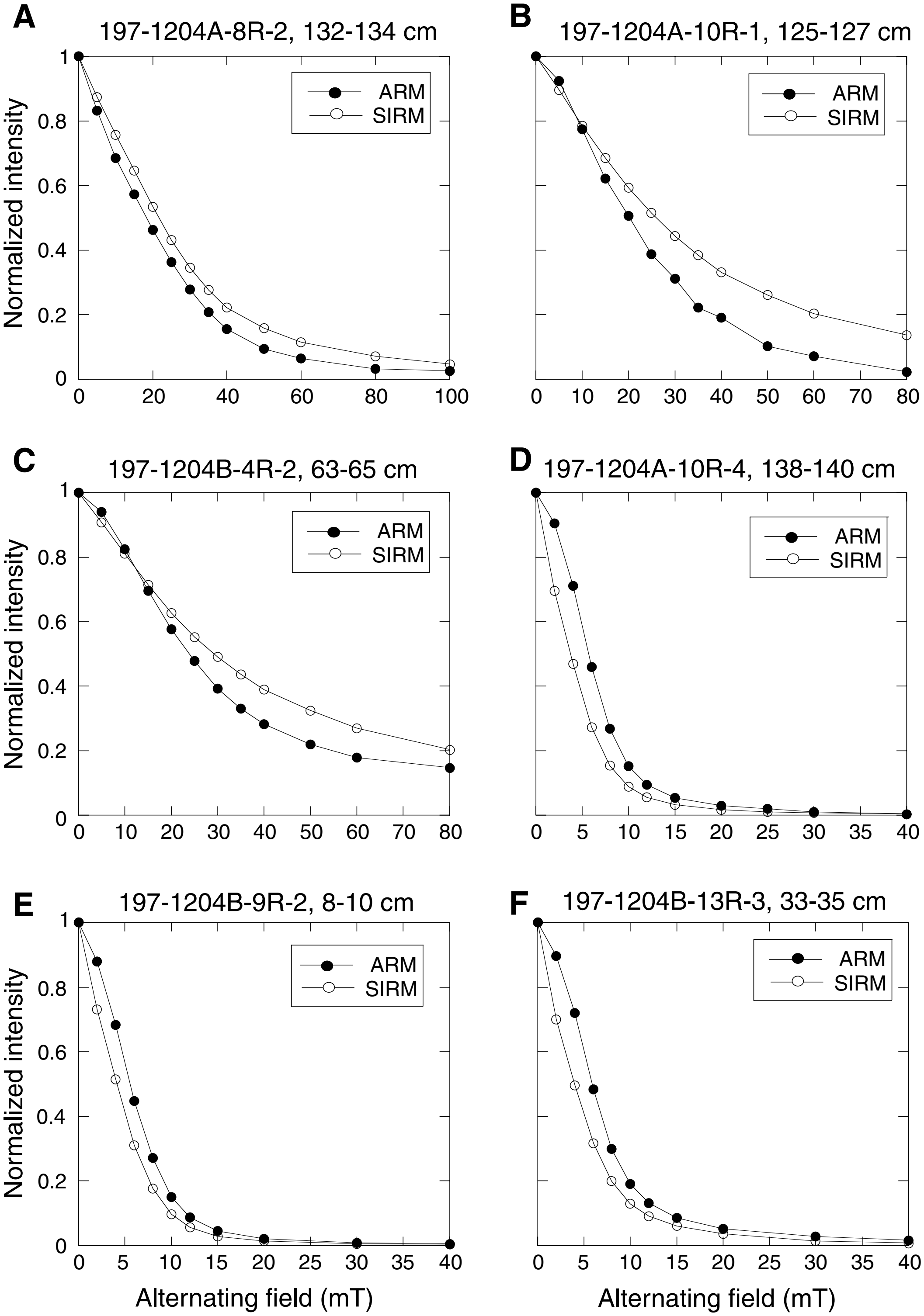

Figure F47. Example of isothermal remanent magnetization (IRM) acquisition and demagnetization (backfield IRM) (see **"Isothermal Remanent Magnetization Acquisition and Coercivity of Remanence Measurements,"** p. 26, in "Paleomagnetism and Rock Magnetism") used to calculate coercivity of remanence from basalt samples from Holes 1204A and 1204B: Samples (**A**) 197-1204A-8R-2, 132–134 cm, (**B**) 197-1204A-10R-1, 125–127 cm, (**C**) 197-1204B-4R-2, 63–65 cm, (**D**) 197-1204A-10R-4, 138–140 cm, (**E**) 197-1204B-9R-2, 8–10 cm, and (**F**) 197-1204B-13R-3, 33–35 cm.

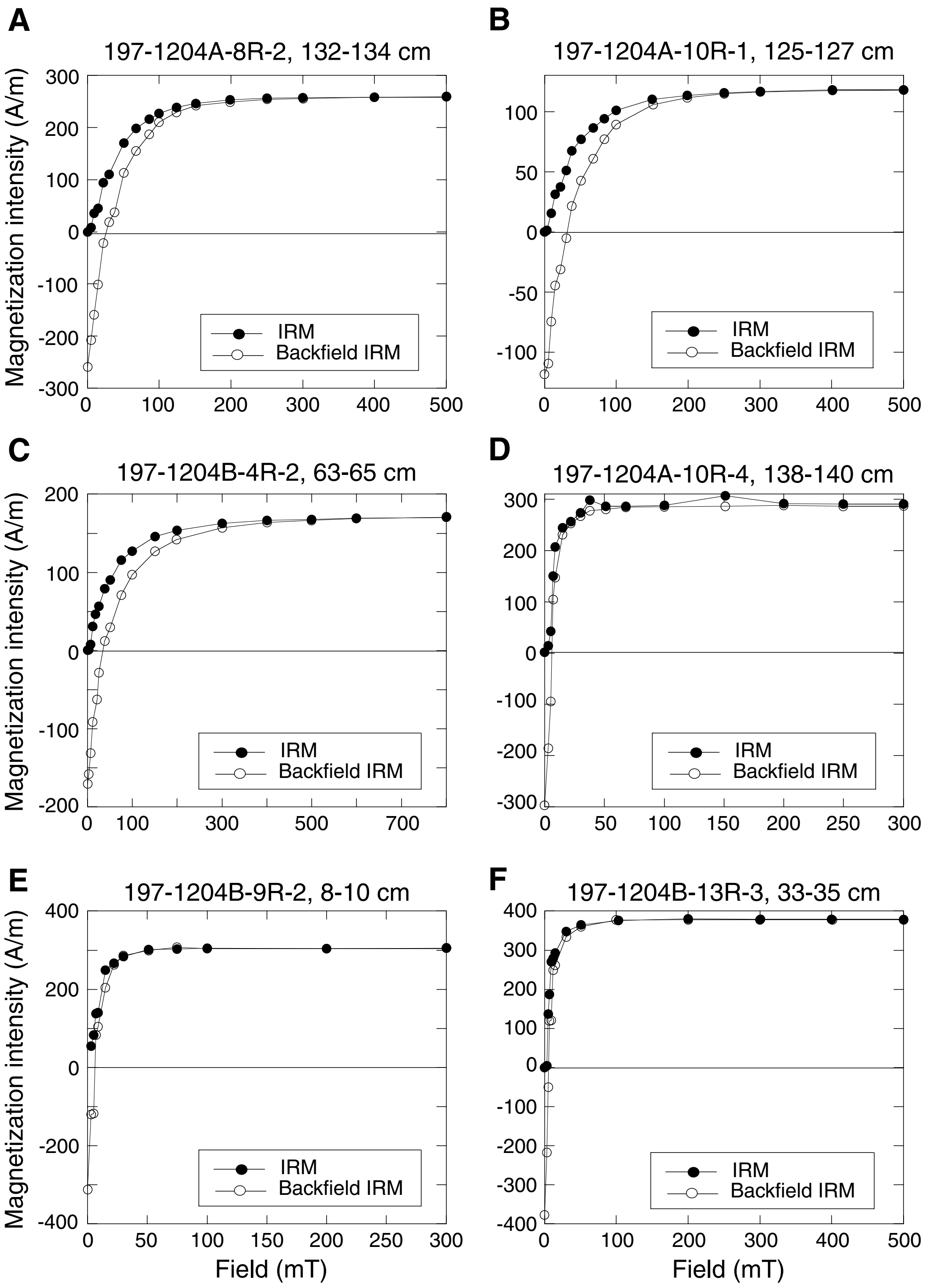

Figure F48. Example orthogonal vector plots showing well-defined magnetic components recorded by Hole 1204A basalt that are not completely demagnetized by the alternating-field treatment applied: Samples (**A**)197-1204A-7R-1, 98–100 cm, and (**B**) 8R-2, 32–34 cm. Open squares = vertical projection of magnetization, solid circles = horizontal projection of magnetization.

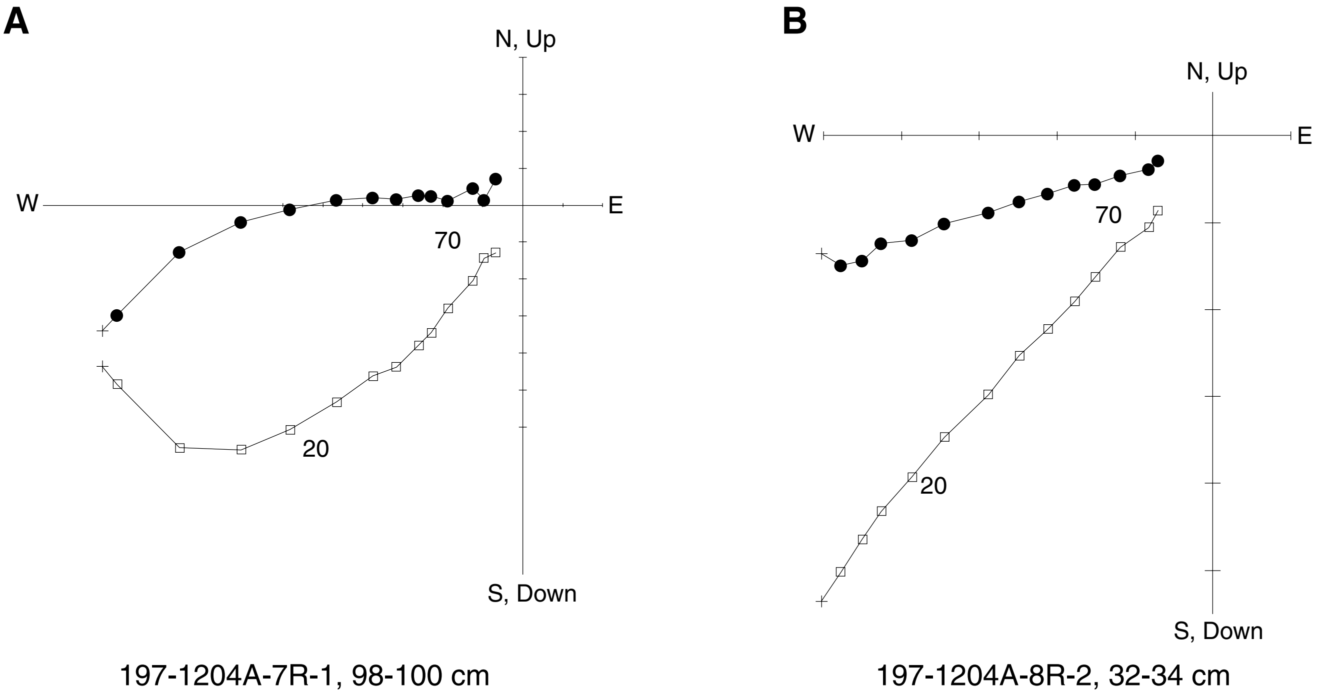

Figure F49. Example orthogonal vector plots showing well-defined magnetic components recorded by Hole 1204B basalt that are not completely demagnetized by the alternating-field treatment applied: Samples (**A**) 197-1204B-2R-5, 136–138 cm, (**B**) 3R-1, 38–40 cm, (**C**) 15R-2, 77–79 cm, (**D**) 15R-3, 83–85 cm, (**E**) 1R-4, 69–71 cm, and (**F**) 2R-4, 100–102 cm. Open squares = vertical projection of magnetization, solid circles = horizontal projection of magnetization.

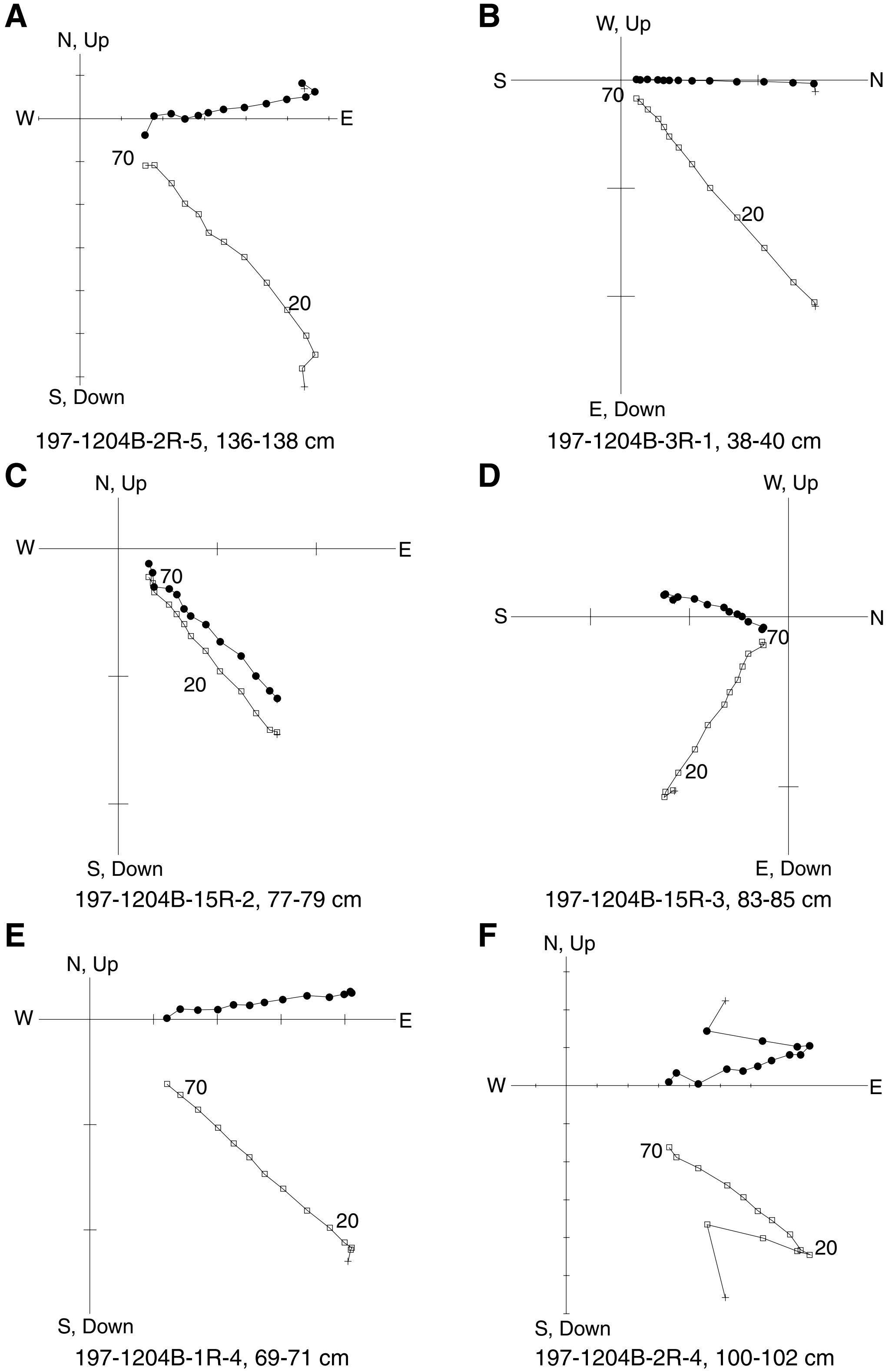

Figure F50. Example orthogonal vector plots showing well-defined, stable magnetic behavior recorded by Hole 1204A basalt: Samples (**A**) 197-1204A-9R-4, 17–19 cm, (**B**) 9R-3, 77–79 cm, (**C**) 9R-1, 73–75 cm, and (**D**) 10R-3, 56–58 cm. Open squares = vertical projection of magnetization, solid circles = horizontal projection of magnetization.

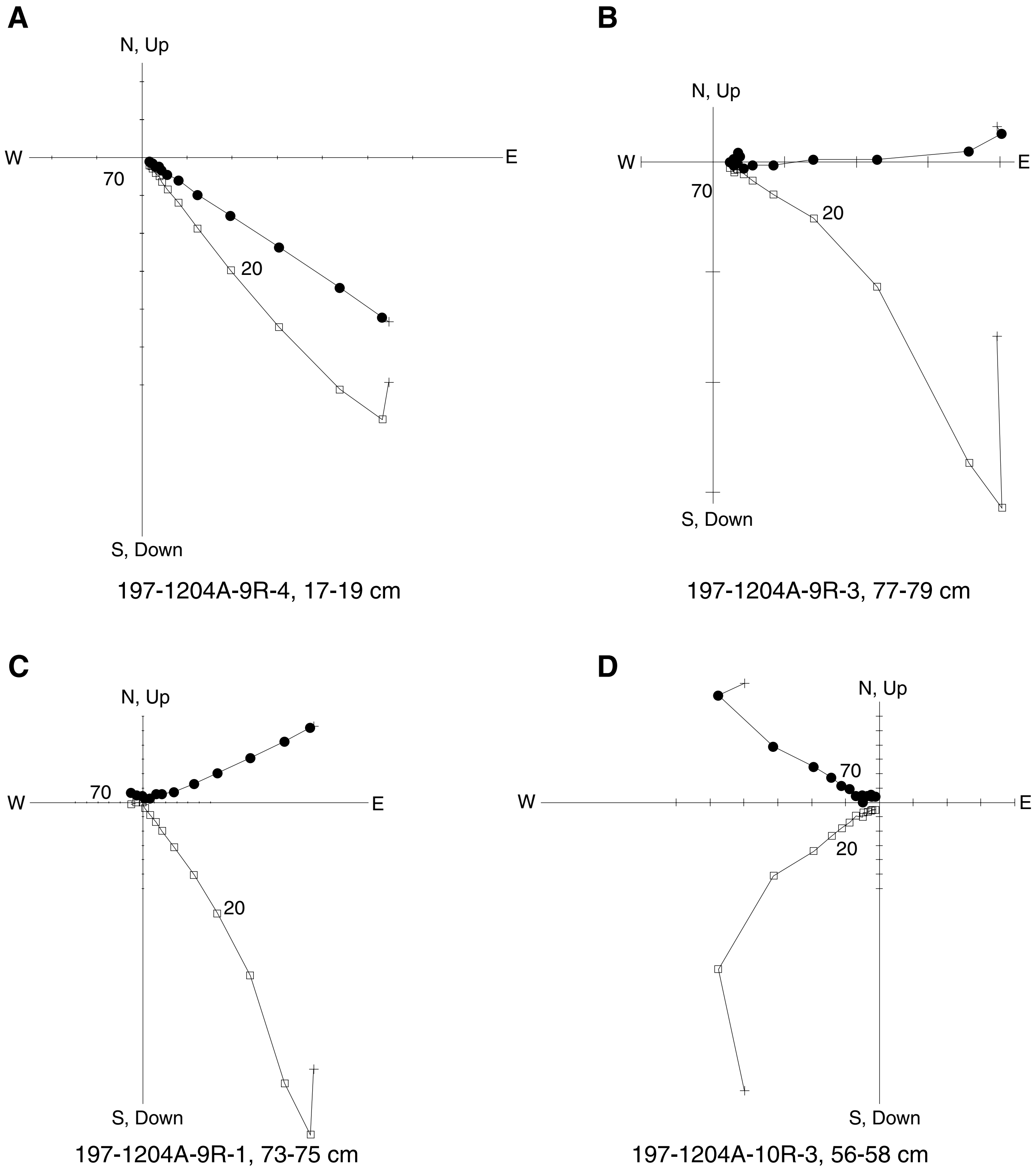

Figure F51. Example orthogonal vector plots showing well-defined, stable magnetic behavior recorded by Hole 1204B basalt: Samples (**A**) 197-1204B-2R-2, 14–16 cm, (**B**) 14R-1, 14–16 cm, (**C**) 13R-4, 82–84 cm, (**D**) 17R-2, 104–106 cm, (**E**) 10R-1, 6–9 cm, and (**F**) 15R-1, 11–13 cm. Open squares = vertical projection of magnetization, solid circles = horizontal projection of magnetization.

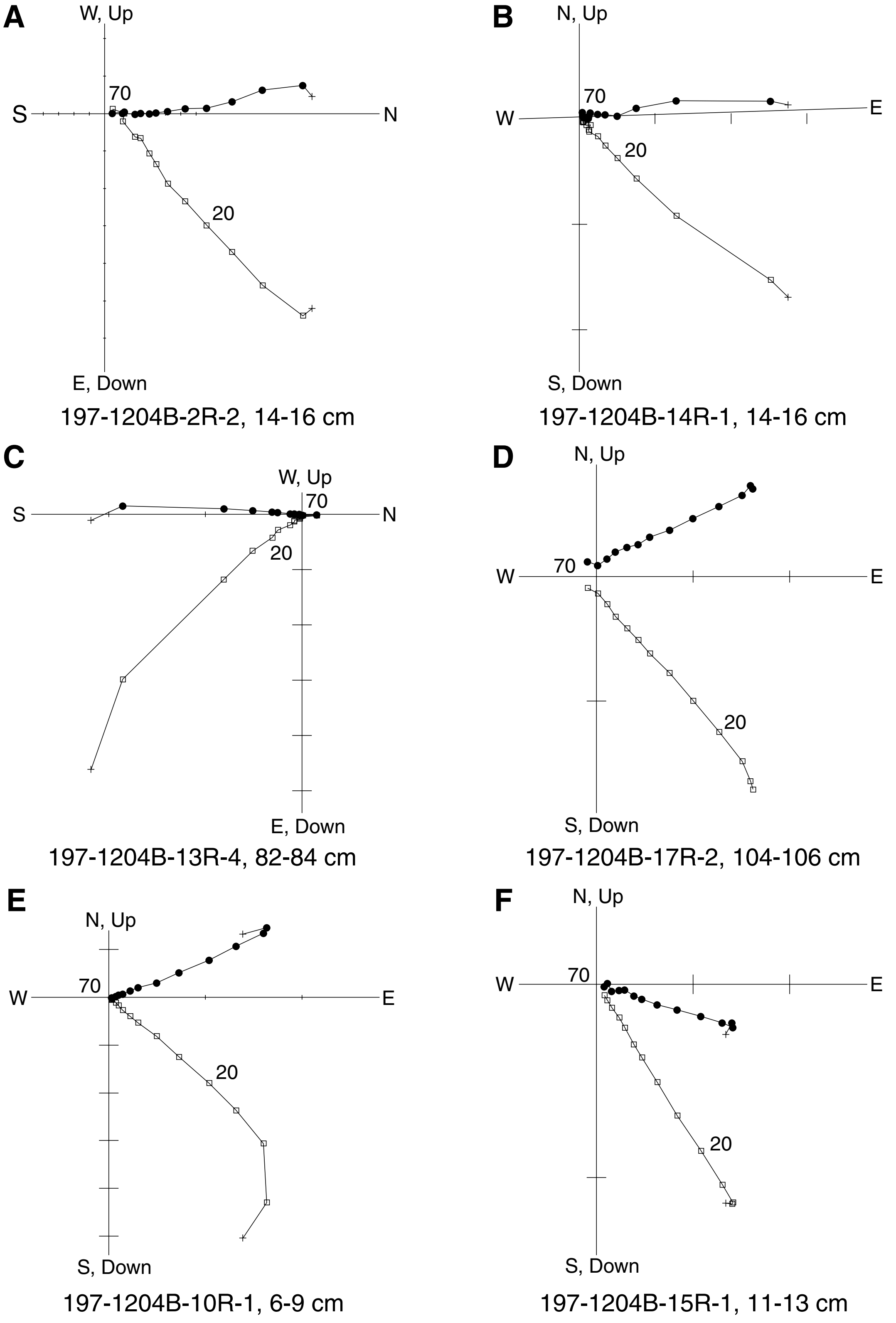

197-1204B-2R-2, 14-16 cm

197-1204B-14R-1, 14-16 cm

197-1204B-13R-4, 82-84 cm

197-1204B-17R-2, 104-106 cm

197-1204B-10R-1, 6-9 cm

197-1204B-15R-1, 11-13 cm

Figure F52. Example orthogonal vector plots showing well-defined, stable magnetic behavior recorded by Hole 1204B diabase: Samples (**A**) 197-1204B-7R-3, 139–141 cm, (**B**) 9R-2, 8–10 cm, (**C**) 8R-2, 21–23 cm, (**D**) 10R-4, 40–42 cm, (**E**) 11R-2, 38–40 cm, and (**F**) 13R-3, 33–35 cm. Open squares = vertical projection of magnetization, solid circles = horizontal projection of magnetization.

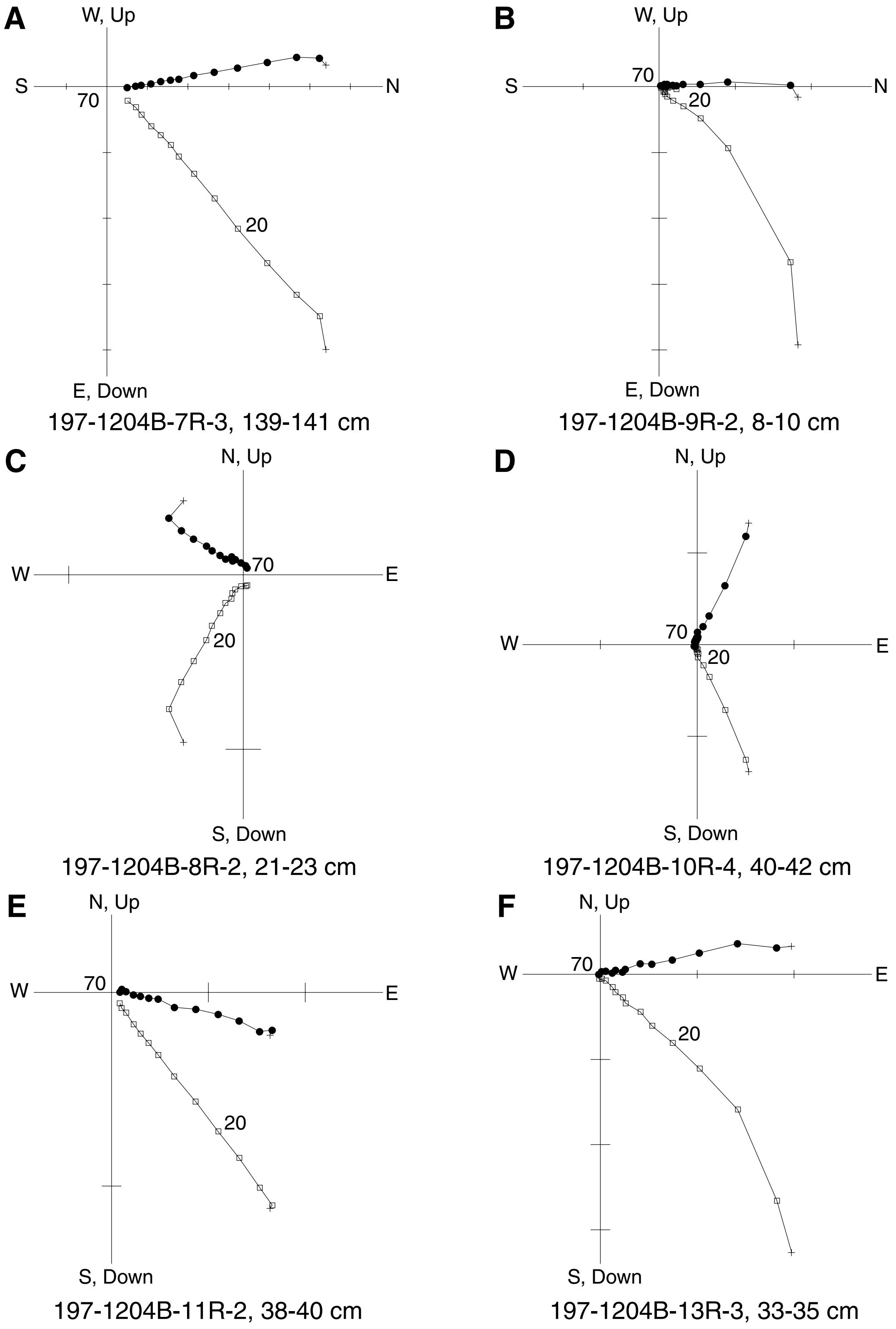

197-1204B-7R-3, 139-141 cm

197-1204B-9R-2, 8-10 cm

197-1204B-8R-2, 21-23 cm

197-1204B-10R-4, 40-42 cm

197-1204B-11R-2, 38-40 cm

197-1204B-13R-3, 33-35 cm

Figure F53. Comparison of magnetic susceptibility and median destructive field values of brown and green-gray basalt samples.

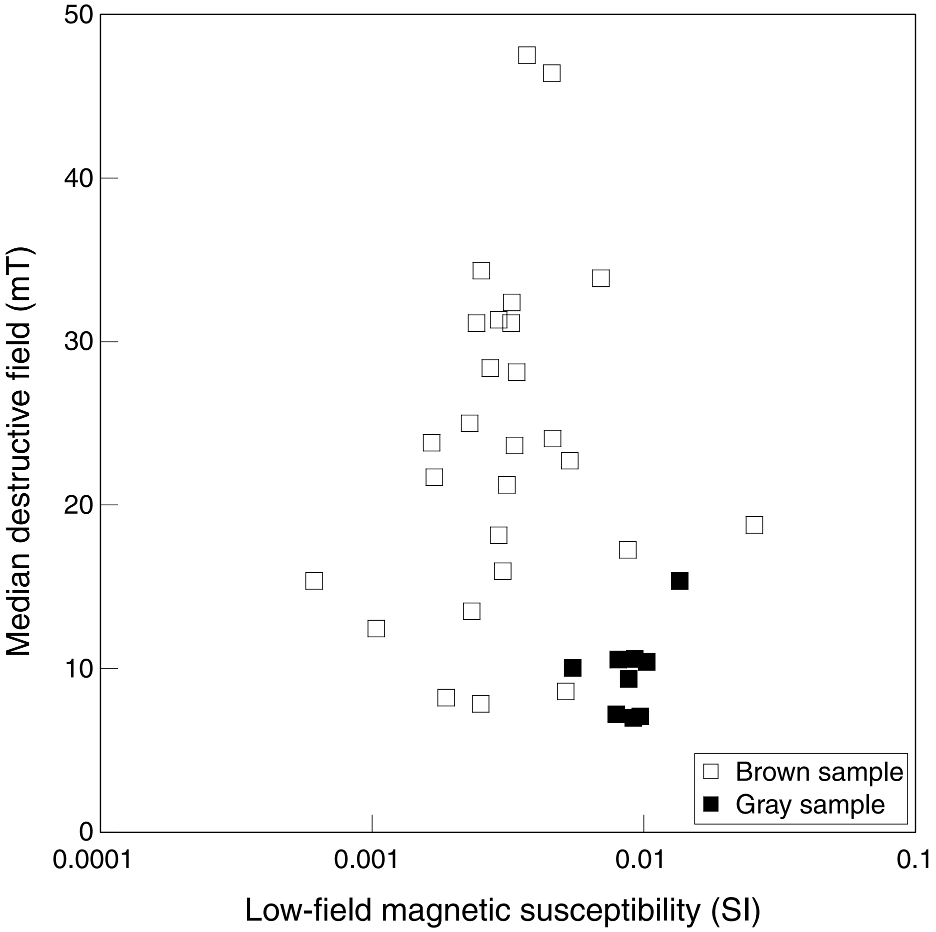

Figure F54. Whole-core measurements of (**A**) GRA bulk density, (**B**) magnetic susceptibility, and (**C**) natural gamma ray vs. depth in the sedimentary units of Hole 1204A.

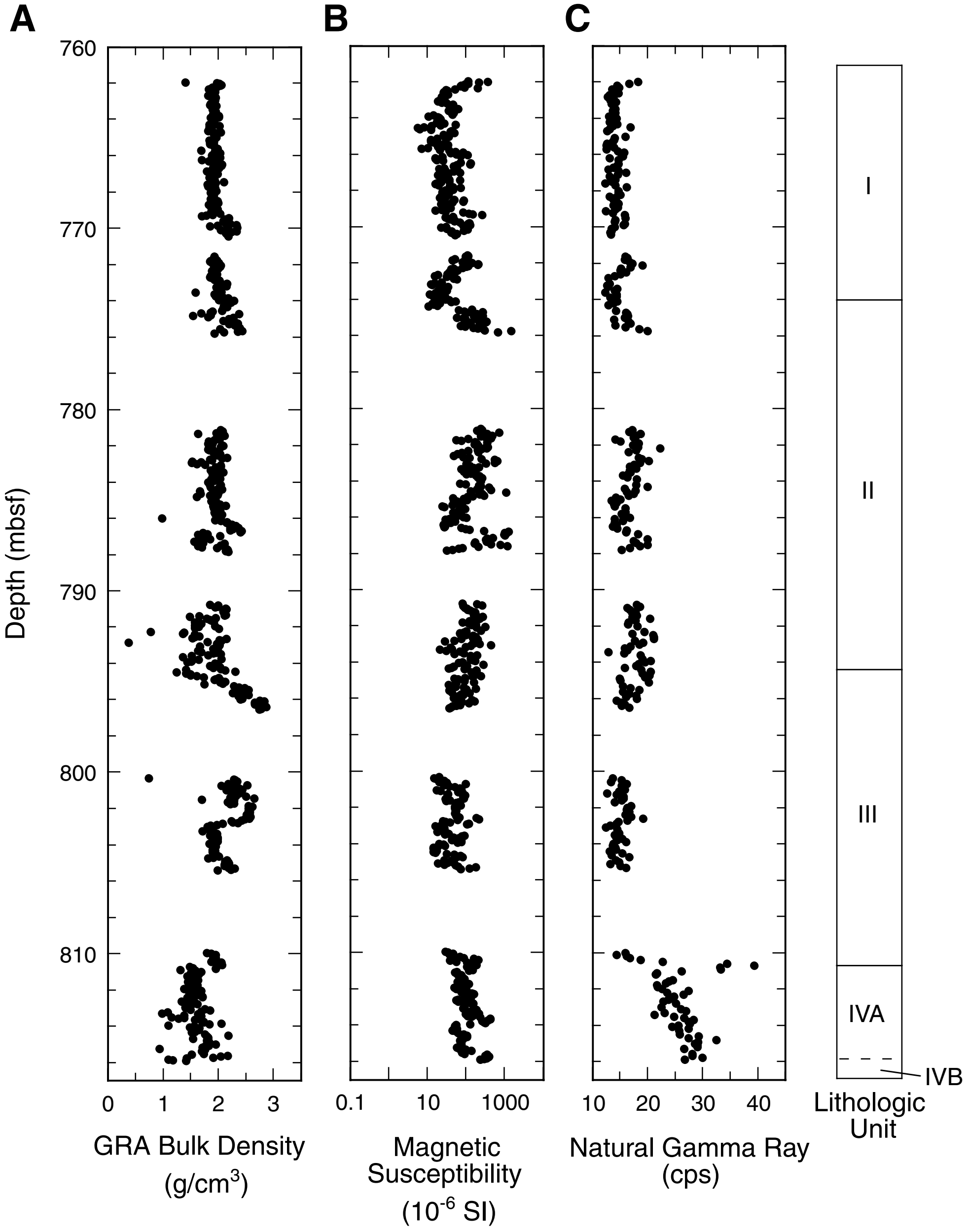

Figure F55. Whole-core measurements of (**A**) GRA bulk density, (**B**) magnetic susceptibility, and (**C**) natural gamma ray vs. depth in the sedimentary units of Hole 1204B.

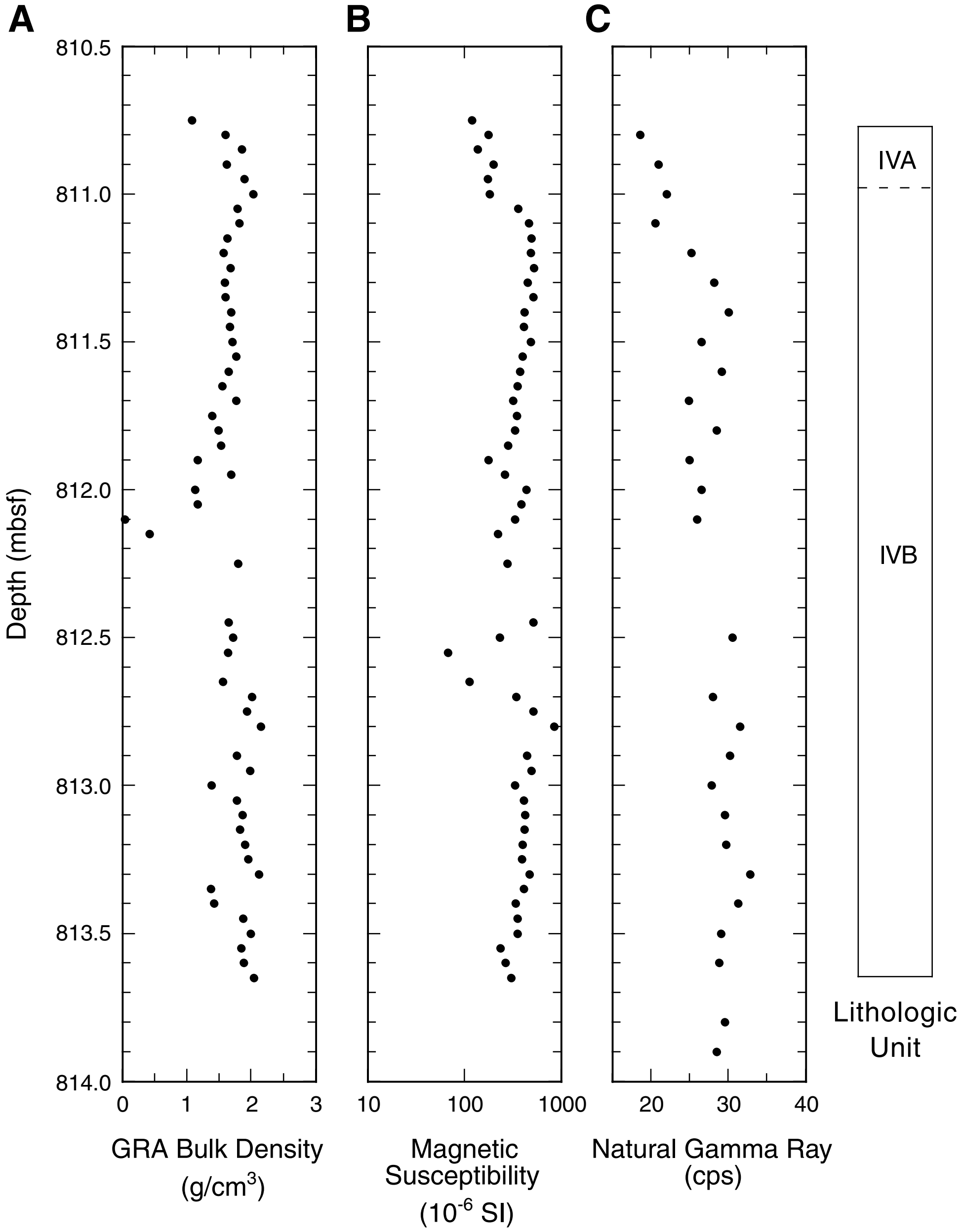

Figure F56. Comparison of natural gamma ray measurements vs. depth in Holes (**A**) 1204A and (**B**) 1204B.

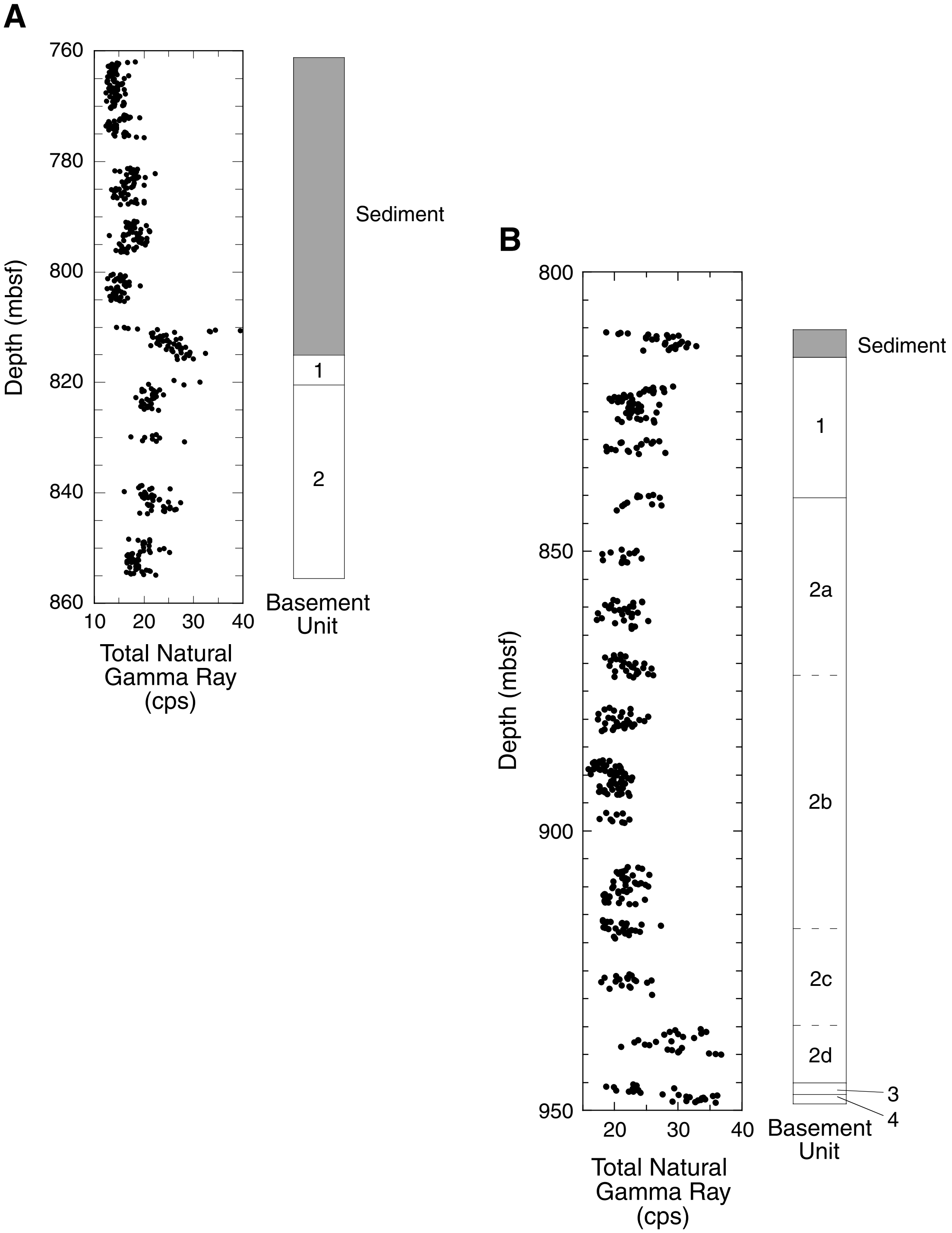

Figure F57. Thermal conductivity measurements vs. depth in Hole 1204B.

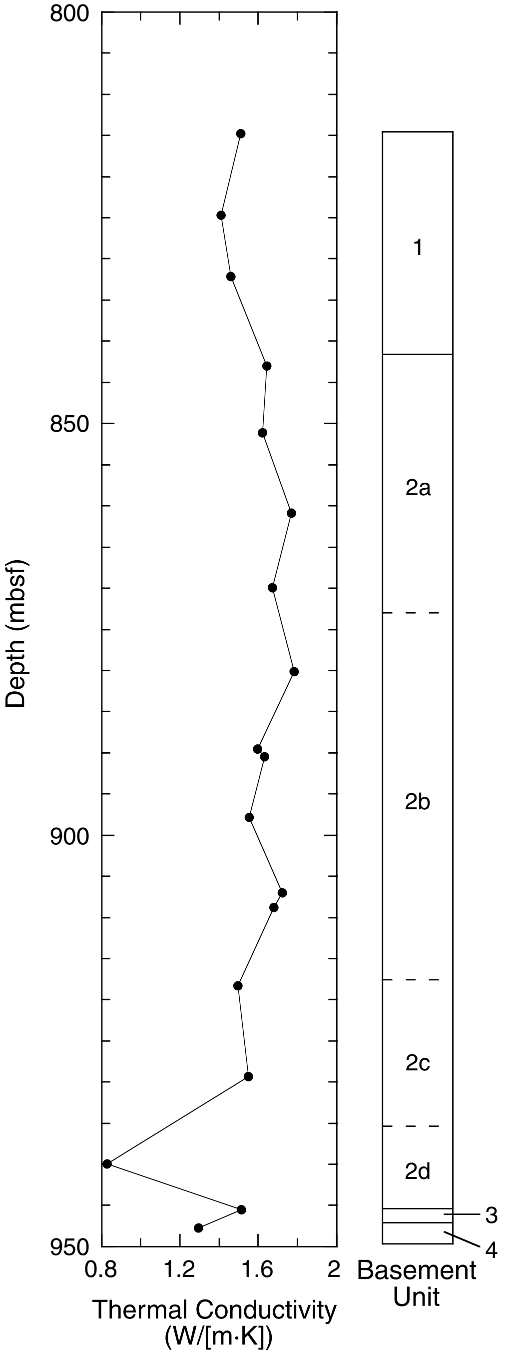

Figure F58. Summary of index properties measurements from the sedimentary units of Hole 1204A. **A.** GRA bulk density. **B.** Bulk density. **C.** Grain density. **D.** Porosity.

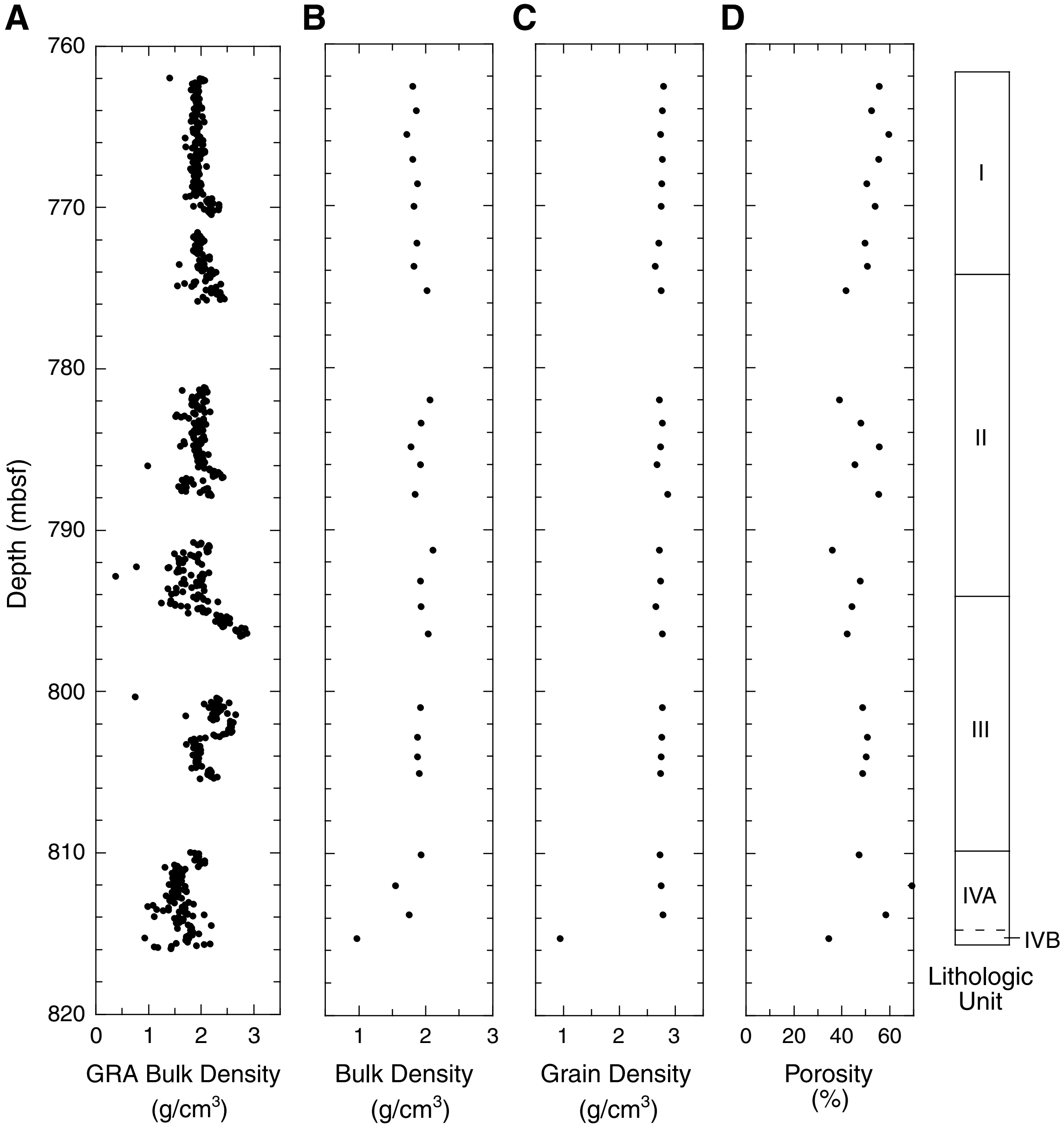

Figure F59. Summary of index properties measurements of basement units in Hole 1204B. **A.** Bulk density, **B.** Grain density. C. Porosity.

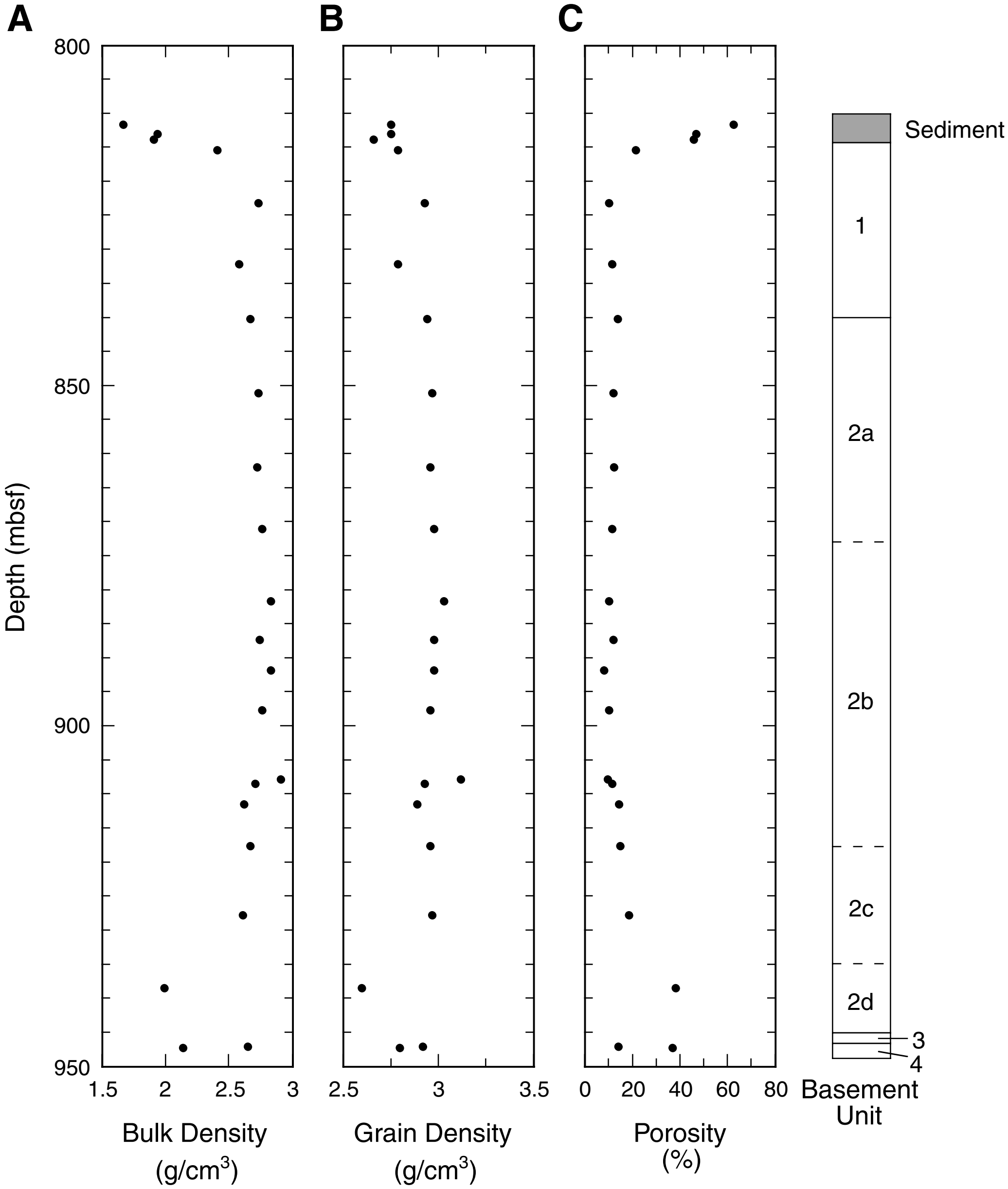

Figure F60. Compressional wave velocity of samples from Holes 1204A and 1204B.

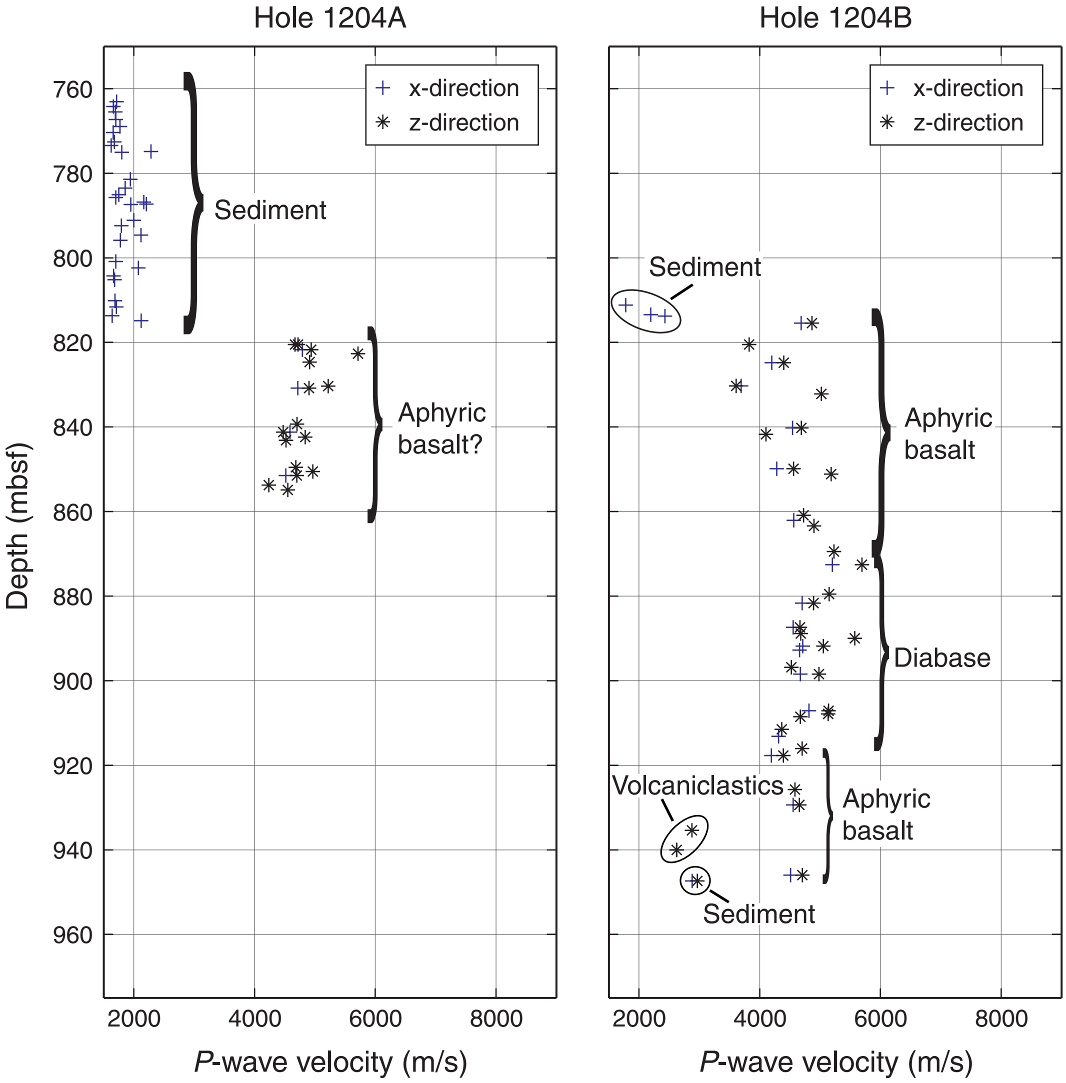

Figure F61. Ship track for Leg 197, Site 1204 seismic reflection survey. Tick marks show half-hour time intervals. Track lines of the *Faranella* survey are shown as well.

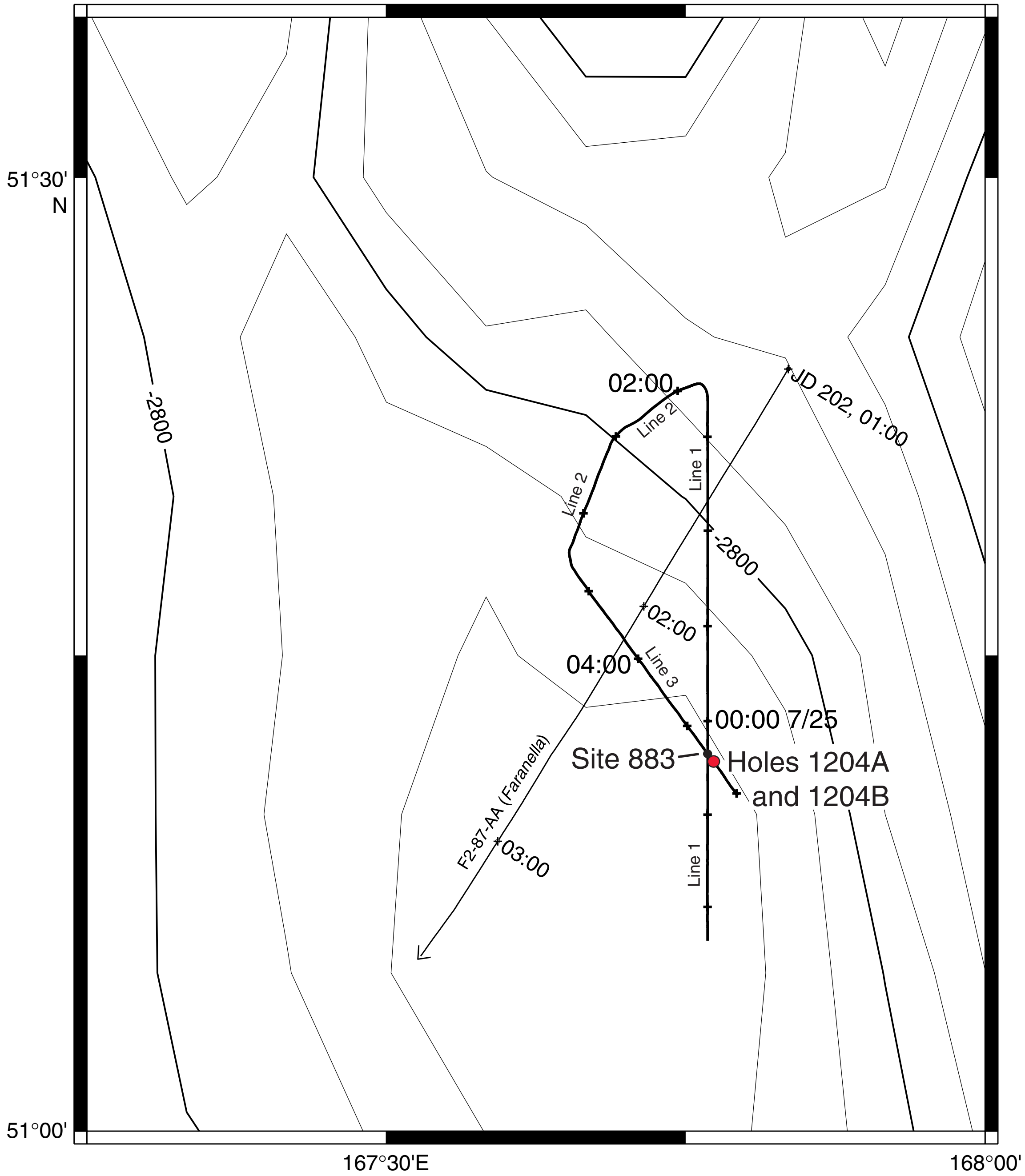

Figure F62. Four-km-long migrated time section of survey Line 1. Data are bandpass filtered between 40 and 100 Hz. Hole 883F is at about shotpoint 610. Trace-to-trace distance = ~18.2 m, vertical exaggeration at the seafloor = ~3:1, bottom of hole = ~4.19 s two-way traveltime.

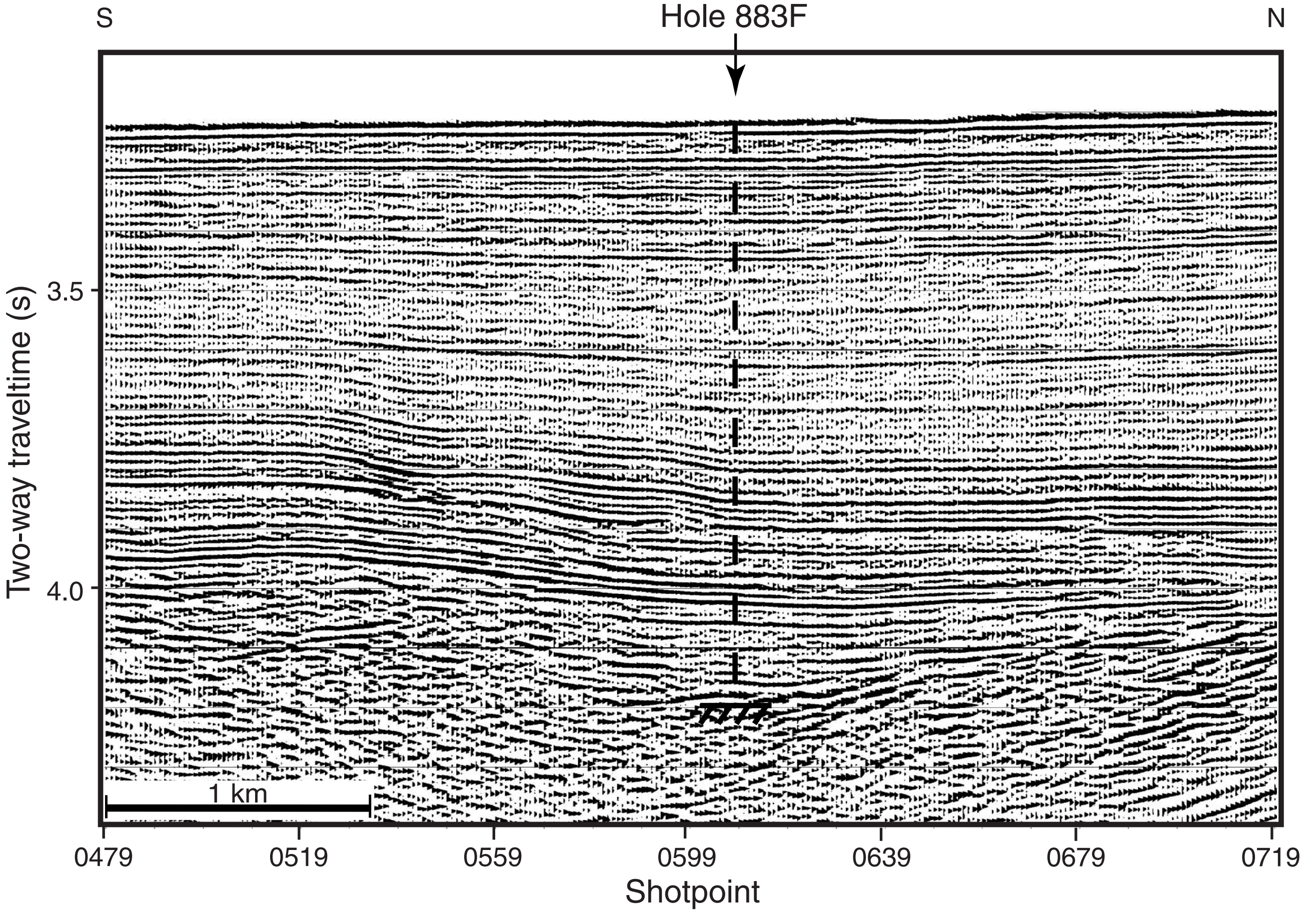

Figure F63. Four-km-long migrated time section of survey Line 3. Data are bandpass filtered between 40 and 100 Hz. Hole 883F occurs at about shotpoint 3517, Hole 1204A at shotpoint 3549, and Hole 1204B at shotpoint 3555. Trace-to-trace distance = ~16.5 m, vertical exaggeration at the seafloor = ~3:1, bottom of Hole 1204B = ~4.2 s two-way traveltime.

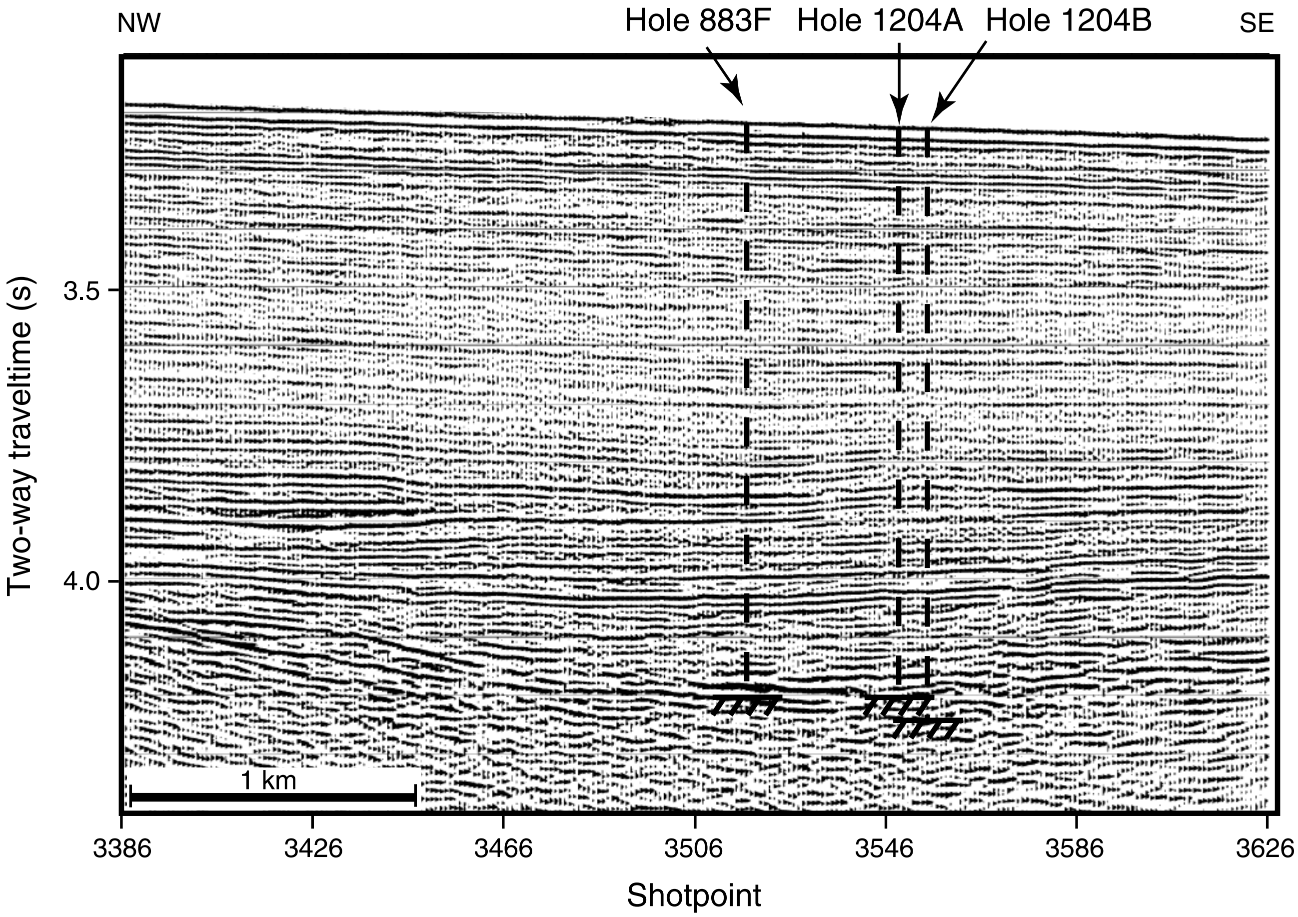

Table T1. Coring summary, Site 1204. (**See table note.** Continued on next page.)

Hole 1204A

Latitude: 51°11.6784′N
Longitude: 167°46.3604′E
Time on site (hr): 173.5 (1530 hr, 25 Jul–2100 hr, 1 Aug 2001)
Time on hole (hr): 71.5 (1530 hr, 25 Jul–1500 hr, 28 Jul 2001)
Seafloor (drill pipe measurement from rig floor, mbrf): 2382.0
Distance between rig floor and sea level (m): 11.0
Water depth (drill pipe measurement from sea level, m): 2371.0
Total depth (drill pipe measurement from rig floor, mbrf): 3262.3
Total penetration (meters below seafloor, mbsf): 880.3
Total length of cored section (m): 118.4
Total length of drilled intervals (m): 761.9
Total core recovered (m): 55.86
Core recovery (%): 47.2
Total number of cores: 14
Total number of drilled intervals: 2

Hole 1204B

Latitude: 51°11.6406′N
Longitude: 167°46.4217′E
Time on hole (hr): 102 (1500 hr, 28 Jul–2100 hr, 1 Aug 2001)
Seafloor (drill pipe measurement from rig floor, mbrf): 2381.0
Distance between rig floor and sea level (m): 11.0
Water depth (drill pipe measurement from sea level, m): 2370.0
Total depth (drill pipe measurement from rig floor, mbrf): 3335.5
Total penetration (meters below seafloor, mbsf): 954.5
Total length of cored section (m): 143.8
Total length of drilled intervals (m): 810.7
Total core recovered (m): 55.93
Core recovery (%): 38.9
Total number of cores: 17
Total number of drilled intervals: 2

Core	Date (2001)	Ship time (local)	Depth (mbsf)		Length (m)		Recovery (%)	Comments
			Top	Bottom	Cored	Recovered		
197-1204A-								
			*****Drilled from 0.0 to 761.9 mbsf*****					
1R	26 Jul	1745	761.9	771.5	9.6	8.71	90.7	
2R	26 Jul	1845	771.5	781.1	9.6	4.62	48.1	
3R	26 Jul	1945	781.1	790.7	9.6	7.04	73.3	
4R	26 Jul	2100	790.7	800.3	9.6	6.13	63.9	
5R	26 Jul	2205	800.3	809.9	9.6	5.32	55.4	
6R	27 Jul	0010	809.9	819.5	9.6	6.38	66.5	
7R	27 Jul	0320	819.5	829.0	9.5	4.71	49.6	AHC
8R	27 Jul	0500	829.0	838.6	9.6	1.51	15.7	
9R	27 Jul	0905	838.6	848.3	9.7	3.83	39.5	AHC
10R	27 Jul	1500	848.3	857.9	9.6	7.61	79.3	AHC
11R	27 Jul	2045	857.9	862.7	4.8	0.00	0.0	AHC
12R	27 Jul	2330	862.7	867.5	4.8	0.00	0.0	AHC
13R	28 Jul	0535	867.5	877.1	9.6	0.00	0.0	AHC
14R	28 Jul	0915	877.1	880.3	3.2	0.00	0.0	AHC
				Cored totals:	118.4	55.86	47.2	
				Drilled totals:	761.9			
				Total:	880.3			
197-1204B-								
			*****Drilled from 0.0 to 810.7 mbsf*****					
1R	29 Jul	2035	810.7	820.3	9.6	4.65	48.4	AHC
2R	29 Jul	2355	820.3	829.9	9.6	6.35	66.2	AHC
3R	30 Jul	0300	829.9	839.6	9.7	2.31	23.8	AHC
4R	30 Jul	0530	839.6	849.3	9.7	2.51	25.9	AHC
5R	30 Jul	0745	849.3	858.6	9.3	1.86	20.0	AHC
6R	30 Jul	1040	858.6	868.2	9.6	4.12	42.9	AHC
7R	30 Jul	1355	868.2	877.8	9.6	3.64	37.9	AHC
8R	30 Jul	1815	877.8	887.1	9.3	3.14	33.8	AHC
9R	30 Jul	2115	887.1	888.8	1.7	2.80	164.7	AHC
10R	31 Jul	0125	888.8	896.6	7.8	4.26	54.6	AHC
11R	31 Jul	0650	896.6	906.3	9.7	1.32	13.6	AHC
12R	31 Jul	1720	906.3	908.3	2.0	1.50	75.0	AHC
13R	31 Jul	2305	908.3	915.9	7.6	4.38	57.6	AHC

Table T1 (continued).

Core	Date (2001)	Ship time (local)	Depth (mbsf)		Length (m)		Recovery (%)	Comments
			Top	Bottom	Cored	Recovered		
14R	1 Aug	0310	915.9	925.6	9.7	3.26	33.6	AHC
15R	1 Aug	0635	925.6	935.2	9.6	2.65	27.6	AHC
16R	1 Aug	0910	935.2	944.9	9.7	3.90	40.2	AHC
17R	1 Aug	1550	944.9	954.5	9.6	3.28	34.2	AHC
				Cored totals:	143.8	55.93	38.9	
				Drilled totals:	810.7			
				Total:	954.5			

Note: AHC = active heave compensation.

Table T2. Carbonate abundance data for Units I, II, III, and IV, Site 1204.

Core, section, interval (cm)	Depth (mbsf)	$CaCO_3$ (wt%)
197-1204A-		
1R-1, 21–22	762.11	78.7
1R-5, 83–84	768.73	89.6
1R-5, 134–135	769.24	65.5
2R-1, 5–6	771.55	50.6
2R-1, 116–117	772.66	92.1
2R-2, 69–70	773.69	88.3
Unit I minimum:		50.6
Unit I maximum:		92.1
Unit I average:		77.4
197-1204A-		
2R-3, 38–39	774.88	2.7
2R-3, 45–46	774.95	85.2
2R-3, 110–111	775.60	85.0
2R-3, 124–125	775.74	0.8
3R-1, 8–9	781.18	69.2
3R-1, 108–109	782.18	1.7
3R-2, 38–39	782.98	10.7
3R-2, 88–89	783.48	88.7
3R-4, 71–72	786.31	76.2
3R-4, 115–116	786.75	68.2
3R-5, 2–3	787.12	23.0
3R-5, 28–29	787.38	71.5
3R-5, 80–81	787.90	88.4
4R-1, 71–72	791.41	49.2
4R-1, 132–133	792.02	9.2
4R-2, 3–4	792.23	16.5
4R-2, 40–41	792.60	6.1
4R-3, 28–29	793.98	76.3
Unit II minimum:		0.8
Unit II maximum:		88.7
Unit II average:		46.0
197-1204A-		
4R-4, 50–51	795.70	82.3
4R-CC, 18–19	796.78	85.8
5R-2, 15–16	801.95	86.4
5R-4, 2–3	804.83	92.7
5R-4, 59–60	805.40	84.2
6R-1, 19–20	810.09	92.7
Unit III minimum:		82.3
Unit III maximum:		92.7
Unit III average:		87.4
197-1204A-		
6R-1, 76–77	810.66	57.5
6R-2, 110–111	812.50	0.2
6R-3, 27–28	813.17	7.2
6R-4, 2–3	814.42	0.1
Unit IV minimum:		0.1
Unit IV maximum:		57.5
Unit IV average:		16.2
197-1204A-		
6R-5, 29–30	815.77	50.6
	Subunit IVB:	50.6
197-1204B-		
1R-2, 111–112	813.31	1.2
1R-3, 30–31	814.00	4.6
Subunit IVB minimum:		1.2
Subunit IVB maximum:		4.6
Subunit IVB average:		2.9

Table T3. Summary of distribution and abundance of nannofossils and biozonal assignments, Hole 1204A. (Continued on next page.)

Core, section, interval (cm)	Depth (mbsf)	Sample code	Zone		Age		Preparation*	Preservation	Group abundance	Nannofossils																							
			From	To	From	To				*Aspidolithus parcus* ssp. *parcus*	*Ceratolithoides aculeus*	*Cretarhabdus crenulatus*	*Cribrosphaerella ehrenbergii*	*Micula concava*	*Micula decussata*	*Quadrum sissinghii*	*Quadrum trifidum*	*Watznaueria barnesae*	*Quadrum gothicum*	*Chiasmolithus bidens*	*Coccolithus pelagicus*	*Cruciplacolithus asymmetricus*	*Cruciplacolithus frequens*	*Cruciplacolithus primus*	*Cruciplacolithus tenuis*	*Discoaster mohleri*	*Fasciculithus thomasii*	*Fasciculithus tympaniformis*	*Heliolithus kleinpellii*	*Placozygus sigmoides*	*Sphenolithus anarrhopus*	*Toweius pertusus*	*Fasciculithus involutus*
197-1204A-																																	
1R-1, 50–51	762.40	BIO	NP15		middle Eocene		Smear slide	M	F												F												
1R-3, 50–51	765.40	BIO	NP15		middle Eocene		Smear slide	M	C												C												
1R-5, 49–50	768.39	BIO	NP15		middle Eocene		Smear slide	M	F												C												
1R-CC, 0–7	770.54	PAL	NP15		middle Eocene		Smear slide	P	F												R												
2R-1, 50–51	772.00	BIO	NP14		middle Eocene	early Eocene	Smear slide	M	F												F												
2R-3, 50–51	775.00	BIO	NP14		middle Eocene	early Eocene	Smear slide	M	F												C												
2R-CC, 22–25	776.09	PAL	NP13		early Eocene		Smear slide	M	F												C												
3R-1, 50–51	781.60	BIO	NP13		early Eocene		Smear slide	M	F																								
3R-3, 50–51	784.60	BIO	NP13		early Eocene		Smear slide	M	F												C												
3R-5, 51–52	787.61	BIO	NP13		early Eocene		Smear slide	M	F												F												
3R-CC, 18–22	788.10	PAL	NP13		early Eocene		Smear slide	M	F												C												
4R-1, 50–51	791.20	BIO	NP12		early Eocene		Smear slide	M	C												F												
4R-3, 50–51	794.20	BIO	NP12		early Eocene		Smear slide	M	F												C												
4R-CC, 20–23	796.80	PAL	NP12		early Eocene		Smear slide	M	F												F												
5R-1, 50–51	800.80	BIO	NP12		early Eocene		Smear slide	M	F												F												
5R-3, 50–51	803.80	BIO	NP12		early Eocene		Smear slide	M	F												C												
5R-CC, 13–16	805.59	PAL	NP12		early Eocene		Smear slide	M	F											R	F										R		
6R-1, 25–26	810.15	BIO	NP8		late Paleocene		Smear slide	M	F											R	F					R		F	F	F	R	R	
6R-1, 50–51	810.40	BIO	NP8		late Paleocene		Smear slide	M	F											R	C					R		F	C	C			R
6R-1, 58–59	810.48	BIO	NP8		late Paleocene		Smear slide	M	C											R	C				R	R		F	F	F	F	R	
6R-1, 79–80	810.69	BIO	NP7		late Paleocene		Smear slide	M	F											F	F	R	R	R	R	R		F	F	F	R	R	R
6R-1, 107–108	810.97	BIO	NP7		late Paleocene		Smear slide	M	F											R	C	R	R	R	R	R	R	F	F	F	R	R	
6R-2, 86–87	812.26	BIO	CC22	CC23	Campanian		Smear slide	M	R		F		R	R	F		R	C	R														
6R-3, 80–81	813.70	BIO	CC22	CC23	Campanian		Smear slide	M	R	R	R	R	R	R	C	R	F	C															

Notes: * = all smear slides were prepared at variable concentrations. Preservation: M = Moderate, P = poor. Abundance: C = common, F = few, R = rare. BIO = biostratigraphy, PAL = paleontology.

Table T3 (continued).

Core, section, interval (cm)	Depth (mbsf)	Sample code	Zone		Age		Preservation*	Preservation	Group abundance	Nannofossils																						
			From	To	From	To				*Toweius eminens*	*Fasciculithus involutus*	*Toweius eminens*	*Zygrhablithus bijugatus*	*Chiasmolithus consuetus*	*Heliolithus riedelii*	*Markalius inversus*	*Campylosphaera dela*	*Coccolithus formosus*	*Discoaster lodoensis*	*Toweius crassus*	*Tribrachiatus orthostylus*	*Chiasmolithus grandis*	*Coronocyclus nitescens*	*Ellipsolithus macellus*	*Sphenolithus radians*	*Clausicoccus fenestratus*	*Discoaster barbadiensis*	*Chiasmolithus solitus*	*Toweius gammation*	*Discoaster sublodoensis*	*Nannotetrina fulgens*	*Reticulofenestra dictyoda*
197-1204A-																																
1R-1, 50–51	762.40	BIO	NP15		middle Eocene		Smear slide	M	F				F			R		R				F	R				R	C				F
1R-3, 50–51	765.40	BIO	NP15		middle Eocene		Smear slide	M	C				F			R	R	F				R	R		R	R	R	C				F
1R-5, 49–50	768.39	BIO	NP15		middle Eocene		Smear slide	M	F				R					F				R			R	R	R	C			R	F
1R-CC, 0–7	770.54	PAL	NP15		middle Eocene		Smear slide	P	F				C			R	R	R				R	R		R		R	C	R		R	F
2R-1, 50–51	772.00	BIO	NP14		middle Eocene	early Eocene	Smear slide	M	F				F					R	R	R		R					R	F		R		
2R-3, 50–51	775.00	BIO	NP14		middle Eocene	early Eocene	Smear slide	M	F				F				R	R	F	R		R					R	F		R		
2R-CC, 22–25	776.09	PAL	NP13		early Eocene		Smear slide	M	F				F				R	R	F	R		R			R		R	F				
3R-1, 50–51	781.60	BIO	NP13		early Eocene		Smear slide	M	F				R				R	R	F	R		R			R							
3R-3, 50–51	784.60	BIO	NP13		early Eocene		Smear slide	M	F				R				R	R	F	F		R			R			F	R			
3R-5, 51–52	787.61	BIO	NP13		early Eocene		Smear slide	M	F				R			R	R		F	R							R	F				
3R-CC, 18–22	788.10	PAL	NP13		early Eocene		Smear slide	M	F				R				R	R	F	R			R		R	R		C	R			
4R-1, 50–51	791.20	BIO	NP12		early Eocene		Smear slide	M	C				R				R		F	R	R	R										
4R-3, 50–51	794.20	BIO	NP12		early Eocene		Smear slide	M	F				R			R	R	R	F	R	F		R		R	R	R					
4R-CC, 20–23	796.80	PAL	NP12		early Eocene		Smear slide	M	F				R				R		F	R	F	R										
5R-1, 50–51	800.80	BIO	NP12		early Eocene		Smear slide	M	F	R		R	R			R	R	R	F	R	F	R	R	R	R							
5R-3, 50–51	803.80	BIO	NP12		early Eocene		Smear slide	M	F	R		R	R				R	R	F	R	F	R										
5R-CC, 13–16	805.59	PAL	NP12		early Eocene		Smear slide	M	F	R		R	R	R		R	R	R	F	R	C											
6R-1, 25–26	810.15	BIO	NP8		late Paleocene		Smear slide	M	F	F		F			R	F																
6R-1, 50–51	810.40	BIO	NP8		late Paleocene		Smear slide	M	F	F	R	F	F	F		R																
6R-1, 58–59	810.48	BIO	NP 8		Late Paleocene		Smear slide	M	C	F		F	R	F	R	R																
6R-1, 79–80	810.69	BIO	NP 7		Late Paleocene		Smear slide	M	F	F	R	F	R																			
6R-1, 107–108	810.97	BIO	NP 7		Late Paleocene		Smear slide	M	F																							
6R-2, 86–87	812.26	BIO	CC22	CC23	Campanian		Smear slide	M	R																							
6R-3, 80–81	813.70	BIO	CC22	CC23	Campanian		Smear slide	M	R																							

Table T4. Summary of distribution and abundance of nannofossils and biozonal assignments, Hole 1204B.

Core, section, interval (cm)	Depth (mbsf)	Sample code	Zone		Age	Preparation*	Preservation	Group abundance	Nannofossils																		
			From	To	From				*Aspidolithus parcus* ssp. *parcus*	*Ceratolithoides aculeus*	*Cretarhabdus crenulatus*	*Cribrosphaerella ehrenbergii*	*Eiffellithus turriseiffelii*	*Marthasterites inconspicuus*	*Micula concava*	*Micula decussata*	*Pervilithus varius*	*Prediscosphaera cretacea*	*Quadrum gothicum*	*Quadrum sissinghii*	*Quadrum trifidum*	*Watznaueria barnesae*	*Tranolithus orionatus*	*Cretarhabdus conicus*	*Micula murus*	*Tegumentum stradneri*	*Micula swastica*
197-1204B-																											
1R-1, 5–6	810.75	BIO	CC25	CC26	Maastrichtian	Smear slide	P	C		C	F	F			C	C		R				C		R	R	R	R
1R-1, 10–11	810.80	BIO	CC25	CC26	Maastrichtian	Smear slide	P	C		C	R	F			F	C		R				C		R	R	R	
1R-1, 15–16	810.85	BIO	CC25	CC26	Maastrichtian	Smear slide	P	C		C		R			F	C						C					
1R-1, 31–32	811.01	BIO	CC25	CC26	Maastrichtian	Smear slide	P	C		C	R	F			F	C		R				C		R	R	R	
1R-2, 89–90	813.09	BIO	CC22	CC23	Campanian	Smear slide	M	F	R		R				R	R					R	R					
1R-3, 19–20	813.89	BIO	CC22	CC23	Campanian	Smear slide	M	F		R	R	R	R		R	R				R	R	R	R				
17R-3, 80–81	948.01	BIO	CC22	CC23	Campanian	Smear slide	M	F		R	R	R	R	R	R	R	R	R	R	R	R	F					
17R-3, 146–147	948.67	BIO				Smear slide																					

Notes: * = all smear slides were prepared at variable concentrations. Preservation: M = moderate, P = poor. Abundance: C = common, F = few, R = rare. BIO = biostratigraphy.

Table T5. Division, naming, and recovery of the basement units and subunits, Site 1204.

Core, section	Top depth (mbsf)	Unit/ Subunit	Unit name	Thickness (m)		Position of unit boundaries in core
				Curated	Calculated	
197-1204A-						
6R-5	815.60	1a, 1b	Volcaniclastic breccia	2.31	6.99	Top of Unit 1 (sediment–basement contact) is at Section 6R-5, 12 cm.
7R-2	820.95	2	Aphyric basalt (lobed)	19.78	35.49	Unit 1b/2 boundary is at the bottom of Section 7R-1.
			Total:	22.09	42.48	
197-1204B-						
1R-3	814.03	1	Aphyric basalt (lobed)	11.81	27.07	Top of Unit 1 (sediment–basement contact) is at Section 1R-3, 33 cm.
4R-2	841.10	2a	Aphyric basalt (lobed)	10.42	30.53	Unit 1/2a boundary is inferred to be at the top of Section 4R-2.
7R-3	872.42	2b	Diabase (massive)	19.48	46.22	Subunit 2a/2b boundary is at Section 7R-3, 125 cm.
14R-2	917.87	2c	Aphyric basalt (lobed)	3.94	17.35	Subunit 2b/2c boundary is at Section 14R-2, 85 cm.
16R-1	935.20	2d	Hyaloclastite lapilli breccia	3.90	9.70	Subunit 2c/2c boundary is at the top of Section 16R-1.
17R-1	944.90	3	Aphyric basalt (lobed)	2.33	2.33	Unit 2d/3 boundary is at the top of Section 17R-1.
17R-3	947.26	4a	Calcareous vitric sandstone	0.67	0.67	Unit 3/4 boundary is at Section 17R-3, 5 cm.
17R-3	947.93	4b	Calcareous vitric mudstone	0.55	0.55	Subunit 4a/4b boundary is at Section 17R-3, 78 cm.
17R-3	948.48	4c	Vitric-lithic breccia (grain flow?)	0.10	0.10	Subunit 4b/4c boundary is at Section 17R-3, 129 cm.
17R-3	948.58	4d	Calcareous vitric-lithic sandstone	0.08	6.32	Subunit 4c/4d boundary is at Section 17R-3, 139 cm.
			Total:	53.24	140.47	

Table T6. Lithologic components of the basement lava units, Hole 1240B. (See table notes. Continued on next page.)

Unit/ Subunit	Core, section	Depth (mbsf)	Unit name	Thickness (m)		Lobe margins		Grain size	Groundmass		Vesicularity (modal%)	Average vesicle size (mm)	Three-fold division	Segregation structures	Comments
				Curated	Cored	Simple	Glassy		Minerals	Texture					
	197-1204B-														
1	1R-3	814.03	Aphyric basalt	1.05	1.05	L (2)	x (2)	fg/ap/G	pl, px, oq		2–10	2	Ucr		Olivine microphenocrysts; pseudomorphed by carbonate or Fe oxyhydroxide throughout the succession
1	1R-4	814.75	Aphyric basalt	1.24	5.25	L (1)	x (1)	fg/ap/G	pl, px, oq		3	0.5	Mai/Lcr	PV	Olivine and plagioclase microphenocrysts
1	2R-1	820.30	Aphyric basalt	1.30	1.30	L (1)	x (1)	fg/ap/G	pl, ol, px, oq		2–10	1	Ucr/Mai	VC/HVS	Olivine and plagioclase microphenocrysts, part of upper vesicular crust and then massive interior of >5-m-thick lobe
1	2R-2	821.60	Aphyric basalt	1.34	1.34			fg	pl, ol, px, oq		2–10	1	Mai		Olivine and plagioclase microphenocrysts, massive interior of ~5-m-thick lobe
1	2R-3	822.93	Aphyric basalt	0.87	0.87			fg	pl, px	igr	0–3	2	Mai		Olivine and plagioclase microphenocrysts, massive interior of ~5-m-thick lobe
1	2R-4	823.80	Aphyric basalt	1.36	1.36			fg	pl, px	igr	0–3	1	Mai		Olivine and plagioclase microphenocrysts, massive interior of ~5-m-thick lobe.
1	2R-5	825.15	Aphyric basalt	1.50	1.50	L (1)	x (1)	fg/ap/G	pl, ol, px, oq	igr	0–25	3	Mai/Lcr		Olivine and plagioclase microphenocrysts; contains the massive interior of ~5-m-thick lobe
1	2R-6	826.67	Aphyric basalt	0.62	3.23	L (1)	x (1)	ap/fg/G	pl, px, oq	igr	4–15	2.0	Ucr/Mai		Olivine microphenocrysts; section may represent a single lobe
1	3R-1	829.90	Aphyric basalt	1.45	1.45	L (1)		fg	pl, ol, px, oq	igr	15–35	2.0			Olivine in groundmass (and as microphenocrysts); Sections 3R-1 and 3R-2 (<90 cm) may represent a single lobe (>2.4 m thick)
1	3R-2	831.35	Aphyric basalt	1.50	1.50	L (1)	x (1)	ap/G	pl, ol, px, oq	igr	5–20	1.5	Ucr/Mai/ Lcr	PV	Olivine in groundmass (and as microphenocrysts); Section 3R-2 (>90 cm) through Section 3R-3 is one lobe
1	3R-3	832.85	Aphyric basalt	0.30	6.75			ap	pl, ol, px, oq	igr	20.0	3.0			Olivine in groundmass (and as microphenocrysts)
1	4R-1	839.60	Aphyric basalt	1.50	1.50	L (5)	x (5)	fg/ap/G	pl, ol, px, oq	igr/ise-Va	2–30	3.0	Ucr/Mai/ Lcr	VC	Olivine in groundmass (and as microphenocrysts)
2a	4R-2	841.10	Aphyric basalt	1.50	1.50	L (4)	x (3)	fg/ap/G	pl, ol, px, oq	igr/ise-Va	5–35	2.0	Ucr/Mai/ Lcr	PV/VC	Olivine in groundmass (and as microphenocrysts)
2a	4R-3	842.60	Aphyric basalt	0.52	6.70	L (2)	x (2)	fg/ap/G	pl, ol, px, oq	igr/ise-Va	5–35	2.0			Olivine in groundmass (and as microphenocrysts)
2a	5R-1	849.30	Aphyric basalt	1.50	1.50	L (2)	x (1)	fg/ap/G	pl, ol, px, oq	igr/ise-Va	2–30	3.0			Olivine in groundmass (and as microphenocrysts)
2a	5R-2	850.80	Aphyric basalt	1.34	7.80	L (2–3)		fg	pl, ol, px, oq	igr	2–30	4.0	Ucr/Mai/ Lcr	VC	Olivine in groundmass (and as microphenocrysts)
2a	6R-1	858.60	Aphyric basalt	1.43	1.43	L (2–4)	x (1)	fg/ap/G	pl, ol, px, oq	igr	0–25	2.5	Ucr/Mai/ Lcr		Olivine in groundmass (and as microphenocrysts)
2a	6R-2	860.03	Aphyric basalt	1.50	1.50	L (3?)		fg	pl, ol, px, oq	igr	0–25	2.5	Ucr/Mai/ Lcr		Olivine in groundmass (and as microphenocrysts)
2a	6R-3	861.53	Aphyric basalt	1.50	1.50	L (6)	x (5)	fg/ap/G	pl, ol, px, oq	igr/ise-Va	0–15	3.0		VC	Olivine in groundmass (and as microphenocrysts); variolitic texture present near some lobe margins
2a	6R-4	863.03	Aphyric basalt	0.98	5.17	L (1)		fg/ap	pl, ol, px, oq	igr/ise-Va	20.0	1.0			Olivine in groundmass (and as microphenocrysts)
2a	7R-1	868.20	Aphyric basalt	1.49	1.49	L (2–3)		fg/ap	pl, ol, px	igr	5–15	1.5			
2a	7R-2	869.69	Aphyric basalt	1.48	1.48	L (2?)		fg/ap	pl, px, oq	igr/ise-Va	7–8	2.0		PV/VC	
2a	7R-3	871.17	Aphyric basalt	1.25	6.63	L		fg/ap	pl, ol, px, oq	igr/ise-Va	3–25	3.0	Ucr		This section contains the upper vesicular crust of Subunit 1b

Table T6 (continued).

Unit/ Subunit	Core, section	Depth (mbsf)	Unit name	Thickness (m)		Lobe margins		Grain size	Groundmass		Vesicularity (modal%)	Average vesicle size (mm)	Three-fold division	Segregation structures	Comments
				Curated	Cored	Simple	Glassy		Minerals	Texture					
2b	7R-3	872.42	Diabase	0.25	0.25	S		mg	pl, ol, px, oq	igr	3–25	3.0	Mai		
2b	8R-1	877.80	Diabase	1.50	1.50	S		mg	pl, ol, px, oq	oph	1–5	2.0	Mai		
2b	8R-2	879.30	Diabase	1.30	1.30	S		mg	pl, ol, px, oq	oph	1–4	2.0	Mai		
2b	8R-3	880.60	Diabase	1.32	6.25	S		mg	pl, ol, px, oq	oph	3–8	1.5	Mai		
2b	9R-1	887.10	Diabase	0.19	0.19	S		mg	pl, ol, px, oq	oph	1–5	1.5	Mai		
2b	9R-2	887.29	Diabase	1.40	1.40	S		mg		oph	1–5	1.5	Mai		
2b	9R-3	888.69	Diabase	1.34	0.11	S		mg	pl, ol, px	oph	2–5	1.0	Mai		
2b	10R-1	888.80	Diabase	1.50	1.50	S		mg	pl, ol, px	oph	1–8	2.0	Mai		
2b	10R-2	890.30	Diabase	1.25	1.25	S		mg	pl, ol, px	oph	5.0	1.0	Mai		
2b	10R-3	891.55	Diabase	0.81	0.81	S		mg	pl, ol, px, oq	oph	2–7	1.0	Mai		
2b	10R-4	892.36	Diabase	1.45	4.24	S		mg	pl, ol, px, oq	oph	3–7	2.0	Mai		
2b	11R-1	896.60	Diabase	1.45	1.45	S		mg	pl, ol, px	oph	5–7	1.0	Mai		
2b	11R-2	898.05	Diabase	0.62	8.25	S		mg	pl, ol, px, oq	oph	3–6	1.5	Mai		
2b	12R-1	906.30	Diabase	1.40	1.40	S		mg	pl, ol, px, oq	oph	4–7	2.0	Mai		
2b	12R-2	907.70	Diabase	0.24	0.60	S		mg	pl, ol, px, oq	oph	1.0	1.0	Mai		
2b	13R-1	908.30	Diabase	1.47	1.47	S		fg	pl, ol, px	igr	3–8	1	Mai		
2b	13R-2	909.77	Diabase	1.39	1.39	S		fg	pl, ol, px	igr	1–10	0.5	Mai		
2b	13R-3	911.16	Diabase	1.17	1.17	S		fg	pl, px, oq	igr	5–8	2.0	Mai		
2b	13R-4	912.33	Diabase	0.91	3.57	S		fg/mg	pl, px, clay	igr	?	0.5	Mai		
2b	14R-1	915.90	Diabase	1.12	1.12	S		fg	pl, ol, px	igr	0–5	0.5	Mai	VC	Top of the basal crust for Subunit 1b
2b	14R-2	917.02	Diabase	0.85	0.85	S		fg/ap	pl, ol?, px	Va	1–10	2.0	Mai/Lcr	PV/VC	VCs contain spinifex-textured pyroxene; groundmass has high abundance of interstitial clay (after glass?)
2c	14R-2	917.87	Aphyric basalt (lobed)	0.65	0.65	L (1)	x (2)	ap	pl, px, ol	Va	1–20	1.5	Mai	VC	VCs contain spinifex-textured pyroxene
2c	14R-3	918.32	Aphyric basalt (lobed)	1.28	7.08	L (1)	x (1)	fg/ap/G	pl, ol, px, oq		2–25	2.0	Mai	PV	
2c	15R-1	925.60	Aphyric basalt (lobed)	1.44	1.44	L (2)	x (1)	fg/ap/G	pl, ol, px, oq	Va	5–30	2.5		PV/VC	VCs contain spinifex-textured pyroxene
2c	15R-2	927.04	Aphyric basalt (lobed)	1.50	1.50	L (3?)	x (1)	fg/ap/G	pl, px, oq	igr/ise	5–30	3.0			VCs contain spinifex-textured pyroxene
2c	15R-3	928.54	Aphyric basalt (lobed)	0.88	6.66	L (3)	x (2)	fg/ap/G	pl, px, oq		5–30	3.0			
2d	16R-1	935.20	Hyaloclastite lapilli breccia	5.10	9.70										The lapilli breccia contains centimeter-sized fragments of small lobes (toes) enveloped by glassy selvage
3	17R-1	944.90	Aphyric basalt (lobed)	1.18	1.18	L (2)	x (1)	fg/ap/G	pl, ol, px, oq		5–25?	1.5	Ucr/Mai		
3	17R-2	946.08	Aphyric basalt (lobed)	1.10	1.10	L (3)	x (4)	fg/ap/G	pl, ol, px, oq		20–25	2.0			
3	17R-3	947.21	Aphyric basalt (lobed)	0.05	0.05	L	x (1)	fg/ap/G	pl, ol, px, oq		20.0	3.0	Lcr	PV	Basal contact of unit; conformable, glassy lobe margins in direct contact with underlying sediment
4a-4d	17R-3	947.26	Clastic sediments	1.40	7.30										

Notes: L = lobe margins present within the section (number in parenthesis indicates number of lobes), S = simple lava in the sense that the section contains lava that is a part of a larger lobe, x = smooth-surfaced glassy lobe margins. Grain size: fg = fine grained, ap = aphanitic, G = glassy selvage (lobe margins), mg = medium grained. Groundmass minerals: pl = plagioclase, px = pyroxene, oq = opaque, ol = olivine. Groundmass texture: igr = intergranular, ise = intersertal, Va = variolitic, oph = subophitic to ophitic. Three-fold division: Ucr = upper crust, Mai = massive lob interior, Lcr = lower crust. PV = pipe vesicles, VC = vesicle cylinders, HVS = horizontal vesicle sheet.

Table T7. Whole-rock major and trace element abundances in basalts determined by ICP-AES, Site 1204. (Continued on next page.)

Hole:	1204A					1204B								
Core, section:	7R-3	9R-1	9R-2	10R-2	10R-3	2R-2	2R-4	4R-3	6R-4	7R-2	7R-3	7R-3	8R-3	9R-2
Interval (cm):	36–37	96–97	50–51	77–79	54–56	48–50	87–89	29–31	21–24	66–69	42–44	140–142	53–55	22–24
Piece:	3	12B	5	5	2	1B	2B	5	4	10	5A	17	8	1B
Unit/Subunit:	2	2	2	2	2	1	1	2a	2a	2a	2a	2b	2b	2b
Rock type:	Aphyric basalt (lobed)	Aphyric basalt (lobed)	Aphyric basalt (lobed)	Aphyric basalt (lobed)	Aphyric basalt (lobed)	Aphyric basalt (lobed)	Aphyric basalt (lobed)	Aphyric basalt (lobed)	Aphyric basalt (lobed)	Aphyric basalt (lobed)	Aphyric basalt (lobed)	Diabase (massive)	Diabase (massive)	Diabase (massive)
Depth (mbsf):	822.68	839.56	840.60	850.54	851.45	822.08	824.67	842.89	863.24	870.33	871.6	872.57	881.29	887.51
Major element oxide (wt%):														
SiO_2	38.39	43.76	43.76	45.62	45.37	43.60	45.44	43.57	39.86	41.38	44.34	43.67	45.98	45.64
TiO_2	2.03	2.15	1.98	2.31	2.12	2.30	2.54	2.37	2.26	2.25	2.32	2.26	1.95	2.17
Al_2O_3	13.63	14.89	14.75	14.69	15.36	16.33	17.44	16.89	13.81	14.43	14.90	14.65	15.16	15.23
Fe_2O_3	10.51	16.07	12.74	14.46	13.84	12.52	15.44	15.02	11.43	12.15	12.30	11.20	14.07	13.77
MnO	0.14	0.20	0.18	0.18	0.14	0.14	0.19	0.23	0.12	0.16	0.20	0.18	0.17	0.15
MgO	3.21	4.62	4.97	6.80	9.31	2.31	2.19	2.10	2.91	3.43	4.98	4.49	7.07	8.55
CaO	19.41	11.69	12.81	10.03	7.43	12.86	9.72	9.58	16.70	15.04	13.34	15.46	9.00	9.08
Na_2O	2.82	3.07	2.96	3.05	3.16	3.32	3.47	2.83	2.95	3.14	2.98	2.95	2.62	3.15
K_2O	0.95	0.84	1.02	0.96	0.41	1.43	1.20	1.57	0.86	1.05	1.30	1.04	1.24	0.38
P_2O_5	0.36	0.30	0.24	0.29	0.25	0.28	0.74	1.92	0.37	0.42	0.30	0.26	0.21	0.24
Totals:	91.43	97.60	95.41	98.40	97.39	95.10	98.37	96.08	91.27	93.45	96.96	96.15	97.46	98.34
LOI	9.48	3.63	4.98	3.15	3.62	3.75	1.93	4.17	7.81	5.56	4.25	5.69	3.20	3.19
Mg#	0.40	0.39	0.46	0.51	0.60	0.29	0.24	0.24	0.36	0.38	0.47	0.47	0.52	0.58
Trace element (ppm):														
Sr	243	244	227	203	198	275	300	333	242	243	248	237	191	200
Ba	68.9	82.9	70.8	81.2	61.9	83.4	118	130	73.5	80.7	86.7	77.6	64.2	58.2
Sc	38.6	40.3	40.9	43.8	34.8	39.0	47.4	41.7	43.2	41.9	46.0	42.3	39.4	40.9
V	342	366	335	362	323	347	440	317	359	370	357	362	341	329
Cr	179	158	171	165	158	147	166	156	173	148	166	168	171	175
Co	59.7	42.7	50.0	46.1	53.9	46.0	55.4	65.2	40.2	45.1	59.7	57.7	43.7	50.6
Ni	39.8	64.1	51.5	65.9	79.6	40.8	57.7	55.4	10.1	36.7	81.4	77.8	124	90.5
Cu	78.1	90.3	85.3	96.4	94.7	119	107	120	88.0	90.9	97.5	95.8	94.1	98.4
Zn	93.4	108	108	102	110	115	143	144	123	123	155	132	169	108
Y	35.5	45.5	33.3	39.0	35.1	40.0	42.9	50.7	38.5	42.9	40.9	35.5	28.8	34.6
Zr	145	159	134	165	148	161	171	168	160	164	156	143	120	145

Notes: LOI = loss on ignition at 1025°C for 4 hrs. Mg# = MgO/(MgO+FeO), in molar percent, with FeO calculated (as 90% of total Fe). In all figures these data are renormalized to 100% to correct for variable LOI. This table is also available in ASCII.

Table T7 (continued).

Hole:	1204B						
Core, section:	10R-3	13R-2	13R-3	14R-2	14R-3	15R-1	17R-1
Interval (cm):	25–27	10–12	32–34	115–117	68–70	131–133	89–90
Piece:	2A	1	1A	5	14	9	13
Unit/Subunit:	2b	2b	2b	2c	2c	2c	3
Rock type:	Diabase (massive)	Diabase (massive)	Diabase (massive)	Aphyric basalt (lobed)	Aphyric basalt (lobed)	Aphyric basalt (lobed)	Aphyric basalt (lobed)
Depth (mbsf):	891.80	909.87	911.48	918.17	919.20	926.91	945.79
Major element oxide (wt%):							
SiO_2	43.43	44.97	46.47	44.75	45.48	45.20	46.06
TiO_2	2.14	2.23	2.28	2.26	2.06	2.17	2.52
Al_2O_3	15.41	14.62	14.29	15.73	15.70	15.33	14.01
Fe_2O_3	13.31	13.79	13.93	12.98	12.21	13.60	14.23
MnO	0.20	0.18	0.17	0.13	0.11	0.19	0.17
MgO	7.28	5.05	8.36	4.23	5.22	5.99	5.12
CaO	10.42	10.83	7.01	10.07	10.42	9.29	10.49
Na_2O	3.02	2.85	3.15	3.13	3.03	2.90	2.88
K_2O	0.81	1.10	0.55	1.27	1.12	1.08	1.14
P_2O_5	0.26	0.29	0.26	0.78	0.37	0.33	0.34
Totals:	96.29	95.92	96.49	95.33	95.73	96.06	96.95
LOI	3.24	4.48	3.71	4.16	4.69	3.98	2.84
Mg#	0.55	0.45	0.57	0.42	0.48	0.49	0.44
Trace element (ppm):							
Sr	203	214	180	264	237	212	219
Ba	79.0	74.8	66.1	90.0	62.1	79.3	79.6
Sc	40.5	41.9	40.9	41.1	38.2	40.5	46.3
V	328	335	339	317	280	333	355
Cr	174	151	152	148	149	169	154
Co	60.0	46.6	47.1	48.6	41.4	57.6	70.7
Ni	97.1	56.9	48.3	48.2	46.4	138	64.1
Cu	110	94.8	97.4	88.0	82.6	90.5	99.7
Zn	111	120	90.5	165	187	178	233
Y	34.3	39.2	33.4	39.8	32.7	35.3	43.7
Zr	152	153	158	156	142	146	177

Table T8. Petrographic summary of the opaque mineralogy of basement rocks, Site 1204.

Basalt unit/ subunit	Core, section, piece, interval (cm)	Size (µm)	Titanomagnetite description	Other opaque minerals	Photomicrograph
	197-1204A-				
2	7R-3 (Piece 3, 36–37)	≤200	~50% altered; maghemite rims on all crystals, but many have relict centers	Goethite is present; Fe oxyhydroxide is pervasive; no sulfide	1204A-106
2	9R-1 (Piece 12B, 96–97)	≤200	~50% altered; maghemite rims on all crystals, but many have relict centers	Goethite is pervasive; no sulfide	1204A-113, 1204A-147
2	9R-2 (Piece 5, 50–51)	≤500	Almost completely replaced by maghemite; rare, small (≤10 µm) relict Ti-Mag centers are present; maghemite is exsolving ulvöspinel	Goethite is pervasive; no sulfide	1204A-114, 1204A-115, 1204A-125
2	10R-2 (Piece 5, 77–79)	≤250	Almost completely replaced by maghemite; rare, small (≤10 µm) relict Ti-Mag centers are present	Goethite is pervasive; no sulfide	1204A-155
2	10R-3 (Piece 2, 54–56)	≤600	Unaltered	Secondary pyrite; no goethite or Fe oxyhydroxide	
	197-1204B-				
1	2R-2 (Piece1B, 48–50)	5–20	Highly altered to maghemite; only larger crystals have relict Ti-Mag centers	Goethite is poorly developed; Fe oxyhydroxide is pervasive; no sulfide	1204A-134
1	2R-4 (Piece 1, 16–19)	≤150	Almost completely replaced by maghemite; rare, small (≤10 µm) relict Ti-Mag centers are present; maghemite is exsolving ulvöspinel	Goethite is present; Fe oxyhydroxide is pervasive; no sulfide	
1	2R-4 (Piece 2, 87–89)	≤40	~50% altered; maghemite rims on all crystals, but many have relict centers	Goethite is pervasive; no sulfide	1204A-148
2a	4R-3 (Piece 5, 29–31)	≤20	Contains maghemite rims; ilmenite oxidation lamellae are present	Goethite is poorly developed; Fe oxyhydroxide is pervasive; no sulfide	
2a	6R-4 (Piece 4, 21–24)	≤120	~50% altered; maghemite rims and many crystals have relict centers	Goethite is poorly developed; Fe oxyhydroxide is pervasive; no sulfide	1204A-149
2a	7R-2 (Piece 16A, 129–131)	≤100	~70% altered; maghemite is pervasive, but a few crystals have relict centers	Goethite is poorly developed; Fe oxyhydroxide is pervasive; no sulfide	1204A-151
2a	7R-3 (Piece 13, 106–108)	≤600	Highly altered to maghemite; only larger crystals have relict Ti-Mag centers	Goethite is poorly developed; Fe oxyhydroxide is pervasive; no sulfide	1204A-152
2b	7R-3 (Piece 17, 140–142)	≤300	Highly altered to maghemite, but many crystals have relict Ti-Mag centers	Goethite is pervasive; no sulfide.	1204A-152
2b	8R-3 (Piece 8, 53–55)	≤800	Highly altered to maghemite; only larger crystals have relict Ti-Mag centers	Goethite is present; Fe oxyhydroxide is pervasive; no sulfide	1204A-137, 1204A-141
2b	9R-2 (Piece 1B, 22–24)	≤1000	Unaltered	Secondary pyrite; no goethite or Fe oxyhydroxide	1204A-153
2b	10R-3 (Piece 2A, 25–27)	≤700	Almost completely replaced by maghemite; rare, small (≤10 µm) relict Ti-Mag centers are present; maghemite is exsolving ulvöspinel	Goethite is pervasive; no sulfide	1204A-142, 1204A-143, 1204A-144
2b	12R-1 (Piece 4A, 28–30)	≤300	Almost completely replaced by maghemite; rare relict Ti-Mag areas parallel to cleavage planes are present	Section contains a vein of goethite; goethite is pervasive in the groundmass; no sulfide	1204A-145, 1204A-146
2b	13R-2 (Piece 1, 10–12)	≤400	Highly altered to maghemite; only larger crystals have relict Ti-Mag centers	Goethite is pervasive; no sulfide	1204A-154
2b	13R-3 (Piece 1A, 32–34)	≤250	Unaltered	Secondary pyrite; no goethite or Fe oxyhydroxide	
2c	14R-2 (Piece 5, 115–117)	≤60	Almost completely replaced by maghemite; rare, small (≤10 µm) relict Ti-Mag centers are present; the majority of crystals are ≤10 µm	Goethite is poorly developed; Fe oxyhydroxide is pervasive; no sulfide	
2c	14R-3 (Piece 14, 68–70)	≤100	Completely altered to maghemite; the majority of crystals are ≤10 µm	Goethite is present; Fe oxyhydroxide is pervasive; no sulfide.	
2c	15R-1 (Piece 9, 131–133)	≤50	~50% altered; maghemite rims on all crystals, but many have relict centers	Goethite is poorly developed; Fe oxyhydroxide is pervasive; no sulfide	1204A-162
3	17R-1 (Piece 13, 89–90)	≤50	Highly altered to maghemite; only larger crystals have relict Ti-Mag centers; the majority of the crystals are ≤10 µm	Goethite is poorly developed; Fe oxyhydroxide is pervasive; no sulfide	

Table T9. Summary of rock magnetic parameters for basalt samples, Site 1204.

Core, section interval (cm)	M_{rs} (A/m)	H_{cr} (mT)	MDF_{ARM} (mT)	MDF_{SIRM} (mT)
197-1204A-				
7R-2, 78–80	261.4	26.4	14.7	20.4
8R-2, 132–134	259.2	26.2	18.3	21.7
9R-3, 77–79	365.0	12.5	14.7	11.2
10R-1, 125–127	118.3	31.5	20.3	26.1
10R-4, 138–140	296.4	6.0	5.7	3.7
197-1204B-				
2R-4, 100–102	203.3	25.9	11.8	17.6
3R-1, 38–40	186.7	21.4	18.0	16.3
4R-2, 63–65	170.9	34.5	23.9	29.2
8R-3, 88–90	157.4	22.4	14.8	18.0
9R-2, 8–10	311.2	6.2	5.6	4.1
10R-2, 18–20	165.8	33.7	17.7	27.1
13R-3, 33–35	378.5	5.6	5.9	4.0
14R-1, 14–16	304.4	4.6	5.6	3.9
15R-1, 11–13	115.0	24.4	21.0	20.0

Note: M_{rs} = saturation remanent magnetization, H_{cr} = coercivity of remanence, MDF = median destructive field, ARM = anyhsteretic remanent magnetization, SIRM = saturation isothermal remanent magnetization.

Table T10. Shipboard characteristic remanent magnetization inclination averages and summary statistics based on principal component analyses of alternating-field demagnetization data, Site 1204.

Hole	Basalt unit/ subunit	*N*	Point inc (°)	Inc_{95} (°)	*k*
197-1204A-					
	1	9	55.5	7.5	50.0
197-1204B-					
	1	7	56.0	11.7	31.1
	2a	8	67.2	17.5	12.3
	2b	16	58.4	6.0	37.1
	2c	4	55.7	12.2	97.1
	2d	2	60.3	—	506.3
	3	2	54.3	—	2272.1
	Average:	6	58.9	6.1	148.2

Notes: Estimate of dispersion (*S*), based on the transformation of Cox (1970) = 8.4. *N* = number of determinations within each unit. Point inc = estimation of the inclination mean based on the averaging method of McFadden and Reid (1982). Inc_{95} = estimation of 95% confidence interval of inclination. *k* = estimate of precision parameter. — = not applicable. *N* for "Average" values is the estimated number of independent time units (see text).

Table T11. Magnetic susceptibility measurements, Site 1204.

Core, section, interval (cm)	Depth (mbsf)	Magnetic susceptibility (10^{-6} SI)	Corrected susceptibility (10^{-6} SI)
197-1204A-			
1R-1, 5	761.95	115.4	115.43
1R-1, 10	762.00	372.2	372.25
1R-1, 15	762.05	217.8	217.87
1R-1, 20	762.10	115.4	115.49
1R-1, 25	762.15	94.8	94.92
1R-1, 30	762.20	76.4	76.54
1R-1, 35	762.25	74.4	74.56
1R-1, 40	762.30	92.0	92.19
1R-1, 45	762.35	200.0	200.21
1R-1, 50	762.40	52.2	52.43
1R-1, 55	762.45	31.0	31.26
1R-1, 60	762.50	34.0	34.30
1R-1, 65	762.55	28.2	28.54
1R-1, 70	762.60	26.6	26.98
1R-1, 75	762.65	33.2	33.62
1R-1, 80	762.70	35.0	35.46
1R-1, 85	762.75	28.8	29.30
1R-1, 90	762.80	28.6	29.14
1R-1, 95	762.85	24.0	24.58
1R-1, 100	762.90	25.4	26.03
1R-1, 105	762.95	24.4	25.07
1R-1, 110	763.00	28.0	28.71
1R-1, 115	763.05	20.8	21.55
1R-1, 120	763.10	19.0	19.79
1R-1, 125	763.15	24.0	24.87
1R-1, 130	763.20	32.6	33.51
1R-1, 135	763.25	47.0	47.99
1R-1, 140	763.30	37.8	38.84
1R-2, 5	763.45	45.6	45.61
1R-2, 10	763.50	62.2	62.21
1R-2, 15	763.55	41.0	41.02
1R-2, 20	763.60	36.4	36.43
1R-2, 25	763.65	45.0	45.03
1R-2, 30	763.70	48.2	48.24
1R-2, 35	763.75	43.4	43.44
1R-2, 40	763.80	45.0	45.05
1R-2, 45	763.85	14.2	14.26
1R-2, 50	763.90	10.8	10.86
1R-2, 55	763.95	18.6	18.67
1R-2, 60	764.00	20.6	20.68
1R-2, 65	764.05	22.0	22.09
1R-2, 70	764.10	22.2	22.30
1R-2, 75	764.15	20.8	20.91
1R-2, 80	764.20	17.8	17.93
1R-2, 85	764.25	17.6	17.74
1R-2, 90	764.30	28.0	28.15
1R-2, 95	764.35	55.2	55.36
1R-2, 100	764.40	21.8	21.97
1R-2, 105	764.45	13.0	13.18
1R-2, 110	764.50	8.2	8.39
1R-2, 115	764.55	5.6	5.80
1R-2, 120	764.60	6.4	6.62
1R-2, 125	764.65	12.2	12.44
1R-2, 130	764.70	43.8	44.05
1R-2, 135	764.75	40.6	40.87
1R-2, 140	764.80	50.0	50.28
1R-3, 5	764.95	27.0	27.01
1R-3, 10	765.00	36.2	36.22
1R-3, 15	765.05	35.6	35.63
1R-3, 20	765.10	29.8	29.84
1R-3, 25	765.15	18.0	18.05
1R-3, 30	765.20	12.6	12.66
1R-3, 35	765.25	12.2	12.27
1R-3, 40	765.30	12.2	12.28
1R-3, 45	765.35	14.2	14.29
1R-3, 50	765.40	18.8	18.90
1R-3, 55	765.45	27.2	27.31
1R-3, 60	765.50	35.2	35.33
1R-3, 65	765.55	30.0	30.15
1R-3, 70	765.60	19.4	19.56
1R-3, 75	765.65	10.2	10.38
1R-3, 80	765.70	7.2	7.40
1R-3, 85	765.75	21.0	21.22
1R-3, 90	765.80	37.6	37.83
1R-3, 95	765.85	54.2	54.45
1R-3, 100	765.90	85.2	85.47
1R-3, 105	765.95	40.8	41.09
1R-3, 110	766.00	55.4	55.71
1R-3, 115	766.05	109.2	109.52
1R-3, 120	766.10	72.0	72.34
1R-3, 125	766.15	25.0	25.38
1R-3, 130	766.20	16.0	16.39
1R-3, 135	766.25	16.0	16.43
1R-3, 140	766.30	17.6	18.05
1R-3, 145	766.35	25.4	25.88
1R-4, 5	766.45	72.8	72.82
1R-4, 10	766.50	132.4	132.43
1R-4, 15	766.55	129.0	129.04
1R-4, 20	766.60	58.2	58.26
1R-4, 25	766.65	48.2	48.27
1R-4, 30	766.70	58.0	58.08
1R-4, 35	766.75	28.2	28.30
1R-4, 40	766.80	20.4	20.51
1R-4, 45	766.85	21.4	21.53
1R-4, 50	766.90	29.6	29.74
1R-4, 55	766.95	48.2	48.35
1R-4, 60	767.00	71.4	71.58
1R-4, 65	767.05	36.6	36.80
1R-4, 70	767.10	21.8	22.03
1R-4, 75	767.15	18.8	19.05
1R-4, 80	767.20	21.0	21.28
1R-4, 85	767.25	22.0	22.30
1R-4, 90	767.30	30.4	30.73
1R-4, 95	767.35	33.8	34.15
1R-4, 100	767.40	37.2	37.58
1R-4, 105	767.45	70.8	71.20
1R-4, 110	767.50	37.8	38.23
1R-4, 115	767.55	22.6	23.05
1R-4, 120	767.60	17.4	17.88
1R-4, 125	767.65	16.2	16.73
1R-4, 130	767.70	20.0	20.55
1R-4, 135	767.75	39.2	39.80
1R-4, 140	767.80	46.6	47.23
1R-4, 145	767.85	72.4	73.07
1R-5, 5	767.95	46.4	46.41
1R-5, 10	768.00	30.4	30.41
1R-5, 15	768.05	25.8	25.82
1R-5, 20	768.10	24.6	24.62
1R-5, 25	768.15	25.0	25.03
1R-5, 30	768.20	35.4	35.44
1R-5, 35	768.25	33.8	33.84
1R-5, 40	768.30	25.8	25.85
1R-5, 45	768.35	22.0	22.05
1R-5, 50	768.40	21.0	21.06
1R-5, 55	768.45	28.8	28.87
1R-5, 60	768.50	50.2	50.28
1R-5, 65	768.55	90.0	90.09
1R-5, 70	768.60	85.2	85.30
1R-5, 75	768.65	45.2	45.31
1R-5, 80	768.70	30.0	30.12
1R-5, 85	768.75	23.4	23.53
1R-5, 90	768.80	26.0	26.14

Note: Only a portion of this table appears here. The complete table is available in ASCII.

Table T12. GRA bulk density measurements, Site 1204.

Core, section, interval (cm)	Depth (mbsf)	Density (g/cm^3)
197-1204A-		
1R-1, 5	761.95	1.406
1R-1, 10	762.00	1.972
1R-1, 15	762.05	2.026
1R-1, 20	762.10	2.062
1R-1, 25	762.15	2.042
1R-1, 30	762.20	1.972
1R-1, 35	762.25	1.895
1R-1, 40	762.30	1.865
1R-1, 45	762.35	1.829
1R-1, 50	762.40	1.859
1R-1, 55	762.45	1.879
1R-1, 60	762.50	1.939
1R-1, 65	762.55	1.909
1R-1, 70	762.60	1.855
1R-1, 75	762.65	1.849
1R-1, 80	762.70	1.814
1R-1, 85	762.75	1.874
1R-1, 90	762.80	1.955
1R-1, 95	762.85	1.908
1R-1, 100	762.90	1.932
1R-1, 105	762.95	1.938
1R-1, 110	763.00	1.903
1R-1, 115	763.05	1.898
1R-1, 120	763.10	1.893
1R-1, 125	763.15	1.866
1R-1, 130	763.20	1.849
1R-1, 135	763.25	1.964
1R-1, 140	763.30	1.947
1R-2, 5	763.45	1.903
1R-2, 10	763.50	1.920
1R-2, 15	763.55	1.953
1R-2, 20	763.60	1.934
1R-2, 25	763.65	1.950
1R-2, 30	763.70	1.906
1R-2, 35	763.75	1.920
1R-2, 40	763.80	2.012
1R-2, 45	763.85	2.013
1R-2, 50	763.90	1.862
1R-2, 55	763.95	1.887
1R-2, 60	764.00	1.897
1R-2, 65	764.05	1.928
1R-2, 70	764.10	1.924
1R-2, 75	764.15	1.918
1R-2, 80	764.20	1.918
1R-2, 85	764.25	1.863
1R-2, 90	764.30	1.838
1R-2, 95	764.35	2.028
1R-2, 100	764.40	1.882
1R-2, 105	764.45	1.840
1R-2, 110	764.50	1.849
1R-2, 115	764.55	1.855
1R-2, 120	764.60	1.855
1R-2, 125	764.65	1.813
1R-2, 130	764.70	2.055
1R-2, 135	764.75	1.948
1R-2, 140	764.80	1.923
1R-3, 5	764.95	1.949
1R-3, 10	765.00	1.963
1R-3, 15	765.05	1.924
1R-3, 20	765.10	1.929
1R-3, 25	765.15	1.839
1R-3, 30	765.20	1.852
1R-3, 35	765.25	1.918
1R-3, 40	765.30	1.848
1R-3, 45	765.35	1.848
1R-3, 50	765.40	1.920
1R-3, 55	765.45	1.911
1R-3, 60	765.50	1.933
1R-3, 65	765.55	1.945
1R-3, 70	765.60	1.984
1R-3, 75	765.65	1.985
1R-3, 80	765.70	1.691
1R-3, 85	765.75	1.942
1R-3, 90	765.80	2.003
1R-3, 95	765.85	2.030
1R-3, 100	765.90	1.956
1R-3, 105	765.95	1.897
1R-3, 110	766.00	1.881
1R-3, 115	766.05	2.003
1R-3, 120	766.10	2.033
1R-3, 125	766.15	1.894
1R-3, 130	766.20	1.874
1R-3, 135	766.25	1.701
1R-3, 140	766.30	1.827
1R-3, 145	766.35	1.881
1R-4, 5	766.45	2.000
1R-4, 10	766.50	2.069
1R-4, 15	766.55	2.062
1R-4, 20	766.60	2.020
1R-4, 25	766.65	1.911
1R-4, 30	766.70	2.010
1R-4, 35	766.75	1.898
1R-4, 40	766.80	1.890
1R-4, 45	766.85	1.801
1R-4, 50	766.90	1.903
1R-4, 55	766.95	1.894
1R-4, 60	767.00	1.983
1R-4, 65	767.05	1.870
1R-4, 70	767.10	1.874
1R-4, 75	767.15	1.865
1R-4, 80	767.20	1.839
1R-4, 85	767.25	1.883
1R-4, 90	767.30	1.935
1R-4, 95	767.35	1.880
1R-4, 100	767.40	1.923
1R-4, 105	767.45	2.107
1R-4, 110	767.50	1.959
1R-4, 115	767.55	1.925
1R-4, 120	767.60	1.802
1R-4, 125	767.65	1.834
1R-4, 130	767.70	1.817
1R-4, 135	767.75	1.948
1R-4, 140	767.80	1.931
1R-4, 145	767.85	1.895
1R-5, 5	767.95	1.969
1R-5, 10	768.00	1.880
1R-5, 15	768.05	1.862
1R-5, 20	768.10	1.905
1R-5, 25	768.15	1.890
1R-5, 30	768.20	1.922
1R-5, 35	768.25	1.896
1R-5, 40	768.30	1.913
1R-5, 45	768.35	1.896
1R-5, 50	768.40	1.860
1R-5, 55	768.45	1.909
1R-5, 60	768.50	1.994
1R-5, 65	768.55	1.887
1R-5, 70	768.60	2.001
1R-5, 75	768.65	1.950
1R-5, 80	768.70	1.835
1R-5, 85	768.75	1.895
1R-5, 90	768.80	1.872
1R-5, 95	768.85	1.875
1R-5, 100	768.90	1.877
1R-5, 105	768.95	1.986
1R-5, 110	769.00	1.950
1R-5, 115	769.05	1.975
1R-5, 120	769.10	1.871
1R-5, 125	769.15	1.916
1R-5, 130	769.20	2.037
1R-5, 135	769.25	1.902
1R-5, 140	769.30	1.781
1R-5, 145	769.35	1.710
1R-6, 5	769.45	2.201
1R-6, 10	769.50	2.132
1R-6, 15	769.55	2.128
1R-6, 20	769.60	2.098
1R-6, 25	769.65	2.131
1R-6, 30	769.70	2.127
1R-6, 35	769.75	2.227
1R-6, 40	769.80	2.334
1R-6, 45	769.85	1.991
1R-6, 50	769.90	1.856
1R-6, 55	769.95	2.346
1R-6, 60	770.00	2.179
1R-6, 65	770.05	2.167
1R-6, 70	770.10	2.054
1R-6, 75	770.15	2.333
1R-6, 80	770.20	2.242
1R-6, 85	770.25	2.138
1R-6, 90	770.30	2.176
1R-6, 95	770.35	2.161
1R-6, 100	770.40	2.184
1R-6, 105	770.45	2.189
2R-1, 5	771.55	1.937
2R-1, 10	771.60	1.932
2R-1, 15	771.65	1.923
2R-1, 20	771.70	1.935
2R-1, 25	771.75	1.979
2R-1, 30	771.80	1.869
2R-1, 35	771.85	1.852
2R-1, 40	771.90	2.013
2R-1, 45	771.95	1.897
2R-1, 50	772.00	2.023
2R-1, 55	772.05	2.053
2R-1, 60	772.10	2.045
2R-1, 65	772.15	1.952
2R-1, 70	772.20	1.996
2R-1, 75	772.25	1.956
2R-1, 80	772.30	1.908
2R-1, 85	772.35	1.885
2R-1, 90	772.40	1.948
2R-1, 95	772.45	1.941
2R-1, 100	772.50	1.936
2R-1, 105	772.55	1.974
2R-1, 110	772.60	1.921
2R-1, 115	772.65	1.858
2R-1, 120	772.70	1.857
2R-1, 125	772.75	1.881
2R-1, 130	772.80	1.980
2R-1, 135	772.85	1.932
2R-1, 140	772.90	2.020
2R-2, 5	773.05	2.163
2R-2, 10	773.10	2.138
2R-2, 15	773.15	2.072
2R-2, 20	773.20	2.154
2R-2, 25	773.25	1.970
2R-2, 30	773.30	1.986
2R-2, 35	773.35	2.028
2R-2, 40	773.40	2.038
2R-2, 45	773.45	1.997
2R-2, 50	773.50	2.058

Note: Only a portion of this table appears here. The complete table is available in ASCII.

Table T13. Natural gamma ray measurements, Site 1204.

Core, section, interval (cm)	Depth (mbsf)	Total counts (cps)
197-1204A-		
1R-1, 10	762.0	18.25
1R-1, 20	762.1	16.75
1R-1, 30	762.2	14.60
1R-1, 40	762.3	14.90
1R-1, 50	762.4	13.60
1R-1, 60	762.5	14.35
1R-1, 70	762.6	14.75
1R-1, 80	762.7	13.15
1R-1, 90	762.8	12.85
1R-1, 100	762.9	13.90
1R-1, 110	763.0	13.25
1R-1, 120	763.1	14.35
1R-1, 130	763.2	13.50
1R-2, 10	763.5	14.25
1R-2, 20	763.6	13.70
1R-2, 30	763.7	14.25
1R-2, 40	763.8	14.05
1R-2, 50	763.9	13.10
1R-2, 60	764.0	14.40
1R-2, 70	764.1	14.20
1R-2, 80	764.2	13.15
1R-2, 90	764.3	14.60
1R-2, 100	764.4	13.70
1R-2, 110	764.5	16.95
1R-2, 120	764.6	13.15
1R-2, 130	764.7	12.75
1R-3, 10	765.0	16.05
1R-3, 20	765.1	14.05
1R-3, 30	765.2	13.95
1R-3, 40	765.3	13.80
1R-3, 50	765.4	12.70
1R-3, 60	765.5	12.60
1R-3, 70	765.6	14.00
1R-3, 80	765.7	12.65
1R-3, 90	765.8	14.65
1R-3, 100	765.9	15.75
1R-3, 110	766.0	15.35
1R-3, 120	766.1	15.55
1R-3, 130	766.2	13.20
1R-3, 140	766.3	14.80
1R-4, 10	766.5	14.75
1R-4, 20	766.6	14.50
1R-4, 30	766.7	13.85
1R-4, 40	766.8	12.95
1R-4, 50	766.9	14.75
1R-4, 60	767.0	16.10
1R-4, 70	767.1	14.70
1R-4, 80	767.2	13.20
1R-4, 90	767.3	13.60
1R-4, 100	767.4	14.20
1R-4, 110	767.5	13.50
1R-4, 120	767.6	12.35
1R-4, 130	767.7	14.15
1R-4, 140	767.8	16.30
1R-5, 10	768.0	14.75
1R-5, 20	768.1	14.75
1R-5, 30	768.2	15.15
1R-5, 40	768.3	13.20
1R-5, 50	768.4	14.15
1R-5, 60	768.5	13.85
1R-5, 70	768.6	14.40
1R-5, 80	768.7	14.75
1R-5, 90	768.8	13.90
1R-5, 100	768.9	14.65
1R-5, 110	769.0	14.25
1R-5, 120	769.1	12.45
1R-5, 130	769.2	13.70
1R-5, 140	769.3	15.95
1R-6, 10	769.5	16.05
1R-6, 20	769.6	14.15
1R-6, 30	769.7	14.05
1R-6, 40	769.8	15.90
1R-6, 50	769.9	15.70
1R-6, 60	770.0	14.05
1R-6, 70	770.1	13.50
1R-6, 80	770.2	13.55
1R-6, 90	770.3	13.30
1R-6, 100	770.4	13.40
2R-1, 10	771.6	16.05
2R-1, 20	771.7	16.40
2R-1, 30	771.8	15.95
2R-1, 40	771.9	16.75
2R-1, 50	772.0	17.25
2R-1, 60	772.1	19.20
2R-1, 70	772.2	16.95
2R-1, 80	772.3	15.25
2R-1, 90	772.4	15.15
2R-1, 100	772.5	16.10
2R-1, 110	772.6	15.10
2R-1, 120	772.7	14.05
2R-1, 130	772.8	12.90
2R-2, 10	773.1	13.15
2R-2, 20	773.2	12.70
2R-2, 30	773.3	12.80
2R-2, 40	773.4	14.50
2R-2, 50	773.5	14.05
2R-2, 60	773.6	12.35
2R-2, 70	773.7	14.40
2R-2, 80	773.8	14.45
2R-2, 90	773.9	13.35
2R-2, 100	774.0	13.50
2R-2, 110	774.1	14.55
2R-2, 120	774.2	13.90
2R-2, 130	774.3	12.95
2R-3, 10	774.6	14.35
2R-3, 20	774.7	16.15
2R-3, 30	774.8	16.40
2R-3, 40	774.9	16.45
2R-3, 50	775.0	15.95
2R-3, 60	775.1	13.95
2R-3, 70	775.2	16.55
2R-3, 80	775.3	16.90
2R-3, 90	775.4	14.20
2R-3, 100	775.5	16.00
2R-3, 110	775.6	18.55
2R-3, 120	775.7	20.00
3R-1, 10	781.2	17.25
3R-1, 20	781.3	16.70
3R-1, 30	781.4	18.75
3R-1, 40	781.5	17.90
3R-1, 50	781.6	17.50
3R-1, 60	781.7	14.20
3R-1, 70	781.8	15.15
3R-1, 80	781.9	18.45
3R-1, 90	782.0	17.40
3R-1, 100	782.1	18.25
3R-1, 110	782.2	22.35
3R-1, 120	782.3	17.90
3R-1, 130	782.4	16.55
3R-2, 10	782.7	18.45
3R-2, 20	782.8	19.00
3R-2, 30	782.9	20.30
3R-2, 40	783.0	18.65
3R-2, 50	783.1	17.60
3R-2, 60	783.2	16.85
3R-2, 70	783.3	18.00
3R-2, 80	783.4	16.80
3R-2, 90	783.5	16.90
3R-2, 100	783.6	16.55
3R-2, 110	783.7	15.60
3R-2, 120	783.8	16.35
3R-2, 130	783.9	18.05
3R-3, 10	784.2	17.95
3R-3, 20	784.3	20.00
3R-3, 30	784.4	15.95
3R-3, 40	784.5	17.85
3R-3, 50	784.6	16.20
3R-3, 60	784.7	17.50
3R-3, 70	784.8	16.60
3R-3, 80	784.9	14.35
3R-3, 90	785.0	15.10
3R-3, 100	785.1	13.50
3R-3, 110	785.2	14.45
3R-3, 120	785.3	13.95
3R-3, 130	785.4	14.10
3R-3, 140	785.5	16.00
3R-4, 10	785.7	16.05
3R-4, 20	785.8	15.35
3R-4, 30	785.9	15.55
3R-4, 40	786.0	16.85
3R-4, 50	786.1	14.10
3R-4, 60	786.2	15.55
3R-4, 70	786.3	14.10
3R-4, 80	786.4	14.40
3R-4, 90	786.5	13.80
3R-4, 100	786.6	14.60
3R-4, 110	786.7	16.25
3R-4, 120	786.8	16.10
3R-4, 130	786.9	18.35
3R-5, 10	787.2	20.05
3R-5, 20	787.3	17.50
3R-5, 30	787.4	18.00
3R-5, 40	787.5	20.00
3R-5, 50	787.6	18.65
3R-5, 60	787.7	16.80
3R-5, 70	787.8	15.30
4R-1, 10	790.8	18.05
4R-1, 20	790.9	18.60
4R-1, 30	791.0	16.40
4R-1, 40	791.1	16.80
4R-1, 50	791.2	17.85
4R-1, 60	791.3	17.25
4R-1, 70	791.4	18.10
4R-1, 80	791.5	17.25
4R-1, 90	791.6	20.50
4R-1, 100	791.7	17.80
4R-1, 110	791.8	16.60
4R-1, 120	791.9	16.50
4R-1, 130	792.0	18.15
4R-2, 10	792.3	19.45
4R-2, 20	792.4	17.30
4R-2, 30	792.5	21.05
4R-2, 40	792.6	21.20
4R-2, 50	792.7	21.15
4R-2, 60	792.8	17.70
4R-2, 70	792.9	19.30
4R-2, 80	793.0	18.50
4R-2, 90	793.1	16.95
4R-2, 100	793.2	15.95

Note: Only a portion of this table appears here. The complete table is available in ASCII.

Table T14. Thermal conductivity measurements, Site 1204.

Core, section, interval (cm)	Depth (mbsf)	Thermal conductivity (W/[m·K])
197-1204A-		
7R-2, 67–85	821.62	1.835
8R-1, 43–56	829.43	1.919
9R-2, 55–67	840.65	1.615
10R-3, 54–76	851.45	1.581
197-1204B-		
1R-4, 0–13	814.75	1.510
2R-4, 89–105	824.69	1.409
3R-2, 74–90	832.09	1.461
4R-3, 40–51	843.00	1.641
5R-2, 26–39	851.06	1.621
6R-2, 79–96	860.82	1.768
7R-2, 24–37	869.91	1.672
8R-2, 78–91	880.08	1.783
9R-3, 82–94	889.51	1.597
10R-2, 12–23	890.42	1.631
11R-1, 124–145	897.84	1.554
12R-1, 69–81	906.99	1.721
13R-1, 50–65	908.80	1.680
14R-2, 124–138	918.26	1.495
15R-3, 77–89	929.31	1.551
16R-4, 45–55	939.96	0.827
17R-1, 55–68	945.45	1.513
17R-3, 52–69	947.73	1.293

Note: This table is also available in **ASCII.**

Table T15. Index properties, Site 1204.

Core, section, interval (cm)	Depth (mbsf)	Water content (%)		Density (g/cm^3)			Porosity (%)	Void ratio
		Bulk	Dry	Bulk	Dry	Grain		
197-1204A-								
1R-1, 73–75	762.63	31.7	46.4	1.80	1.23	2.79	55.8	1.26
1R-2, 73–75	764.13	28.8	40.5	1.86	1.32	2.77	52.3	1.10
1R-3, 71–73	765.61	35.7	55.6	1.72	1.10	2.74	59.8	1.49
1R-4, 73–75	767.13	31.5	45.9	1.80	1.23	2.77	55.4	1.24
1R-5, 73–75	768.63	27.4	37.8	1.88	1.37	2.76	50.4	1.02
1R-6, 63–65	770.03	30.4	43.6	1.82	1.27	2.75	53.9	1.17
2R-1, 81–83	772.31	27.2	37.3	1.87	1.37	2.71	49.7	0.99
2R-2, 73–75	773.73	28.6	40.0	1.82	1.30	2.64	50.8	1.03
2R-3, 73–75	775.23	21.2	26.9	2.02	1.60	2.75	41.9	0.72
3R-1, 90–92	782.00	19.5	24.2	2.06	1.65	2.72	39.1	0.64
3R-2, 81–83	783.41	25.4	34.0	1.93	1.44	2.77	48.0	0.92
3R-3, 79–81	784.89	31.9	46.9	1.78	1.22	2.74	55.6	1.25
3R-4, 40–42	786.00	24.2	31.9	1.92	1.46	2.67	45.4	0.83
3R-5, 70–72	787.80	30.8	44.5	1.84	1.27	2.86	55.4	1.24
4R-1, 56–58	791.26	17.5	21.2	2.11	1.74	2.72	36.0	0.56
4R-2, 97–99	793.17	25.5	34.2	1.92	1.43	2.74	47.8	0.92
4R-3, 106–108	794.76	23.5	30.7	1.93	1.48	2.65	44.3	0.80
4R-4, 125–127	796.45	21.2	26.9	2.04	1.60	2.77	42.1	0.73
5R-1, 68–70	800.98	26.0	35.2	1.92	1.42	2.77	48.7	0.95
5R-2, 103–105	802.83	27.6	38.1	1.88	1.36	2.76	50.7	1.03
5R-3, 73–75	804.03	27.4	37.8	1.88	1.36	2.75	50.3	1.01
5R-4, 24–26	805.05	26.3	35.7	1.90	1.40	2.74	48.8	0.95
6R-1, 17–19	810.07	25.1	33.6	1.93	1.44	2.73	47.3	0.90
6R-2, 58–60	811.98	45.7	84.1	1.55	0.84	2.75	69.3	2.26
6R-3, 88–90	813.78	34.1	51.7	1.75	1.16	2.78	58.4	1.40
6R-4, 84–86	815.24	36.3	56.9	1.72	1.10	2.80	60.9	1.56
7R-3, 118–122	823.50	3.4	3.5	2.78	2.68	2.95	9.2	0.10
8R-1, 16–21	829.16	3.7	3.9	2.73	2.63	2.92	10.0	0.11
9R-2, 108–110	841.18	5.4	5.7	2.76	2.61	3.05	14.6	0.17
10R-3, 55–57	851.46	4.4	4.6	2.69	2.58	2.91	11.5	0.13
197-1204B-								
1R-1, 95–97	811.65	38.4	62.3	1.67	1.03	2.75	62.6	1.67
1R-2, 92–94	813.12	24.7	32.8	1.94	1.46	2.75	46.8	0.88
1R-3, 17–19	813.87	24.6	32.7	1.91	1.44	2.66	45.9	0.85
1R-4, 73–75	815.48	9.1	10.0	2.41	2.19	2.79	21.5	0.27
2R-3, 25–27	823.18	3.8	4.0	2.73	2.63	2.93	10.3	0.12
3R-2, 84–86	832.19	4.6	4.8	2.58	2.46	2.79	11.6	0.13
4R-1, 61–63	840.21	5.4	5.7	2.67	2.53	2.94	14.0	0.16
5R-2, 33–35	851.13	4.6	4.8	2.73	2.60	2.97	12.2	0.14
6R-3, 52–54	862.05	4.7	4.9	2.72	2.59	2.96	12.4	0.14
7R-2, 140–142	871.07	4.3	4.5	2.76	2.64	2.98	11.6	0.13
8R-3, 88–90	881.64	3.7	3.8	2.83	2.72	3.03	10.2	0.11
9R-2, 7–9	887.36	4.5	4.8	2.74	2.61	2.98	12.2	0.14
10R-3, 27–29	891.82	2.9	3.0	2.83	2.74	2.98	8.1	0.09
11R-1, 107–115	897.67	3.8	4.0	2.76	2.65	2.96	10.3	0.12
12R-2, 12–14	907.83	3.4	3.5	2.91	2.81	3.12	9.7	0.11
13R-1, 19–21	908.49	4.4	4.6	2.71	2.59	2.93	11.5	0.13
13R-3, 33–35	911.49	5.6	5.9	2.62	2.47	2.89	14.3	0.17
14R-2, 67–69	917.69	5.8	6.1	2.67	2.51	2.96	15.0	0.18
15R-2, 77–79	927.81	7.3	7.9	2.61	2.42	2.97	18.6	0.23
16R-3, 40–51	938.52	19.7	24.6	1.99	1.60	2.60	38.4	0.62
17R-2, 104–106	947.12	5.5	5.8	2.65	2.50	2.92	14.2	0.17
17R-3, 12–14	947.33	17.7	21.5	2.14	1.76	2.80	37.0	0.59

Note: This table is also available in **ASCII.**

Table T16. Compressional wave velocity measurements, Site 1204.

Core, section, interval (cm)	Depth (mbsf)	Direction	Velocity (m/s)
197-1204A-			
1R-1, 116.2	763.06	x	1714.7
1R-2, 83.1	764.23	x	1661.2
1R-3, 59.9	765.50	x	1693.9
1R-4, 89	767.29	x	1699.7
1R-5, 102.7	768.93	x	1770.1
1R-6, 95	770.35	x	1656.4
2R-1, 108.9	772.59	x	1678.1
2R-2, 41.7	773.42	x	1623.7
2R-3, 36.8	774.87	x	2283.5
2R-3, 55.2	775.05	x	1799.8
3R-1, 32.8	781.43	x	1942.3
3R-2, 88.7	783.49	x	1855.4
3R-3, 98.6	785.09	x	1749.5
3R-4, 15	785.75	x	1699.8
3R-4, 121.8	786.82	x	2165.6
3R-5, 17.5	787.28	x	2207.8
3R-5, 30.8	787.41	x	1947.9
4R-1, 43.3	791.13	x	1997.3
4R-2, 20.6	792.41	x	1793.2
4R-3, 90.7	794.61	x	2119.7
4R-4, 64.2	795.84	x	1777.5
5R-1, 55.4	800.85	x	1700.8
5R-2, 55.9	802.36	x	2075.1
5R-3, 97.8	804.28	x	1663.6
5R-4, 35.8	805.17	x	1680.9
6R-1, 26.4	810.16	x	1687.9
6R-2, 22	811.62	x	1711.9
6R-3, 78.7	813.69	x	1640.6
6R-4, 49.1	814.89	x	2122.2
7R-1, 99	820.49	z	4719.2
7R-1, 99	820.49	z	4670.8
7R-2, 79	821.74	x	4793.4
7R-2, 79	821.74	z	4937.1
7R-3, 35	822.67	z	5714.7
7R-4, 86	824.68	z	4911.0
8R-1, 133	830.33	z	5220.2
8R-2, 33	830.83	x	4714.9
8R-2, 33	830.83	z	4901.7
9R-1, 74	839.34	z	4702.6
9R-2, 110	841.20	x	4588.4
9R-2, 110	841.20	z	4476.0
9R-3, 78	842.38	z	4838.9
9R-4, 18	843.15	z	4519.7
10R-1, 126	849.56	z	4683.1
10R-2, 75	850.52	z	4966.6
10R-3, 57	851.48	x	4518.9
10R-3, 57	851.48	z	4700.8
10R-4, 139	853.75	z	4235.5
10R-5, 107	854.89	z	4551.2
197-1204B-			
1R-1, 46	811.16	x	1778.9
1R-2, 123.7	813.44	x	2195.3
1R-3, 9.2	813.79	x	2428.7
1R-4, 70	815.45	x	4687.7
1R-4, 70	815.45	z	4864.8
2R-1, 22	820.52	z	3823.4
2R-4, 101	824.81	x	4198.2
2R-4, 101	824.81	z	4397.8
3R-1, 39	830.29	x	3692.0
3R-1, 39	830.29	z	3609.3
3R-2, 85	832.20	z	5020.3
4R-1, 62	840.22	x	4543.6
4R-1, 62	840.22	z	4688.8
4R-2, 64	841.74	z	4101.9
5R-1, 58	849.88	x	4281.1
5R-1, 58	849.88	z	4561.9
5R-2, 34	851.14	z	5182.3
6R-2, 84	860.87	z	4725.6
6R-3, 53	862.06	x	4562.6
6R-4, 38	863.41	z	4898.3
7R-1, 126	869.46	z	5231.2
7R-3, 140	872.57	x	5203.5
7R-3, 140	872.57	z	5692.9
8R-2, 22	879.52	z	5149.9
8R-3, 89	881.65	x	4704.2
8R-3, 89	881.65	z	4890.9
9R-2, 9	887.38	x	4555.5
9R-2, 9	887.38	z	4668.3
9R-3, 127	889.96	z	5575.2
10R-1, 6	888.86	z	4681.2
10R-3, 28	891.83	x	4712.4
10R-3, 28	891.83	z	5054.2
10R-4, 41	892.77	x	4659.3
11R-1, 26	896.86	z	4524.6
11R-2, 39	898.44	x	4674.0
11R-2, 39	898.44	z	4982.8
12R-1, 80	907.10	x	4814.5
12R-1, 80	907.10	z	5141.5
12R-2, 13	907.84	z	5133.2
13R-1, 20	908.50	z	4674.6
13R-3, 34	911.50	z	4366.0
13R-4, 83	913.16	x	4312.3
14R-1, 15	916.05	z	4702.7
14R-2, 67	917.69	x	4194.2
14R-2, 67	917.69	z	4393.1
15R-1, 12	925.72	z	4585.2
15R-3, 84	929.38	x	4553.0
15R-3, 84	929.38	z	4657.6
16R-1, 18	935.38	z	2877.5
16R-4, 50	940.01	x	2622.9
16R-4, 50	940.01	z	2624.6
17R-1, 108	945.98	x	4509.7
17R-1, 108	945.98	z	4707.9
17R-3, 13	947.34	x	2879.7
17R-3, 13	947.34	z	2967.8

Note: This table is also available in ASCII.

Table T17. SIOSEIS process parameters for predictive deconvolution, bandpass filtering, and finite-difference migration.

```
Line 1:
  decon
    fno 479 lno 479 sedts 3.17 4.3 fillen .3 pdist .006 prewhi 1 double yes end
    fno 574 lno 574 sedts 3.165 4.4 fillen .3 pdist .006 prewhi 1 double yes end
    fno 680 lno 680 sedts 3.15 4.4 fillen .3 pdist .006 prewhi 1 double yes end
    fno 719 lno 719 sedts 3.14 4.3 fillen .3 pdist .006 prewhi 1 double yes end
    end
  filter
    fno 479 lno 719 pass 40 100 fillen 55 end
    end
  fdmigr
    fno 479 lno 479 vtp 1500 3.215 1650 4.08 3300 5
    dx 18.2 nx 441 bpad 100 epad 100 tsteps 3.7 .1 4.0 .01 4.7 .005 end
    fno 552 lno 552 vtp 1500 3.215 1650 4.13 3300 5
    dx 18.2 nx 441 bpad 100 epad 100 tsteps 3.7 .1 4.0 .01 4.7 .005 end
    fno 576 lno 632 vtp 1500 3.215 1650 4.17 3300 5
    dx 18.2 nx 441 bpad 100 epad 100 tsteps 3.7 .1 4.0 .01 4.7 .005 end
    fno 719 lno 719 vtp 1500 3.195 1650 4.045 3300 5
    dx 18.2 nx 441 bpad 100 epad 100 tsteps 3.7 .1 4.0 .01 4.7 .005 end
    end

Line 3:
  decon
    fno 3386 lno 3386 sedts 3.14 4.4 fillen .3 pdist .006 prewhi 1 double yes end
    fno 3468 lno 3468 sedts 3.16 4.5 fillen .3 pdist .006 prewhi 1 double yes end
    fno 3546 lno 3546 sedts 3.18 4.5 fillen .3 pdist .006 prewhi 1 double yes end
    fno 3626 lno 3626 sedts 3.20 4.4 fillen .3 pdist .006 prewhi 1 double yes end
    end
  filter
    fno 3386 lno 3626 pass 40 100 fillen 55 end
    end
  fdmigr
    fno 3386 lno 3386 vtp 1500 3.180 1650 4.100 3000 5
    dx 16.5 nx 441 bpad 100 epad 100 tsteps 3.7 .1 4.0 .01 4.7 .005 end
    fno 3441 lno 3441 vtp 1500 3.200 1650 4.175 3000 5
    dx 16.5 nx 441 bpad 100 epad 100 tsteps 3.7 .1 4.0 .01 4.7 .005 end
    fno 3482 lno 3482 vtp 1500 3.210 1650 4.17 3000 5
    dx 16.5 nx 441 bpad 100 epad 100 tsteps 3.7 .1 4.0 .01 4.7 .005 end
    fno 3505 lno 3505 vtp 1500 3.215 1650 4.17 3000 5
    dx 16.5 nx 441 bpad 100 epad 100 tsteps 3.7 .1 4.0 .01 4.7 .005 end
    fno 3626 lno 3626 vtp 1500 3.245 1650 4.15 3000 5
    dx 16.5 nx 441 bpad 100 epad 100 tsteps 3.7 .1 4.0 .01 4.7 .005 end
    end
```

Note: Processing was performed in the order shown. (See also **http://sioseis.ucsd.edu.**)